U.PORTO

FEUP FACULDADE DE ENGENHARIA
UNIVERSIDADE DO PORTO

AN EFFICIENT METHOD FOR MODELLING THE NONLINEAR TRAIN-BRIDGE INTERACTION

Sérgio Gonçalves Moreira das Neves

2016

A dissertation presented to the Faculty of Engineering of the University of Porto for the degree of Doctor in Civil Engineering.

Supervisor: Prof. Alvaro Azevedo (FEUP, Portugal)
Co-Supervisor: Prof. Rui Calçada (FEUP, Portugal)

FCT Fundação para a Ciência e a Tecnologia
MINISTÉRIO DA CIÊNCIA, TECNOLOGIA E ENSINO SUPERIOR
POPH PROGRAMA OPERACIONAL POTENCIAL HUMANO
QREN QUADRO DE REFERÊNCIA ESTRATÉGICO NACIONAL PORTUGAL 2007.2013
GOVERNO DA REPÚBLICA PORTUGUESA
UNIÃO EUROPEIA Fundo Social Europeu

“An expert is someone who knows some of the worst mistakes that can be made in his subject, and how to avoid them.”

Werner Heisenberg

To my parents, brother and grandparents

ABSTRACT

An accurate, robust and efficient vehicle-structure interaction (VSI) method, referred to as the direct method, has been developed to help close the gap between commercial finite element (FE) and multibody simulation (MBS) programs. FE programs can accurately simulate the deformation of the vehicles and structures but have simplified contact formulations that cannot efficiently take into account normal and tangential contact forces. MBS programs can efficiently account for the latter but do not simulate the deformations of the structure with the same level of detail. Over the last decades, there has been a proliferation of studies proposing VSI methods in order to close this gap. However, these studies often lack a thorough comparison between the proposed and existing methods. A comprehensive literature review covering VSI methods based on equilibrium of contact forces, variational formulations and condensation techniques is presented here. The direct method proved to be the most suitable approach.

The direct method is implemented in MATLAB and the structures and vehicles are modelled using ANSYS. This program allows the development of models with a high degree of complexity and with several types of FE. This methodology is also valid when the vehicles are modelled using multibody systems. An enhanced node-to-segment contact element that includes a Hertzian spring, which relates the forces acting at the contact region with its local deformations, is proposed. The constraint equations that relate the displacements of the vehicles and structure are imposed only when contact occurs; this allows for an effective simulation of the loss of contact. The results obtained with the direct method are compared with semi-analytical solutions and those calculated with ANSYS in order to validate the accuracy and efficiency of the proposed method.

The passage of the Korean high-speed train over a railway viaduct is analysed using the direct method. Special focus is given to the development and validation of the numerical models. The model of the viaduct is calibrated using a FE model updating technique that compares the numerical response with measured data. The influence of isolated defects and periodic irregularities, local deformations of the viaduct slab and force-deflection relationship of the Hertzian spring on wheel-rail contact forces and vertical accelerations of the slab is analysed in detail.

RESUMO

Na presente dissertação é proposto um método preciso, robusto e eficiente para analisar a interação veículo-estrutura, designado por método direto, tendo em vista colmatar a lacuna existente entre programas comerciais de elementos finitos e de sistemas multicorpo. Os programas de elementos finitos simulam adequadamente as deformações dos veículos e das estruturas, mas utilizam formulações simplificadas que não permitem considerar eficientemente as forças normais e tangenciais de contacto. Os programas de simulação de sistemas multicorpo consideram adequadamente estas forças mas não simulam as deformações das estruturas com o necessário nível de detalhe. Nas últimas décadas, tem havido uma proliferação de estudos propondo métodos de interação veículo-estrutura por forma a colmatar esta lacuna. No entanto, estes carecem de uma comparação rigorosa com os métodos existentes. É apresentada neste trabalho uma revisão bibliográfica exaustiva de métodos deste tipo baseados no equilíbrio das forças de contacto, formulações variacionais e técnicas de condensação. O método direto provou ser a abordagem mais adequada.

O método direto encontra-se implementado em MATLAB. As estruturas e os veículos são modelados com o programa ANSYS, que permite desenvolver modelos complexos com diferentes tipos de elementos finitos. Esta metodologia é igualmente válida quando os veículos são modelados com sistemas multicorpo. É proposto um elemento de contacto ponto-elemento que inclui uma mola de Hertz que relaciona as forças com as deformações na região de contacto. As equações de restrição que relacionam os deslocamentos dos veículos e da estrutura são apenas impostas quando ocorre contacto, permitindo assim uma simulação efetiva da perda de contacto. Os resultados obtidos com recurso ao método direto são comparados com soluções semi-analíticas e com os resultados calculados com o programa ANSYS por forma a validar a precisão e eficiência do método proposto.

O método direto foi aplicado na análise da passagem de um comboio de alta velocidade Coreano sobre um viaduto ferroviário. É dedicada uma atenção especial ao desenvolvimento e validação dos correspondentes modelos numéricos. O modelo do viaduto é calibrado com recurso a uma metodologia que compara a resposta numérica com resultados experimentais. A influência das irregularidades pontuais e distribuídas da via, das deformações locais da laje e da relação força-deformação da mola de Hertz nas forças de contacto roda-carril e nas acelerações verticais da laje é analisada detalhadamente.

LIST OF PUBLICATIONS

The following publications have been derived from the development of this thesis.

Articles in indexed international journals

- Montenegro, P. A., Neves, S. G. M., Calçada, R., Tanabe, M., & Sogabe, M. (2015). Wheel-rail contact formulation for analyzing the lateral train-structure dynamic interaction. *Computers & Structures, 152*, 200-214. DOI:10.1016/j.compstruc.2015.01.004.
- Neves, S. G. M., Montenegro, P. A., Azevedo, A. F. M., & Calçada, R. (2014). A direct method for analyzing the nonlinear vehicle-structure interaction. *Engineering Structures, 69*, 83-89. DOI:10.1016/j.engstruct.2014.02.027.
- Neves, S. G. M., Azevedo, A. F. M., & Calçada, R. (2012). A direct method for analyzing the vertical vehicle-structure interaction. *Engineering Structures, 34*, 414-420. DOI:10.1016/j.engstruct.2011.10.010.

Proceedings in international conferences

- Montenegro, P. A., Neves, S. G. M., Calçada, R., Tanabe, M., & Sogabe, M. (2014). A nonlinear vehicle-structure interaction methodology for the assessment of the train running safety. In A. Cunha, E. Caetano, P. Ribeiro, & G. Müller (Eds.), *EURODYN 2014 - 9th International Conference on Structural Dynamics*. Porto, Portugal.
- Montenegro, P. A., Neves, S. G. M., Calçada, R., Tanabe, M., & Sogabe, M. (2014). A three dimensional train-structure interaction methodology: Experimental validation. In J. Pombo (Ed.), *Railways 2014 - 2nd International Conference on Railway Technology: Research, Development and Maintenance*. Ajaccio, Corsica. Stirlingshire, UK: Civil-Comp Press. DOI:10.4203/ccp.104.71.
- Neves, S. G. M., Montenegro, P. A., Azevedo, A. F. M., & Calçada, R. (2014). A direct method for analyzing the nonlinear vehicle-structure interaction in high-speed railway lines. In J. Pombo (Ed.), *Railways 2014 - 2nd International Conference on Railway Technology: Research, Development and Maintenance*. Ajaccio, Corsica. Stirlingshire, UK: Civil-Comp Press. DOI:10.4203/ccp.104.81.

- Montenegro, P. A., Neves, S. G. M., Azevedo, A. F. M., & Calçada, R. (2013). A nonlinear vehicle-structure interaction methodology with wheel-rail detachment and reattachment. In M. Papadrakakis, N.D.Lagaros, & V. Plevris (Eds.), *COMPDYN 2013 – 4th International Conference on Computational Methods in Structural Dynamics and Earthquake Engineering*. Kos Island, Greece.
- Neves, S., Azevedo, A., & Calçada, R. (2008). Development of an efficient finite element model for the dynamic analysis of the train-bridge interaction. *IABMAS 2008 – 4th International Conference on Bridge Maintenance, Safety and Management*. Seoul, Korea.
- Azevedo, A., Neves, S., & Calçada, R. (2008). Dynamic analysis of the train-bridge interaction: an accurate and efficient numerical method. *EURODYN 2008 - 7th European Conference on Structural Dynamics*. Southampton, United Kingdom.

ACKNOWLEDGEMENTS / AGRADECIMENTOS

The work carried out in this thesis lasted longer than I had anticipated and it would have lasted even longer without the support of all who have accompanied me during this period. I want to express my sincere gratitude to all friends and colleagues whose friendship, understanding and support made this journey easier. In particular, I would like to express my special appreciation and thanks to:

- My supervisor, Prof. Álvaro Azevedo, for his unconditional support, mentorship and depth of knowledge demonstrated throughout my work. The lessons learnt from this are an invaluable tool for the future.
- My co-supervisor, Prof. Rui Calçada, for his motivation and broad range of knowledge in the field of railways. Being part of the railway research group lead by him, Centro de Saber da Ferrovia (CSF), has been an enriching experience.
- My thesis committee, Prof. José Goicolea, Prof. Constança Rigueiro, Prof. Cecília Vale and Prof. Rui Faria, for the insightful discussion and encouragement, which were an important contribution for improving this work.
- Fundação para a Ciência e a Tecnologia for the financial support provided under Grant No. SFRH/BD/39190/2007.
- REFER for the data provided regarding the Alverca viaduct and all the support given to the ambient vibration tests carried out.
- To all my colleagues of the Institute of Railway Research (IRR) of the University of Huddersfield, in particular Dr. Yann Bezin and Prof. Simon Iwnicki, for all the support, patience and motivation. I am very grateful for having been given the opportunity to continue my research career at IRR.
- My friend Dr. Pedro Montenegro for all his friendship, patience and collaboration in the development and implementation of the vehicle-structure interaction algorithm presented in this work. Working closely with him has been a very enriching experience.
- Profs. Rui Faria and João Guedes, from the Faculty of Engineering of the University of Porto, for the very helpful discussions that we had throughout this work.

- My friend Diogo Ribeiro for all the helpful discussions and support given.
- My friend Emily Hurst for all the support given and for reviewing the English of a Latin.
- My friends Dimitrios Kostovasilis, Gareth Tucker, Ilaria Grossoni and Yousif Muhamedsalih for reviewing my work.
- All friends of the research group CSF, namely, Alejandro Tejada, Andreia Meixedo, Cristiana Bonifácio, Cristina Ribeiro, Diogo Ribeiro, Joana Delgado, João Barbosa, João Francisco, João Rocha, Joel Malveiro, Nuno Ribeiro, Nuno Santos and Pedro Jorge.
- All other friends of the Faculty of Engineering, namely, Alexandre Costa, Fernando Bastos, Isabel Horta, Luís Macedo, Mário Marques, Miguel Araújo, Miriam López, Nuno Pereira, Ricardo Monteiro, Rui Barros and Sara Rios.
- To my best friend, Bruno Silva, for sharing the most important moments of my life.
- À minha família mais chegada, nomeadamente, aos meus pais, avós, ao meu irmão Pedro e cunhada Ângela, bem como ao meu sobrinho e afilhado Tiaguinho – a todos eles dedico esta tese, com a convicção de que o maior presente que lhes posso dar é o da sua conclusão, por forma a poder finalmente ter a disponibilidade que eles merecem.
- Agradeço duma maneira muito especial à minha querida avó Aurora, que faleceu no passado mês de Outubro, por todo o carinho e apoio que sempre me deu.

CONTENTS

1 Introduction 1

1.1 Background 1

1.2 Objectives and scope 3

1.3 Outline of the thesis 4

2 Overview of vehicle-structure interaction methods 7

2.1 Introduction 7

2.2 Direct equilibrium of contact forces 10

2.2.1 Formulation of the equations of motion 10

2.2.2 Direct integration of the equations of motion 11

2.2.3 Contact constraint equations 12

2.2.4 Direct method 13

2.2.5 Iterative methods 13

2.2.6 Numerical example 17

2.3 Variational formulations 20

2.3.1 Formulation of the equilibrium equations 21

2.3.2 Lagrange multiplier method 22

2.3.3 Penalty method 23

2.4 Condensation methods 24

2.5 Concluding remarks 26

3 Wheel-rail contact mechanics 29

3.1 Introduction 29

3.2 Basic concepts and definitions 30

3.3 Hertz theory 31

3.3.1 Geometry of non-conforming surfaces 33

3.3.2 Pressure distribution and elastic deformation....39
3.4 Numerical example....48
3.5 Concluding remarks....56

4 An efficient method for analysing the vehicle-structure interaction....57

4.1 Introduction....57
4.2 Vehicle-structure interaction method....58
4.2.1 Contact and target elements....58
4.2.2 Formulation of the equations of motion....60
4.2.3 Direct integration of the equations of motion....62
4.2.4 Formulation of the contact constraint equations....62
4.2.5 Complete system of equations....63
4.3 Semi-analytical solutions....65
4.3.1 Beam transverse vibration theory....65
4.3.1.1 Equation of undamped motion....65
4.3.1.2 Vibration mode shapes and frequencies....66
4.3.1.3 Modal analysis of forced dynamic response....68
4.3.2 Moving force....68
4.3.3 Moving mass....69
4.3.4 Moving sprung mass....70
4.4 Numerical examples and verification....72
4.4.1 Simply supported beam subjected to one moving sprung mass....72
4.4.2 Simply supported beam subjected to fifty moving sprung masses....74
4.5 Concluding remarks....79

5 Enhanced nonlinear contact element....81

5.1 Introduction....81
5.2 Vehicle-structure interaction method....81

5.2.1 Enhanced contact element ... 81
5.2.2 Formulation of the equations of motion ... 83
5.2.3 Incremental formulation for nonlinear analysis ... 85
5.2.4 Formulation of the contact constraint equations ... 86
5.2.5 Complete algorithm ... 88
5.3 Numerical examples and verification ... 90
5.3.1 Two simply supported spans modelled with 2D beam elements ... 90
5.3.2 Two simply supported spans modelled with 3D solid elements ... 95
5.3.3 Inclined rigid beam ... 97
5.4 Concluding remarks ... 99

6 Modelling and dynamic analysis of the train-track system ... 101

6.1 Introduction ... 101
6.2 Numerical modelling of the KHST ... 102
6.2.1 General description ... 102
6.2.2 Finite element model ... 103
6.2.3 Static and modal analyses ... 108
6.2.4 Simplified model of the KHST ... 110
6.3 Numerical modelling of the track ... 112
6.3.1 General description ... 112
6.3.2 Geometrical and mechanical properties ... 113
6.3.3 Finite element model ... 115
6.3.4 Response in the frequency domain ... 116
6.3.5 Damping of the track ... 118
6.3.6 Optimisation of the mesh ... 118
6.4 Dynamic response of the train-track system ... 122
6.4.1 Influence of the 2D track model ... 123
6.4.2 Influence of the Hertzian contact spring ... 131

6.4.3 Influence of the numerical dissipation of the time integration scheme 133
6.4.4 Comparison between the MATLAB and ANSYS programs.........................135
6.5 Concluding remarks...138

7 Case study of the Alverca railway viaduct...141

7.1 Introduction...141
7.2 Numerical modelling of the Alverca viaduct...142
7.2.1 General description...142
7.2.2 Geometrical and mechanical properties...144
7.2.3 Finite element model...145
7.2.4 Modal parameters...147
7.2.5 Ambient vibration test...148
7.2.6 Model updating techniques...151
7.2.6.1 Sensitivity analysis...151
7.2.6.2 Optimisation algorithms..153
7.2.6.3 Automatic mode pairing..154
7.2.6.4 Optimisation of the mesh..155
7.2.6.5 Model updating of the Alverca viaduct...158
7.2.7 Damping of the viaduct...164
7.3 Dynamic response of the train-viaduct system......................................166
7.3.1 Influence of the transition between plane track and viaduct.........166
7.3.2 Influence of the track irregularities...169
7.3.2.1 Isolated defects..169
7.3.2.2 Periodic irregularities..176
7.3.3 Influence of the Hertzian contact spring..179
7.3.4 Comparison between the MATLAB and ANSYS programs...........181
7.4 Concluding remarks...186

8 Conclusions and future developments 189

8.1 Conclusions 189

8.2 Future developments 192

Appendix A – A 2-by-2 block factorisation solver 195

Appendix B – A 3-by-3 block factorisation solver 197

Appendix C – Validation of the model updating techniques 201

References 213

ABBREVIATIONS AND SYMBOLS

The abbreviations, symbols and notations used throughout this thesis are listed below.

ABBREVIATIONS

2D / 3D	Two-dimensional / Three-dimensional
d.o.f.	Degree Of Freedom
EC	European Commission
EN	European Norm
FE	Finite Element
KHST	Korean High-Speed Train
MAC	Modal Assurance Criterion
MBS	Multibody Simulation

SYMBOLS

a	Transverse displacement
$\mathbf{a}$	Nodal displacements vector
a, b	Semi-axes of the elliptical contact area
a_0	Amplitude of the irregularity
A_0 to A_5	Constants of the HHT-α method
A	Cross-sectional area / Hertz geometric parameter
B	Hertz geometric parameter
$\mathbf{C}$	Viscous damping matrix
C_1, C_2	Geometric constants used in the Hertz theory
$\mathbf{D}$	Matrix relating the contact forces to the equivalent nodal loads / Diagonal matrix
E	Young's modulus
f	Natural cyclic frequency
$\mathbf{F}$	Load vector
F_n	Applied normal force

g	Acceleration of gravity
G	Shear modulus
h	Gap between two undeformed surfaces
$\mathbf{H}$	Matrix relating the nodal displacements to the displacements of the contact nodes and auxiliary points of the target elements
i	Iteration counter
I	Moment of inertia
$\mathbf{I}$	Identity matrix
k	Spring stiffness / Ellipse axes ratio
$\mathbf{K}$	Stiffness matrix
$\bar{k}$	Parameter used to control the wavelength of the isolated defect
$\overline{\mathbf{K}}$	Effective stiffness matrix
k_h	Linearized value of the stiffness of the Hertzian spring around the static wheel load
K_h	Constant of the Hertz force law
L	Span length
$\mathbf{L}$	Lower triangular matrix
m	Mass per unit length / Hertz coefficient
$\mathbf{M}$	Mass matrix
n	Hertz coefficient
N_1	Contact node of the wheel
N_2, N_3	Nodes of the target element of the structure
N_4	Node of the Hertzian spring of the contact element
p	Applied pressure distribution / Applied force
P	Auxiliary internal point of the target element
$\mathbf{P}$	Externally applied nodal loads vector
r	Rolling radius of the wheel
$\mathbf{r}$	Vector of irregularities between the contact and target elements
r_0	Nominal rolling radius of the wheel
R	Principal radius of curvature
$\mathbf{R}$	Vector of nodal forces corresponding to the internal element stresses

$\mathbf{S}$	Support reactions vector
$\mathbf{U}$	Upper triangular matrix
v	Displacement of a point / Vehicle speed
x, y, z	Cartesian coordinate system
$\mathbf{X}$	Contact forces vector
α	Parameter of the HHT-α method / Penalty parameter
β	Parameter of the Newmark method
γ	Parameter of the Newmark method / Contact angle
δ	Deflection / Displacement
Δt	Time step
ε	Tolerance
θ	Auxiliary angle used in the Hertz theory / Rotation of a point
λ	Lagrange multiplier / Wavelength
ν	Poisson's ratio
ξ_1, ξ_2, ξ_3	Local coordinate system of the contact pair
ρ	Density / Spectral radius
Φ_i	Eigenvector of mode i
$\boldsymbol{\psi}$	Residual forces vector
ω	Natural circular frequency

NOTATIONS

$\Delta(\cdot)$	Incremental or variation of $(\cdot)$
$\dot{(\cdot)}$	First time derivative of $(\cdot)$
$\ddot{(\cdot)}$	Second time derivative of $(\cdot)$
$\lVert(\cdot)\rVert$	Norm of $(\cdot)$
$(\cdot)_0$	Referred to the initial value of $(\cdot)$
$(\cdot)_{bg}$	Referred to the bogie
$(\cdot)_{cb}$	Referred to the carbody
$(\cdot)^{ce}$	Referred to the contact element

$(\cdot)_{\exp}$	Referred to experimental
$(\cdot)_F$	Referred to the free d.o.f.
$(\cdot)^i$	Referred to the iteration i
$(\cdot)_I$	Referred to the free d.o.f. (excluding *R* and *Y* types)
$(\cdot)_{\hat{I}}$	Referred to the free d.o.f. of the structure
$(\cdot)_{\tilde{I}}$	Referred to the free d.o.f. of the vehicles
$(\cdot)_{num}$	Referred to numerical
$(\cdot)_p$	Referred to the primary suspension
$(\cdot)_P$	Referred to the prescribed d.o.f.
$(\cdot)_r$	Referred to the rail
$(\cdot)_R$	Referred to the free d.o.f of the contact elements (excluding *Y* type)
$(\cdot)_s$	Referred to the secondary suspension
$(\cdot)^t$	Referred to the previous time step
$(\cdot)^{t+\Delta t}$	Referred to the current time step
$(\cdot)^{te}$	Referred to the target element
$(\cdot)^{theo}$	Referred to theoretical
$(\cdot)^{updt}$	Referred to updated
$(\cdot)_w$	Referred to the wheel
$(\cdot)_{ws}$	Referred to the wheelset
$(\cdot)_Y$	Referred to the d.o.f of the internal nodes added by the contact elements

1 INTRODUCTION

1.1 BACKGROUND

The railway sector faces very demanding challenges that are critical for the well-being and mobility of people. The greenhouse gases produced by human activities are causing global warming and changes to the climate. According to the Intergovernmental Panel on Climate Change (IPCC), without urgent action climate changes will lead to severe and irreversible impacts across the planet. At the 21st United Nations Climate Change Conference, held in Paris in December 2015, 195 countries adopted the first legally binding global climate agreement (Paris Agreement, 2015). This agreement defines the actions necessary to limit the rise in global average temperature to below 2°C when compared to pre-industrial levels. In order to achieve this goal, the European Commission (EC) published a roadmap setting the target of cutting the emissions by 80-95% below 1990 levels by 2050 (White paper, 2011). The EC also published a study showing that a reduction of at least 60% of emissions is required from the transport sector to achieve the defined targets by 2050 (EC communication, 2011). The CO_2 emissions in 2013 from different modes of passenger transport are shown in Fig. 1.1 (EEA Report n. 7, 2014), with rail transport having the lowest values. The average number of passengers per vehicle considered is also indicated in the figure.

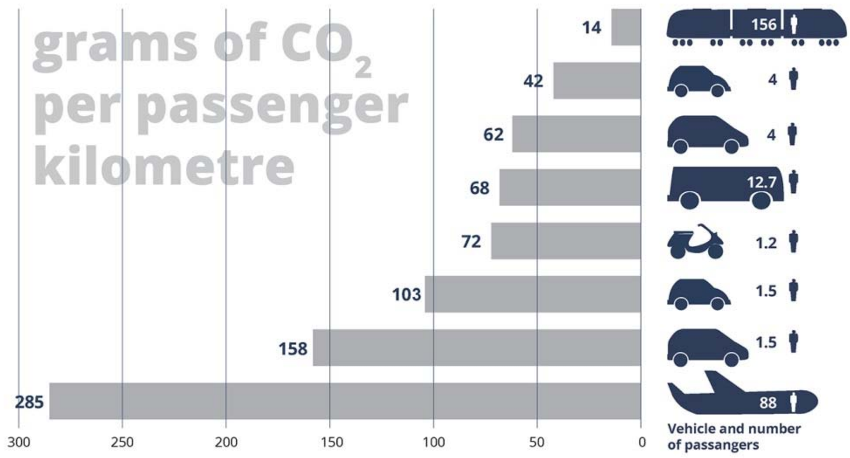

Figure 1.1 – CO_2 emissions in 2013 by transport mode (train, small and large cars, bus, two-wheeler and aircraft).

Besides having a low environmental impact, rail transport also plays a critical role in the mobility of people and goods, thus contributing to the economic and social development of most countries. The EC policy states that by 2050 most of medium-distance passenger transport should go by rail and that 50% of road freight over 300 km should shift to other modes such as rail or waterborne transport (White paper, 2011). To meet these goals, the length of high-speed rail network that existed in 2011 has to be tripled by 2030 and a coherent network including links and accessibility between all major cities and core network airports has to be developed by 2050. To achieve this, it would be necessary to triple the number of kilometres of lines built annually with an estimated investment of 300 to €500 billion (Civity, 2013). These objectives provide unique research opportunities such as Shift2Rail, which is a joint effort of several stakeholders of the European rail sector to drive innovation. This project has an estimated budget of €920 million (Shift2Rail, 2014).

The ambitious plans set for the transport sector lead to a high rate of construction of railway lines. Also, high-speed lines, when compared to conventional lines, have to satisfy stricter design requirements such as larger curve radii and smaller gradients. These factors result in less flexibility for defining the rail corridors and often lead to lines with an increased ratio of bridges, viaducts and tunnels. There are several lines in China and Japan in which the total length of bridges, viaducts or tunnels comprises more than 80% of the total length of the line (Montenegro, 2015). The expansion of the European high-speed rail network might lead to some lines in which the ratio of these types of structures is around 50% (Civity, 2013). All these factors will inevitably lead to a significant number of cases in which the vehicle-structure interaction has to be taken into account. For example, Yau *et al.* (1999) concluded that the design of high-speed railway bridges can be mainly governed by serviceability limit states, such as the passenger comfort, rather than by the ultimate limit states of the bridge. Zhai and Cai (1997) concluded that the wheel and rail irregularities induce severe dynamic disturbances and, as a consequence, large impact forces occur; this results in damage to the wheels, rails and other vehicle and track components. Taking into account the train-track interaction is also essential for predicting railway-induced vibrations such as the free-field response (Lombaert & Degrande, 2009). These vibrations can cause disturbance to nearby residents, malfunctioning of sensitive equipment and damage to buildings (Jones & Hunt, 2011). Also, according to Thompson (2009), the rolling noise caused by the wheel-rail interaction is the most important source of noise from railway operations. Therefore, having accurate, robust and efficient algorithms for analysing the vehicle-structure interaction is an essential prerequisite for achieving the challenging objectives mentioned above.

1.2 OBJECTIVES AND SCOPE

Do the available methods for analysing the vehicle-structure interaction simultaneously satisfy the fundamental requirements in terms of accuracy, robustness and efficiency? Commercial finite element (FE) programs can accurately simulate the nonlinear behaviour and deformation of the vehicles and structures but have simplified contact formulations that cannot efficiently take into account the wheel and rail geometry and the normal and tangential forces transmitted across the contact interface. Multibody simulation (MBS) programs provide comprehensive libraries of detailed vehicle models and can efficiently take into account the wheel and rail geometry, but might not simulate the deformation of the structure adequately. Over the last decades, the scientific community has witnessed a proliferation of studies proposing different vehicle-structure interaction methods in order to close the gap between FE and MBS programs. However, these studies often lack a thorough comparison between the proposed and existing methods. Several studies do not even mention well-known methods implemented in some of the most widely used commercial software, such as the Lagrange multiplier and penalty methods. Does it make sense to propose a new method without clearly demonstrating its advantages and disadvantages against other methods?

With these questions in mind, the first objective of this study is to carry out a comprehensive literature review of vehicle-structure interaction methods and to assist the reader in comparing their main advantages and disadvantages. Only deterministic methods formulated in the time domain are addressed here. This review covers a wide range of methods based on the direct equilibrium of the contact forces, variational formulations or condensation techniques.

The main objective of this work is to continue the development of the vehicle-structure interaction algorithm proposed by Neves (2008), referred to as the direct method. The structures and vehicles can be modelled with several types of FE and with a high degree of complexity. The methodology proposed here is also valid when the vehicles are modelled using multibody system techniques. The method proposed by Neves (2008) does not allow for wheel-rail separation and does not account for the local deformations and highly concentrated stresses which arise in the vicinity of the contact region. In the formulation developed in this work, a search algorithm is used to detect which elements are in contact. Therefore, the constraint equations that relate the displacements of the vehicle and structure are imposed only when contact occurs. Also, an enhanced contact element, which includes an additional Hertzian spring relating the forces acting at the contact region with the local deformations, is proposed. The developed algorithm does not consider the wheel and rail geometry and thus only takes into account the vehicle-structure interaction in the normal contact direction. The objective is to develop an accurate, robust and efficient method that can be later extended to three-dimensional contact problems. This is therefore an important first step towards closing the gap between FE and MBS programs. Special focus is given to the validation of the proposed method. The results calculated using the direct method are compared with those obtained with the ANSYS commercial software (2014a) and with semi-analytical solutions.

The proposed method is used to analyse the passage of the Korean high-speed train (KHST) over the Alverca single track viaduct, located on the Northern Line of the Portuguese railway network. The model of the viaduct is calibrated and validated using an FE model updating technique that compares the response of the numerical model with data measured during an ambient vibration test performed by Malveiro *et al.* (2013). The influence of the force-deflection relationship of the Hertzian contact spring, the track irregularities and the three-dimensional deformation of the slab of the viaduct are analysed in detail. Although the computational efficiency of a vehicle-structure interaction method is of critical importance, most studies addressing these methods do not provide enough information on the subject. The efficiency of the proposed method is validated here against the widely used ANSYS commercial software.

1.3 OUTLINE OF THE THESIS

The design of robust and efficient algorithms to treat train-bridge interaction problems depends on a wide range of topics, which are organised into eight chapters. The background, objectives and scope, and outline of the thesis are described in this chapter.

A comprehensive literature review and comparison of the existing methods for solving vehicle-structure interaction problems is presented in the second chapter. Special attention is given to the accuracy, robustness, efficiency and simplicity of the algorithms. In the methods discussed in this chapter, the vehicle and structure are modelled separately but are coupled using different techniques, namely, direct equilibrium of the contact forces, variational formulations or condensation algorithms.

The vehicle-structure interaction methods presented in the second chapter guarantee the equilibrium of the contact forces and the constraint equations but do not take into account the local deformations that arise in the vicinity of the contact region. The formulation proposed in this thesis uses an enhanced node-to-segment contact element, which includes an additional Hertzian spring that relates the contact forces to the local deformations of the contact region. The third chapter discusses the Hertz contact theory, with special focus given to its assumptions and limitations. Hertz provided a few tabulated values to calculate the force-deflection relationship of the contact spring as a function of a parameter that depends only on the geometrical properties of the two contacting bodies. The computer program Maple is used to provide additional tabulated values.

An accurate, efficient and simple formulation for analysing the vehicle-structure interaction, referred to as direct method, is explained in the fourth chapter. At each instant, the equations of motion of the structure and vehicles are complemented with additional constraint equations that relate the nodal displacements of the vehicles to the displacements of the corresponding points of the structure. These equations form a single system that is solved directly. The node-to-segment contact element presented in this chapter does not allow separation and does not take into account the local deformations that arise in the vicinity of the contact region. Some numerical examples to validate the accuracy of the proposed formulation against semi-analytical solutions are provided.

In the fifth chapter, a search algorithm is used to detect which elements are in contact, with the constraints imposed only when contact occurs. Also, an enhanced node-to-segment contact element, which includes an additional Hertzian spring that relates the forces acting at the interface to the local deformations in the vicinity of the contact region, is proposed. Due to the nonlinear nature of the constraint equations and Hertzian spring, an incremental formulation based on the Newton-Raphson method is adopted. The results calculated using the direct method are compared with those obtained with the ANSYS commercial software to validate the accuracy and efficiency of the proposed method.

The numerical modelling and dynamic analysis of the train-track system is explained in the sixth chapter. The KHST is adopted in this work. The ballast and sleepers of the track are modelled with 3D solid elements. A 2D track model is used before and after the 3D track to support the vehicle. The influence of using a 2D rigid or flexible track model, the force-deflection relationship considered for the Hertzian spring and the numerical dissipation provided by the time integration scheme are studied in this chapter. The results calculated using the direct method are validated against those calculated with ANSYS and the efficiency of both approaches is compared.

The dynamic interaction that occurs during the passage of the KHST over the Alverca viaduct, located on the Northern Line of the Portuguese railway network, is analysed and discussed in the seventh chapter. The development of the finite element model of the viaduct is explained in detail. Its geometrical and mechanical properties are calibrated using an FE model updating technique that compares the numerical response of the viaduct with data measured during an ambient vibration test performed by Malveiro *et al.* (2013). The influence of the track irregularities, ballast instability, local deformations of the slab of the viaduct and force-deflection relationship of the Hertzian spring are analysed in this chapter. The accuracy and efficiency of the direct method proposed in Chapters 4 and 5 are validated by comparing the results calculated using the proposed method and ANSYS.

The final conclusions and suggestions for future research in the field of train-bridge interaction are presented in the eighth chapter.

2 OVERVIEW OF VEHICLE-STRUCTURE INTERACTION METHODS

2.1 INTRODUCTION

The dynamic response of structures subjected to the passage of vehicles has been studied for more than one hundred years. The scientific community has witnessed the proliferation of several studies proposing different vehicle-structure interaction algorithms that lack a detailed comparison with the already existing methods. The main objective of this chapter is to assist the reader in comparing the main advantages and disadvantages of the vehicle-structure interaction methods that are more relevant to the present work.

There are two fundamentally different approaches to evaluating the dynamic behaviour of structures: deterministic and nondeterministic. If the excitation is assumed to be known as a function of time, a deterministic approach is used. On the other hand, if the excitation is a random function described by statistical means, nondeterministic methods have to be used. Also, the dynamic behaviour can be evaluated in the frequency domain or in the time domain. The frequency domain methods require less computational effort but may impose some restrictions when dealing with nonperiodic effects and nonlinear structural models (Popp *et al.*, 1999). There are several nonlinearities that should be considered, such as nonlinear suspensions, nonlinear contact, the state dependent rail pads and ballast properties, and the loss of contact between sleepers and ballast (Nielsen *et al.*, 2003; Nielsen & Oscarsson, 2004). In the present work, only the deterministic approach and time domain methods are adopted.

The dynamic response of structures subjected to the passage of vehicles can be studied using different models: moving loads, moving masses or moving vehicles. Most of the earlier studies aimed to obtain simplified analytical solutions to be used in structural design. The moving load model has been adopted by several researchers (Biggs, 1964; Frýba, 1999) and can be used to analyse systems in which the inertial forces of the vehicle are small when compared with those of the structure, and when the response of the vehicle is not important. Analytical solutions can be obtained for simple cases, allowing a better understanding of the main parameters that influence the response of the system (Goicolea

& Antolin, 2012). When the inertial forces of the vehicle cannot be neglected, the moving mass model is more suitable (Willis, 1849; Biggs, 1964; Ting *et al.*, 1974; Inbanathan & Wieland, 1987; Akin & Mofid, 1989). However, this type of model is also unable to simulate the response of the vehicle and to consider important effects such as bouncing and pitching of the masses of the vehicle and the irregularities at the wheel-rail interface. Therefore, in most cases, the moving vehicle model must be adopted to properly account for the interaction between the two subsystems. A review and comparison of the existing methods for solving the vehicle-structure contact problem is presented in this chapter. Special attention is given to the accuracy, robustness, efficiency and simplicity of the different methods.

The vehicle-structure system can be modelled using finite element or multibody simulation software. Most of the multibody simulation programs use simplified track models that may not adequately take into account the deformations of the track and the bridge. For this reason, the methods based on multibody simulation are not addressed in this work. Diana *et al.* (2002) studied numerically and experimentally the passenger comfort in railway vehicles and concluded that the accelerations of the carbody significantly depend on its structural flexibility. Therefore, traditional rigid body models that do not account for the flexibility of the vehicle components might not accurately assess the passenger comfort.

The finite element models can take into account the structural flexibility of all the components of the vehicle-structure system. These models can be defined using two main methodologies: one that formulates the structural matrices for the entire system, i.e., without separating the two subsystems into independent meshes, and another that models the structure and vehicle as two separate subsystems with non-matching meshes. Since most of the contact mechanics literature only addresses methodologies dealing with non-matching meshes, the former methods are not addressed in this work. A description of these methods can be found in Au *et al.* (2001), Song *et al.* (2003) and Xia and Zhang (2005). Figure 2.1 shows a general vehicle model moving over a simple structure. The two subsystems are modelled separately and have non-matching meshes. When studying the contact between two bodies, one conventionally has a contact surface and the other a target surface. In this work, it is assumed that the contact surfaces belong to the vehicle and that the structure contains the target surfaces. The displacements of the contact nodes of the vehicle and the corresponding points of the target elements of the structure are denoted by v^{ce} and v^{te}. The superscripts *ce* and *te* indicate contact and target element, respectively. The displacements of the target elements correspond to auxiliary interior points of the elements and are not degrees of freedom (d.o.f.) of the system.

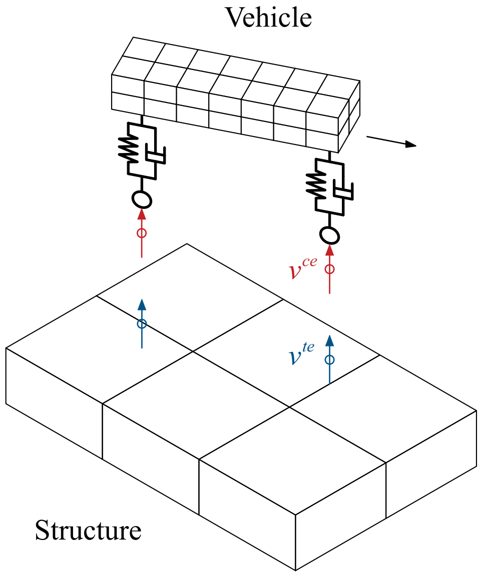

Figure 2.1 – Schematic illustration of the vehicle-structure system.

This chapter describes three different approaches that model the vehicle and structure separately but deal with the coupling using different techniques: direct equilibrium of contact forces, variational formulations and condensation methods. When the coupling between the vehicle and structure is taken into account by establishing the equilibrium of the contact forces directly and imposing the contact constraint equations, the contact forces are considered explicitly and treated as external forces applied on the right-hand side of the equation of motion (see Section 2.2). The variational formulations described in Section 2.3 take into account the variations of the total energy of the system instead of considering explicitly the inertial, damping and elastic forces. A term is added to the total energy of the system to impose the constraint equations. These methods are well-known in the optimisation theory and contact mechanics and are used by most of the commercial finite element packages to handle contact problems. The approach based on condensation methods is described in Section 2.4 and uses the equations that relate the displacements of the vehicle and structure to condense out all the vehicle d.o.f.

2.2 DIRECT EQUILIBRIUM OF CONTACT FORCES

In this approach, the coupling between the vehicle and structure is taken into account by establishing directly the equilibrium of the contact forces and by imposing contact constraint equations. Thus, the contact forces are considered explicitly and treated as external forces in the equation of motion. The equations of motion and the contact constraint equations form a single system of linear equations. Two different types of methods are available for solving this system: the direct method developed by Azevedo *et al.* (2007) and Neves (2008), and the iterative methods (Veletsos & Huang, 1970; Hwang & Nowak, 1991; Wang & Huang, 1992; Green & Cebon, 1994; Yang & Fonder, 1996; Delgado & Santos, 1997).

2.2.1 Formulation of the equations of motion

The equations of motion governing the dynamic response of the vehicle-structure system represented in Fig. 2.1 can be expressed as

$$\mathbf{M}\,\ddot{\mathbf{a}} + \mathbf{C}\,\dot{\mathbf{a}} + \mathbf{K}\,\mathbf{a} = \mathbf{F} \tag{2.1}$$

where **M** is the mass matrix, **C** is the viscous damping matrix, **K** is the stiffness matrix, **F** is the load vector and **a** are the nodal displacements. The dots represent differentiation with respect to time. For the sake of clarity, the formulation presented in this section assumes linear elastic material behaviour, deformation-independent loading and that there is no loss of contact between the vehicle and structure. The nonlinear contact is addressed in Chapter 5.

The load vector can be expressed as

$$\mathbf{F} = \mathbf{P} + \mathbf{D}^{ce}\,\mathbf{X}^{ce} + \mathbf{D}^{te}\,\mathbf{X}^{te} \tag{2.2}$$

where **P** corresponds to the externally applied nodal loads, whose values are known, and **X** are the forces acting at the contact and target elements, whose values are unknown. Each matrix **D** relates the forces acting at the contact interface to the equivalent nodal loads. According to Newton’s third law, the contact forces acting on the vehicle and structure (see Fig. 2.1) must be of equal magnitude and opposite direction, i.e.,

$$\mathbf{X}^{ce} + \mathbf{X}^{te} = \mathbf{0} \tag{2.3}$$

Substituting Eq. (2.3) into Eqs. (2.2) leads to

$$\mathbf{F} = \mathbf{P} + \mathbf{D}\,\mathbf{X} \tag{2.4}$$

where

$$\mathbf{X} = \mathbf{X}^{ce} \tag{2.5}$$

$$\mathbf{D} = \mathbf{D}^{ce} - \mathbf{D}^{te} \tag{2.6}$$

Substituting Eq. (2.4) into Eq. (2.1) gives

$$\mathbf{M}\,\ddot{\mathbf{a}} + \mathbf{C}\,\dot{\mathbf{a}} + \mathbf{K}\,\mathbf{a} = \mathbf{P} + \mathbf{D}\,\mathbf{X} \tag{2.7}$$

2.2.2 Direct integration of the equations of motion

In this chapter, Eq. (2.7) is solved using the Newmark direct integration method. This step-by-step method divides the loading and the response history into a sequence of time steps and employs numerical integration techniques to satisfy the equations of motion at each discrete time interval. This technique assumes a variation of the displacements, velocities and accelerations within each step. The displacements and velocities can be expressed in terms of the accelerations or an alternative relationship can be assumed. In any case, only one unknown vector remains. The assumption made about this variation determines the accuracy, stability and computational cost of the method (Bathe, 1996). For the case of a nonlinear analysis, the procedure discussed in this section may be easily modified into an incremental form. The equations of motion (2.7) at the current time step ($t + \Delta t$) are given by

$$\mathbf{M}\,\ddot{\mathbf{a}}^{t+\Delta t} + \mathbf{C}\,\dot{\mathbf{a}}^{t+\Delta t} + \mathbf{K}\,\mathbf{a}^{t+\Delta t} = \mathbf{P}^{t+\Delta t} + \mathbf{D}^{t+\Delta t}\,\mathbf{X}^{t+\Delta t} \tag{2.8}$$

In the Newmark method, the velocities and accelerations at the current time step are approximated with (Newmark, 1959; Bathe, 1996)

$$\dot{\mathbf{a}}^{t+\Delta t} = A_1\left(\mathbf{a}^{t+\Delta t} - \mathbf{a}^{t}\right) - A_4\,\dot{\mathbf{a}}^{t} - A_5\,\ddot{\mathbf{a}}^{t} \tag{2.9}$$

$$\ddot{\mathbf{a}}^{t+\Delta t} = A_0\left(\mathbf{a}^{t+\Delta t} - \mathbf{a}^{t}\right) - A_2\,\dot{\mathbf{a}}^{t} - A_3\,\ddot{\mathbf{a}}^{t} \tag{2.10}$$

where the superscript t indicates the previous time step and

$$A_0 = \frac{1}{\beta\,\Delta t^2} \qquad A_1 = \frac{\gamma}{\beta\,\Delta t} \qquad A_2 = \frac{1}{\beta\,\Delta t}$$
$$A_3 = \frac{1}{2\beta} - 1 \qquad A_4 = \frac{\gamma}{\beta} - 1 \qquad A_5 = \Delta t\left(\frac{\gamma}{2\beta} - 1\right) \tag{2.11}$$

The parameters γ and β control the stability and accuracy of the method. Substituting Eqs. (2.9) and (2.10) into Eq. (2.8) and rearranging the terms yields

$$\overline{\mathbf{K}}\,\mathbf{a}^{t+\Delta t} = \overline{\mathbf{F}} + \mathbf{D}^{t+\Delta t}\,\mathbf{X}^{t+\Delta t} \tag{2.12}$$

where

$$\overline{\mathbf{K}} = A_0\,\mathbf{M} + A_1\,\mathbf{C} + \mathbf{K} \tag{2.13}$$

and

$$\overline{\mathbf{F}} = \mathbf{P}^{t+\Delta t} + \mathbf{M}\left[A_0\,\mathbf{a}^t + A_2\,\dot{\mathbf{a}}^t + A_3\,\ddot{\mathbf{a}}^t\right] + \mathbf{C}\left[A_1\,\mathbf{a}^t + A_4\,\dot{\mathbf{a}}^t + A_5\,\ddot{\mathbf{a}}^t\right] \tag{2.14}$$

2.2.3 Contact constraint equations

The constraint equations that guarantee that there is no separation between the contact elements of the vehicle and the target elements of the structure (see Fig. 2.1) are given by

$$\mathbf{v}^{ce} - \mathbf{v}^{te} = \mathbf{r} \tag{2.15}$$

where $\mathbf{r}$ are the irregularities between the contact and target elements. The displacements of the contact nodes and auxiliary points of the target elements are given by

$$\mathbf{v}^{ce} = \mathbf{H}^{ce}\,\mathbf{a} \tag{2.16}$$

$$\mathbf{v}^{te} = \mathbf{H}^{te}\,\mathbf{a} \tag{2.17}$$

where each transformation matrix $\mathbf{H}$ relates the vector of nodal displacements $\mathbf{a}$ to the displacements of the contact nodes and auxiliary points of the target elements. Substituting Eqs. (2.16) and (2.17) into Eq. (2.15) leads to

$$\mathbf{H}\,\mathbf{a} = \mathbf{r} \tag{2.18}$$

where

$$\mathbf{H} = \mathbf{H}^{ce} - \mathbf{H}^{te} \tag{2.19}$$

2.2.4 Direct method

Azevedo *et al.* (2007) and Neves (2008) developed an accurate, efficient and robust algorithm in which the equations of motion of the vehicle and structure are complemented with additional constraint equations that relate the displacements of the contact nodes of the vehicle to the corresponding displacements of the target elements of the structure. These equations form a single system with displacements and contact forces as unknowns. Rewriting Eq. (2.18) for the current time step leads to

$$-\mathbf{H}^{t+\Delta t}\,\mathbf{a}^{t+\Delta t} = -\mathbf{r}^{t+\Delta t} \tag{2.20}$$

Equations (2.12) and (2.20) can be expressed in matrix form leading to the following system of equations

$$\begin{bmatrix} \overline{\mathbf{K}} & -\mathbf{D}^{t+\Delta t} \\ -\mathbf{H}^{t+\Delta t} & \mathbf{0} \end{bmatrix} \begin{bmatrix} \mathbf{a}^{t+\Delta t} \\ \mathbf{X}^{t+\Delta t} \end{bmatrix} = \begin{bmatrix} \overline{\mathbf{F}} \\ -\mathbf{r}^{t+\Delta t} \end{bmatrix} \tag{2.21}$$

The symmetry of the coefficient matrix can be demonstrated using Betti's theorem, i.e.,

$$\mathbf{H} = \mathbf{D}^{T} \tag{2.22}$$

The system of equations (2.21) is solved directly, leading to a robust and accurate algorithm. This becomes even more important for the case of a nonlinear analysis, where convergence is a critical issue. Since some diagonal terms of the coefficient matrix are null, the system is solved using an optimised block factorisation algorithm that takes into account the specific properties of each block, namely, symmetry, positive definiteness and bandwidth. The implementation of the direct method in a finite element computer program is straightforward for the reason that only the contact algorithm needs to be implemented and no additional finite elements have to be developed.

2.2.5 Iterative methods

Classic iterative methods for solving a system of linear equations date to the late eighteenth century (Burden & Faires, 1997). In order to solve a linear system of the form **A x** = **b** using iterative techniques, the matrix **A** can be decomposed into

$$\mathbf{A} = \mathbf{M} - \mathbf{N} \tag{2.23}$$

The iterative technique starts with an initial vector $\mathbf{x}^0$ and generates a sequence of approximate solution vectors by computing

$$\mathbf{M}\mathbf{x}^{i+1} = \mathbf{N}\mathbf{x}^{i} + \mathbf{b} \tag{2.24}$$

where i is the iteration counter. This sequence converges to the unique solution if and only if

$$\rho\left(\mathbf{M}^{-1}\mathbf{N}\right) < 1 \tag{2.25}$$

in which ρ is the spectral radius (Burden & Faires, 1997). A lower spectral radius leads to a faster convergence.

Iterative techniques were first applied to vehicle-structure interaction problems by Veletsos and Huang (1970) and since then have been used by Hwang and Nowak (1991), Wang and Huang (1992), Green and Cebon (1994), Yang and Fonder (1996), Delgado and Santos (1997), Zhang *et al.* (2008), Ribeiro (2012) and Liu *et al.* (2014). In order to define the different steps involved in an iterative procedure, it is necessary to partition the system of linear equations (2.21) into the form

$$\begin{bmatrix} \overline{\mathbf{K}}_{\hat{I}\hat{I}} & \overline{\mathbf{K}}_{\hat{I}\tilde{I}} & \overline{\mathbf{K}}_{\hat{I}X} & -\mathbf{D}_{\hat{I}X}^{t+\Delta t} \\ \overline{\mathbf{K}}_{\tilde{I}\hat{I}} & \overline{\mathbf{K}}_{\tilde{I}\tilde{I}} & \overline{\mathbf{K}}_{\tilde{I}X} & -\mathbf{D}_{\tilde{I}X}^{t+\Delta t} \\ \overline{\mathbf{K}}_{X\hat{I}} & \overline{\mathbf{K}}_{X\tilde{I}} & \overline{\mathbf{K}}_{XX} & -\mathbf{D}_{XX}^{t+\Delta t} \\ -\mathbf{H}_{X\hat{I}}^{t+\Delta t} & -\mathbf{H}_{X\tilde{I}}^{t+\Delta t} & -\mathbf{H}_{XX}^{t+\Delta t} & \mathbf{0} \end{bmatrix} \begin{bmatrix} \mathbf{a}_{\hat{I}}^{t+\Delta t} \\ \mathbf{a}_{\tilde{I}}^{t+\Delta t} \\ \mathbf{a}_{X}^{t+\Delta t} \\ \mathbf{X}_{X}^{t+\Delta t} \end{bmatrix} = \begin{bmatrix} \overline{\mathbf{F}}_{\hat{I}} \\ \overline{\mathbf{F}}_{\tilde{I}} \\ \overline{\mathbf{F}}_{X} \\ -\mathbf{r}_{X}^{t+\Delta t} \end{bmatrix} \tag{2.26}$$

according to the classification of d.o.f. presented in Table 2.1.

Table 2.1 – Classification of degrees of freedom.

Type	Description
$\hat{I}$	free d.o.f. of the structure
$\tilde{I}$	free d.o.f. of the vehicles
X	contact d.o.f. of the vehicles

Since the meshes of the vehicle and structure are independent, $\overline{\mathbf{K}}_{\hat{I}\tilde{I}}$, $\overline{\mathbf{K}}_{\hat{I}X}$, $\overline{\mathbf{K}}_{\tilde{I}\hat{I}}$ and $\overline{\mathbf{K}}_{X\hat{I}}$ are null matrices. Also, since the contact forces are assumed to be applied along the X type d.o.f. of the vehicle, $\mathbf{D}_{XX}^{t+\Delta t}$ and $\mathbf{H}_{XX}^{t+\Delta t}$ are identity matrices. Therefore, Eq. (2.26) can be written as

$$\begin{bmatrix} \overline{\mathbf{K}}_{\hat{I}\hat{I}} & \mathbf{0} & \mathbf{0} & -\mathbf{D}_{\hat{I}X}^{t+\Delta t} \\ \mathbf{0} & \overline{\mathbf{K}}_{\tilde{I}\tilde{I}} & \overline{\mathbf{K}}_{\tilde{I}X} & \mathbf{0} \\ \mathbf{0} & \overline{\mathbf{K}}_{X\tilde{I}} & \overline{\mathbf{K}}_{XX} & -\mathbf{I}_{XX} \\ -\mathbf{H}_{X\hat{I}}^{t+\Delta t} & \mathbf{0} & -\mathbf{I}_{XX} & \mathbf{0} \end{bmatrix} \begin{bmatrix} \mathbf{a}_{\hat{I}}^{t+\Delta t} \\ \mathbf{a}_{\tilde{I}}^{t+\Delta t} \\ \mathbf{a}_{X}^{t+\Delta t} \\ \mathbf{X}_{X}^{t+\Delta t} \end{bmatrix} = \begin{bmatrix} \overline{\mathbf{F}}_{\hat{I}} \\ \overline{\mathbf{F}}_{\tilde{I}} \\ \overline{\mathbf{F}}_{X} \\ -\mathbf{r}_{X}^{t+\Delta t} \end{bmatrix} \tag{2.27}$$

Wang and Huang (1992) apply the Gauss-Seidel iterative method to solve this system of linear equations. Before applying this iterative technique, the rows and columns of Eq. (2.27) are reordered to obtain

$$\begin{bmatrix} -\mathbf{I}_{XX} & \mathbf{0} & \mathbf{0} & -\mathbf{H}_{X\hat{I}}^{t+\Delta t} \\ \overline{\mathbf{K}}_{\tilde{I}X} & \overline{\mathbf{K}}_{\tilde{I}\tilde{I}} & \mathbf{0} & \mathbf{0} \\ \overline{\mathbf{K}}_{XX} & \overline{\mathbf{K}}_{X\tilde{I}} & -\mathbf{I}_{XX} & \mathbf{0} \\ \mathbf{0} & \mathbf{0} & -\mathbf{D}_{\hat{I}X}^{t+\Delta t} & \overline{\mathbf{K}}_{\hat{I}\hat{I}} \end{bmatrix} \begin{bmatrix} \mathbf{a}_{X}^{t+\Delta t} \\ \mathbf{a}_{\tilde{I}}^{t+\Delta t} \\ \mathbf{X}_{X}^{t+\Delta t} \\ \mathbf{a}_{\hat{I}}^{t+\Delta t} \end{bmatrix} = \begin{bmatrix} -\mathbf{r}_{X}^{t+\Delta t} \\ \overline{\mathbf{F}}_{\tilde{I}} \\ \overline{\mathbf{F}}_{X} \\ \overline{\mathbf{F}}_{\hat{I}} \end{bmatrix} \tag{2.28}$$

In the Gauss-Seidel iterative method, the decomposition described in Eq. (2.23) is given by

$$\mathbf{M} = \mathbf{L} + \mathbf{D} \tag{2.29}$$

$$\mathbf{N} = -\mathbf{U} \tag{2.30}$$

where **D** is the diagonal matrix whose diagonal entries are those of **A,** and **L** and **U** are the strictly lower and upper triangular parts of **A**, respectively. Although iterative techniques have been applied to vehicle-structure interaction problems for more than four decades, there is little information in the literature concerning their convergence characteristics. Green and Cebon (1994) report some convergence problems for the case of vehicles with large wheel forces with frequency content higher than 10 Hz. Yang and Fonder (1996) provide some useful information about the convergence characteristics of the iterative methods proposed in their work but are mainly focused on the number of iterations necessary to achieve convergence. In the present work, the convergence of the iterative methods can be verified more accurately and reliably using the inequality (2.25). Hence, it is easier to identify which blocks of the coefficient matrix of Eq. (2.28) might lead to a slow convergence or even divergence.

Substituting Eqs. (2.28) to (2.30) into Eq. (2.24) leads to

$$\begin{bmatrix} -\mathbf{I}_{XX} & \mathbf{0} & \mathbf{0} & \mathbf{0} \\ \overline{\mathbf{K}}_{\tilde{I}X} & \overline{\mathbf{K}}_{\tilde{I}\tilde{I}} & \mathbf{0} & \mathbf{0} \\ \overline{\mathbf{K}}_{XX} & \overline{\mathbf{K}}_{X\tilde{I}} & -\mathbf{I}_{XX} & \mathbf{0} \\ \mathbf{0} & \mathbf{0} & -\mathbf{D}_{\hat{I}X}^{t+\Delta t} & \overline{\mathbf{K}}_{\hat{I}\hat{I}} \end{bmatrix} \begin{bmatrix} \mathbf{a}_X^{t+\Delta t,i+1} \\ \mathbf{a}_{\tilde{I}}^{t+\Delta t,i+1} \\ \mathbf{X}_X^{t+\Delta t,i+1} \\ \mathbf{a}_{\hat{I}}^{t+\Delta t,i+1} \end{bmatrix} = \begin{bmatrix} \mathbf{H}_{X\hat{I}}^{t+\Delta t}\,\mathbf{a}_{\hat{I}}^{t+\Delta t,i} \\ \mathbf{0} \\ \mathbf{0} \\ \mathbf{0} \end{bmatrix} + \begin{bmatrix} -\mathbf{r}_X^{t+\Delta t} \\ \overline{\mathbf{F}}_{\tilde{I}} \\ \overline{\mathbf{F}}_X \\ \overline{\mathbf{F}}_{\hat{I}} \end{bmatrix} \tag{2.31}$$

Hence, each iteration i+1 consists of the following steps:

1) Calculate the displacements of the contact nodes of the vehicle

$$\mathbf{a}_X^{t+\Delta t,i+1} = \mathbf{r}_X^{t+\Delta t} - \mathbf{H}_{X\hat{I}}^{t+\Delta t}\,\mathbf{a}_{\hat{I}}^{t+\Delta t,i} \tag{2.32}$$

where the vector $\mathbf{a}_{\hat{I}}^{t+\Delta t,i}$ contains the nodal displacements of the structure calculated in the previous iteration. In the first iteration of each time step, the displacements $\mathbf{a}_{\hat{I}}^{t+\Delta t,i}$ are equal to those calculated in the previous time step.

2) Calculate the free nodal displacements of the vehicle

$$\overline{\mathbf{K}}_{\tilde{I}\tilde{I}}\,\mathbf{a}_{\tilde{I}}^{t+\Delta t,i+1} = \overline{\mathbf{F}}_{\tilde{I}} - \overline{\mathbf{K}}_{\tilde{I}X}\,\mathbf{a}_X^{t+\Delta t,i+1} \tag{2.33}$$

3) Calculate the contact forces

$$\mathbf{X}_X^{t+\Delta t,i+1} = -\overline{\mathbf{F}}_X + \overline{\mathbf{K}}_{X\tilde{I}}\,\mathbf{a}_{\tilde{I}}^{t+\Delta t,i+1} + \overline{\mathbf{K}}_{XX}\,\mathbf{a}_X^{t+\Delta t,i+1} \tag{2.34}$$

4) Calculate the free nodal displacements of the structure

$$\overline{\mathbf{K}}_{\hat{I}\hat{I}}\,\mathbf{a}_{\hat{I}}^{t+\Delta t,i+1} = \overline{\mathbf{F}}_{\hat{I}} + \mathbf{D}_{\hat{I}X}^{t+\Delta t}\,\mathbf{X}_X^{t+\Delta t,i+1} \tag{2.35}$$

5) Check the convergence criterion

$$\frac{\left\|\mathbf{a}_{\hat{I}}^{t+\Delta t,i+1} - \mathbf{a}_{\hat{I}}^{t+\Delta t,i}\right\|}{\left\|\mathbf{a}_{\hat{I}}^{t+\Delta t,i+1}\right\|} \le \varepsilon \tag{2.36}$$

where ε is a specified tolerance. A tolerance between 10^{-8} and 10^{-5} is usually sufficient to obtain an accurate solution (Yang & Fonder, 1996). If the desired degree of convergence is achieved, the procedure may proceed to the next time step, otherwise the iteration counter is incremented and the iterative process continues to step 1).

Unlike the direct method, the iterative method does not treat the contact forces as unknowns of the system of linear equations. These variables are calculated using Eq. (2.34).

Yang and Fonder (1996) proposed an iterative procedure that uses under-relaxation or Aitken acceleration techniques to improve the convergence characteristics of the method. Under-relaxation methods can be used to obtain convergence of some systems that are not convergent when using the Gauss-Seidel method.

2.2.6 Numerical example

A simple numerical example consisting of a beam clamped at both ends with a concentrated load applied at midspan is shown in Fig. 2.2a. The main objective is to evaluate the convergence of the Gauss-Seidel iterative method independently of the application rather than to evaluate the convergence of the method when used to solve vehicle-structure interaction problems. The Young's modulus E is equal to 200 GPa and the cross-sectional areas of the left and right beams are 4 and 1 cm^2, respectively. The initial structure is divided into two separate structures in order to analyse the interaction between both parts (see Fig. 2.2b).

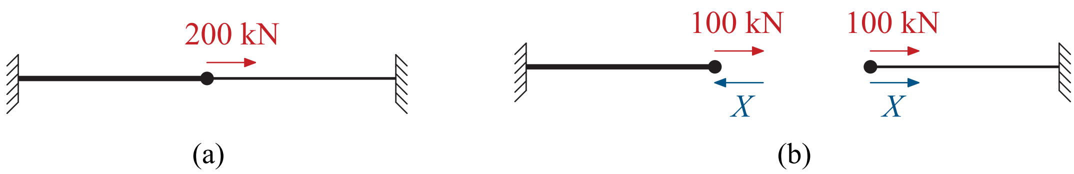

Figure 2.2 – Beam clamped at both ends: a) as a single structure and b) as two separate structures.

In order to use the expressions presented in Section 2.2.5 for the analysis of the vehicle-structure interaction, it will be assumed that the left and right beams correspond to the structure and vehicle, respectively. The use of Eq. (2.27) to define the equilibrium and contact constraint equations of the system leads to

$$\begin{bmatrix} k_{\hat{I}} & 0 & 1 \\ 0 & k_X & -1 \\ 1 & -1 & 0 \end{bmatrix} \begin{bmatrix} a_{\hat{I}} \\ a_X \\ X \end{bmatrix} = \begin{bmatrix} F_{\hat{I}} \\ F_X \\ 0 \end{bmatrix} \tag{2.37}$$

where $F_{\hat{I}} = F_X = 100$ kN. Calculating the stiffness coefficients using Hooke's law yields

$$\begin{aligned} k_{\hat{\imath}} &= 8 \times 10^7 \text{ N/m} \\ k_X &= 2 \times 10^7 \text{ N/m} \end{aligned} \tag{2.38}$$

Solving the system of linear equations (2.37) directly results in

$$\begin{aligned} a_{\hat{\imath}} &= 2\,\text{mm} \\ a_X &= 2\,\text{mm} \\ X &= -60\,\text{kN} \end{aligned} \tag{2.39}$$

In order to solve the interaction problem using the Gauss-Seidel iterative method, the equilibrium and contact constraint equations are now defined using Eq. (2.28), leading to

$$\begin{bmatrix} -1 & 0 & 1 \\ k_X & -1 & 0 \\ 0 & 1 & k_{\hat{\imath}} \end{bmatrix} \begin{bmatrix} a_X \\ X \\ a_{\hat{\imath}} \end{bmatrix} = \begin{bmatrix} 0 \\ F_X \\ F_{\hat{\imath}} \end{bmatrix} \tag{2.40}$$

According to Eqs. (2.25), (2.29) and (2.30), since the spectral radius of $\mathbf{M}^{-1}\mathbf{N}$ is equal to 0.25, the iterative process converges to the exact solution. Substituting Eqs. (2.40), (2.29) and (2.30) into Eq. (2.24) leads to

$$\begin{bmatrix} -1 & 0 & 0 \\ k_X & -1 & 0 \\ 0 & 1 & k_{\hat{\imath}} \end{bmatrix} \begin{bmatrix} a_X^{i+1} \\ X^{i+1} \\ a_{\hat{\imath}}^{i+1} \end{bmatrix} = \begin{bmatrix} -a_{\hat{\imath}}^{i} \\ 0 \\ 0 \end{bmatrix} + \begin{bmatrix} 0 \\ F_X \\ F_{\hat{\imath}} \end{bmatrix} \tag{2.41}$$

The sequence of approximations of $a_{\hat{\imath}}$, a_X and X obtained using $a_{\hat{\imath}}^0 = 0$ and Eq. (2.41) are plotted in Fig. 2.3. A tolerance of 10^{-5} is used for checking the convergence criterion defined by Eq. (2.36). This tolerance is satisfied after ten iterations and the values obtained using Eq. (2.36) are plotted in Fig. 2.4.

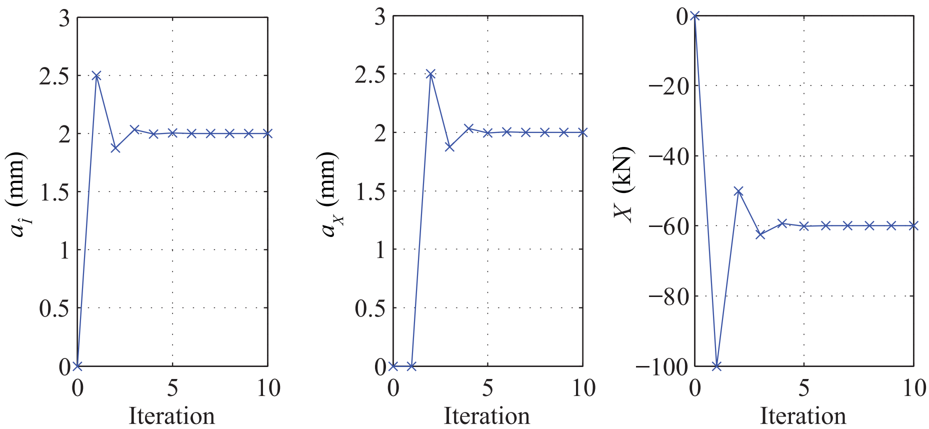

Figure 2.3 – Sequence of approximate solutions.

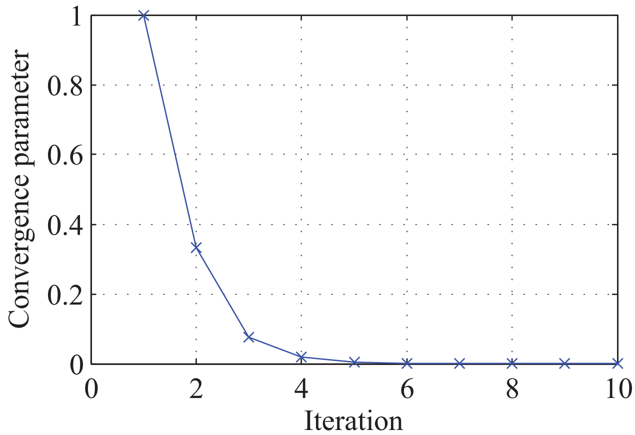

Figure 2.4 – Values of the convergence parameter.

The convergence of the iterative process depends on how the rows and columns of Eq. (2.27) are reordered. To verify this assumption a different reordering is performed resulting in

$$\begin{bmatrix} 1 & 0 & -1 \\ k_{\hat{I}} & 1 & 0 \\ 0 & -1 & k_X \end{bmatrix} \begin{bmatrix} a_{\hat{I}} \\ X \\ a_X \end{bmatrix} = \begin{bmatrix} 0 \\ F_{\hat{I}} \\ F_X \end{bmatrix} \tag{2.42}$$

According to Eqs. (2.25), (2.29) and (2.30), since the spectral radius of $\mathbf{M}^{-1}\mathbf{N}$ is equal to 4, the iterative process does not converge. Substituting Eqs. (2.42), (2.29) and (2.30) into Eq. (2.24) leads to

$$\begin{bmatrix} 1 & 0 & 0 \\ k_{\hat{I}} & 1 & 0 \\ 0 & -1 & k_X \end{bmatrix} \begin{bmatrix} a_{\hat{I}}^{i+1} \\ X^{i+1} \\ a_X^{i+1} \end{bmatrix} = \begin{bmatrix} a_X^i \\ 0 \\ 0 \end{bmatrix} + \begin{bmatrix} 0 \\ F_{\hat{I}} \\ F_X \end{bmatrix} \tag{2.43}$$

The sequence of approximations of $a_{\hat{I}}$, a_X and X obtained using $a_X^0 = 0$ and Eq. (2.43) are plotted in Fig. 2.5.

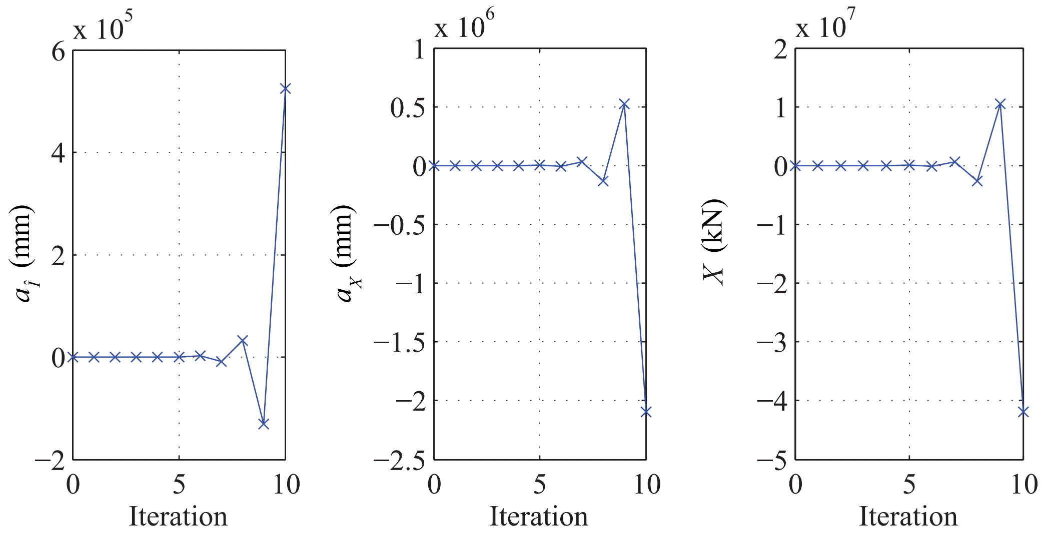

Figure 2.5 – Sequence of approximate solution vectors.

It can be concluded that even for a very simple system of linear equations the iterative techniques might diverge if an inadequate permutation of rows and columns is chosen. The numerical example presented here is not a typical vehicle-structure interaction problem. When the iterative methods are applied to these problems, the permutation of rows and columns used takes into account the specific properties of the structure and vehicle, which usually leads to a convergent procedure. Nevertheless, there is little information in the literature concerning the convergence characteristics of iterative methods when used in the analysis of the dynamic vehicle–structure interaction, and so special care must be taken when using this type of procedures.

2.3 VARIATIONAL FORMULATIONS

The equations of motion of any dynamic system can be established using scalar quantities in a variational form known as the Hamilton's principle (Clough & Penzien, 1993). This formulation takes into account the variations of the kinetic and potential energy terms instead of considering explicitly the inertial and elastic forces. There are several formulations available to incorporate the contact constraints into the variational formulation such as the Lagrange multiplier method, the penalty method and the augmented Lagrangian method, among others. The augmented Lagrangian method combines the Lagrange multiplier and penalty methods. These methods are well-known in the optimisation theory and contact mechanics and are used by most of the commercial finite element packages to handle contact problems. A term is added to the total energy of the system to impose the constraint equations. All these methods have advantages and disadvantages in terms of efficiency, accuracy and robustness, and thus have to be applied according to the problem at hand. An extensive overview of these formulations can be found in Wriggers (2002).

In order to avoid cumbersome mathematical expressions, the equilibrium equations are derived for a static analysis. In this case, the Hamilton's principle reduces to the principle of minimum potential energy. The variational formulations presented in this section are equally valid for dynamic analysis (Clough & Penzien, 1993).

2.3.1 Formulation of the equilibrium equations

A variational formulation consists of determining the set of values $a_1, \ldots, a_n$ (state variables) for which a given functional $\prod(a_1, \ldots, a_n)$ is a maximum, a minimum or has a saddle point (Bathe, 1996). The condition for obtaining the solution of the problem is given by

$$\delta \prod = 0 \tag{2.44}$$

where

$$\delta \prod = \frac{\partial \prod}{\partial a_1} \delta a_1 + \cdots + \frac{\partial \prod}{\partial a_n} \delta a_n \tag{2.45}$$

For Eq. (2.44) to be valid for any variation $\delta \mathbf{a}$ it is necessary that

$$\frac{\partial \prod}{\partial a_i} = 0 \quad \text{for } i = 1, \ldots, n \tag{2.46}$$

In a linear structural analysis, when the displacements are used as state variables, $\prod$ is the total potential energy given by

$$\prod = U + W \tag{2.47}$$

where U is the strain energy of the system and W is the potential energy of the external loads defined as

$$U = \frac{1}{2} \mathbf{a}^T \mathbf{K}\, \mathbf{a} \tag{2.48}$$

$$W = -\mathbf{a}^T \mathbf{F} \tag{2.49}$$

Substituting Eqs. (2.48) and (2.49) into Eq. (2.47) gives

$$\Pi = \frac{1}{2}\mathbf{a}^T \mathbf{K}\, \mathbf{a} - \mathbf{a}^T \mathbf{F} \tag{2.50}$$

Applying Eq. (2.44) yields

$$\delta \mathbf{a}^T \mathbf{K}\, \mathbf{a} - \delta \mathbf{a}^T \mathbf{F} = 0 \tag{2.51}$$

which is true for all $\delta \mathbf{a}$ and hence

$$\mathbf{K}\, \mathbf{a} = \mathbf{F} \tag{2.52}$$

2.3.2 Lagrange multiplier method

The Lagrange multiplier method adds a term to the total potential energy of the system that contains the constraints to be imposed (Wriggers, 2002). In order to impose the constraints equations (2.18), the right-hand side of Eq. (2.50) is modified as follows

$$\Pi = \frac{1}{2}\mathbf{a}^T \mathbf{K}\, \mathbf{a} - \mathbf{a}^T \mathbf{F} + \boldsymbol{\lambda}^T \left(\mathbf{H}\, \mathbf{a} - \mathbf{r}\right) \tag{2.53}$$

where $\boldsymbol{\lambda}$ are additional state variables known as Lagrange multipliers. Therefore, Eq. (2.45) is now

$$\delta \Pi = \frac{\partial \Pi}{\partial a_1}\delta a_1 + \cdots + \frac{\partial \Pi}{\partial a_n}\delta a_n + \frac{\partial \Pi}{\partial \lambda_1}\delta \lambda_1 + \cdots + \frac{\partial \Pi}{\partial \lambda_m}\delta \lambda_m \tag{2.54}$$

where m is the number of constraint equations. For Eq. (2.44) to be valid for any variation $\delta \mathbf{a}$ and $\delta \boldsymbol{\lambda}$ it is necessary that

$$\frac{\partial \Pi}{\partial a_i} = 0 \quad \text{for } i = 1, \ldots, n \tag{2.55}$$

$$\frac{\partial \Pi}{\partial \lambda_j} = 0 \quad \text{for } j = 1, \ldots, m \tag{2.56}$$

Hence, Eq. (2.53) leads to

$$\delta \mathbf{a}^T \mathbf{K}\, \mathbf{a} - \delta \mathbf{a}^T \mathbf{F} + \delta \mathbf{a}^T \mathbf{H}^T\, \boldsymbol{\lambda} + \delta \boldsymbol{\lambda}^T \left(\mathbf{H}\, \mathbf{a} - \mathbf{r}\right) = 0 \tag{2.57}$$

Since $\delta\mathbf{a}$ and $\delta\boldsymbol{\lambda}$ can be varied independently, Eq. (2.57) leads to following equations in matrix form

$$\begin{bmatrix} \mathbf{K} & \mathbf{H}^T \\ \mathbf{H} & \mathbf{0} \end{bmatrix} \begin{bmatrix} \mathbf{a} \\ \boldsymbol{\lambda} \end{bmatrix} = \begin{bmatrix} \mathbf{F} \\ \mathbf{r} \end{bmatrix} \tag{2.58}$$

Since this system is equivalent to the system of linear equations (2.21), it can be concluded that the Lagrange multiplier and direct methods lead to the same system of equations. The Lagrange multipliers correspond to the forces acting on the contact interface, but with opposite sign. All the remarks made in Section 2.2.4 regarding accuracy, robustness and efficiency of the direct method are also valid for the Lagrange multiplier method. The main advantage of the direct equilibrium of forces performed by the direct method, when compared to the variational formulations, is a better understanding of the physical meaning of the equations. This allows an easier identification of possible errors and optimisation of the algorithm, which are particularly important in complex problems such as the vehicle-structure interaction.

2.3.3 Penalty method

The penalty method also adds a term to the total potential energy of the system but without introducing additional variables. The right-hand side of Eq. (2.50) is modified to (Wriggers, 2002)

$$\Pi = \frac{1}{2}\mathbf{a}^T\mathbf{K}\,\mathbf{a} - \mathbf{a}^T\mathbf{F} + \frac{\alpha}{2}\left(\mathbf{H}\,\mathbf{a} - \mathbf{r}\right)^T\left(\mathbf{H}\,\mathbf{a} - \mathbf{r}\right) \tag{2.59}$$

where α is a constant whose value should be significantly larger than the diagonal terms of $\mathbf{K}$. Applying Eq. (2.44) yields

$$\delta\mathbf{a}^T\mathbf{K}\,\mathbf{a} - \delta\mathbf{a}^T\mathbf{F} + \delta\mathbf{a}^T\alpha\,\mathbf{H}^T\mathbf{H}\,\mathbf{a} - \delta\mathbf{a}^T\alpha\,\mathbf{H}^T\mathbf{r} = 0 \tag{2.60}$$

which is true for all $\delta\mathbf{a}$ and hence

$$\left(\mathbf{K} + \alpha\,\mathbf{H}^T\,\mathbf{H}\right)\mathbf{a} = \mathbf{F} + \alpha\,\mathbf{H}^T\mathbf{r} \tag{2.61}$$

The penalty method adds a large value to the terms of the stiffness matrix associated with the coupled d.o.f. and adds the corresponding forces, thus ensuring that the constrained equations are satisfied. The term added to the energy of the system is similar to the potential energy of a spring. In terms of computational efficiency, since no additional variables are introduced, the bandwidth of the coefficient matrix is preserved, which is important for avoiding an increase of the computational effort. However, the stiffness matrix becomes time-dependent which leads to an increase of the computational effort. Hence, evaluating whether the penalty method leads to an overall increase of the computational efficiency is not a straightforward task. Another disadvantage of the penalty method is that it might lead to non-physical penetration. For very large values of the penalty parameter, the penetration tends to zero, but smaller values might lead to non-physical penetration. However, very large values of the penalty parameter might lead to ill-conditioned systems, and consequently to inaccurate solutions. Several standard finite element codes choose the penalty parameter as a function of the mesh size (Wriggers, 2002). It is possible to adapt Eq. (2.61) so that different values of α are applied. García Orden and Goicolea (2000) developed a time-integration approach for nonlinear multibody dynamics in which the constraints are imposed using the penalty method. A reasonable stability and precision is achieved.

2.4 CONDENSATION METHODS

In this type of methods, the equations of motion of the vehicle and structure are formulated separately. All the d.o.f. of the vehicle (slave) are expressed in terms of the master d.o.f. of the structure elements contacting the vehicle, taking into account the constraint equations. Then, this relation between slave and master d.o.f. is used to condense out all the slave d.o.f. This results in new vehicle-structure interaction elements that maintain their initial d.o.f. Since the d.o.f. are condensed out at the element level, a conventional assembly process can be applied to form the structural matrices.

Garg and Dukkipati (1984) considered a moving train composed of four-axle vehicles and a lumped mass model for the bridge and applied the static condensation method proposed by Guyan (1965) to eliminate the d.o.f. The reduced stiffness matrix corresponding to the independent d.o.f. and the transformation matrix relating the dependent and independent d.o.f. are calculated by a partial Gauss-Jordan elimination. This method is simple to apply but introduces approximations that might lead to relatively large errors when applied to dynamic problems (Paz, 1997). Paz (1984) developed the dynamic condensation method that uses an iterative procedure to solve the eigenvalue problem in order to obtain accurate solutions for the higher modes of the system. The modified dynamic condensation method described in Paz (1989) is an improved version that substantially reduces the number of numerical operations required.

Yang and Lin (1995) modelled the vehicles as lumped masses supported by spring-dampers and the bridge with beam elements (see Fig. 2.6). The d.o.f. of the vehicle in contact with the bridge are eliminated using the modified dynamic condensation method. Because of the approximations made by the authors in relating the dependent and independent d.o.f., the dynamic response of the vehicle is not calculated accurately. This limitation has been overcome in the work presented by Yang and Yau (1997).

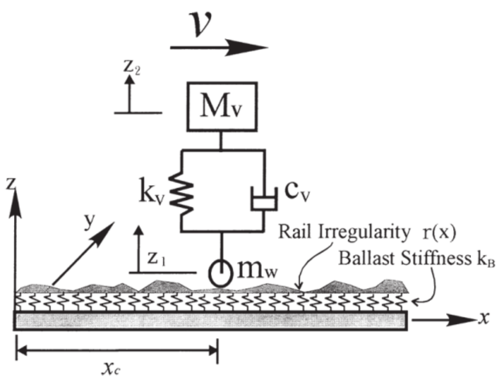

Figure 2.6 – Vehicle-bridge interaction element (Yau *et al.*, 1999).

Since the vehicles considered in Yang and Lin (1995) and Yang and Yau (1997) are modelled as discrete sprung masses, the derived vehicle-bridge interaction elements ignore the pitching effect of the vehicles, which is important for accurately calculating the vehicle response, especially if the track irregularities have a significant influence. Yang *et al.* (1999) developed the improved vehicle-bridge interaction element shown in Fig. 2.7 to overcome this drawback. The vehicle is now modelled as a rigid beam supported by two spring-dampers. Finally, Yang and Wu (2001) developed a procedure capable of simulating vehicles with a higher degree of complexity.

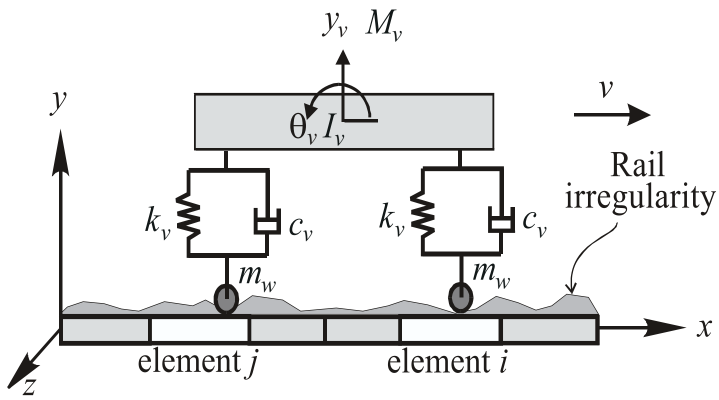

Figure 2.7 – Vehicle-bridge interaction element that accounts for the pitching effect (Montenegro, 2015).

The detailed formulations of the vehicle-bridge interaction methods described in this section, as well as several case studies on high-speed railways, can be found in Yang (2004). The main disadvantage of the methods described in this section is that no separation between the vehicles and structure is allowed. Also, the equations of motion of the coupled vehicle-bridge system might be difficult to determine if nonlinearities are considered in the vehicle models. The vehicle-structure interaction algorithms based on the condensation methods avoid the iterative procedure described in Section 2.2.5, but since the positions of the contact points change over time, the system matrices are usually time-dependent and must be updated and factorised at each time step. Hence, evaluating the computational efficiency of these methods is not a straightforward task.

2.5 CONCLUDING REMARKS

This chapter describes three different approaches that formulate the equations of motion of the vehicle and structure separately: direct equilibrium of contact forces, variational formulations and condensation methods. All these methods are explained in detail using the same nomenclature to assist the reader in comparing their main advantages and disadvantages. Special focus is given to the accuracy, robustness, efficiency and simplicity of the different methods. As far as the author is aware, there are few published studies that discuss all the methods addressed here with the same level of detail.

The direct and iterative methods are used to establish directly the equilibrium of contact forces. Although iterative techniques have been applied to vehicle-structure interaction problems for more than four decades, there is little information in the literature concerning their convergence properties. In this work, it has been shown that even for a simple system of equations the iterative techniques can diverge. Also, an analytical expression is provided to verify in an accurate and reliable manner the convergence characteristics of the iterative methods. Since the direct method avoids the iterative procedure, it leads to a more robust and accurate algorithm. This becomes even more important for the case of a nonlinear analysis, where convergence is a critical issue. In terms of computational efficiency, the direct method does not preserve the bandwidth of the coefficient matrix due to the additional variables and therefore a single system of equations requires more time to be solved. However, the iterative procedure is avoided. Therefore, comparing the computational efficiency of these two types of methods is not a straightforward task.

The variational formulations are well-known in the optimisation theory and contact mechanics and are used by most of the commercial finite element packages to deal with contact problems. The Lagrange multiplier method leads to the same system of equations as the direct method, and so the same conclusions in terms of computational efficiency apply. The penalty method does not introduce additional variables, but the stiffness matrix becomes time-dependent. Again, comparing the computational efficiency of these methods is a difficult task. Also, the penalty method might not satisfy exactly the constraint equations. The main advantage of the direct equilibrium of forces, when compared to the variational formulations, is a better understanding of the physical meaning of the equations. The approaches that establish the direct equilibrium of forces are based on simple concepts that are easily understood, such as the formulation of the equations of motion and constraint equations. This also allows an easier identification of possible errors and a better optimisation of the algorithm.

Since the condensation methods eliminate the d.o.f. of the vehicle contacting the structure at the element level, a conventional assembly process can be applied to form the structural matrices. The main disadvantage of these methods is that no separation between the vehicles and structure is allowed. Also, the equations of motion of the coupled vehicle-bridge system might be difficult to determine if nonlinearities are considered in the vehicle models. The vehicle-structure interaction algorithms based on the condensation methods avoid the iterative procedure, but the system matrices are usually time-dependent and must be updated and factorised at each time step.

All the vehicle-structure interaction methods described in this chapter have one of the following disadvantages: requiring an iterative procedure, introducing additional variables into the system of linear equations or leading to time-dependent structural matrices. Estimating the degradation of the computational efficiency implied by each of these disadvantages is a very difficult task. The only objective way to perform this evaluation is to solve the same numerical example using the different methods. As far as the author is aware, this type of comparison has not yet been published. Therefore, the selection of the most suitable vehicle-structure interaction method cannot be based on the computational efficiency. The only disadvantage of the direct and the Lagrange multiplier methods is the introduction of additional variables. Unlike the Lagrange multiplier method, the direct method is based on simple concepts that are easily understood and therefore is the only method adopted here. This method is further developed in this work.

3 WHEEL-RAIL CONTACT MECHANICS

3.1 INTRODUCTION

One of the main objectives of this thesis is to develop an accurate and robust algorithm to analyse the vehicle-structure interaction. The comprehensive overview of vehicle-structure interaction methods presented in Chapter 2 focuses on how to formulate the equations of motion of the structural system and how to impose contact constraint equations that relate the displacements of the two subsystems. These approaches guarantee the equilibrium of the contact forces but do not take into account the local deformations and highly concentrated stresses that arise in the vicinity of the contact region. Most of the existing methods treat the contact forces in the normal and tangential directions as external forces. The formulation proposed here uses an enhanced node-to-segment contact element, which includes an additional Hertzian spring that relates more accurately the contact forces to the local deformations (see Chapter 5). The present work only addresses contact in the normal direction, being the extension of the proposed formulation to three-dimensional contact problems described in Montenegro *et al.* (2015). The main objective of this chapter is to provide a thorough understanding of the behaviour of the contact interface and to describe the theory necessary to relate the forces acting at the interface with the local deformations of the contact region. The basic concepts and definitions of contact mechanics used here are presented in Section 3.2.

The Hertz contact theory is discussed in detail in Section 3.3, in which a special focus is given to its assumptions and limitations. The equations defining the geometry of the wheel and rail surfaces and the relation between the pressure distribution and elastic deformations at the contact region are also explained in detail. More than a century ago, Hertz (1882) provided tabulated values to calculate the force-deflection relationship of the contact spring as a function of a parameter that depends only on the geometrical properties of the two contacting bodies. However, only a few values were provided, while others must be interpolated. Shabana *et al.* (2001) developed an alternative approach where these values can be obtained approximately by closed-form expressions, but the magnitude of the errors is large. These errors are significantly reduced in this work by using the computer program

Maple® (2009) to accurately solve the equations related to the Hertz theory in order to provide additional values of the parameters involved in the calculation of the contact stiffness. The linear and nonlinear force-deflection relationships of the Hertzian spring are also presented in Section 3.3. A simple example consisting in the calculation of a contact lookup table for a single wheel-rail pair is described in Section 3.4. This is useful as a validation of the mathematical expressions presented in Section 3.3 and also provides a good understanding of the interaction between wheel and rail for different lateral displacements of the wheelset. The parameters defining the Hertz force law are calculated assuming the wheelset centred on the track and are used throughout this thesis.

3.2 BASIC CONCEPTS AND DEFINITIONS

The contact between two solid bodies can be conforming or non-conforming (Johnson, 1999). In a conforming contact, the surfaces of the two bodies fit closely together without deformation. Otherwise, if the two bodies have dissimilar profiles, the contact is non-conforming. In railway applications, the wheel and rail generally have dissimilar profiles, especially along the longitudinal direction of the track, and therefore the assumption of non-conforming contact is often used (Shabana *et al.*, 2007). Along the lateral direction, the wheel and rail profiles can touch at a single point, at multiple points or along a line (see Fig. 3.1). The contact conditions depend on the amount of wear, which significantly influences the shape of the wheels and rails. For example, multi-point contact occurs when the wheel also touches the rail in its flange and line contact can occur when the worn shapes of the wheel and gauge side of the rail head have similar radii (Iwnicki, 2006). Only the single-point contact is addressed in the present work.

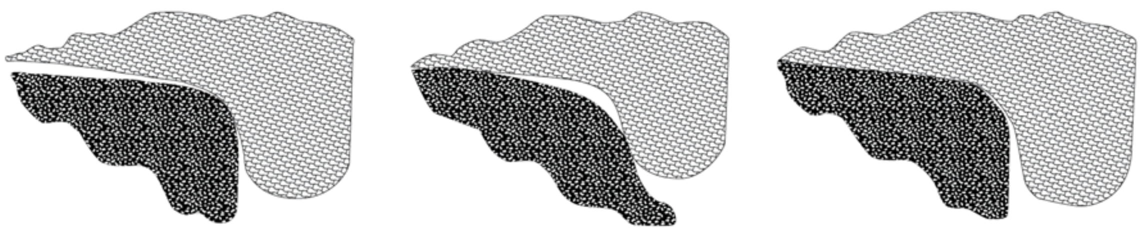

(a) (b) (c)

Figure 3.1 –Wheel and rail single-point (a), multi-point (b) and line (c) contact (Iwnicki, 2006).

When two non-conforming contacting bodies are loaded, they deform in the vicinity of the contact point, touching over an area. The surface forces transmitted across the contact area depend on the geometry of both surfaces and can be decomposed into normal and tangential forces. The tangential contact problem is not addressed in this work. Wiest *et al.* (2008) compared different approaches for simulating the wheel-rail contact: using a three-dimensional finite element model of the wheel and rail developed with the Abaqus commercial software (2005), Hertz theory, and the non-Hertzian method implemented in the CONTACT program (Vollebregt, 2009). The finite element analysis provides the most accurate results but has a very high computational cost. The contact forces and location of the contact points are calculated using the GENSYS multibody simulation program (2004), whilst the finite element software is only used to analyse one cross-section. In a wide range of railway applications, the plastic deformation in the contact area does not need to be taken into account and the relation between the contact forces and the local deformations in the vicinity of the contact region can be accurately predicted using the Hertz theory or non-Hertzian methods. Only the Hertz theory is considered here due to its much lower computational cost.

3.3 HERTZ THEORY

In 1882, Hertz presented a theoretical solution for determining the shape of the contact area and stress distribution at the contact interface of two non-conforming elastic bodies as a function of the normal load (Hertz, 1882; Hertz *et al.*, 1896). The first assumption made is that the contact area is elliptical. This assumption is based on the observation of interference fringes at the contact of two glass lenses (Johnson, 1999). Figure 3.2 shows the interference fringes for the case of two equal cylindrical lenses with their axes inclined 45°.

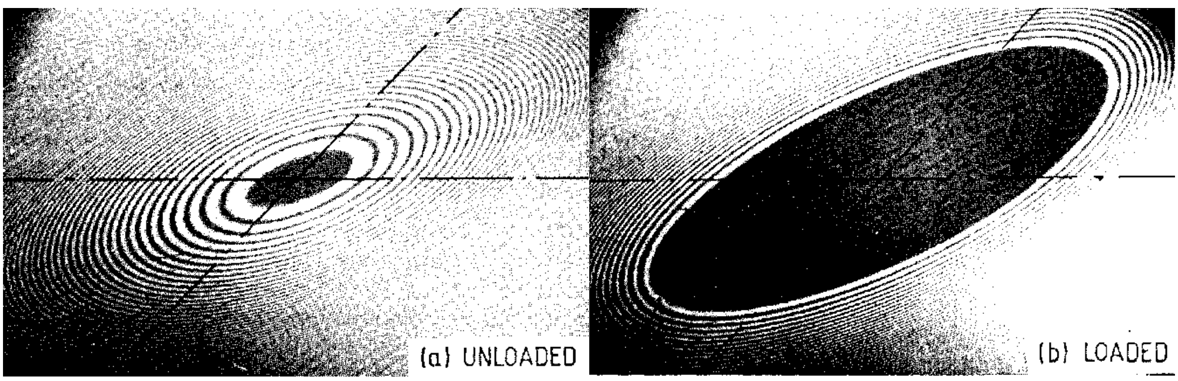

(a) (b)

Figure 3.2 – Interference fringes at the contact of two (a) unloaded and (b) loaded equal cylindrical lenses with their axes inclined 45° (Johnson, 1999).

Hertz further assumed that, for calculating the local deformations, each body is an elastic, isotropic and homogeneous half-space loaded over a small elliptical region of its plane surface. With this simplification, widely used in contact mechanics, the concentrated stresses acting at the contact interface can be treated separately from the global distribution of stresses. This assumption is valid when the size of the contact area is small when compared with the dimensions of the two bodies and the relative radii of curvature of the surfaces. The second condition is necessary to ensure firstly that the surfaces near the contact region can be approximated by plane surfaces of a half-space, and secondly, that the strains in the contact region are small enough to be within the scope of the linear theory of elasticity. Wiest *et al.* (2008) and Yan and Fischer (2000) compare the results obtained with the Hertz theory with those obtained using three-dimensional finite element models and concluded that the theoretical results are accurate even when one of the minimum curvature radii of the contacting bodies is smaller than the dimension of the contact area, which violates one of the assumptions made.

Hertz also assumed that each surface is topographically smooth on both macro and micro scale. On the macro scale, this means that the profiles of the surfaces in the contact region are continuous up to their second derivative. On the micro scale, this assumption disregards small surface roughness, which could lead to a discontinuous contact or a highly local variation in the contact pressure. Greenwood *et al.* (1984) theoretically and experimentally studied the influence of the surface roughness on the evolution of the contact area and pressure. They analysed a typical wheel of radius 400 mm and a railhead of a well-used main line and concluded that generally, the wheel-rail contact is very smooth and that the Hertz theory accurately models the contact between both surfaces.

Finally, the Hertz theory neglects the effects of the friction forces. The normal forces at the contact interface are only influenced by friction if the elastic constants of the two materials are different and if the materials are compressible. Normally, in these cases, slip may occur, i.e., the tangential displacements of both bodies may be different. Such slip will be opposed by friction and if the friction coefficient is sufficiently high the slip may not even occur. For wheel-rail contact the influence of the tangential forces on the normal forces is generally not significant and decreases when the difference between the elastic constants of the bodies in contact decreases (Johnson, 1999).

The assumptions used in Hertz theory can then be summarised as follows (Johnson, 1999; Shabana *et al.*, 2007):

- the profiles of the surfaces are non-conforming in the contact region and continuous up to their second derivative;
- each solid can be considered as an elastic, isotropic and homogeneous half-space;
- the size of the contact area is small when compared with the dimensions of the two bodies and the relative radii of curvature of the surfaces;
- the strains are small;
- the surfaces are frictionless.

3.3.1 Geometry of non-conforming surfaces

A general case of contact between two elastic bodies is illustrated in Fig. 3.3. The origins of the Cartesian coordinate systems are at the point of first contact, the axes x_w, y_w, x_r and y_r lie in the tangential plane common to both surfaces and the axes z_w and z_r lie along the common normal, with the positive direction towards the respective body.

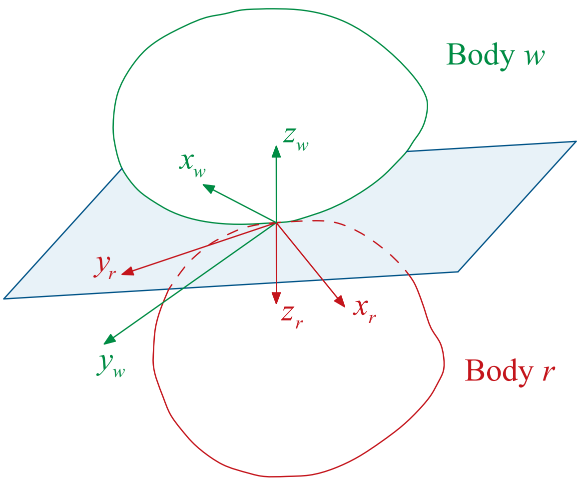

Figure 3.3 – Two bodies touching at a single point (adapted from Shabana *et al.* (2007)).

The profile of each surface in the region close to the origin can be approximated by a second order polynomial of the form

$$z_w = A_w x_w^2 + B_w y_w^2 + C_w x_w y_w \tag{3.1}$$

$$z_r = A_r x_r^2 + B_r y_r^2 + C_r x_r y_r \tag{3.2}$$

where A_w, B_w, C_w, A_r, B_r and C_r are constants that depend on the geometry of the respective surface. The gap (h) between the two undeformed surfaces is given by

$$h = z_w + z_r \tag{3.3}$$

Equation (3.3) may also be written in the form

$$h = A x^2 + B y^2 + C x y \tag{3.4}$$

where A, B and C are geometric constants. The axes x_w, y_w, x_r and y_r can be chosen so that the terms $C_w x_w y_w$ and $C_r x_r y_r$ are zero. Hence, Eqs. (3.1) and (3.2) can be rewritten as

$$z_w = \frac{1}{2R'_w} x_w^2 + \frac{1}{2R''_w} y_w^2 \tag{3.5}$$

$$z_r = \frac{1}{2R'_r} x_r^2 + \frac{1}{2R''_r} y_r^2 \tag{3.6}$$

where R'_w, R''_w, R'_r and R''_r are the principal radii of curvature of the surfaces of the bodies w and r. The radius of curvature is assumed to be positive if the unit tangent vector rotates counterclockwise as a function of the parameter along the curve, and negative otherwise. Substituting Eqs. (3.5) and (3.6) into Eq. (3.3) leads to

$$h = \frac{1}{2R'_w} x_w^2 + \frac{1}{2R''_w} y_w^2 + \frac{1}{2R'_r} x_r^2 + \frac{1}{2R''_r} y_r^2 \tag{3.7}$$

The Cartesian coordinate systems of the bodies w and r may not be coincident, as shown in Fig. 3.4.

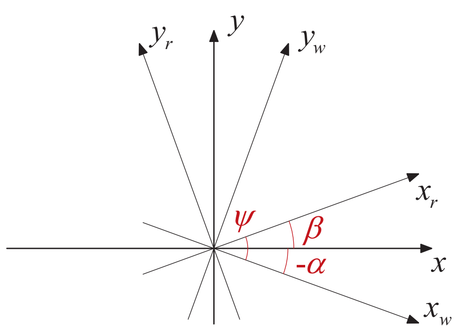

Figure 3.4 – Tangential plane common to both surfaces.

The transformations of the coordinates of the two surfaces from their respective coordinate systems to the global coordinate system shown in Fig. 3.4 are given by

$$x_w = x\cos\alpha - y\sin\alpha \tag{3.8}$$

$$y_w = x\sin\alpha + y\cos\alpha \tag{3.9}$$

$$x_r = x\cos\beta + y\sin\beta \tag{3.10}$$

$$y_r = -x\sin\beta + y\cos\beta \tag{3.11}$$

Substituting Eqs. (3.8) to (3.11) into Eq. (3.7) and using the following double-angle formula

$$\sin 2\alpha = 2\sin\alpha\cos\alpha \tag{3.12}$$

gives

$$\begin{aligned} h &= \frac{1}{2R'_w}\left(x^2\cos^2\alpha - xy\sin 2\alpha + y^2\sin^2\alpha\right) \\ &+ \frac{1}{2R''_w}\left(x^2\sin^2\alpha + xy\sin 2\alpha + y^2\cos^2\alpha\right) \\ &+ \frac{1}{2R'_r}\left(x^2\cos^2\beta + xy\sin 2\beta + y^2\sin^2\beta\right) \\ &+ \frac{1}{2R''_r}\left(x^2\sin^2\beta - xy\sin 2\beta + y^2\cos^2\beta\right) \end{aligned} \tag{3.13}$$

Rearranging terms and equating the result to Eq. (3.4) leads to

$$A = \frac{1}{2R'_w}\cos^2\alpha + \frac{1}{2R''_w}\sin^2\alpha + \frac{1}{2R'_r}\cos^2\beta + \frac{1}{2R''_r}\sin^2\beta \tag{3.14}$$

$$B = \frac{1}{2R'_w}\sin^2\alpha + \frac{1}{2R''_w}\cos^2\alpha + \frac{1}{2R'_r}\sin^2\beta + \frac{1}{2R''_r}\cos^2\beta \tag{3.15}$$

$$C = \frac{1}{2}\left(\frac{1}{R'_r} - \frac{1}{R''_r}\right)\sin 2\beta - \frac{1}{2}\left(\frac{1}{R'_w} - \frac{1}{R''_w}\right)\sin 2\alpha \tag{3.16}$$

In order to simplify the notation, the constants C_1 and C_2, which depend on the geometrical properties of the two bodies are introduced and defined as follows

$$C_1 = A + B \tag{3.17}$$

$$C_2 = A - B \tag{3.18}$$

Substituting Eqs. (3.14) and (3.15) into Eq. (3.17) results in

$$\begin{aligned} C_1 &= \frac{1}{2R'_w}\left(\cos^2\alpha + \sin^2\alpha\right) + \frac{1}{2R''_w}\left(\sin^2\alpha + \cos^2\alpha\right) \\ &+ \frac{1}{2R'_r}\left(\cos^2\beta + \sin^2\beta\right) + \frac{1}{2R''_r}\left(\sin^2\beta + \cos^2\beta\right) \end{aligned} \tag{3.19}$$

which is equivalent to

$$C_1 = \frac{1}{2}\left(\frac{1}{R'_w} + \frac{1}{R''_w} + \frac{1}{R'_r} + \frac{1}{R''_r}\right) \tag{3.20}$$

Substituting Eqs. (3.14) and (3.15) into Eq. (3.18) yields

$$\begin{aligned} C_2 &= \frac{1}{2R'_w}\left(\cos^2\alpha - \sin^2\alpha\right) + \frac{1}{2R''_w}\left(\sin^2\alpha - \cos^2\alpha\right) \\ &+ \frac{1}{2R'_r}\left(\cos^2\beta - \sin^2\beta\right) + \frac{1}{2R''_r}\left(\sin^2\beta - \cos^2\beta\right) \end{aligned} \tag{3.21}$$

Using the following double-angle formula

$$\cos 2\alpha = \cos^2\alpha - \sin^2\alpha \tag{3.22}$$

leads to

$$C_2 = \frac{1}{2}\left(\frac{1}{R'_w} - \frac{1}{R''_w}\right)\cos 2\alpha + \frac{1}{2}\left(\frac{1}{R'_r} - \frac{1}{R''_r}\right)\cos 2\beta \tag{3.23}$$

The axes x and y can be chosen so that the term Cxy in Eq. (3.4) is equal to zero, so that

$$h = Ax^2 + By^2 \tag{3.24}$$

For Eq. (3.24) to be valid, Eq. (3.16) must be equal to zero, which results in

$$\frac{1}{2}\left(\frac{1}{R'_w} - \frac{1}{R''_w}\right)\sin 2\alpha = \frac{1}{2}\left(\frac{1}{R'_r} - \frac{1}{R''_r}\right)\sin 2\beta \tag{3.25}$$

The triangle represented in Fig. 3.5 can be drawn based on Fig. 3.4 and Eqs. (3.25) and (3.23).

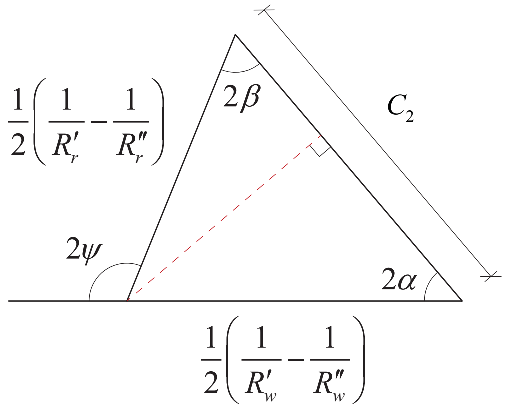

Figure 3.5 – Geometric relations between the contacting surfaces.

By applying the law of cosines to the triangle shown in Fig. 3.5, Eq. (3.23) can be written as

$$C_2=\frac{1}{2}\sqrt{\left(\frac{1}{R'_w}-\frac{1}{R''_w}\right)^2+\left(\frac{1}{R'_r}-\frac{1}{R''_r}\right)^2+2\left(\frac{1}{R'_w}-\frac{1}{R''_w}\right)\left(\frac{1}{R'_r}-\frac{1}{R''_r}\right)\cos 2\psi} \tag{3.26}$$

For calculating the pressure distribution and the elastic deformation (see Section 3.3.2) it is convenient to introduce the auxiliary angle θ expressed as

$$\cos\theta=-\frac{C_2}{C_1} \tag{3.27}$$

and to define A and B in terms of C_1 and θ. Adding Eqs. (3.17) and (3.18) gives

$$A=\frac{1}{2}\left(C_1+C_2\right) \tag{3.28}$$

The half-angle formula for the sine is

$$\sin^2\frac{\theta}{2}=\frac{1}{2}\left(1-\cos\theta\right) \tag{3.29}$$

Substituting Eq. (3.27) into Eq. (3.29) results in

$$\sin^2\frac{\theta}{2}=\frac{1}{2}\left(1+\frac{C_2}{C_1}\right) \tag{3.30}$$

Multiplying Eq. (3.30) by C_1 and substituting into Eq. (3.28) yields

$$A = C_1 \sin^2 \frac{\theta}{2} \tag{3.31}$$

Subtracting Eq. (3.18) from Eq. (3.17) gives

$$B = \frac{1}{2}(C_1 - C_2) \tag{3.32}$$

The half-angle formula for the cosine is

$$\cos^2 \frac{\theta}{2} = \frac{1}{2}(1 + \cos\theta) \tag{3.33}$$

Substituting Eq. (3.27) into Eq. (3.33) results in

$$\cos^2 \frac{\theta}{2} = \frac{1}{2}\left(1 - \frac{C_2}{C_1}\right) \tag{3.34}$$

Multiplying Eq. (3.34) by C_1 and substituting into Eq. (3.32) yields

$$B = C_1 \cos^2 \frac{\theta}{2} \tag{3.35}$$

The Cartesian coordinate systems defined in Fig. 3.3 are now represented in Fig. 3.6 for the case of a wheel and rail touching at a single point. The subscripts *w* and *r* denote wheel and rail, respectively.

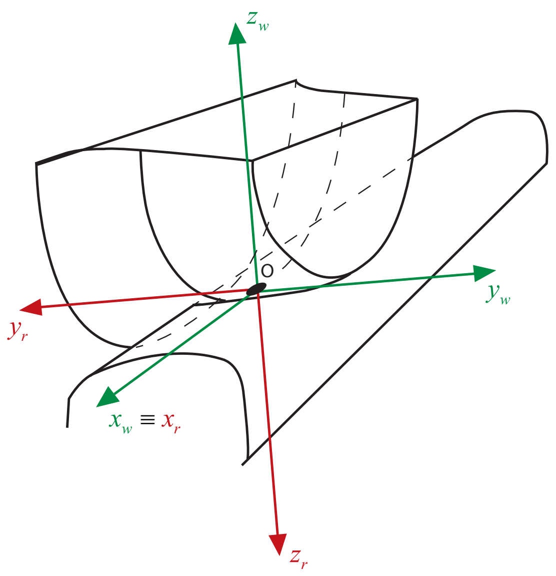

Figure 3.6 – Wheel and rail touching at a single point (adapted from Iwnicki (2006)).

The wheel rolling radius *r*, its principal radius of curvature R'_w and the contact angle γ are represented in Fig. 3.7. When the wheelset is centred on the track, the rolling radius *r* corresponds to the nominal rolling radius r_0. The contact angle is measured with respect to a horizontal line. The principal radius of curvature is given by

$$R'_w = \frac{r}{\cos\gamma} \tag{3.36}$$

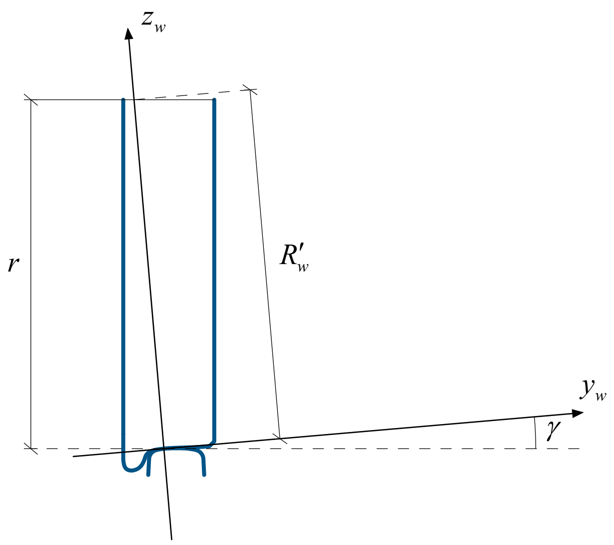

Figure 3.7 – Calculation of the longitudinal radius of the wheel (adapted from Iwnicki (2006)).

3.3.2 Pressure distribution and elastic deformation

One of the assumptions made by Hertz for calculating the local deformations is that each body is a homogeneous half-space loaded over a small elliptical region of its plane surface. The contact pressure can be assumed to satisfy the following requirements for the equilibrium of both bodies (Shabana *et al.*, 2007):

1) the total applied normal force (F_n) must to be equal to the total resisting force generated by the vertical component of the pressure in the contact area;
2) the displacements far enough from the contact area can be neglected;
3) the normal stresses outside the contact region are equal to zero;
4) the normal stresses acting on both bodies are in balance within the contact region;
5) the shear stresses τ_{xz} and τ_{yz} along the surfaces of the bodies are zero.

These requirements can be satisfied by assuming that the pressure distribution in the contact area is a quadratic function of x and y expressed by

$$p(x,y) = p_0\sqrt{1-\left(\frac{x}{a}\right)^2-\left(\frac{y}{b}\right)^2} \tag{3.37}$$

where p_0 is the maximum pressure, and a and b are the semi-axes of the elliptical contact area. Since the pressure distribution is semi-ellipsoidal, the total normal load is given by

$$F_n = \frac{2}{3}\,p_0\,\pi\,a\,b \tag{3.38}$$

Substituting Eq. (3.38) into Eq. (3.37) yields

$$p(x,y) = \frac{3F_n}{2\pi a b}\sqrt{1-\left(\frac{x}{a}\right)^2-\left(\frac{y}{b}\right)^2} \tag{3.39}$$

The deformed surfaces in the neighbourhood of the applied normal forces F_n are shown in the cross-section depicted in Fig. 3.8.

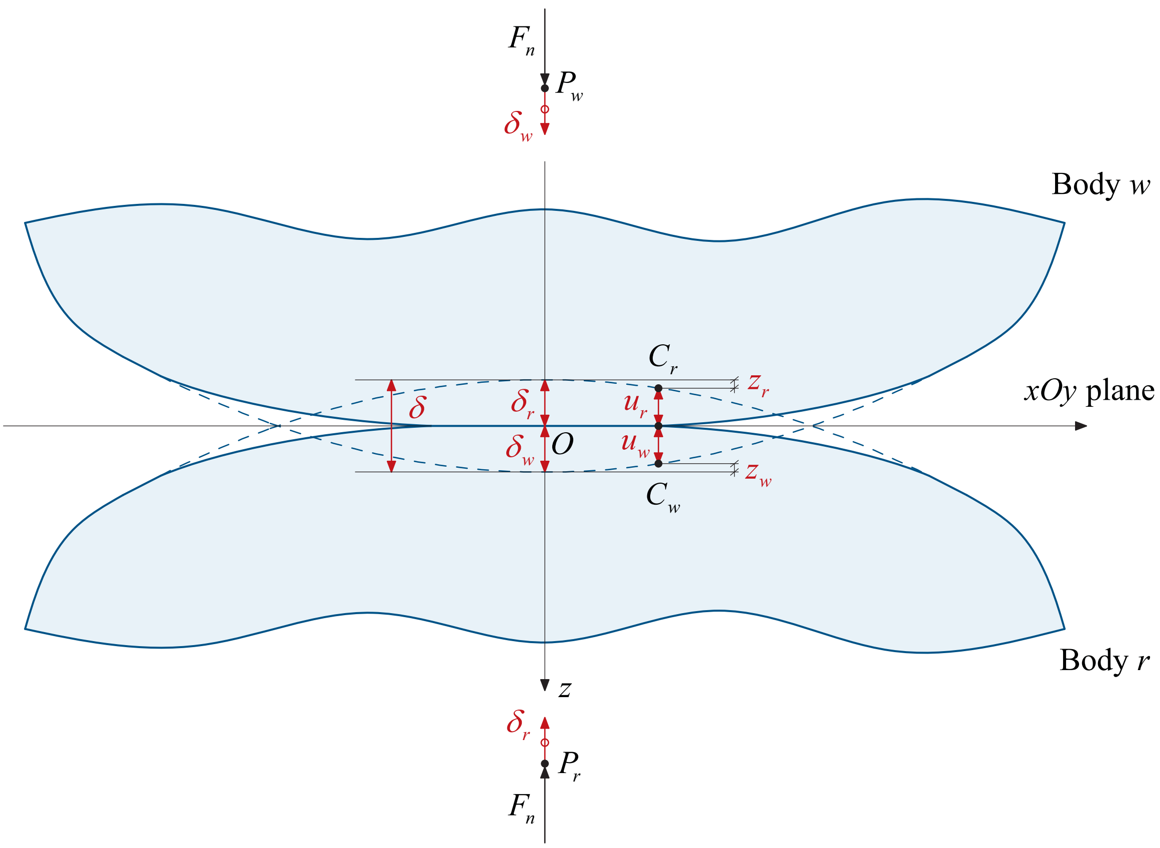

Figure 3.8 – Deformed surfaces in the neighbourhood of the applied normal forces.

The displacements of the points P_w and P_r due to the applied pressure are δ_w and δ_r, respectively, as represented in Fig. 3.8. Without deformation, the profiles would overlap as shown by the dashed lines. The contact pressure causes a displacement of u_w and u_r of the points C_w and C_r. If after deformation the points C_w and C_r are in contact, then

$$u_w + u_r + h = \delta_w + \delta_r \tag{3.40}$$

where h is given by Eq. (3.3). Substituting Eq. (3.24) into Eq. (3.40) results in

$$u_w + u_r = \delta - A\,x^2 - B\,y^2 \tag{3.41}$$

where δ is the total displacement given by

$$\delta = \delta_w + \delta_r \tag{3.42}$$

The pressure $p(x,y)$ defined by Eq. (3.39) produces a displacement given by (Shabana *et al.*, 2007)

$$u_w + u_r = \frac{L - M\,x^2 - N\,y^2}{\pi\,E_{wr}} \tag{3.43}$$

in which

$$L = \frac{3F_n}{4}\int_0^\infty \frac{dw}{\sqrt{(a^2+w)(b^2+w)\,w}} \tag{3.44}$$

$$M = \frac{3F_n}{4}\int_0^\infty \frac{dw}{\sqrt{(a^2+w)^3(b^2+w)\,w}} \tag{3.45}$$

$$N = \frac{3F_n}{4}\int_0^\infty \frac{dw}{\sqrt{(a^2+w)(b^2+w)^3\,w}} \tag{3.46}$$

$$\frac{1}{E_{wr}} = \frac{1-\nu_w^2}{E_w} + \frac{1-\nu_r^2}{E_r} \tag{3.47}$$

where ν is the Poisson's ratio, and E_w and E_r are the Young's modulus of the bodies w and r. Making the substitution $w = b^2 z^2$ in the integrals of Eqs. (3.44) to (3.46) leads to

$$L = \frac{3F_n}{2a} \int_0^\infty \frac{dz}{\sqrt{(1+k^2z^2)(1+z^2)}} \tag{3.48}$$

$$M = \frac{3F_n}{2a^3} \int_0^\infty \frac{dz}{\sqrt{(1+k^2z^2)^3(1+z^2)}} \tag{3.49}$$

$$N = \frac{3F_n}{2a^3k^2} \int_0^\infty \frac{dz}{\sqrt{(1+k^2z^2)(1+z^2)^3}} \tag{3.50}$$

where k is the ellipse axes ratio expressed as

$$k = \frac{b}{a} \tag{3.51}$$

Substituting Eq. (3.41) into Eq. (3.43) leads to

$$\delta - A\,x^2 - B\,y^2 = \frac{L - M\,x^2 - N\,y^2}{\pi\,E_{wr}} \tag{3.52}$$

Equating the coefficients of both sides of Eq. (3.52) and substituting Eqs. (3.48) to (3.50) gives

$$\delta = \frac{3F_n}{2\pi\,a\,E_{wr}} \int_0^\infty \frac{dz}{\sqrt{(1+k^2z^2)(1+z^2)}} \tag{3.53}$$

$$A = \frac{3F_n}{2\pi\,a^3E_{wr}} \int_0^\infty \frac{dz}{\sqrt{(1+k^2z^2)^3(1+z^2)}} \tag{3.54}$$

$$B = \frac{3F_n}{2\pi\,a^3k^2E_{wr}} \int_0^\infty \frac{dz}{\sqrt{(1+k^2z^2)(1+z^2)^3}} \tag{3.55}$$

Substituting Eqs. (3.31) and (3.35) into Eqs. (3.54) and (3.55), respectively, and rearranging the terms gives

$$a^3 = \frac{3F_n}{2\pi\,E_{wr}} \; \frac{1}{C_1 \sin^2\dfrac{\theta}{2}} \int_0^\infty \frac{dz}{\sqrt{(1+k^2z^2)^3(1+z^2)}} \tag{3.56}$$

$$a^3 = \frac{3F_n}{2\pi k^2 E_{wr}} \, \frac{1}{C_1 \cos^2 \dfrac{\theta}{2}} \int_0^\infty \frac{dz}{\sqrt{\left(1+k^2z^2\right)\left(1+z^2\right)^3}} \tag{3.57}$$

Dividing Eq. (3.56) by Eq. (3.57) results in

$$\tan^2 \frac{\theta}{2} \int_0^\infty \frac{dz}{\sqrt{\left(1+k^2z^2\right)\left(1+z^2\right)^3}} = k^2 \int_0^\infty \frac{dz}{\sqrt{\left(1+k^2z^2\right)^3\left(1+z^2\right)}} \tag{3.58}$$

Equation (3.56) can be rewritten as

$$a = m\left(\frac{3F_n}{4C_1 \, E_{wr}}\right)^{\frac{1}{3}} \tag{3.59}$$

where

$$m = \left[\frac{2}{\pi \sin^2 \dfrac{\theta}{2}} \int_0^\infty \frac{dz}{\sqrt{\left(1+k^2z^2\right)^3\left(1+z^2\right)}}\right]^{\frac{1}{3}} \tag{3.60}$$

Substituting Eq. (3.51) into Eq. (3.57) and rearranging the terms leads to

$$b = n\left(\frac{3F_n}{4C_1 \, E_{wr}}\right)^{\frac{1}{3}} \tag{3.61}$$

in which

$$n = \left[\frac{2k}{\pi \cos^2 \dfrac{\theta}{2}} \int_0^\infty \frac{dz}{\sqrt{\left(1+k^2z^2\right)\left(1+z^2\right)^3}}\right]^{\frac{1}{3}} \tag{3.62}$$

In Eq. (3.58) the variable k depends only on the angle θ. Hertz solved this equation only for a few values of θ by reducing to elliptic integrals and using the Legendre's tables (Hertz, 1882). The coefficients m and n obtained by Hertz are presented in Table 3.1.

Table 3.1 –Coefficients *m* and *n* provided by Hertz.

θ (°)	90	80	70	60	50	40	30	20	10	0
m	1.0	1.1278	1.2835	1.4858	1.7542	2.1357	2.7307	3.7779	6.6120	∞
n	1.0	0.8927	0.8017	0.7171	0.6407	0.5673	0.4930	0.4079	0.3186	0.0

The coefficients *m* and *n* can be interpolated for other values of θ. Shabana *et al.* (2001) developed an alternative approach where the coefficients *m* and *n* are obtained approximately by closed-form expressions as functions of θ. These coefficients are defined by

$$m(\theta) = A_m \tan\left(\theta - \frac{\pi}{2}\right) + \frac{B_m}{\theta^{C_m}} + D_m \tag{3.63}$$

$$n(\theta) = \frac{1}{A_n \tan\left(\theta - \frac{\pi}{2}\right) + 1} + B_n \theta^{C_n} + D_n \sin(\theta) \tag{3.64}$$

where A_i, B_i, C_i and D_i ($i = m, n$) are indicated in Table 3.2.

Table 3.2 – Coefficients used in the closed-form functions $m(\theta)$ and $n(\theta)$.

Coefficient	Value
A_m	-1.086419052477
B_m	-0.106496432832
C_m	1.35
D_m	1.057885958251
A_n	-0.773444080706
B_n	0.256695354565
C_n	0.2
D_n	-0.280958376499

The Hertz coefficients *m* and *n* defined in Table 3.1 and the closed-form functions proposed by Shabana *et al.* (2001) are plotted in Fig. 3.9.

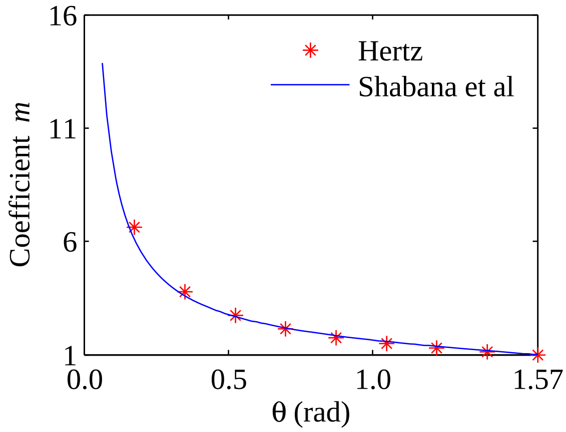

(a)

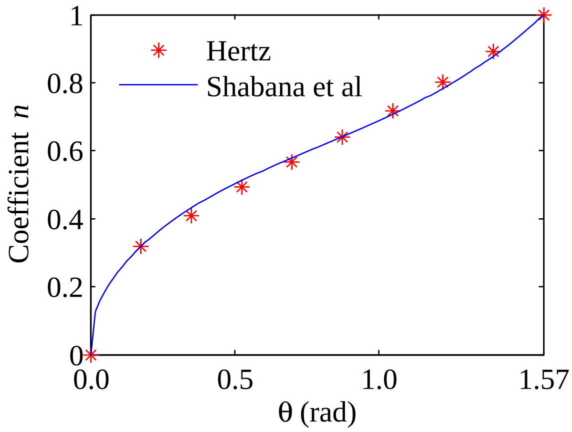

(b)

Figure 3.9 – Comparison between the coefficients obtained by Hertz and Shabana: (a) m and (b) n.

The maximum percentage error of the coefficients obtained by Shabana *et al.* (2001) relative to the classical values provided by Hertz is about 7.8%. Working with errors of this magnitude can presently be avoided by using computer programs that can solve a wide range of equations with very high accuracy and efficiency using numerical methods. Equations (3.58), (3.60) and (3.62) have been solved using the Maple program, being the obtained values for m and n presented in Table 3.3.

Table 3.3 – Coefficients m and n obtained using Maple.

θ (°)	m	n	θ (°)	m	n	θ (°)	m	n
0	∞	0	32	2.58593597	0.50820247	64	1.39907311	0.74926407
2	22.24316987	0.16919126	34	2.45615758	0.52315083	66	1.35910610	0.76579654
4	13.29245688	0.21891949	36	2.33902624	0.53795322	68	1.32115990	0.78266689
6	9.78829925	0.25522363	38	2.23270699	0.55265280	70	1.28507084	0.79990447
8	7.85604435	0.28506133	40	2.13570910	0.56728863	72	1.25069205	0.81753976
10	6.61145526	0.31098350	42	2.04680807	0.58189653	74	1.21789124	0.83560454
12	5.73420446	0.33425365	44	1.96498803	0.59650972	76	1.18654892	0.85413209
14	5.07821059	0.35560421	46	1.88939861	0.61115939	78	1.15655677	0.87315741
16	4.56669587	0.37550408	48	1.81932211	0.62587516	80	1.12781634	0.89271744
18	4.15518440	0.39427507	50	1.75414831	0.64068542	82	1.10023787	0.91285131
20	3.81601123	0.41214974	52	1.69335473	0.65561767	84	1.07373929	0.93360060
22	3.53100444	0.42930310	54	1.63649128	0.67069879	86	1.04824535	0.95500964
24	3.28770175	0.44587129	56	1.58316788	0.68595529	88	1.02368685	0.97712582
26	3.07725198	0.46196317	58	1.53304465	0.70141354	90	1	1
28	2.89318365	0.47766784	60	1.48582396	0.71709992			
30	2.73064812	0.49305979	62	1.44124393	0.73304108			

The Hertz coefficients *m* and *n* defined in Table 3.1 and those obtained using Maple are plotted in Fig. 3.10. The maximum percentage error of the coefficients obtained using Maple relative to the classical values provided by Hertz is now 2.4%, which is more than three times lower than the error of the coefficients calculated by Shabana *et al.* (2001).

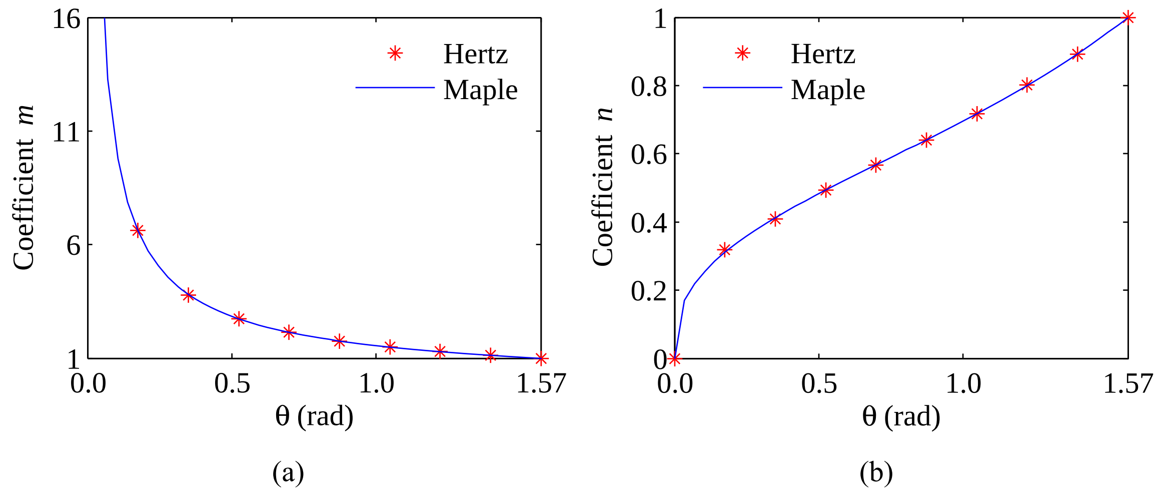

Figure 3.10 – Comparison between the coefficients obtained by Hertz and using Maple: (a) *m* and (b) *n*.

Substituting Eq. (3.59) into Eq. (3.53) leads to

$$\delta = \frac{3F_n}{2\pi m \left(\dfrac{3F_n}{4C_1 E_{wr}}\right)^{\frac{1}{3}} E_{wr}} \int_0^{\infty} \frac{dz}{\sqrt{\left(1+k^2z^2\right)\left(1+z^2\right)}} \tag{3.65}$$

After some mathematical manipulations Eq. (3.65) can be rewritten as

$$F_n = K_h \delta^{\frac{3}{2}} \tag{3.66}$$

where K_h is a constant that depends on the geometrical and material properties of the two contacting bodies and is given by

$$K_h = \frac{4\pi E_{wr} \beta}{3\sqrt{C_1}} \tag{3.67}$$

and

$$\beta = \sqrt{\pi}\left(\frac{m}{2}\right)^{\frac{3}{2}}\left[\int_0^{\infty}\frac{dz}{\sqrt{\left(1+k^2z^2\right)\left(1+z^2\right)}}\right]^{-\frac{3}{2}} \tag{3.68}$$

Equation (3.66) is the well-known Hertz force law. Again, only a few values are available for the β coefficient (Goldsmith, 1960). Table 3.4 shows more values of β that have been calculated using Maple.

Table 3.4 – Coefficient β obtained using Maple.

θ (°)	β	θ (°)	β	θ (°)	β
2	4.192081617	34	0.474819074	66	0.338190577
4	2.359074070	36	0.458365771	68	0.334835486
6	1.699217875	38	0.443659142	70	0.331834710
8	1.352557987	40	0.430457423	72	0.329169620
10	1.136749874	42	0.418563522	74	0.326824152
12	0.988602899	44	0.407815178	76	0.324784534
14	0.880207572	46	0.398077627	78	0.323039069
16	0.797257315	48	0.389238056	80	0.321577947
18	0.731632355	50	0.381201371	82	0.320393095
20	0.678368453	52	0.373886912	84	0.319478066
22	0.634253074	54	0.367225888	86	0.318827932
24	0.597111766	56	0.361159352	88	0.318439227
26	0.565418142	58	0.355636581	90	0.318309887
28	0.538067980	60	0.350613784		
30	0.514241966	62	0.346053050		
32	0.493318927	64	0.341921499		

Linearizing the Hertzian spring is advantageous for improving the computational efficiency and is essential, for example, for performing linear analyses. The difference between the linear and nonlinear force-deflection relationships is analysed in detail in Chapters 5 to 7. The stiffness of the Hertzian spring can be calculated by differentiating the force-deflection relationship given by Eq. (3.66), i.e.,

$$k_h = \frac{dF_n}{d\delta} \Leftrightarrow k_h = \frac{3}{2}K_h\delta^{\frac{1}{2}} \tag{3.69}$$

The deflection of the spring for the static wheel load Q is calculated using Eq. (3.66) and is given by

$$\delta_Q = Q^{\frac{2}{3}} K_h^{-\frac{2}{3}} \tag{3.70}$$

Substituting Eq. (3.70) into Eq. (3.69) leads to the linearized value of the contact stiffness k_h around the static wheel load

$$k_h = \frac{3}{2} K_h^{\frac{2}{3}} Q^{\frac{1}{3}} \tag{3.71}$$

3.4 NUMERICAL EXAMPLE

In order to validate the mathematical expressions that are used to calculate the parameters defining the Hertz force law, a simple example that consists of the calculation of a contact lookup table for a single wheel-rail pair is considered (see Fig. 3.11). The vertical rail profile 60E1 (BS EN 13674-1:2011, 2011), also known as UIC 60, and the wheel profile s1002 (BS EN 13715:2006+A1:2010, 2006) are used. In order to determine the contact point, the wheel and rail profiles are placed relative to each other assuming the wheelset centred on the track and then a prescribed lateral displacement is applied to the wheel. The variables Z_w and Z_r correspond to the height of the wheel and rail points, respectively. The location of the contact point is given by the minimal vertical distance between wheel and rail profiles. The rail gauge is the distance between the left and right rails, measured 14 mm below the crown of the rail, and is equal to 1435 mm. The wheelset gauge, also known as flangeback spacing, is the distance between the inner flanges of the wheels and is equal to 1360 mm. The following additional data is considered: Young's modulus $E = 210$ GPa, Poisson's ratio $\nu = 0.3$, wheel nominal rolling radius $r_0 = 460$ mm and wheel load $F = 83385$ kN (8.5 t). The range of lateral displacements considered is +/-20 mm with a step size of 0.1 mm.

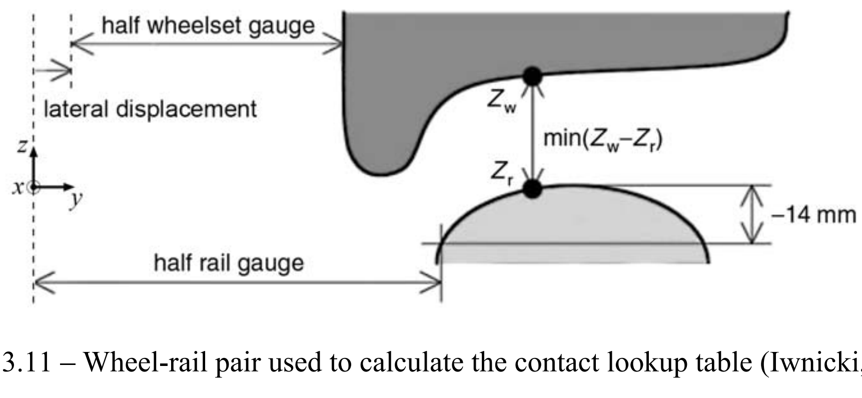

Figure 3.11 – Wheel-rail pair used to calculate the contact lookup table (Iwnicki, 2006).

The profiles, tangential angles and curvatures of the rail and wheel are plotted in Figs. 3.12 and 3.13, respectively.

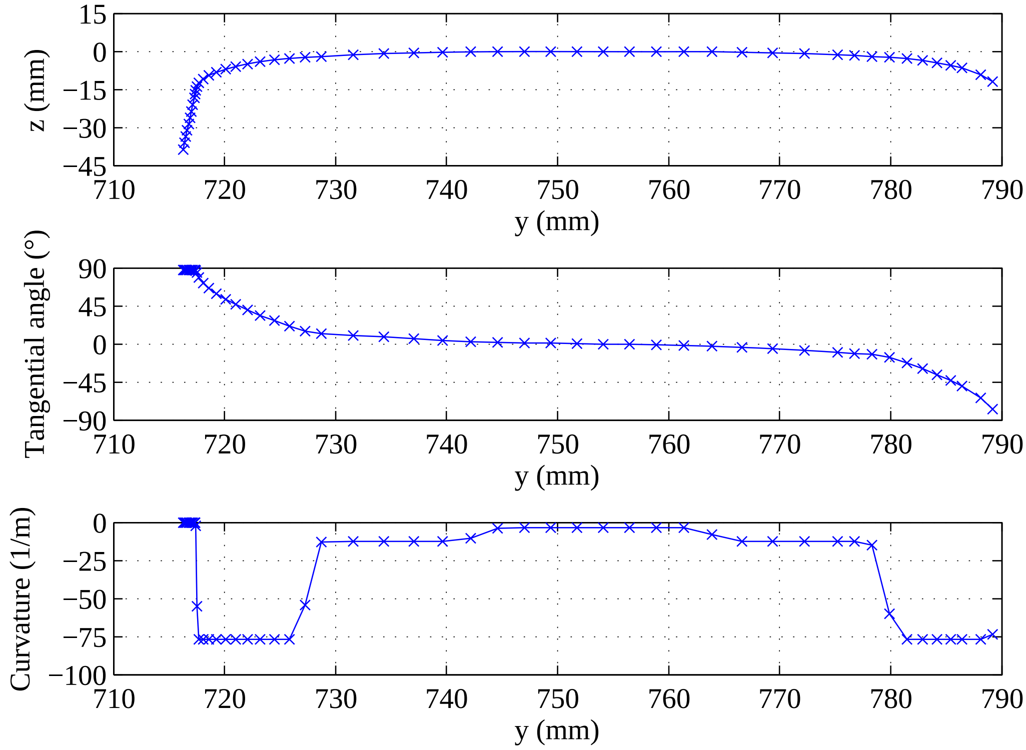

Figure 3.12 – Profile, tangential angle and curvature of the rail.

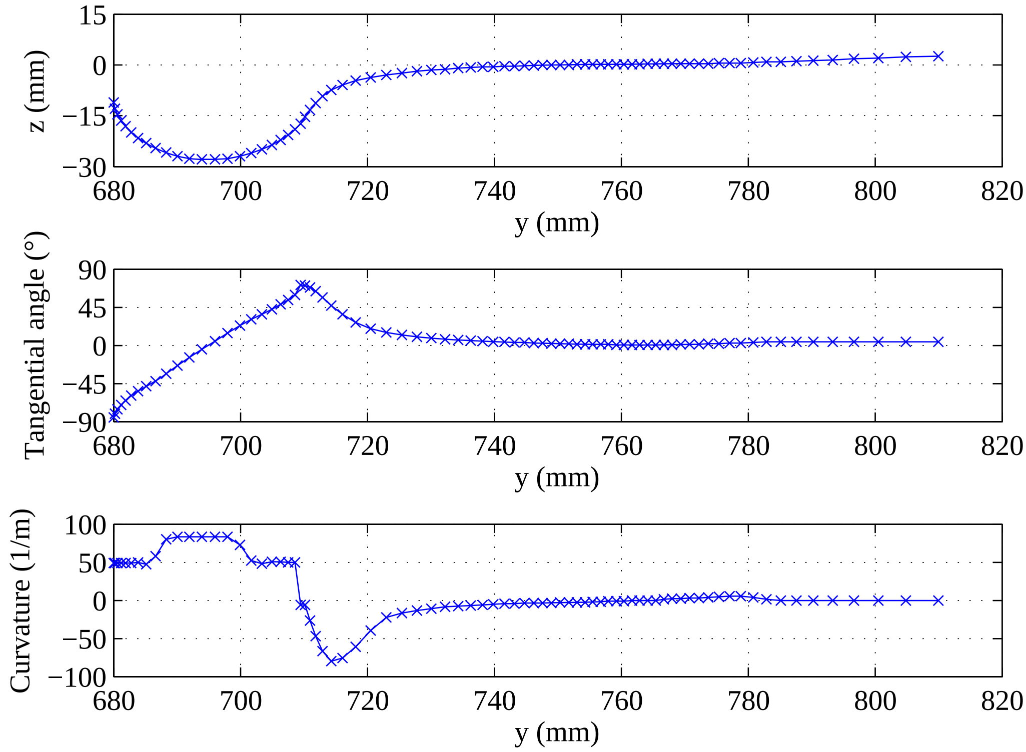

Figure 3.13 – Profile, tangential angle and curvature of the wheel.

The code necessary to calculate the contact point between wheel and rail and to generate the contact lookup table has been implemented in MATLAB® (2013). The roll angle, i.e., the wheel rotation about the *x* axis, is neglected (see Fig. 3.11). The results calculated with MATLAB are compared against those obtained with the multibody simulation software VAMPIRE® (2014). The contact lookup table calculated with this software takes into account the left and right wheels, the roll angle of the wheelset and two-point contact. Hence, the results calculated with VAMPIRE are slightly different, and more accurate, than those calculated with MATLAB. Also, the wheel and rail profiles are defined using spline functions that are based on a set of user supplied points. The smoothing and interpolation performed during the geometrical processing of the profiles might also be different. The contact angle as a function of the wheel lateral displacement is plotted in Fig. 3.14. Flange contact occurs for wheel lateral displacements less than -6.6 mm and greater than 6.6 mm for the left and right wheels, respectively, as indicated by the solid vertical lines plotted in the figures. In MATLAB, the contact angle is calculated using the rail and wheel profiles. Since the location of the contact point is given by the minimum vertical distance between wheel and rail profiles, the solution is not exact. Therefore, especially for high values of the contact angle, there is a slight difference between the contact angles calculated using the two profiles. More accurate algorithms for calculating the location of the contact point are described in Montenegro (2015).

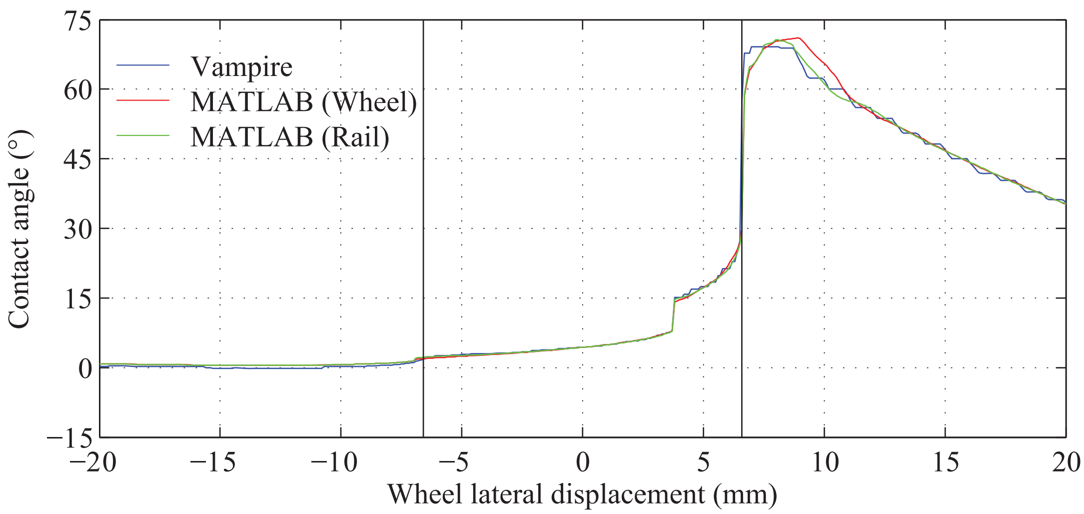

Figure 3.14 – Contact angle.

The contact ellipse semi-axes ratio a/b as a function of the wheel lateral displacement is shown in Fig. 3.15. The letters *a* and *b* correspond to the longitudinal and transverse semi-axes, respectively. As explained before, the algorithms implemented in MATLAB and VAMPIRE for calculating a contact lookup table are slightly different. These differences become more evident when flange contact occurs, i.e., for wheel lateral displacements greater than 6.6 mm. Also, the calculation of the semi-axes ratio of the contact ellipse is very sensitive to the geometrical processing of the profiles.

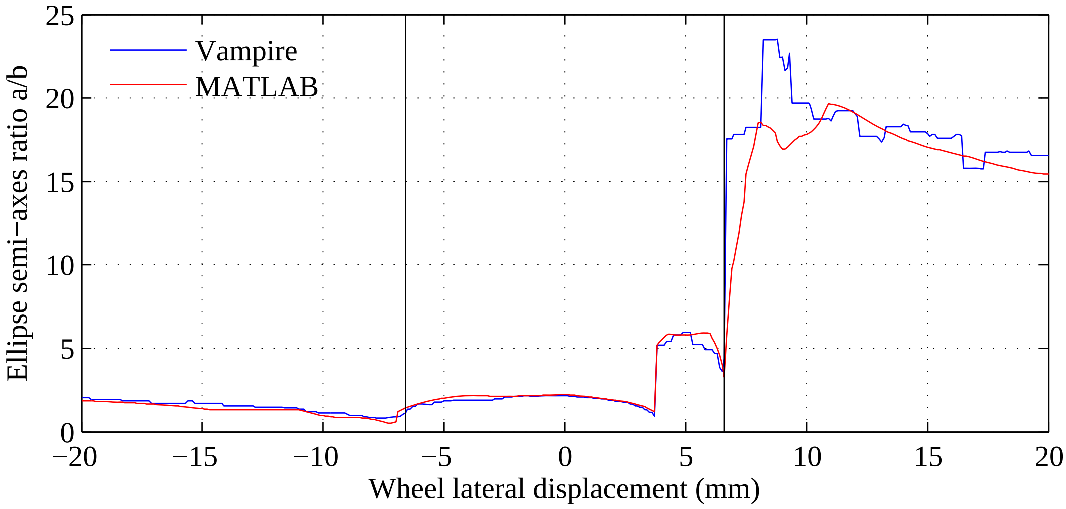

Figure 3.15 –Semi-axes ratio a/b of the contact ellipse.

The contact patches of the left and right wheels when the wheelset is centred on the track are plotted in Fig. 3.16. In this case, the semi-axes ratio a/b is equal to 2.2.

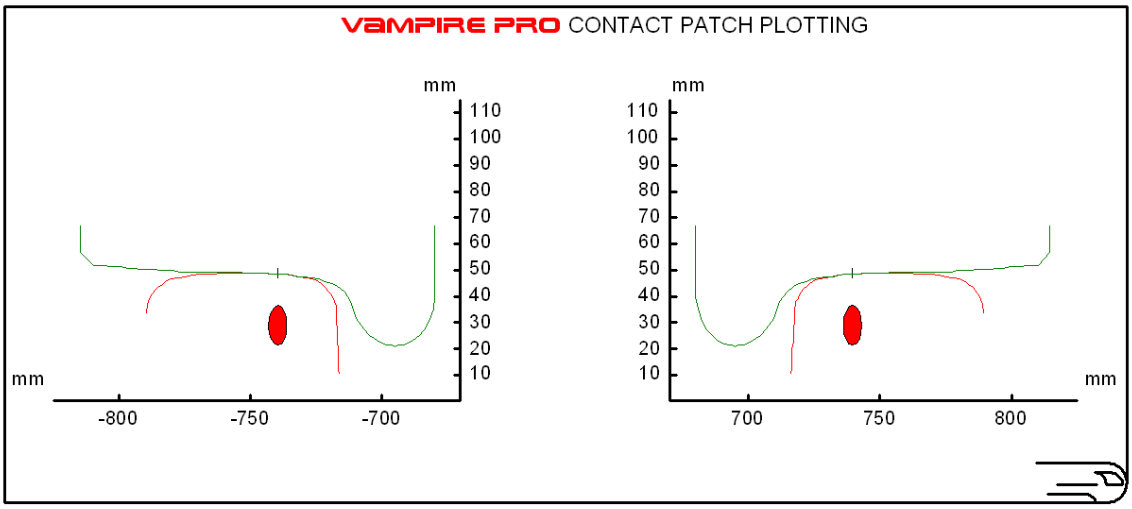

Figure 3.16 – Contact patches for the wheelset centred on the track.

Generally, a discontinuity in the contact angle function corresponds to a jump of the contact point. If these jumps lead to ellipses very close to each other, the Hertzian assumption of a constant curvature in the contact area might be no longer valid (Iwnicki, 2006). The lateral position of the contact point as a function of the wheel lateral displacement is shown in Fig. 3.17. It is interesting to note that the wheel and contact points move in the opposite direction, i.e., a movement of the wheel to the right leads to a movement of the contact point to the left.

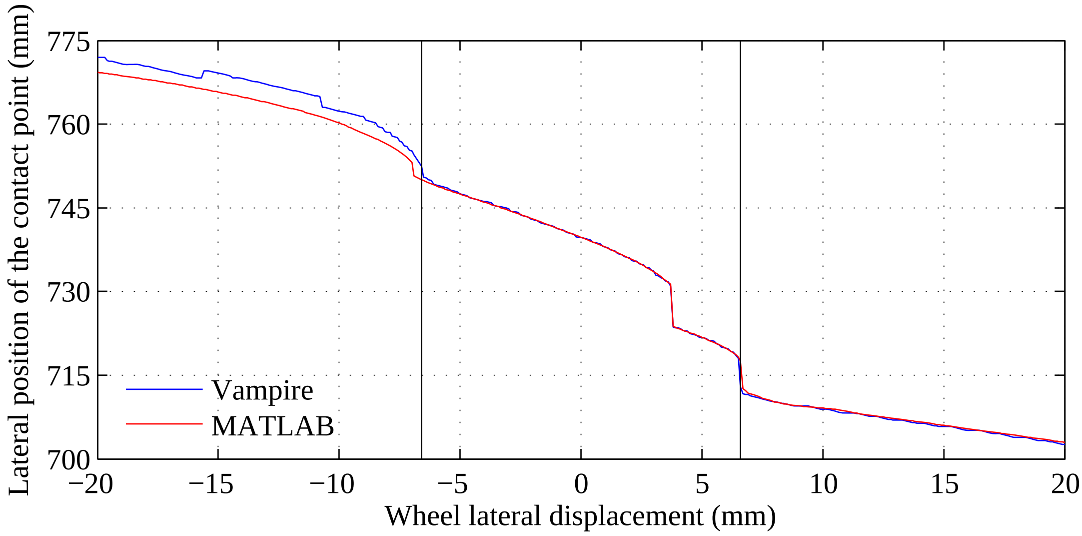

Figure 3.17 – Lateral position of the contact point.

Two significant discontinuities can be observed in Figs. 3.14 and 3.17 for wheel lateral displacements equal to 3.7 and 6.6 mm. When the lateral displacement changes from 3.7 to 3.8 mm, the lateral position of the contact point changes from 731 to 723.6 mm. The curvature of the rail at the lateral coordinates 731 and 723.6 mm is equal to 12.5 and 76.9 m^{-1}, respectively (see Fig. 3.12). This jump of the right contact point significantly depends on the abrupt change of curvature. The contact patches of the left and right wheels for the lateral displacements of 3.7 and 3.8 mm are plotted in Figs. 3.18 and 3.19, respectively. The abrupt change of curvature is also evidenced by the significant variation in the shape of the right contact patch.

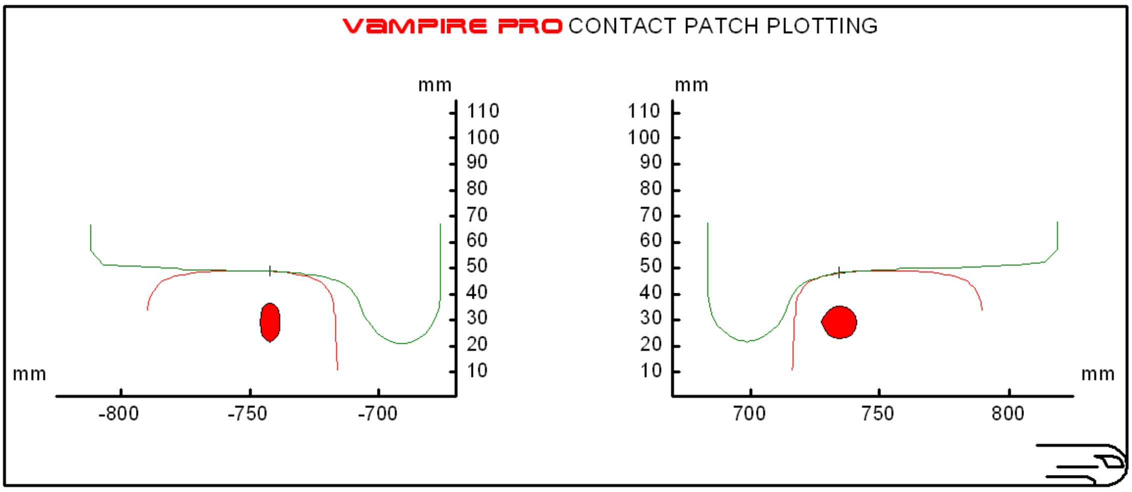

Figure 3.18 – Contact patches for a lateral displacement of 3.7 mm.

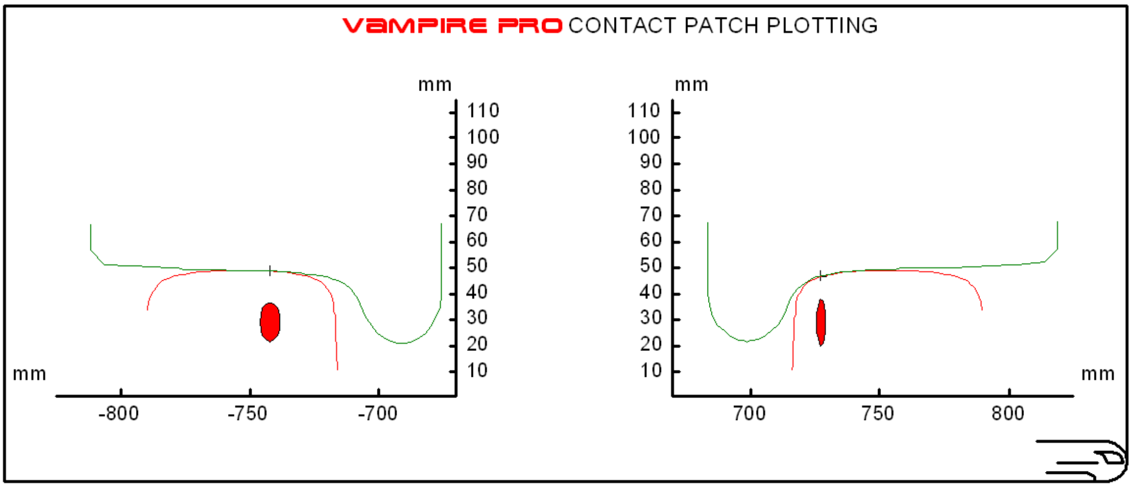

Figure 3.19 – Contact patches for a lateral displacement of 3.8 mm.

The contact patches of the left and right wheels for the lateral displacements of 6.6 and -6.6 mm are shown in Figs. 3.20 and 3.21. Flange contact occurs in both cases.

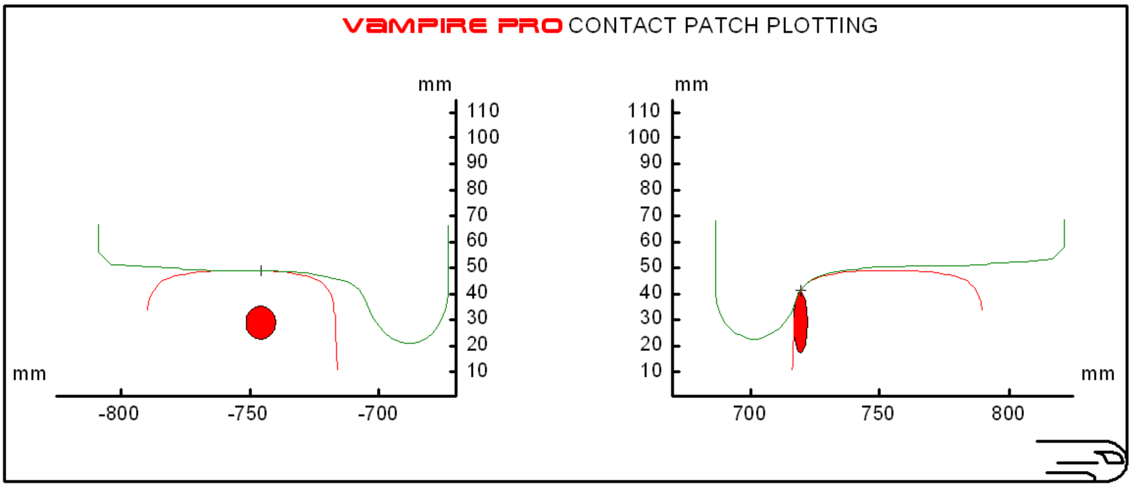

Figure 3.20 – Contact patches for a lateral displacement of 6.6 mm.

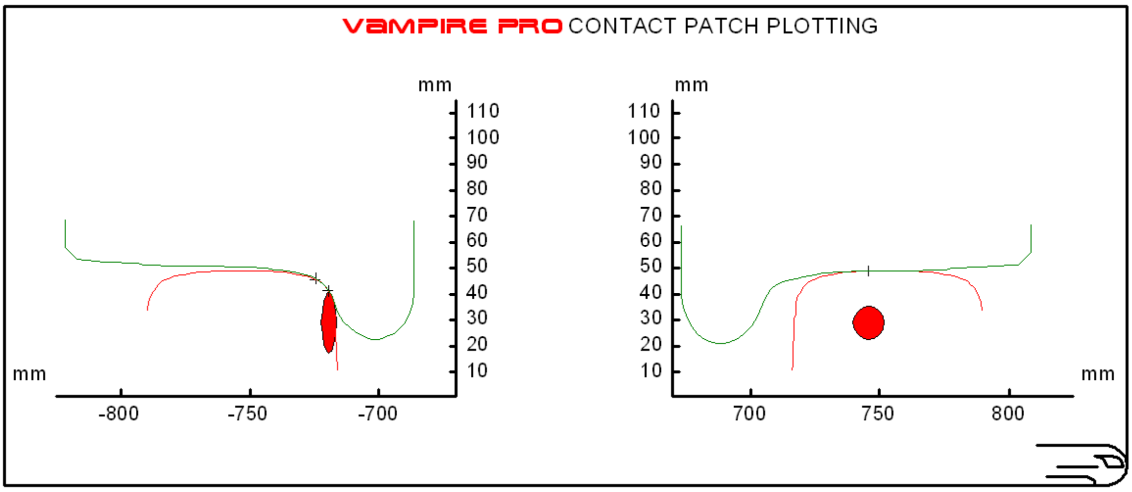

Figure 3.21 – Contact patches for a lateral displacement of -6.6 mm.

The elliptical contact area as a function of the wheel lateral displacement is plotted in Fig. 3.22. There is a reasonable agreement between the results obtained with the MATLAB and VAMPIRE programs. As explained before, the algorithms implemented in the two programs for calculating a contact lookup table are slightly different.

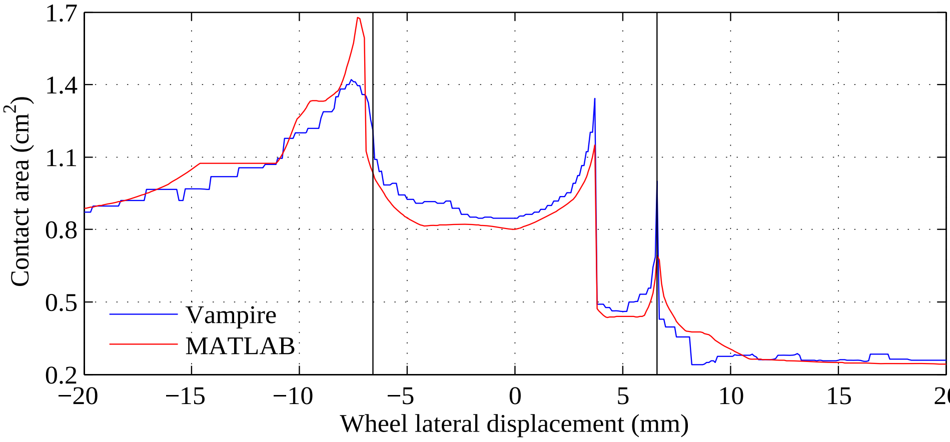

Figure 3.22 – Elliptical contact area.

This numerical example is also used to calculate the Hertzian constant K_h and the corresponding linearized contact stiffness k_h around the static wheel load (see Section 3.3.2). The wheelset is assumed to be centred on the track. Since the present work does not take into account the wheel-rail interaction in the lateral direction, the value K_h calculated in this section remains unchanged is used throughout the thesis. The coordinate systems of the wheel and rail are represented in Fig. 3.6. The parameter K_h is obtained based on the following steps:

1) since the rail is straight, the longitudinal curvature κ_r' is equal to zero;

2) the contact angle is equal to 4.6°; see Fig. 3.14;

3) the principal radius of curvature R_w' of the wheel is equal to 0.4615 m; see Eq. (3.36) and Fig. 3.7; the curvature κ_w' of the wheel is equal to 2.165 m^{-1};

4) the lateral position of the contact point is equal to 739.7 mm; see Fig. 3.17;

5) lateral curvature of the rail $\kappa_r'' = 12.43\,\mathrm{m}^{-1}$; see Figs. 3.6 and 3.12 (the sign is inverted because the coordinate systems used are different);

6) lateral curvature of the wheel $\kappa_w'' = -5.147\,\mathrm{m}^{-1}$; see Fig. 3.13;

7) since the wheelset has zero yaw rotation, $\psi = 0$;

8) $C_1 = 4.722$ m^{-1}; see Eq. (3.20);

9) $C_2 = -2.557$ m^{-1}; see Eq. (3.26) and Fig. 3.5;

10) $\theta = 57.21°$; see Eq. (3.27);

11) $\beta = 0.3578$; see Table 3.4;

12) $E_{wr} = 115.4\,\text{GPa}$; see Eq. (3.47);

13) $K_h = 7.958 \times 10^7\ \text{kN/m}^{3/2}$; see Eq. (3.67).

The linearized value of the contact stiffness around a static wheel load of 83385 N is obtained using Eq. (3.71) and is equal to 1.212×10^6 kN/m. The nonlinear and linear force-deflection relationships of the contact spring are plotted in Fig. 3.23. Both these relationships have been implemented in the enhanced node-to-segment contact element proposed in Chapter 5.

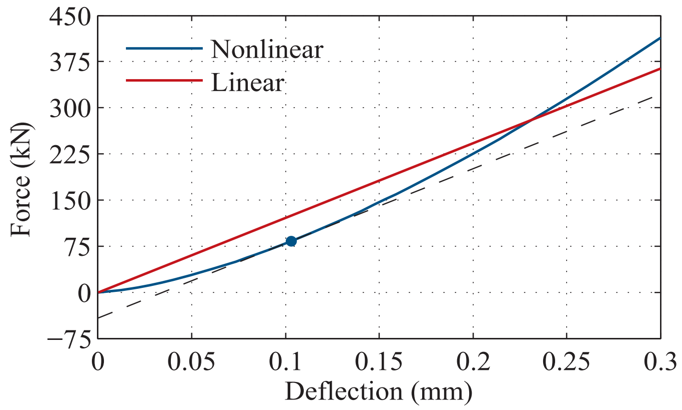

Figure 3.23 – Linear and nonlinear force-deflection relationships of the Hertzian contact spring.

3.5 CONCLUDING REMARKS

The Hertz contact theory has been explained in detail in this chapter. A special focus is given to its assumptions and limitations. The tabulated values provided by Hertz, more than a century ago, to calculate the force-deflection relationship of the contact spring are complemented with additional values obtained using the Maple software. The vehicle-structure interaction algorithm described in Chapter 5 uses an enhanced node-to-segment contact element that includes an Hertzian spring to account for the local deformations in the vicinity of the contact region. The mathematical expressions that are used to calculate the parameters defining the Hertz force law are validated using a simple example that consists of the calculation of a contact lookup table for a single wheel-rail pair. The results obtained with MATLAB are compared with those calculated with the VAMPIRE software and a good agreement is obtained. Since the present thesis only addresses contact in the normal direction, the Hertzian constant K_h is calculated assuming the wheelset centred on the track. This value is used throughout this thesis.

4 AN EFFICIENT METHOD FOR ANALYSING THE VEHICLE-STRUCTURE INTERACTION

4.1 INTRODUCTION

The more well-known commercial finite element (FE) and multibody simulation (MBS) programs do not satisfy all the requirements for performing an efficient and accurate analysis of the dynamic behaviour of the vehicle-structure system. Most of the MBS programs, such as VI-Rail® or Simpack®, are able to accurately simulate the behaviour of the vehicle and provide a comprehensive library of vehicle models, but cannot properly take into account the deformation and nonlinear behaviour of the structure. FE programs can accurately model the behaviour of the track and structures but use more simplified contact formulations that cannot adequately take into account the wheel and rail geometry and the normal and tangential forces transmitted across the contact interface.

A state-of-the-art review of the vehicle-structure interaction methods is given in Chapter 2. Three different approaches are described: direct equilibrium of the contact forces, variational formulations and condensation methods. The direct method described in Section 2.2.4 proved to be the most suitable approach and is therefore adopted in this work. The formulation of this method is explained in more detail in Section 4.2. Also, the direct integration of the equations of motion described in this chapter uses the HHT-α method (Hilber *et al.*, 1977; Faria, 1994) instead of the Newmark method described in Section 2.2.2. The structures and vehicles are developed using an FE software (FEMIX), and can, therefore, be modelled with a high degree of complexity and with several types of FE. The methodology proposed here is equally valid when the vehicles are modelled using multibody system techniques. Semi-analytical solutions of the equation governing the transverse vibration of a simply supported beam subjected to a moving force, a moving mass and a moving sprung mass are formulated in Section 4.3. Two numerical examples are used in Section 4.4 to verify the accuracy and efficiency of the direct method. The results obtained with the proposed method are compared with the semi-analytical solutions mentioned before.

Since in the present work the tangential forces transmitted across the contact interface are not considered, the lateral vehicle-structure interaction cannot be taken into account. To determine these forces, the relative velocity between the two bodies at the contact point has to be considered, as well as the material and geometric properties of the wheel and rail. Montenegro (2015) extended the formulation proposed here to three-dimensional contact problems (see also Montenegro *et al.* (2015)). Therefore, the work presented here can be seen as a first step towards closing the gap between FE and MBS computer programs. Antolín *et al.* (2012) developed a wheel-rail contact method in which the structure is modelled using a commercial FE program and the vehicles are modelled using multibody systems. The works carried out by Montenegro *et al.* (2015) and Antolín *et al.* (2012) are an important contribution to the field. However, no information is given about the computational efficiency of the proposed methods.

4.2 VEHICLE-STRUCTURE INTERACTION METHOD

4.2.1 Contact and target elements

A general vehicle model moving over a simple structure is represented in Fig. 4.1. When studying the contact between two bodies, it is necessary to identify the region where contact might occur. The surface of one body is conventionally assumed to be a contact surface and the surface of the other body is assumed to be a target surface (see Fig. 4.1). This contact pair concept is widely used in computational contact mechanics.

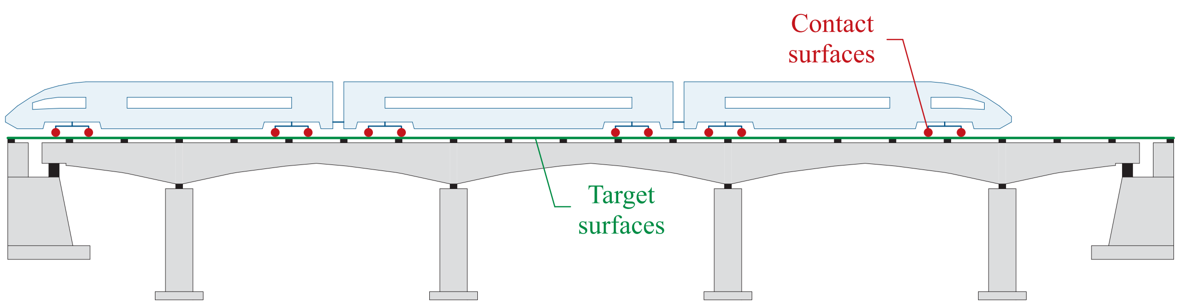

Figure 4.1 – Contact pair concept.

Figure 4.2 shows the two-dimensional node-to-segment contact element implemented in the present formulation and the local coordinate system (ξ_1, ξ_2, ξ_3) of the contact pair. The ξ_1 axis follows the longitudinal axis of the target element, the ξ_2 axis always points towards the contact node and the ξ_3 axis completes the right-handed system. The forces acting at the contact interface are denoted by X. Since the lateral vehicle-structure interaction is not taken into account, the displacement vector of an arbitrary point is defined by two translations, v_{ξ_1} and v_{ξ_2}, and a rotation θ_{ξ_3} about the ξ_3 axis. The superscripts *ce* and *te* indicate contact and target elements, respectively. The contact node N_1 is a nodal point of the vehicle and the nodes N_2 and N_3 of the target element are nodal points of the structure. The point P is an auxiliary internal point of the target element.

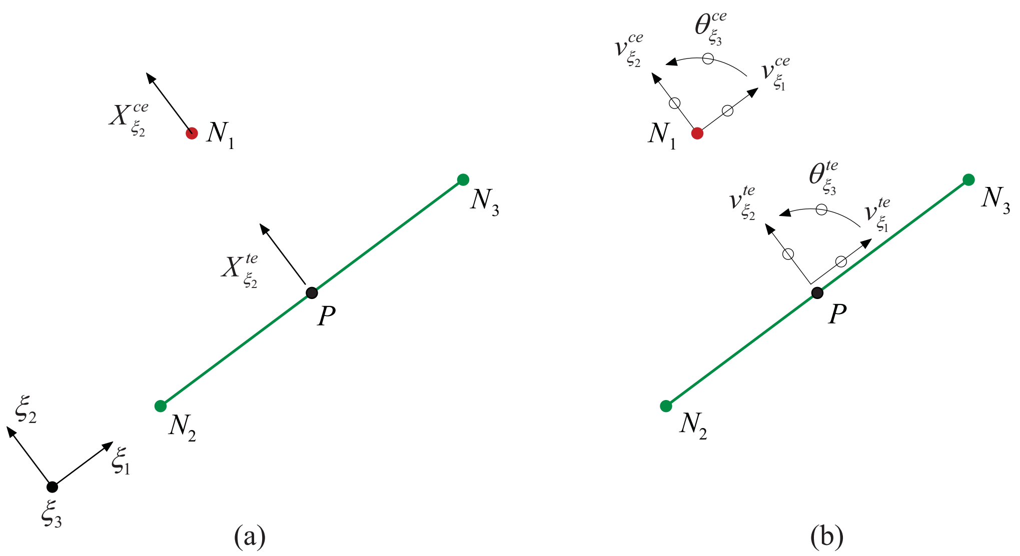

Figure 4.2 – Node-to-segment contact element: (a) forces and (b) displacements at the contact interface.

According to Newton's third law, the forces acting at the contact interface must be of equal magnitude and opposite direction, i.e.,

$$\mathbf{X}^{ce} + \mathbf{X}^{te} = \mathbf{0} \tag{4.1}$$

Since the node-to-segment contact element used in the formulation presented here neglects the tangential forces and moments transmitted across the contact interface, the contact constraint equations only relate the displacement v_{ξ_2} of the contact node to the corresponding displacement of the auxiliary point P. Each constraint equation is defined in the local coordinate system of the contact pair. Since no sliding or separation is allowed, these equations are given by

$$\mathbf{v}^{ce} - \mathbf{v}^{te} = \mathbf{r} \tag{4.2}$$

where $\mathbf{r}$ are the irregularities between the contact and target elements. A positive irregularity implies an increase of the distance between the contact and target elements (see

Fig. 4.2). Since the auxiliary point P does not belong to the mesh of the structure, the constraint equations that relate the displacements of the auxiliary point and those of the node N_1 are transformed in order to be associated with the degrees of freedom (d.o.f.) of the nodes of the target element. This procedure is also applied to the forces acting at the auxiliary point P.

4.2.2 Formulation of the equations of motion

The HHT-α method is an implicit time integration scheme that is generally accurate and stable (Hilber *et al.*, 1977). Assuming linear elastic material behaviour and deformation-independent loading, the equations of motion of the vehicle-structure system are given by

$$\mathbf{M}\,\ddot{\mathbf{a}}^{t+\Delta t} + \mathbf{C}\left[(1+\alpha)\,\dot{\mathbf{a}}^{t+\Delta t} - \alpha\,\dot{\mathbf{a}}^{t}\right] + \mathbf{K}\left[(1+\alpha)\,\mathbf{a}^{t+\Delta t} - \alpha\,\mathbf{a}^{t}\right] = (1+\alpha)\,\mathbf{F}^{t+\Delta t} - \alpha\,\mathbf{F}^{t} \tag{4.3}$$

where $\mathbf{M}$ is the mass matrix, $\mathbf{C}$ is the viscous damping matrix, $\mathbf{K}$ is the stiffness matrix, $\mathbf{F}$ is the load vector, $\mathbf{a}$ are the displacements and α is the parameter of the time integration scheme. The dots represent differentiation with respect to time and the superscripts t and $t+\Delta t$ indicate the previous and current time steps, respectively. By adopting $\alpha = 0$, this algorithm reduces to the Newmark method; for other values, numerical dissipation is introduced, which is useful for controlling the spurious high-frequency content (Rigueiro, 2007).

To solve Eq. (4.3) let the F type d.o.f. represent the free nodal d.o.f., whose values are unknown, and let the P type d.o.f. represent the prescribed nodal d.o.f., whose values are known. Thus, the load vector can be expressed as

$$\mathbf{F}_F = \mathbf{P}_F + \mathbf{D}_{FX}^{ce}\,\mathbf{X}^{ce} + \mathbf{D}_{FX}^{te}\,\mathbf{X}^{te} \tag{4.4}$$

$$\mathbf{F}_P = \mathbf{P}_P + \mathbf{D}_{PX}^{ce}\,\mathbf{X}^{ce} + \mathbf{D}_{PX}^{te}\,\mathbf{X}^{te} + \mathbf{S} \tag{4.5}$$

where $\mathbf{P}$ corresponds to the externally applied nodal loads whose values are known and $\mathbf{S}$ are the support reactions, whose values are unknown. Each matrix $\mathbf{D}$ relates the contact forces, defined in the local coordinate system of the respective contact pair, to the nodal forces defined in the global coordinate system (see Fig. 4.2).

Substituting Eq. (4.1) into Eqs. (4.4) and (4.5) leads to

$$\mathbf{F}_F = \mathbf{P}_F + \mathbf{D}_{FX}\ \mathbf{X} \tag{4.6}$$

$$\mathbf{F}_P = \mathbf{P}_P + \mathbf{D}_{PX}\ \mathbf{X} + \mathbf{S} \tag{4.7}$$

where

$$\mathbf{X}=\mathbf{X}^{ce} \tag{4.8}$$

$$\mathbf{D}_{FX} = \mathbf{D}_{FX}^{ce} - \mathbf{D}_{FX}^{te} \tag{4.9}$$

$$\mathbf{D}_{PX} = \mathbf{D}_{PX}^{ce} - \mathbf{D}_{PX}^{te} \tag{4.10}$$

Substituting Eqs. (4.6) and (4.7) into Eq. (4.3), and partitioning the result into F and P type d.o.f., gives

$$\begin{aligned}
&\begin{bmatrix} \mathbf{M}_{FF} & \mathbf{M}_{FP} \\ \mathbf{M}_{PF} & \mathbf{M}_{PP} \end{bmatrix} \begin{bmatrix} \ddot{\mathbf{a}}_F^{t+\Delta t} \\ \ddot{\mathbf{a}}_P^{t+\Delta t} \end{bmatrix} + \begin{bmatrix} \mathbf{C}_{FF} & \mathbf{C}_{FP} \\ \mathbf{C}_{PF} & \mathbf{C}_{PP} \end{bmatrix} \left[(1+\alpha) \begin{bmatrix} \dot{\mathbf{a}}_F^{t+\Delta t} \\ \dot{\mathbf{a}}_P^{t+\Delta t} \end{bmatrix} - \alpha \begin{bmatrix} \dot{\mathbf{a}}_F^{t} \\ \dot{\mathbf{a}}_P^{t} \end{bmatrix} \right] \\
&\quad + \begin{bmatrix} \mathbf{K}_{FF} & \mathbf{K}_{FP} \\ \mathbf{K}_{PF} & \mathbf{K}_{PP} \end{bmatrix} \left[(1+\alpha) \begin{bmatrix} \mathbf{a}_F^{t+\Delta t} \\ \mathbf{a}_P^{t+\Delta t} \end{bmatrix} - \alpha \begin{bmatrix} \mathbf{a}_F^{t} \\ \mathbf{a}_P^{t} \end{bmatrix} \right] \\
&= (1+\alpha) \begin{bmatrix} \mathbf{P}_F^{t+\Delta t} + \mathbf{D}_{FX}^{t+\Delta t}\ \mathbf{X}^{t+\Delta t} \\ \mathbf{P}_P^{t+\Delta t} + \mathbf{D}_{PX}^{t+\Delta t}\ \mathbf{X}^{t+\Delta t} + \mathbf{S}^{t+\Delta t} \end{bmatrix} - \alpha \begin{bmatrix} \mathbf{P}_F^{t} + \mathbf{D}_{FX}^{t}\ \mathbf{X}^{t} \\ \mathbf{P}_P^{t} + \mathbf{D}_{PX}^{t}\ \mathbf{X}^{t} + \mathbf{S}^{t} \end{bmatrix}
\end{aligned} \tag{4.11}$$

Transferring the unknowns to the left-hand side leads to

$$\mathbf{M}_{FF}\ \ddot{\mathbf{a}}_F^{t+\Delta t} + (1+\alpha)\mathbf{C}_{FF}\ \dot{\mathbf{a}}_F^{t+\Delta t} + (1+\alpha)\mathbf{K}_{FF}\ \mathbf{a}_F^{t+\Delta t} - (1+\alpha)\,\mathbf{D}_{FX}^{t+\Delta t}\ \mathbf{X}^{t+\Delta t} = \overline{\mathbf{F}}_F \tag{4.12}$$

and

$$\begin{aligned}
\mathbf{S}^{t+\Delta t} &= -\mathbf{P}_P^{t+\Delta t} - \mathbf{D}_{PX}^{t+\Delta t}\ \mathbf{X}^{t+\Delta t} \\
&+ \frac{1}{1+\alpha}\left[\mathbf{M}_{PF}\ \ddot{\mathbf{a}}_F^{t+\Delta t} + \mathbf{M}_{PP}\ \ddot{\mathbf{a}}_P^{t+\Delta t}\right] + \mathbf{C}_{PF}\ \dot{\mathbf{a}}_F^{t+\Delta t} + \mathbf{C}_{PP}\ \dot{\mathbf{a}}_P^{t+\Delta t} + \mathbf{K}_{PF}\ \mathbf{a}_F^{t+\Delta t} + \mathbf{K}_{PP}\ \mathbf{a}_P^{t+\Delta t} \\
&+ \frac{\alpha}{1+\alpha}\left[\mathbf{S}^t + \mathbf{P}_P^t + \mathbf{D}_{PX}^t\ \mathbf{X}^t - \mathbf{C}_{PF}\ \dot{\mathbf{a}}_F^t - \mathbf{C}_{PP}\ \dot{\mathbf{a}}_P^t - \mathbf{K}_{PF}\ \mathbf{a}_F^t - \mathbf{K}_{PP}\ \mathbf{a}_P^t\right]
\end{aligned} \tag{4.13}$$

where

$$\begin{aligned}
\overline{\mathbf{F}}_F &= (1+\alpha)\mathbf{P}_F^{t+\Delta t} - \alpha\,\mathbf{P}_F^t - \alpha\,\mathbf{D}_{FX}^t\ \mathbf{X}^t - \mathbf{M}_{FP}\,\ddot{\mathbf{a}}_P^{t+\Delta t} \\
&- (1+\alpha)\mathbf{C}_{FP}\,\dot{\mathbf{a}}_P^{t+\Delta t} + \alpha\left[\mathbf{C}_{FF}\,\dot{\mathbf{a}}_F^t + \mathbf{C}_{FP}\,\dot{\mathbf{a}}_P^t\right] - (1+\alpha)\mathbf{K}_{FP}\,\mathbf{a}_P^{t+\Delta t} + \alpha\left[\mathbf{K}_{FF}\,\mathbf{a}_F^t + \mathbf{K}_{FP}\,\mathbf{a}_P^t\right]
\end{aligned} \tag{4.14}$$

4.2.3 Direct integration of the equations of motion

The HHT-α method is an implicit time integration scheme that is generally accurate and stable (Hughes, 2000; Faria *et al.*, 2002). In this method, the velocity and acceleration at the current time step are approximated using the same expressions presented for the Newmark method in Section 2.2.2. Thus,

$$\dot{\mathbf{a}}^{t+\Delta t} = A_1 \left(\mathbf{a}^{t+\Delta t} - \mathbf{a}^t\right) - A_4\, \dot{\mathbf{a}}^t - A_5\, \ddot{\mathbf{a}}^t \tag{4.15}$$

$$\ddot{\mathbf{a}}^{t+\Delta t} = A_0 \left(\mathbf{a}^{t+\Delta t} - \mathbf{a}^t\right) - A_2\, \dot{\mathbf{a}}^t - A_3\, \ddot{\mathbf{a}}^t \tag{4.16}$$

Substituting Eqs. (4.15) and (4.16) into Eq. (4.12), and rearranging the terms, yields

$$\overline{\mathbf{K}}_{FF}\, \mathbf{a}_F^{t+\Delta t} - (1+\alpha)\, \mathbf{D}_{FX}^{t+\Delta t}\, \mathbf{X}^{t+\Delta t} = \overline{\mathbf{F}}_F \tag{4.17}$$

where

$$\overline{\mathbf{K}}_{FF} = A_0\, \mathbf{M}_{FF} + (1+\alpha)\, A_1\, \mathbf{C}_{FF} + (1+\alpha)\, \mathbf{K}_{FF} \tag{4.18}$$

$$\overline{\mathbf{F}}_F = \overline{\overline{\mathbf{F}}}_F + \mathbf{M}_{FF} \left[A_0\, \mathbf{a}_F^t + A_2\, \dot{\mathbf{a}}_F^t + A_3\, \ddot{\mathbf{a}}_F^t\right] + (1+\alpha)\, \mathbf{C}_{FF} \left[A_1\, \mathbf{a}_F^t + A_4\, \dot{\mathbf{a}}_F^t + A_5\, \ddot{\mathbf{a}}_F^t\right] \tag{4.19}$$

In matrix notation, Eq. (4.17) may be expressed as

$$\begin{bmatrix} \overline{\mathbf{K}}_{FF} & \overline{\mathbf{D}}_{FX} \end{bmatrix} \begin{bmatrix} \mathbf{a}_F^{t+\Delta t} \\ \mathbf{X}^{t+\Delta t} \end{bmatrix} = \begin{bmatrix} \overline{\mathbf{F}}_F \end{bmatrix} \tag{4.20}$$

where

$$\overline{\mathbf{D}}_{FX} = -(1+\alpha)\, \mathbf{D}_{FX}^{t+\Delta t} \tag{4.21}$$

4.2.4 Formulation of the contact constraint equations

The constraint equations (4.2) relate the displacements of the contact nodes to the corresponding displacements of the target elements (see Fig. 4.2). The displacements of the contact nodes for the current time step are given by

$$\mathbf{v}^{ce} = \mathbf{H}_{XF}^{ce}\, \mathbf{a}_F^{t+\Delta t} + \mathbf{H}_{XP}^{ce}\, \mathbf{a}_P^{t+\Delta t} \tag{4.22}$$

where each matrix $\mathbf{H}^{ce}$ transforms the displacements of the contact nodes from the global coordinate system to the local coordinate system of the contact pair. Similarly, the displacements of the auxiliary points of the target elements are given by

$$\mathbf{v}^{te} = \mathbf{H}_{XF}^{te}\,\mathbf{a}_F^{t+\Delta t} + \mathbf{H}_{XP}^{te}\,\mathbf{a}_P^{t+\Delta t} \tag{4.23}$$

where each matrix $\mathbf{H}^{te}$ relates the nodal displacements of the target elements, defined in the global coordinate system, to the displacements of the auxiliary points defined in the local coordinate system of each contact pair. Substituting Eqs. (4.22) and (4.23) into Eq. (4.2) yields

$$\mathbf{H}_{XF}\,\mathbf{a}_F^{t+\Delta t} = \mathbf{r} - \mathbf{H}_{XP}\,\mathbf{a}_P^{t+\Delta t} \tag{4.24}$$

where

$$\mathbf{H}_{XF} = \mathbf{H}_{XF}^{ce} - \mathbf{H}_{XF}^{te} \tag{4.25}$$

$$\mathbf{H}_{XP} = \mathbf{H}_{XP}^{ce} - \mathbf{H}_{XP}^{te} \tag{4.26}$$

Multiplying Eq. (4.24) by $-(1+\alpha)$ gives

$$\overline{\mathbf{H}}_{XF}\,\mathbf{a}_F^{t+\Delta t} = \overline{\mathbf{r}} \tag{4.27}$$

where

$$\overline{\mathbf{H}}_{XF} = -(1+\alpha)\,\mathbf{H}_{XF} \tag{4.28}$$

and

$$\overline{\mathbf{r}} = -(1+\alpha)\left(\mathbf{r} - \mathbf{H}_{XP}\,\mathbf{a}_P^{t+\Delta t}\right) \tag{4.29}$$

4.2.5 Complete system of equations

Equations (4.20) and (4.27) can be expressed in matrix form leading to the following complete system of linear equations

$$\begin{bmatrix} \overline{\mathbf{K}}_{FF} & \overline{\mathbf{D}}_{FX} \\ \overline{\mathbf{H}}_{XF} & \mathbf{0} \end{bmatrix} \begin{bmatrix} \mathbf{a}_F^{t+\Delta t} \\ \mathbf{X}_X^{t+\Delta t} \end{bmatrix} = \begin{bmatrix} \overline{\mathbf{F}}_F \\ \overline{\mathbf{r}} \end{bmatrix} \tag{4.30}$$

The symmetry of the coefficient matrix (4.30) can be demonstrated using the Betti's theorem. Since the time required to solve the system of linear equations (4.30) may represent a large percentage of the total solution time (Bathe, 1996), the efficiency of the solver is very important. The present method uses an efficient and stable block factorisation algorithm (see Appendix A) that takes into account the specific properties of each block, namely, symmetry, positive definiteness and bandwidth. The coefficient matrix is composed of the stiffness matrix $\overline{\mathbf{K}}_{FF}$ and three additional blocks ($\overline{\mathbf{D}}_{FX}$, $\overline{\mathbf{H}}_{XF}$ and $\mathbf{0}$). When compared to other vehicle-structure interaction methods that do not introduce additional variables (see Chapter 2), the solution of the system requires the additional matrix operations (A.5), (A.6), (A.7), (A.11), (A.12) and part of (A.13) (see Appendix A). For large structural systems, where the number of F type d.o.f. and the number of contact forces are usually of the order of tens of thousands and tens, respectively, of all the additional operations only the time required by (A.5) is significant when compared with the total solution time. In general, the effective stiffness matrix $\overline{\mathbf{K}}_{FF}$ remains constant during a linear analysis or has to be updated and factorised only at certain times during a nonlinear analysis. Since in the proposed method only the additional blocks of the coefficient matrix (4.30) are modified, further factorisations (A.4) are avoided. For large structural systems, the additional forward substitutions (A.5) require less computational effort than the additional factorisations (A.4), and so the proposed method can be more efficient than those that need to factorise the stiffness matrix at every time step (see Chapter 2).

The direct method and has been implemented in FEMIX, which is a general purpose finite element computer program (FEMIX). This program is based on the displacement method and has a large library of types of finite elements available, namely 3D frames and trusses, plane stress elements, flat or curved elements for shells, and 3D solid elements. Linear elements may have two or three nodes, plane stress and shell elements may be 4, 8 or 9-noded and 8 or 20-noded hexahedra may be used in 3D solid analyses. This element library is complemented with a set of point, line and surface springs that model elastic contact with the supports, and also a few types of interface elements to model inter-element contact. Embedded line elements can be added to other types of elements in order to model reinforcement bars. All these types of elements can be simultaneously included in the analysis, with the exception of some incompatible combinations. The analysis may be static or dynamic and the material behaviour may be linear or nonlinear.

Data input is facilitated by the possibility of importing CAD models. Post processing is performed with a general purpose scientific visualisation program named *drawmesh* (Azevedo *et al.*, 2003). Advanced numerical techniques are available, such as the Newton-Raphson method combined with arc-length techniques and path dependent or independent algorithms. When the size of the systems of linear equations is very large, a preconditioned conjugate gradient method can be advantageously used. In the context of the dynamic analysis of structures with moving loads and vehicle-structure interaction, the behaviour of the materials is considered linear and the displacements are assumed to be small enough to avoid geometrically nonlinear phenomena.

4.3 SEMI-ANALYTICAL SOLUTIONS

Due to the complexity associated with contact problems, a rigorous and comprehensive validation of the algorithm is very important. For this purpose, semi-analytical solutions of the equation governing the transverse vibration of a simply supported beam subjected to a moving force, a moving mass and a moving sprung mass are formulated in this section. The formulation presented in this section is also valid for other support conditions.

4.3.1 Beam transverse vibration theory

4.3.1.1 Equation of undamped motion

A simply supported beam, with flexural rigidity *EI* and mass per unit length *m*, subjected to an applied force *p* is shown in Fig. 4.3.

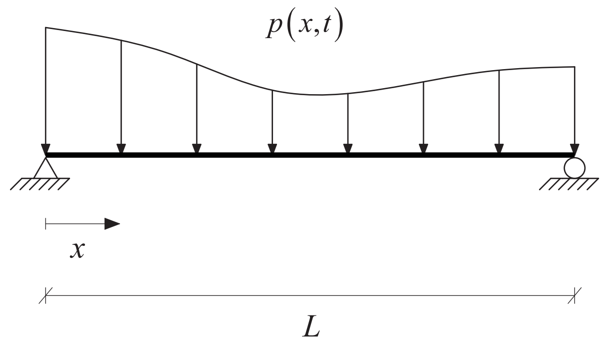

Figure 4.3 – Straight beam subjected to applied forces.

The partial differential equation governing the transverse vibration of a straight beam subjected to an external force, neglecting damping, rotational inertial effects and shear deformation, is given by (Chopra, 2007)

$$m\frac{\partial^2 a}{\partial t^2}+\frac{\partial^2}{\partial x^2}\left[EI\frac{\partial^2 a}{\partial x^2}\right] = p \tag{4.31}$$

where a is the transverse displacement. For the special case of a beam with uniform cross-section and a homogeneous material, E, I and m are constant. Thus Eq. (4.31) becomes

$$m\frac{\partial^2 a}{\partial t^2}+EI\frac{\partial^4 a}{\partial x^4} = p \tag{4.32}$$

To obtain a unique solution, the boundary conditions at each end of the beam and the initial displacement and velocity must be imposed.

4.3.1.2 Vibration mode shapes and frequencies

For the case of free vibration Eq. (4.32) becomes

$$m\frac{\partial^2 a}{\partial t^2}+EI\frac{\partial^4 a}{\partial x^4} = 0 \tag{4.33}$$

Considering a solution of the form

$$a(x,t) = \phi(x)\,q(t) \tag{4.34}$$

then

$$\frac{\partial^2 a}{\partial t^2} = \phi(x)\,\ddot{q}(t) \tag{4.35}$$

$$\frac{\partial^4 a}{\partial x^4} = \phi^{\mathrm{IV}}(x)\,q(t) \tag{4.36}$$

where dots denote differentiation with respect to time and primes denote a differentiation with respect to x. Substituting Eqs. (4.35) and (4.36) into Eq. (4.33) leads to

$$m\,\phi(x)\,\ddot{q}(t)+EI\,\phi^{\mathrm{IV}}(x)\,q(t) = 0 \tag{4.37}$$

which, when divided by $m\,\phi(x)\,q(t)$, becomes

$$-\frac{\ddot{q}(t)}{q(t)} = \frac{E\,I\,\phi^{\mathrm{IV}}(x)}{m\,\phi(x)} \tag{4.38}$$

The expression on the left-hand side of this equation is a function of t only and the one on the right depends only on x. For Eq. (4.38) to be valid for all values of t and x, both expressions must be constant. Assuming a constant value of ω^2, Eq. (4.38) becomes

$$\ddot{q} + \omega^2 q = 0 \tag{4.39}$$

$$E\,I\,\phi^{\mathrm{IV}}(x) - \omega^2 m\,\phi(x) = 0 \tag{4.40}$$

Thus, the partial differential equation (4.33) can be expressed by two ordinary differential equations, one governing the time function $q(t)$, and the other governing the spatial function $\phi(x)$.

Equation (4.40) can be rewritten as

$$\phi^{\mathrm{IV}}(x) - \beta^4 \phi(x) = 0 \tag{4.41}$$

being

$$\beta^4 = \frac{\omega^2 m}{E\,I} \tag{4.42}$$

The general solution of Eq. (4.41) is

$$\phi(x) = C_1 \sin\beta x + C_2 \cos\beta x + C_3 \sinh\beta x + C_4 \cosh\beta x \tag{4.43}$$

where C_1, C_2, C_3 and C_4 are unknown constants that depend on the boundary conditions at each end of the beam. For a single-span beam, applying four boundary conditions, two at each end of the beam, provides a solution for the natural frequencies and modes. The natural frequencies ω_n and modes of vibration $\phi_n(x)$ of a uniform simply supported beam are given by (Chopra, 2007)

$$\omega_n = \frac{n^2 \pi^2}{L^2}\sqrt{\frac{E\,I}{m}} \quad n = 1, 2, 3, \ldots \tag{4.44}$$

$$\phi_n(x) = C_1 \sin\frac{n\,\pi\,x}{L} \tag{4.45}$$

where n is the index of the vibration mode.

4.3.1.3 Modal analysis of forced dynamic response

Assuming that the associated eigenvalue problem of Eq. (4.40) has been solved to obtain the vibration mode shapes and frequencies, the total displacement is given by a linear combination of all the modes

$$a(x,t) = \sum_{n=1}^{\infty} a_n(x,t) = \sum_{n=1}^{\infty} \phi_n(x)\, q_n(t) \tag{4.46}$$

Due to the orthogonality properties of the vibration modes, Eq. (4.32) can be transformed into the following infinite set of ordinary differential equations

$$\ddot{q}_n(t) + \omega_n^2\, q_n(t) = \frac{P_n(t)}{M_n} \tag{4.47}$$

Each equation has one modal coordinate $q_n(t)$ as the unknown. The generalised mass M_n and the generalised force $P_n(t)$ for the nth mode are given by

$$M_n = m \int_0^L \left[\phi_n(x)\right]^2 dx \tag{4.48}$$

$$P_n(t) = \int_0^L p(x,t)\, \phi_n(x)\, dx \tag{4.49}$$

4.3.2 Moving force

Figure 4.4 shows the simply supported beam illustrated in Fig. 4.3 subjected to a time-varying force $p_0(t)$ moving at a constant speed v.

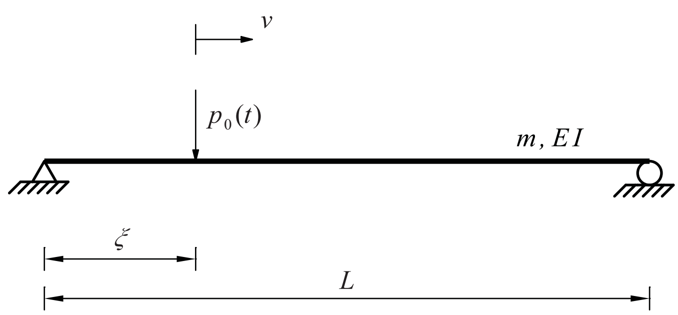

Figure 4.4 – Simply supported beam subjected to a moving force.

The position of the force at time t, assuming a constant speed, is defined by

$$\xi = v\,t \tag{4.50}$$

Substituting $p(x,t) = p_0(t)\,\delta(x-\xi)$, where $\delta(x-\xi)$ is the Dirac delta function centred at ξ, into Eq. (4.49) leads to (Chopra, 2007)

$$P_n(t) = p_0(t)\,\phi_n(\xi) \tag{4.51}$$

Substituting Eq. (4.51) into Eq. (4.47) gives the following partial differential equation governing the transverse vibration of a straight beam subjected to a moving force.

$$\ddot{q}_n(t) + \omega_n^2\, q_n(t) = \frac{p_0(t)\,\phi_n(\xi)}{M_n} \tag{4.52}$$

4.3.3 Moving mass

Figure 4.5 shows the simply supported beam illustrated in Fig. 4.3 subjected to a mass M moving at a constant speed v. The displacement of the contact point is denoted by a^c.

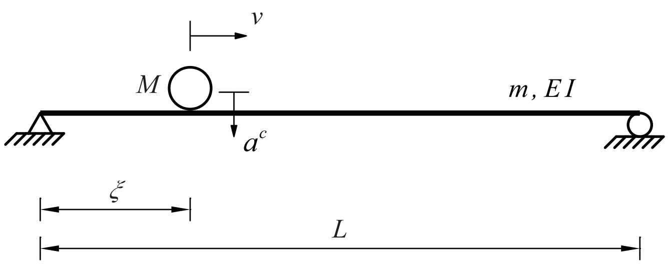

Figure 4.5 – Simply supported beam subjected to a moving mass.

The force applied to the beam at any instant is the gravity force minus the inertia force due to the acceleration of the mass (Biggs, 1964). Therefore

$$p_0(t) = M\,g - M\,\ddot{a}^c(t) \tag{4.53}$$

where $\ddot{a}^c$ is the acceleration of the mass and g is the acceleration of gravity. When there is no loss-of-contact between the mass and the beam

$$a^c(t) = a^b(\xi,t) \tag{4.54}$$

where a^b is the displacement of the beam at the mass location ξ. Substituting Eq. (4.46) into Eq. (4.54) leads to

$$a^c(t) = \sum_{m=1}^{\infty} \phi_m(\xi)\, q_m(t) \tag{4.55}$$

The mass acceleration is the second derivative of Eq. (4.55). Since the mass location ξ given by Eq. (4.50) is a function of time, the mass acceleration is given by

$$\ddot{a}^c(t) = \sum_{m=1}^{\infty} \ddot{\phi}_m(\xi)\, q_m(t) + 2\,\dot{\phi}_m(\xi)\, \dot{q}_m(t) + \phi_m(\xi)\, \ddot{q}_m(t) \tag{4.56}$$

Substituting Eq. (4.56) into Eq. (4.53) leads to

$$p_0(t) = M\, g - M \sum_{m=1}^{\infty} \ddot{\phi}_m(\xi)\, q_m(t) + 2\,\dot{\phi}_m(\xi)\, \dot{q}_m(t) + \phi_m(\xi)\, \ddot{q}_m(t) \tag{4.57}$$

Substituting Eq. (4.57) into Eq. (4.52) and rearranging results in

$$\begin{aligned} \ddot{q}_n(t) + \omega_n^2\, q_n(t) + \frac{M\, \phi_n(\xi) \sum_{m=1}^{\infty} \ddot{\phi}_m(\xi) q_m(t) + 2\,\dot{\phi}_m(\xi) \dot{q}_m(t) + \phi_m(\xi) \ddot{q}_m(t)}{M_n} \\ = \frac{M\, g\, \phi_n(\xi)}{M_n} \end{aligned} \tag{4.58}$$

For the case of several moving masses Eq. (4.58) becomes

$$\begin{aligned} \ddot{q}_n(t) + \omega_n^2\, q_n(t) + \sum_{i=1}^{N_m} \frac{M_i\, \phi_n(\xi_i) \sum_{m=1}^{\infty} \ddot{\phi}_m(\xi_i) q_m(t) + 2\dot{\phi}_m(\xi_i) \dot{q}_m(t) + \phi_m(\xi_i) \ddot{q}_m(t)}{M_n} \\ = \frac{g}{M_n} \sum_{i=1}^{N_m} M_i\, \phi_n(\xi_i) \end{aligned} \tag{4.59}$$

where N_m is the number of moving masses.

4.3.4 Moving sprung mass

Figure 4.6 shows the simply supported beam illustrated in Fig. 4.3 subjected to a moving sprung mass. The displacements of the contact point and sprung mass are denoted by a^c and a^m, respectively. The stiffness of the spring is denoted by k.

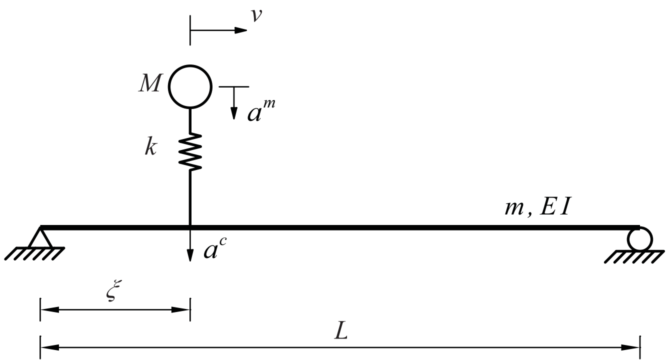

Figure 4.6 – Simply supported beam subjected to a moving sprung mass.

The force applied to the beam at any instant is (Biggs, 1964)

$$p_0(t) = M\,g + k\left[a^m(t) - a^c(t)\right] \tag{4.60}$$

The term $M\,g$ is included because a^m is measured from the neutral spring position. Assuming there is no loss-of-contact between the sprung mass and the beam, the displacement of the contact point is given by Eq. (4.55). Substituting this equation into Eq. (4.60) leads to

$$p_0(t) = M\,g + k\,a^m(t) - k\sum_{m=1}^{\infty}\phi_m(\xi)\,q_m(t) \tag{4.61}$$

Substituting Eq. (4.61) into Eq. (4.52) and rearranging results in

$$\ddot{q}_n(t) + \omega_n^2\,q_n(t) + \frac{k\,\phi_n(\xi)}{M_n}\left[\sum_{m=1}^{\infty}\left[\phi_m(\xi)\,q_m(t)\right] - a^m(t)\right] = \frac{M\,g\,\phi_n(\xi)}{M_n} \tag{4.62}$$

The equation of motion of the sprung mass is given by

$$M\,\ddot{a}^m(t) + k\left[a^m(t) - \sum_{m=1}^{\infty}\phi_m(\xi)\,q_m(t)\right] = 0 \tag{4.63}$$

For the case of several moving sprung masses, Eqs. (4.62) becomes

$$\ddot{q}_n(t) + \omega_n^2\,q_n(t) + \frac{1}{M_n}\sum_{i=1}^{N_m}\left[k_i\,\phi_n(\xi_i)\left[\sum_{m=1}^{\infty}\left[\phi_m(\xi_i)\,q_m(t)\right] - a_i^m(t)\right]\right] = \frac{g}{M_n}\sum_{i=1}^{N_m}M_i\,\phi_n(\xi_i) \tag{4.64}$$

where N_m is the number of moving sprung masses.

The equation of motion of the sprung mass i is defined by

$$M_i \, \ddot{a}_i^m(t) + k_i \left[a_i^m(t) - \sum_{m=1}^{\infty} \phi_m(\xi_i) \, q_m(t) \right] = 0 \tag{4.65}$$

4.4 NUMERICAL EXAMPLES AND VERIFICATION

Two numerical examples are used to verify the accuracy and efficiency of the direct method and its implementation in the FEMIX computer program. The first example consists of a simply supported beam subjected to a single moving sprung mass and the second consists of the same beam subjected to 50 moving sprung masses. In both examples, the results obtained with the direct method are compared with semi-analytical solutions.

4.4.1 Simply supported beam subjected to one moving sprung mass

The simply supported beam illustrated in Fig. 4.6 is subjected to a moving sprung mass. The properties of the system correspond to those adopted by Yang and Yau (1997), being the beam length $L = 25.0$ m and the geometrical and mechanical properties the following: Young's modulus $E = 2.87$ GPa, Poisson's ratio $\nu = 0.2$, moment of inertia $I = 2.90$ m^4, mass per unit length $m = 2{,}303$ kg/m, suspended mass $M = 5{,}750$ kg and spring stiffness $k = 1{,}595$ kN/m. Some of these properties are very different from those of typical railway structures. However, this simply supported beam is adopted here because it is used by many researchers in the validation of vehicle-structure interaction algorithms. The first natural frequency of the beam is $\omega_1 = 30.02$ rad/s, the natural frequency of the spring-mass system is $\omega_v = 16.66$ rad/s and the mass ratio is $M_v/(mL) = 0.1$. The sprung mass moves at a constant speed $v = 100$ km/h.

The FEMIX 4.0 computer program is used to perform the dynamic finite element analysis. The following parameters for the HHT-α method are considered: $\Delta t = 0.001$ s, $\beta = 0.25$, $\gamma = 0.5$ and $\alpha = 0$. The semi-analytical solution of Eqs. (4.62) and (4.63) is obtained considering the contribution of the first twenty modes of vibration, using the same integration method and parameters. The structure is discretised with 50 beam elements and the total number of time steps is 900.

The semi-analytical solutions for the vertical displacement and acceleration at the midpoint of the beam and the corresponding finite element approximations based on the direct method are plotted in Figs. 4.7 and 4.8.

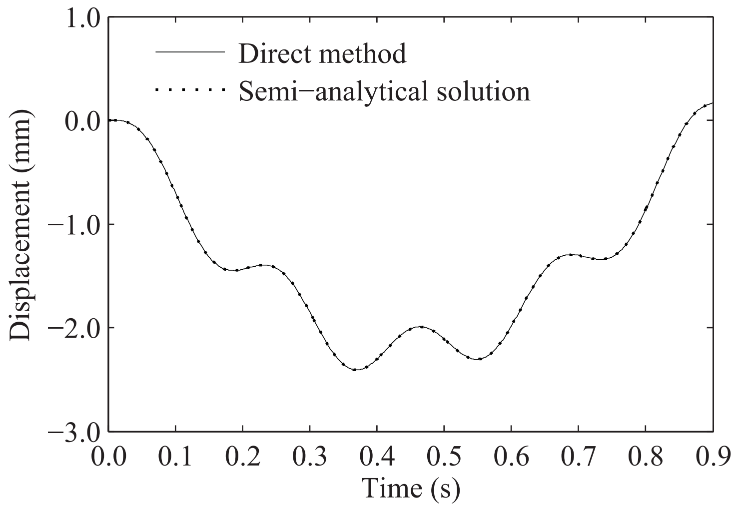

Figure 4.7. Vertical displacement at the midpoint of the beam.

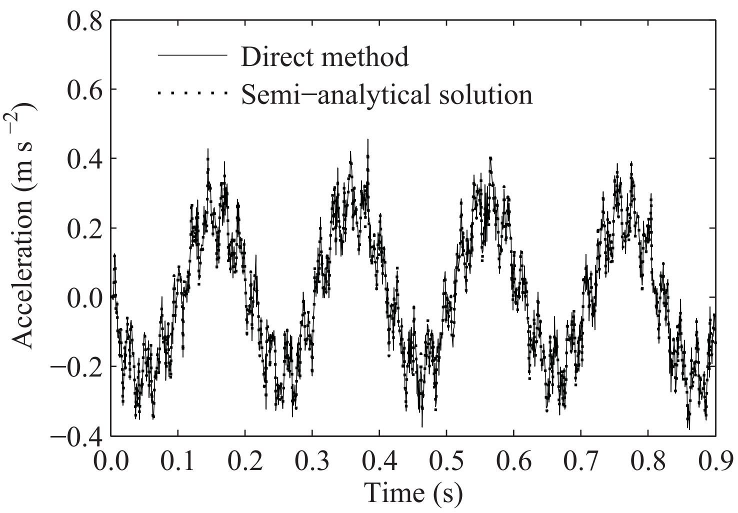

Figure 4.8**.** Vertical acceleration at the midpoint of the beam.

The dynamic responses of the sprung mass, in terms of vertical displacement and acceleration, are shown in Figs. 4.9 and 4.10.

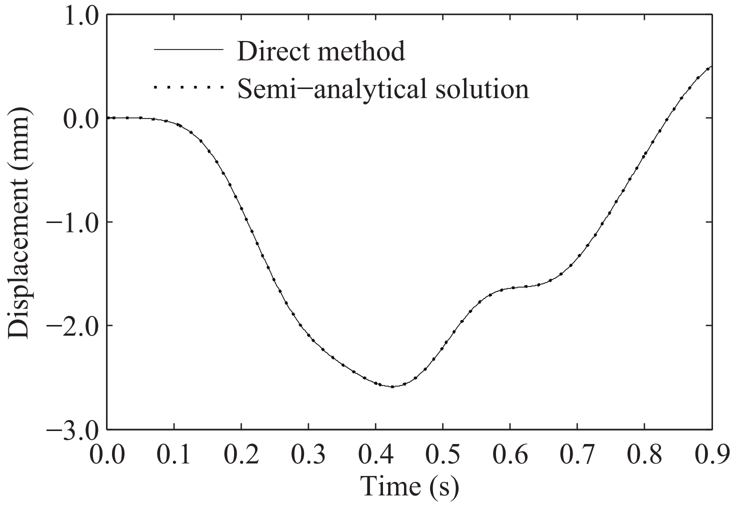

Figure 4.9. Vertical displacement of the sprung mass.

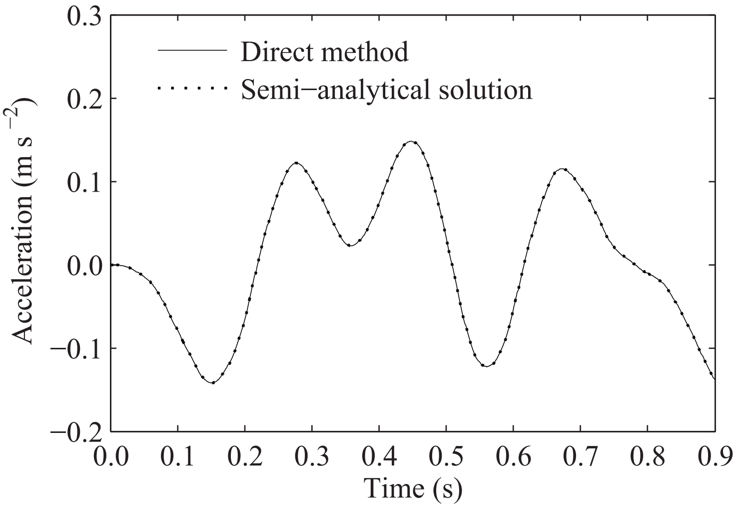

Figure 4.10. Vertical acceleration of the sprung mass.

The results obtained with the proposed formulation perfectly match the corresponding semi-analytical solutions. The comparison between the results obtained and those published by Yang and Yau (1997) shows that the inclusion of additional modes of vibration leads to a better agreement, especially for the case of the sprung mass response.

4.4.2 Simply supported beam subjected to fifty moving sprung masses

The beam described in Section 4.4.1 is now subjected to 50 sprung masses moving at a constant speed $v = 47.7$ km/h. The distance between masses is 3.0 m, with M and k unaltered. A simple sinusoidal function defined by Eq. (4.66) is considered for the validation of the effects of irregularities at the contact interface.

$$r(\xi) = a_0 \sin\left(\frac{2\pi\xi}{\lambda}\right) \tag{4.66}$$

In Eq. (4.66), a_0 is the amplitude (0.5 mm) and λ is the wavelength (5.0 m) of the irregularity. The wavelength chosen is one fifth of the span length. The speed of the sprung masses and the wavelength of the irregularity are such that the frequency of excitation is equal to the natural frequency of the spring-mass system.

To take into account the effects of irregularities at the contact interface, a term is added to Eqs. (4.64) and (4.65), leading to

$$\begin{aligned} \ddot{q}_n(t) + \omega_n^2\, q_n(t) + \sum_{i=1}^{N_v} \frac{\delta_i\, k_{vi}\, \phi_n(\xi_i) \sum_{m=1}^{\infty} \phi_m(\xi_i)\, q_m(t)}{M_n} - \sum_{i=1}^{N_v} \frac{\delta_i\, k_{vi}\, \phi_n(\xi_i)\, z_i}{M_n} \\ = \sum_{i=1}^{N_v} \frac{\delta_i \left(M_{vi}\, g - k_{vi}\, r_i\right) \phi_n(\xi_i)}{M_n} \end{aligned} \tag{4.67}$$

$$M_{vi}\, \ddot{z}_i + k_{vi} \left[z_i - r_i - \sum_{m=1}^{\infty} \phi_m(\xi_i)\, q_m(t) \right] = 0 \tag{4.68}$$

where r_i is the irregularity between the beam and the sprung mass i.

The parameters used in the dynamic finite element analysis and in the semi-analytical solution of Eqs. (4.67) and (4.68) coincide with those used in the previous example. The total number of time steps is now 14,000.

The semi-analytical solutions for the vertical displacement and acceleration of the first sprung mass over the time interval [0, 3](s) and the corresponding finite element approximations based on the direct method are plotted in Figs. 4.11 and 4.12.

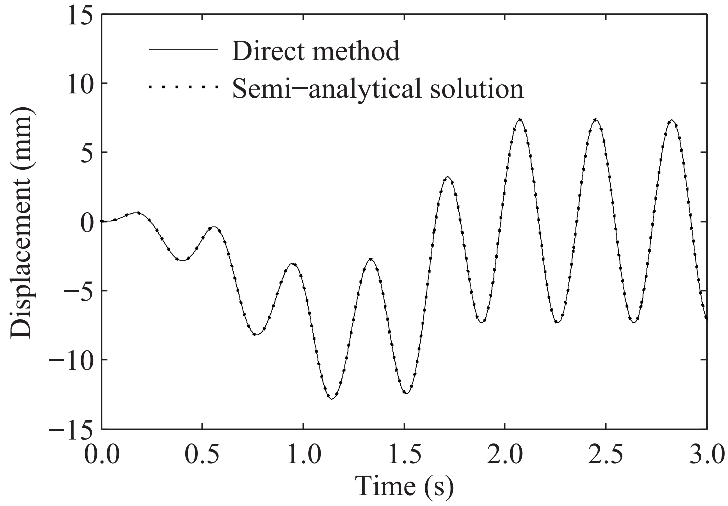

Figure 4.11. Vertical displacement of the first sprung mass.

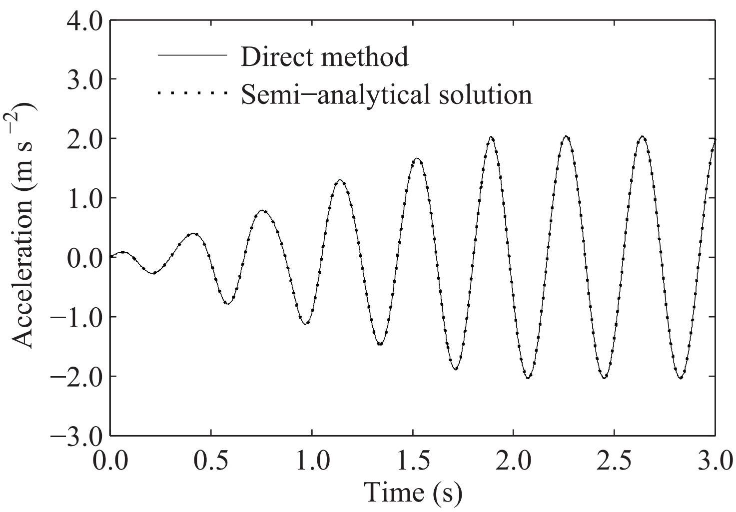

Figure 4.12. Vertical acceleration of the first sprung mass.

The vertical displacement and acceleration of the last sprung mass over the time interval [11, 14](s) are shown in Figs. 4.13 and 4.14.

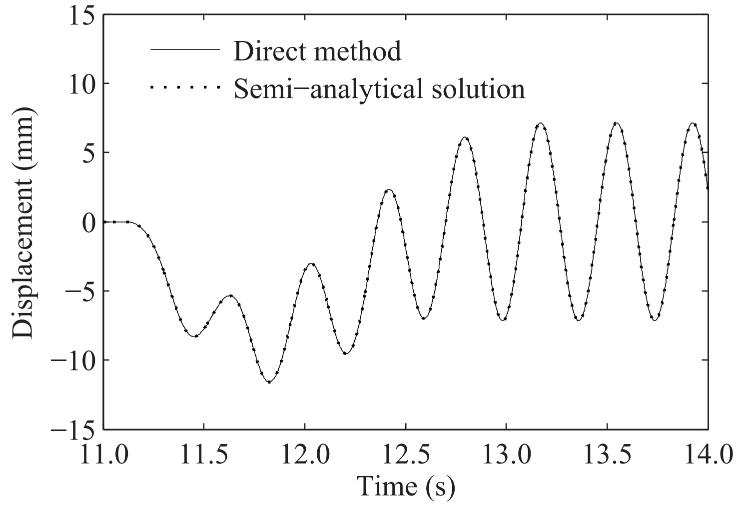

Figure 4.13. Vertical displacement of the last sprung mass.

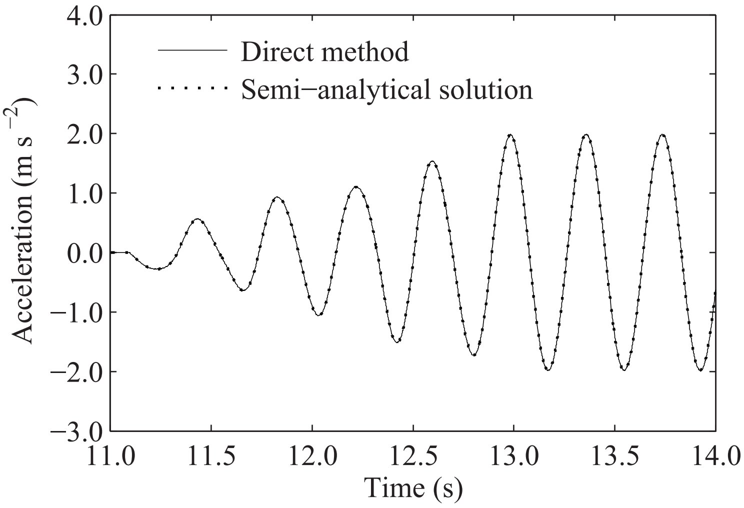

Figure 4.14. Vertical acceleration of the last sprung mass.

The results obtained with the direct method show a very good agreement with the corresponding semi-analytical solutions.

In order to test the efficiency of the direct method, the beam analysed in this section is now discretised with 10,000 8-node solid elements (10×10×100) and has 36,597 unconstrained d.o.f. This beam has a rectangular cross section of width $b = 2.2272$ m and height $h = 2.5$ m (see Fig. 4.15). The parameters used in the previous analysis remain unchanged.

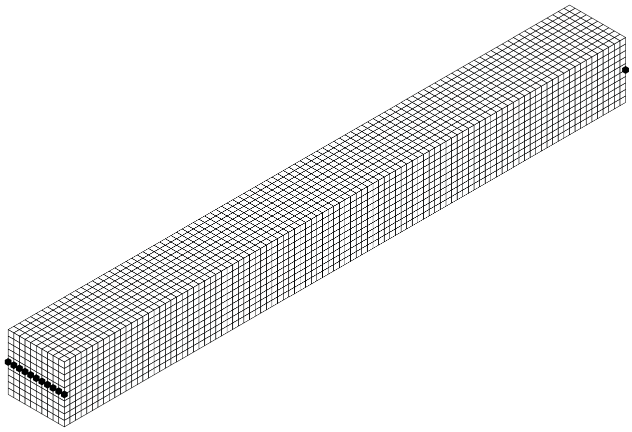

Figure 4.15. Simply supported beam modelled with three-dimensional solid elements.

The vertical displacement of the first sprung mass over the time interval [0, 3](s) is shown in Fig. 4.16.

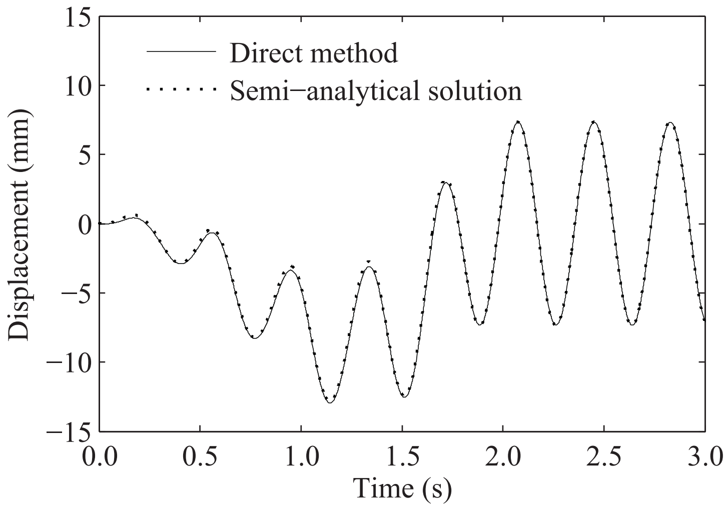

Figure 4.16. Vertical displacement of the first sprung mass.

The vertical displacement of the last sprung mass over the time interval [11, 14](s) is plotted in Fig. 4.17.

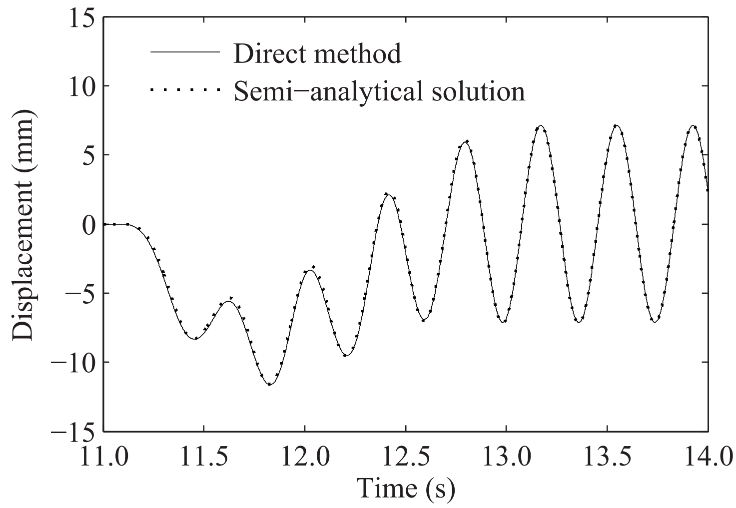

Figure 4.17. Vertical displacement of the last sprung mass.

The results obtained with the proposed method show a good agreement with the corresponding semi-analytical solution.

A workstation with an Intel Core i7-860 processor running at 2.80 GHz has been used to perform the calculations. Using a single core, the execution time is 10572 seconds. According to the author experience, this result is satisfactory.

4.5 CONCLUDING REMARKS

The direct method described in Section 2.2.4 has been further developed in this chapter. It is an accurate, efficient and simple method for analysing the vehicle-structure interaction. The several subsystems can be discretised with complex meshes composed of different types of finite elements using the FEMIX software. The methodology proposed here is also valid when the vehicles are modelled using multibody systems. In the direct method, the equations of motion of the vehicles and structure form a single system that is solved directly, thus avoiding the iterative procedure used by other authors to satisfy the compatibility of displacements. Generally, iterative methods are less accurate and may even diverge, as demonstrated in Section 2.2.6. The direct integration of the equations of motion is performed using the HHT-α method, which is able to control the spurious high-frequency content by introducing numerical damping. In other FE programs, such as ANSYS (2014a), the finite element mesh of the structure must take into account the irregularities, and so the structural matrices have to be calculated and assembled for each set of irregularities. Since in the direct method, the constraint equations include the irregularities, there is no need to change the finite element mesh.

The implementation of the direct method in a finite element computer program is straightforward for the reason that only the contact algorithm needs to be implemented and no additional finite elements have to be developed. The accuracy and efficiency of the direct method have been confirmed using two numerical examples. An excellent agreement between the results obtained with the proposed method and the corresponding semi-analytical solutions is observed.

The node-to-segment contact element used in this chapter does not allow separation and does not take into account the local deformations and highly concentrated stresses that arise in the vicinity of the contact region (see Chapter 3). These limitations are addressed in Chapter 5.

5 ENHANCED NONLINEAR CONTACT ELEMENT

5.1 INTRODUCTION

In the direct method proposed in Chapter 4, the coupling between the vehicle and structure is taken into account by directly establishing the equilibrium of the contact forces and imposing the contact constraint equations. However, the node-to-segment contact element used does not allow separation. Also, the local deformations and highly concentrated stresses which arise in the vicinity of the contact region, explained in Chapter 3, are not taken into account.

In the formulation presented in this chapter, a search algorithm is used to detect which elements are in contact, with the constraint equations imposed only when contact occurs. Since only frictionless contact is considered, the constraint equations are purely geometrical and relate the displacements of the contact node to the displacements of the corresponding target element. An enhanced node-to-segment contact element, which includes an Hertzian spring that relates the forces acting at the interface to the local deformations, is proposed here. Due to the nonlinear nature of the constraint equations and of the Hertzian spring, an incremental formulation based on the Newton-Raphson method is adopted. Three numerical examples are used to demonstrate the accuracy and computationally efficiency of the proposed method.

5.2 VEHICLE-STRUCTURE INTERACTION METHOD

5.2.1 Enhanced contact element

The enhanced node-to-segment contact element represented in Fig. 5.1 includes the additional Hertzian spring described in Chapter 3 to take into account the local deformations and highly concentrated stresses which arise in the vicinity of the contact region. The forces X acting at the contact interface and the displacements of the contact point and the corresponding point of the target element (v^{ce} and v^{te}) are defined in the local coordinate system of the contact pair (ξ_1, ξ_2, ξ_3). The ξ_1 axis has the direction of the longitudinal axis of the target element, the ξ_2 axis always points towards the contact node and the ξ_3 axis completes the right-handed system. The superscripts *ce* and *te* indicate contact and target element, respectively. The node N_1 is a nodal point of the vehicle and the nodes N_2 and N_3 are nodal points of the structure. The point P is an auxiliary internal point of a target element of the structure. When contact occurs, the proposed enhanced node-to-segment contact element adds the internal node N_4 and the finite element connecting this node to the node N_1 in order to take into account the behaviour of the contact interface in the normal direction. In this case, the node N_4 and the auxiliary point P are coincident. The constraint equations that relate the displacements of these nodes are imposed using the direct method proposed in Chapter 4, which is extended to deal with nonlinear contact problems.

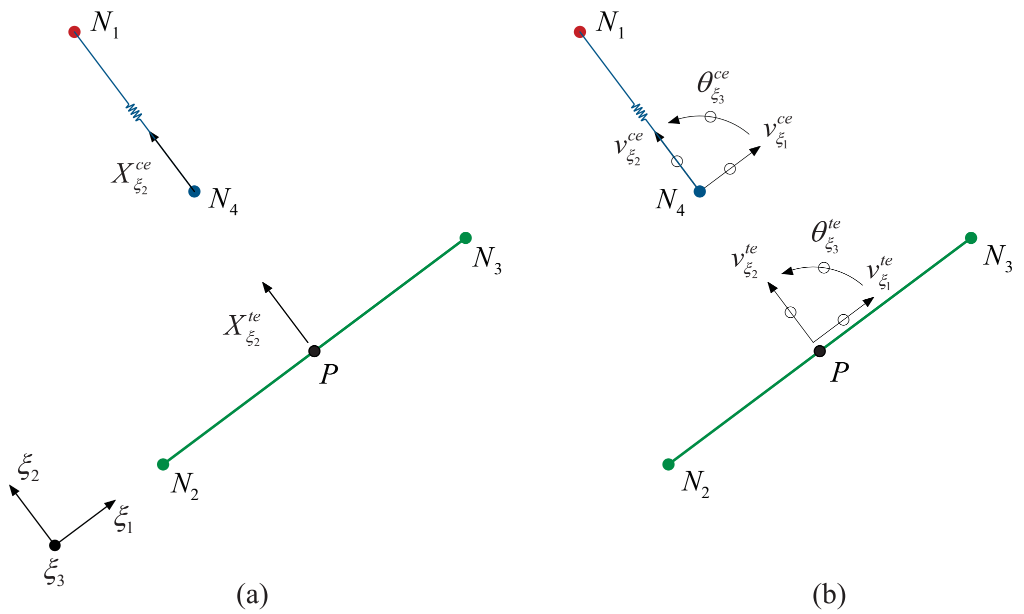

Figure 5.1. Node-to-segment contact element: (a) forces and (b) displacements at the contact interface.

According to Newton's third law, the forces acting at the contact interface must be of equal magnitude and opposite direction, i.e.,

$$\mathbf{X}^{ce} + \mathbf{X}^{te} = \mathbf{0} \tag{5.1}$$

The displacement vector of an arbitrary point is defined by two translations, v_{ξ_1} and v_{ξ_2}, and a rotation θ_{ξ_3} about the ξ_3 axis. Since this type of contact element neglects the tangential forces and moments transmitted across the contact interface, the contact constraint equations only relate the displacement v_{ξ_2} of the contact node to the corresponding displacement of the auxiliary point P. Each constraint equation is defined in the local coordinate system of the contact pair and comprises the non-penetration condition for the normal direction. These equations are given by

$$\mathbf{v}^{ce} - \mathbf{v}^{te} \geq \mathbf{r} \tag{5.2}$$

where $\mathbf{r}$ are the irregularities between the contact and target elements. A positive irregularity implies an increase of the distance between the contact and target elements (see Fig. 5.1). In the ANSYS commercial software (2014a), the finite element mesh of the structure must include the irregularities, and so the structural matrices have to be calculated and assembled for each set of irregularities. In the formulation proposed here, this is avoided because the irregularities are included in the constraint equations.

5.2.2 Formulation of the equations of motion

Assuming that the applied loads are deformation-independent and that the nodal forces corresponding to the internal element stresses may depend nonlinearly on the nodal displacements, the equations of motion of the vehicle-structure system given in Section 4.2.2 may be rewritten in the form

$$\mathbf{M}\,\ddot{\mathbf{a}}^{t+\Delta t} + \mathbf{C}\left[(1+\alpha)\,\dot{\mathbf{a}}^{t+\Delta t} - \alpha\,\dot{\mathbf{a}}^{t}\right] + (1+\alpha)\,\mathbf{R}^{t+\Delta t} - \alpha\,\mathbf{R}^{t} = (1+\alpha)\,\mathbf{F}^{t+\Delta t} - \alpha\,\mathbf{F}^{t} \tag{5.3}$$

where $\mathbf{M}$ is the mass matrix, $\mathbf{C}$ is the viscous damping matrix, $\mathbf{R}$ are the nodal forces corresponding to the internal element stresses, $\mathbf{F}$ are the externally applied nodal loads and $\mathbf{a}$ are the nodal displacements. The elastic forces depend nonlinearly on the nodal displacements due to the nonlinear nature of the contact. In the present work, the nonlinear inertia effects, such as the centrifugal and gyroscopic effects, are neglected. The superscripts t and $t+\Delta t$ indicate the previous and current time steps, respectively.

To solve Eq. (5.3) let the F type degrees of freedom (d.o.f.) represent the free nodal d.o.f., whose values are unknown, and let the P type d.o.f. represent the prescribed nodal d.o.f., whose values are known. Thus, the load vector can be expressed as

$$\mathbf{F}_F = \mathbf{P}_F + \mathbf{D}_{FX}^{ce}\;\mathbf{X}^{ce} + \mathbf{D}_{FX}^{te}\;\mathbf{X}^{te} \tag{5.4}$$

$$\mathbf{F}_P = \mathbf{P}_P + \mathbf{D}_{PX}^{ce}\;\mathbf{X}^{ce} + \mathbf{D}_{PX}^{te}\;\mathbf{X}^{te} + \mathbf{S} \tag{5.5}$$

where $\mathbf{P}$ corresponds to the externally applied nodal loads whose values are known, $\mathbf{S}$ are the support reactions and $\mathbf{X}$ are the forces acting at the contact interface shown in Fig. 5.1.

Each matrix **D** relates the contact forces, defined in the local coordinate system of the respective contact pair, to the nodal forces defined in the global coordinate system.

Substituting Eq. (5.1) into Eqs. (5.4) and (5.5) leads to

$$\mathbf{F}_F = \mathbf{P}_F + \mathbf{D}_{FX}\,\mathbf{X} \tag{5.6}$$

$$\mathbf{F}_P = \mathbf{P}_P + \mathbf{D}_{PX}\,\mathbf{X} + \mathbf{S} \tag{5.7}$$

where

$$\mathbf{X} = \mathbf{X}^{ce} \tag{5.8}$$

$$\mathbf{D}_{FX} = \mathbf{D}_{FX}^{ce} - \mathbf{D}_{FX}^{te} \tag{5.9}$$

$$\mathbf{D}_{PX} = \mathbf{D}_{PX}^{ce} - \mathbf{D}_{PX}^{te} \tag{5.10}$$

Substituting Eqs. (5.6) and (5.7) into Eq. (5.3) and partitioning into *F* and *P* type d.o.f. gives

$$\begin{bmatrix} \mathbf{M}_{FF} & \mathbf{M}_{FP} \\ \mathbf{M}_{PF} & \mathbf{M}_{PP} \end{bmatrix} \begin{bmatrix} \ddot{\mathbf{a}}_F^{t+\Delta t} \\ \ddot{\mathbf{a}}_P^{t+\Delta t} \end{bmatrix} + \begin{bmatrix} \mathbf{C}_{FF} & \mathbf{C}_{FP} \\ \mathbf{C}_{PF} & \mathbf{C}_{PP} \end{bmatrix} \left[(1+\alpha) \begin{bmatrix} \dot{\mathbf{a}}_F^{t+\Delta t} \\ \dot{\mathbf{a}}_P^{t+\Delta t} \end{bmatrix} - \alpha \begin{bmatrix} \dot{\mathbf{a}}_F^{t} \\ \dot{\mathbf{a}}_P^{t} \end{bmatrix} \right] + (1+\alpha) \begin{bmatrix} \mathbf{R}_F^{t+\Delta t} \\ \mathbf{R}_P^{t+\Delta t} \end{bmatrix} - \alpha \begin{bmatrix} \mathbf{R}_F^{t} \\ \mathbf{R}_P^{t} \end{bmatrix}$$
$$= (1+\alpha) \begin{bmatrix} \mathbf{P}_F^{t+\Delta t} + \mathbf{D}_{FX}^{t+\Delta t}\,\mathbf{X}^{t+\Delta t} \\ \mathbf{P}_P^{t+\Delta t} + \mathbf{D}_{PX}^{t+\Delta t}\,\mathbf{X}^{t+\Delta t} + \mathbf{S}^{t+\Delta t} \end{bmatrix} - \alpha \begin{bmatrix} \mathbf{P}_F^{t} + \mathbf{D}_{FX}^{t}\,\mathbf{X}^{t} \\ \mathbf{P}_P^{t} + \mathbf{D}_{PX}^{t}\,\mathbf{X}^{t} + \mathbf{S}^{t} \end{bmatrix} \tag{5.11}$$

Transferring the unknowns to the left-hand side leads to

$$\mathbf{M}_{FF}\,\ddot{\mathbf{a}}_F^{t+\Delta t} + (1+\alpha)\mathbf{C}_{FF}\,\dot{\mathbf{a}}_F^{t+\Delta t} + (1+\alpha)\mathbf{R}_F^{t+\Delta t} - (1+\alpha)\,\mathbf{D}_{FX}^{t+\Delta t}\,\mathbf{X}^{t+\Delta t} = \overline{\mathbf{F}}_F \tag{5.12}$$

and

$$\begin{aligned} \mathbf{S}^{t+\Delta t} &= -\mathbf{P}_P^{t+\Delta t} - \mathbf{D}_{PX}^{t+\Delta t}\,\mathbf{X}^{t+\Delta t} \\ &+ \frac{1}{1+\alpha}\left[\mathbf{M}_{PF}\,\ddot{\mathbf{a}}_F^{t+\Delta t} + \mathbf{M}_{PP}\,\ddot{\mathbf{a}}_P^{t+\Delta t}\right] + \mathbf{C}_{PF}\,\dot{\mathbf{a}}_F^{t+\Delta t} + \mathbf{C}_{PP}\,\dot{\mathbf{a}}_P^{t+\Delta t} + \mathbf{R}_P^{t+\Delta t} \\ &+ \frac{\alpha}{1+\alpha}\left[\mathbf{S}^{t} + \mathbf{P}_P^{t} + \mathbf{D}_{PX}^{t}\,\mathbf{X}^{t} - \mathbf{C}_{PF}\,\dot{\mathbf{a}}_F^{t} - \mathbf{C}_{PP}\,\dot{\mathbf{a}}_P^{t} - \mathbf{R}_P^{t}\right] \end{aligned} \tag{5.13}$$

where

$$\begin{aligned} \overline{\mathbf{F}}_F &= (1+\alpha)\mathbf{P}_F^{t+\Delta t} - \alpha\,\mathbf{P}_F^{t} - \alpha\,\mathbf{D}_{FX}^{t}\,\mathbf{X}^{t} - \mathbf{M}_{FP}\,\ddot{\mathbf{a}}_P^{t+\Delta t} \\ &- (1+\alpha)\mathbf{C}_{FP}\,\dot{\mathbf{a}}_P^{t+\Delta t} + \alpha\left[\mathbf{C}_{FF}\,\dot{\mathbf{a}}_F^{t} + \mathbf{C}_{FP}\,\dot{\mathbf{a}}_P^{t}\right] + \alpha\,\mathbf{R}_F^{t} \end{aligned} \tag{5.14}$$

5.2.3 Incremental formulation for nonlinear analysis

Since the present problem is nonlinear, Eq. (5.12) is rewritten in the form

$$\boldsymbol{\psi}_F\left(\mathbf{a}_F^{t+\Delta t},\mathbf{X}^{t+\Delta t}\right)=\mathbf{0} \tag{5.15}$$

where $\boldsymbol{\psi}$ is the residual forces vector, given by

$$\boldsymbol{\psi}_F\left(\mathbf{a}_F^{t+\Delta t},\mathbf{X}^{t+\Delta t}\right)=\overline{\mathbf{F}}_F-\mathbf{M}_{FF}\,\ddot{\mathbf{a}}_F^{t+\Delta t}-(1+\alpha)\mathbf{C}_{FF}\,\dot{\mathbf{a}}_F^{t+\Delta t}-(1+\alpha)\mathbf{R}_F^{t+\Delta t}+(1+\alpha)\,\mathbf{D}_{FX}^{t+\Delta t}\,\mathbf{X}^{t+\Delta t} \tag{5.16}$$

The nodal velocities and accelerations depend on the nodal displacements and, for this reason, are not independent unknowns. In the HHT-α method, the velocity and acceleration at the current time step are approximated using the same expressions presented for the Newmark method in Section 2.2.2. Thus,

$$\dot{\mathbf{a}}^{t+\Delta t}=A_1\left(\mathbf{a}^{t+\Delta t}-\mathbf{a}^t\right)-A_4\,\dot{\mathbf{a}}^t-A_5\,\ddot{\mathbf{a}}^t \tag{5.17}$$

$$\ddot{\mathbf{a}}^{t+\Delta t}=A_0\left(\mathbf{a}^{t+\Delta t}-\mathbf{a}^t\right)-A_2\,\dot{\mathbf{a}}^t-A_3\,\ddot{\mathbf{a}}^t \tag{5.18}$$

An iterative scheme based on the Newton-Raphson method (Owen & Hinton, 1980) is used to solve Eq. (5.15). Assuming that the solution at the ith iteration has been previously evaluated and neglecting second and higher order terms, the Taylor series for $\boldsymbol{\psi}_F$ about $\left(\mathbf{a}_F^{t+\Delta t,i},\mathbf{X}^{t+\Delta t,i}\right)$ is given by

$$\begin{aligned}\boldsymbol{\psi}_F\left(\mathbf{a}_F^{t+\Delta t,i+1},\mathbf{X}^{t+\Delta t,i+1}\right)=\boldsymbol{\psi}_F\left(\mathbf{a}_F^{t+\Delta t,i},\mathbf{X}^{t+\Delta t,i}\right)+\left[\left.\frac{\partial\boldsymbol{\psi}_F}{\partial\mathbf{a}_F^{t+\Delta t}}\right|_{\left(\mathbf{a}_F^{t+\Delta t,i},\mathbf{X}^{t+\Delta t,i}\right)}\right]\left(\mathbf{a}_F^{t+\Delta t,i+1}-\mathbf{a}_F^{t+\Delta t,i}\right)\\+\left[\left.\frac{\partial\boldsymbol{\psi}_F}{\partial\mathbf{X}^{t+\Delta t}}\right|_{\left(\mathbf{a}_F^{t+\Delta t,i},\mathbf{X}^{t+\Delta t,i}\right)}\right]\left(\mathbf{X}^{t+\Delta t,i+1}-\mathbf{X}^{t+\Delta t,i}\right)\end{aligned} \tag{5.19}$$

Substituting Eqs. (5.16) to (5.18) into Eq. (5.19), and assuming that the residual forces vector at iteration i+1 fulfils the condition given by Eq. (5.15), leads to

$$\begin{aligned}&\boldsymbol{\psi}_F\left(\mathbf{a}_F^{t+\Delta t,i},\mathbf{X}^{t+\Delta t,i}\right)\\&+\left[-A_0\,\mathbf{M}_{FF}-(1+\alpha)\,A_1\,\mathbf{C}_{FF}-(1+\alpha)\left[\left.\frac{\partial\mathbf{R}_F}{\partial\mathbf{a}_F^{t+\Delta t}}\right|_{\mathbf{a}_F^{t+\Delta t,i}}\right]\right]\left(\mathbf{a}_F^{t+\Delta t,i+1}-\mathbf{a}_F^{t+\Delta t,i}\right)\\&+(1+\alpha)\,\mathbf{D}_{FX}^{t+\Delta t,i}\left(\mathbf{X}^{t+\Delta t,i+1}-\mathbf{X}^{t+\Delta t,i}\right)=\mathbf{0}\end{aligned} \tag{5.20}$$

Equation (5.20) can be rewritten as

$$\overline{\mathbf{K}}_{FF}\ \Delta\mathbf{a}_F^{i+1} - (1+\alpha)\,\mathbf{D}_{FX}^{t+\Delta t,i}\ \Delta\mathbf{X}^{i+1} = \boldsymbol{\psi}_F^i \tag{5.21}$$

where $\overline{\mathbf{K}}_{FF}$ is the current effective stiffness matrix defined by

$$\overline{\mathbf{K}}_{FF} = A_0\,\mathbf{M}_{FF} + (1+\alpha)\,A_1\,\mathbf{C}_{FF} + (1+\alpha)\left[\left.\frac{\partial\mathbf{R}_F}{\partial\mathbf{a}_F^{t+\Delta t}}\right|_{\mathbf{a}_F^{t+\Delta t,i}}\right] \tag{5.22}$$

and

$$\Delta\mathbf{a}_F^{i+1} = \mathbf{a}_F^{t+\Delta t,i+1} - \mathbf{a}_F^{t+\Delta t,i} \tag{5.23}$$

$$\Delta\mathbf{X}^{i+1} = \mathbf{X}^{t+\Delta t,i+1} - \mathbf{X}^{t+\Delta t,i} \tag{5.24}$$

$$\boldsymbol{\psi}_F^i = \boldsymbol{\psi}_F\left(\mathbf{a}_F^{t+\Delta t,i}, \mathbf{X}^{t+\Delta t,i}\right) \tag{5.25}$$

In matrix notation, Eq. (5.21) can be expressed as

$$\begin{bmatrix}\overline{\mathbf{K}}_{FF} & \overline{\mathbf{D}}_{FX}\end{bmatrix}\begin{bmatrix}\Delta\mathbf{a}_F^{i+1}\\ \Delta\mathbf{X}^{i+1}\end{bmatrix} = \boldsymbol{\psi}_F^i \tag{5.26}$$

being

$$\overline{\mathbf{D}}_{FX} = -(1+\alpha)\,\mathbf{D}_{FX}^{t+\Delta t,i} \tag{5.27}$$

After the evaluation of the solution at iteration i+1, the current residual forces vector is calculated using Eq. (5.16). The iteration scheme continues until the condition

$$\frac{\left\|\boldsymbol{\psi}_F^{i+1}\right\|}{\left\|\mathbf{P}_F^{t+\Delta t}\right\|} \leq \varepsilon \tag{5.28}$$

is fulfilled, where ε is a specified tolerance.

5.2.4 Formulation of the contact constraint equations

When contact occurs, the non-penetration condition given by Eq. (5.2) is fulfilled if

$$\mathbf{v}^{ce} - \mathbf{v}^{te} = \mathbf{r} \tag{5.29}$$

If a contact node is not in contact with any target element, the corresponding constraint equation is not considered. The displacements of the contact nodes (see Fig. 5.1) are given by

$$\mathbf{v}^{ce} = \mathbf{H}_{XF}^{ce}\,\mathbf{a}_F^{t+\Delta t,i+1} + \mathbf{H}_{XP}^{ce}\,\mathbf{a}_P^{t+\Delta t} \tag{5.30}$$

where each transformation matrix $\mathbf{H}^{ce}$ transforms the displacements of the contact nodes from the global coordinate system to the local coordinate system of the contact pair. The displacements of the auxiliary points of the target elements are given by

$$\mathbf{v}^{te} = \mathbf{H}_{XF}^{te}\,\mathbf{a}_F^{t+\Delta t,i+1} + \mathbf{H}_{XP}^{te}\,\mathbf{a}_P^{t+\Delta t} \tag{5.31}$$

where each transformation matrix $\mathbf{H}^{te}$ relates the nodal displacements of the target elements, defined in the global coordinate system, to the displacements of the auxiliary points defined in the local coordinate system of each contact pair.

Substituting Eqs. (5.30) and (5.31) into Eq. (5.29) yields

$$\mathbf{H}_{XF}\,\mathbf{a}_F^{t+\Delta t,i+1} = -\mathbf{g} + \mathbf{r} - \mathbf{H}_{XP}\,\mathbf{a}_P^{t+\Delta t} \tag{5.32}$$

where

$$\mathbf{H}_{XF} = \mathbf{H}_{XF}^{ce} - \mathbf{H}_{XF}^{te} \tag{5.33}$$

$$\mathbf{H}_{XP} = \mathbf{H}_{XP}^{ce} - \mathbf{H}_{XP}^{te} \tag{5.34}$$

Substituting Eq. (5.23) into Eq. (5.32) leads to

$$\mathbf{H}_{XF}\,\Delta\mathbf{a}_F^{i+1} = -\mathbf{g} + \mathbf{r} - \mathbf{H}_{XP}\,\mathbf{a}_P^{t+\Delta t} - \mathbf{H}_{XF}\,\mathbf{a}_F^{t+\Delta t,i} \tag{5.35}$$

Multiplying Eq. (5.35) by $-(1+\alpha)$ gives

$$\overline{\mathbf{H}}_{XF}\,\Delta\mathbf{a}_F^{i+1} = \overline{\mathbf{r}} \tag{5.36}$$

where

$$\overline{\mathbf{H}}_{XF} = -(1+\alpha)\,\mathbf{H}_{XF} \tag{5.37}$$

and

$$\overline{\mathbf{r}} = -(1+\alpha)\left(\mathbf{r} - \mathbf{H}_{XP}\,\mathbf{a}_P^{t+\Delta t} - \mathbf{H}_{XF}\,\mathbf{a}_F^{t+\Delta t,i}\right) \tag{5.38}$$

5.2.5 Complete algorithm

The incremental formulation of the equations of motion of the vehicle-structure system, presented in Section 5.2.3, is applicable to either linear or nonlinear analyses. These equations and the contact constraints presented in Section 5.2.4 form a complete system whose unknowns are incremental nodal displacements and contact forces. Equations (5.26) and (5.36) can be expressed in matrix form leading to the following system of equations

$$\begin{bmatrix} \overline{\mathbf{K}}_{FF} & \overline{\mathbf{D}}_{FX} \\ \overline{\mathbf{H}}_{XF} & \mathbf{0} \end{bmatrix} \begin{bmatrix} \Delta \mathbf{a}_F^{i+1} \\ \Delta \mathbf{X}^{i+1} \end{bmatrix} = \begin{bmatrix} \boldsymbol{\psi}\left(\mathbf{a}_F^{t+\Delta t,i}, \mathbf{X}^{t+\Delta t,i}\right) \\ \overline{\mathbf{r}} \end{bmatrix} \tag{5.39}$$

Using Betti's theorem, it can be demonstrated that the matrix in Eq. (5.39) is symmetric. Since the time required for solving the system of linear equations presented in Eq. (5.39) may represent a significant percentage of the total solution time, the efficiency of the solver is very important. The system matrix is partitioned into the following form in order to improve the efficiency of the solver.

$$\begin{bmatrix} \overline{\mathbf{K}}_{II} & \overline{\mathbf{K}}_{IR} & \overline{\mathbf{K}}_{IY} & \overline{\mathbf{D}}_{IX} \\ \overline{\mathbf{K}}_{RI} & \overline{\mathbf{K}}_{RR} & \overline{\mathbf{K}}_{RY} & \overline{\mathbf{D}}_{RX} \\ \overline{\mathbf{K}}_{YI} & \overline{\mathbf{K}}_{YR} & \overline{\mathbf{K}}_{YY} & \overline{\mathbf{D}}_{YX} \\ \overline{\mathbf{H}}_{XI} & \overline{\mathbf{H}}_{XR} & \overline{\mathbf{H}}_{XY} & \mathbf{0} \end{bmatrix} \begin{bmatrix} \Delta \mathbf{a}_I^{i+1} \\ \Delta \mathbf{a}_R^{i+1} \\ \Delta \mathbf{a}_Y^{i+1} \\ \Delta \mathbf{X}^{i+1} \end{bmatrix} = \begin{bmatrix} \boldsymbol{\psi}_I^i \\ \boldsymbol{\psi}_R^i \\ \boldsymbol{\psi}_Y^i \\ \overline{\mathbf{r}} \end{bmatrix} \tag{5.40}$$

The F type d.o.f. are partitioned into I, R and Y type d.o.f. The Y type d.o.f. correspond to the d.o.f of the internal nodes added by the contact elements (see node N_4 in Fig. 5.1). These d.o.f. have to be grouped together because they are only active when contact occurs, and so the size of the matrices relating these d.o.f. is time-dependent. Since the laws for the contact interface are nonlinear, the matrices of the contact elements are also time-dependent. The R type d.o.f. correspond to all the nodal d.o.f of the contact elements, except for the Y type d.o.f., which have already been separately grouped together (see node N_1 in Fig. 5.1). The I type d.o.f. are all the remaining F type d.o.f. The R type d.o.f. can also include the d.o.f of other finite elements that have nonlinear behaviour such as the spring-dampers modelling the suspensions of vehicles. The present formulation uses the efficient block factorisation algorithm described in Appendix B, which is based on that presented in Appendix A. Table 5.1 describes all the aspects regarding the dynamic analysis of the vehicle-structure interaction.

Table 5.1 – Summary of the nonlinear dynamic analysis algorithm.

1.	Factorise $\overline{\mathbf{K}}_{FF}$ and calculate $\mathbf{L}_{21}$ (see Appendix B).
2.	Start the time integration loop ($t=0$).
3.	Calculate the external load vector $\mathbf{P}^{t+\Delta t}$.
4.	Assume the following predictors for the accelerations and contact forces: a) $\ddot{\mathbf{a}}_F^{t+\Delta t} = \mathbf{0}$ b) $\mathbf{X}^{t+\Delta t} = \mathbf{X}^t$ Calculate the initial displacements and velocities: a) $\mathbf{a}_F^{t+\Delta t} = \mathbf{a}_F^t + \dot{\mathbf{a}}_F^t \Delta t + (1/2 - \beta)\ddot{\mathbf{a}}_F^t \Delta t^2$ b) $\dot{\mathbf{a}}_F^{t+\Delta t} = \dot{\mathbf{a}}_F^t + (1-\gamma)\ddot{\mathbf{a}}_F^t \Delta t$
5.	Start the Newton-Raphson iteration loop ($i=0$).
6.	Check the contact status using inequality (5.2) and calculate matrices **D** and **H** for the existing constraints.
7.	Evaluate the residual forces vector $\boldsymbol{\psi}\left(\mathbf{a}_F^{t+\Delta t,i}, \mathbf{X}^{t+\Delta t,i}\right)$using Eq. (5.16).
8.	Check the convergence criteria (ε is a specified tolerance): a) if $\left\Vert\boldsymbol{\psi}\right\Vert / \left\Vert\mathbf{P}_F^{t+\Delta t}\right\Vert \le \varepsilon$, convergence achieved; continue to next time step (step 3) b) if $\left\Vert\boldsymbol{\psi}\right\Vert / \left\Vert\mathbf{P}_F^{t+\Delta t}\right\Vert > \varepsilon$, convergence not achieved; continue to step 9
9.	If required, update the effective stiffness matrix using Eq. (5.22).
10.	Solve the system of equations (5.39) using the block factorisation solver (see Appendix B) to obtain $\Delta\mathbf{a}_F^{i+1}$ and $\Delta\mathbf{X}^{i+1}$.
11.	Update the displacements, velocities, accelerations and contact forces: a) $\mathbf{a}_F^{t+\Delta t,i+1} = \mathbf{a}_F^{t+\Delta t,i} + \Delta\mathbf{a}_F^{i+1}$ b) $\dot{\mathbf{a}}_F^{t+\Delta t,i+1} = \dfrac{\gamma}{\beta\Delta t}\left(\mathbf{a}_F^{t+\Delta t,i+1} - \mathbf{a}_F^t\right) + \left(1-\dfrac{\gamma}{\beta}\right)\dot{\mathbf{a}}_F^t + \Delta t\left(1-\dfrac{\gamma}{2\beta}\right)\ddot{\mathbf{a}}_F^t$ c) $\ddot{\mathbf{a}}_F^{t+\Delta t,i+1} = \dfrac{1}{\beta\Delta t^2}\left(\mathbf{a}_F^{t+\Delta t,i+1} - \mathbf{a}_F^t\right) - \dfrac{1}{\beta\Delta t}\dot{\mathbf{a}}_F^t - \left(\dfrac{1}{2\beta} - 1\right)\ddot{\mathbf{a}}_F^t$ d) $\mathbf{X}^{t+\Delta t,i+1} = \mathbf{X}^{t+\Delta t,i} + \Delta\mathbf{X}^{i+1}$
12.	Increment the iteration counter i and continue to step 6.

The direct method proposed in Chapter 4 has been implemented in FEMIX, which is a general purpose finite element computer program (FEMIX). This program is developed using the programming language ANSI-C, which is a low-level programming language. MATLAB® (2013) is a very popular high-level language widely used in industry and academia that provides extensive libraries of prebuilt functions. Using MATLAB significantly reduces development time and also promotes collaboration. MATLAB is used in a wide variety of fields such as algorithm development, modelling, prototyping and development of graphical user interfaces. Therefore, the vehicle-structure interaction method proposed in this chapter has been implemented in MATLAB, with the vehicles and structures modelled using ANSYS. All the data regarding these models, such as the structural matrices, the definition of the target elements, the contact nodes of the vehicle and the support conditions are exported from ANSYS in batch mode and subsequently imported to MATLAB. The remaining data, namely the irregularities between the wheel and rail and the externally applied loads are stored in an external database and imported directly to MATLAB.

5.3 NUMERICAL EXAMPLES AND VERIFICATION

In order to validate the accuracy and efficiency of the proposed methodology, a numerical example consisting of two simply supported spans subjected to four moving sprung masses is presented. The geometrical and mechanical properties of the simply supported beam described in Section 4.4 are the same as those adopted by Yang and Yau (1997), which is a widely cited article in the field of vehicle-structure interaction. However, some of the adopted values are not very realistic and do not correspond to any existing railway structure. Hence, a new example is considered in this section. The results calculated using the direct method are compared with those obtained with the ANSYS commercial software. In the analyses performed with ANSYS, the Lagrange multiplier method is used. The system of linear equations used in this method is the same as that used in the direct method, as explained in Section 2.3.2.

The algorithm developed here only takes into account the vehicle-structure interaction in the normal contact direction. However, the objective is to develop a generic method that can later be extended to three-dimensional contact problems. The formulation of the enhanced node-to-segment contact element allows the target element to have any orientation in space and thus could be used in the analysis of inclined and curved tracks. In order to validate this formulation, a numerical example consisting of an inclined rigid beam subjected to the passage of a two-axle vehicle is also considered. The results obtained with the proposed method are compared with analytical solutions.

5.3.1 Two simply supported spans modelled with 2D beam elements

The structure represented in Fig. 5.2 consists of two simply supported spans modelled with two-dimensional beam elements and subjected to four moving sprung masses (only two are shown). Each span is modelled with 50 finite elements. The geometrical and mechanical properties of the system are the following: length of each span $L = 20$ m, Young's modulus $E = 25$ GPa, Poisson's ratio $\nu = 0.2$, cross-sectional area $A = 6\,\mathrm{m}^2$, moment of inertia $I = 3\,\mathrm{m}^4$, mass per unit length $m = 30$ t/m, suspended mass $M_v = 30$ t and spring stiffness $k_v = 156\,550$ kN/m. The distance between each sprung mass is $d = 20$ m. The sprung masses are supported before and after the simply supported spans using rigid beams. The fundamental frequency of the simply supported beams is 6.1 Hz and the natural frequency of the spring-mass system is 11.5 Hz.

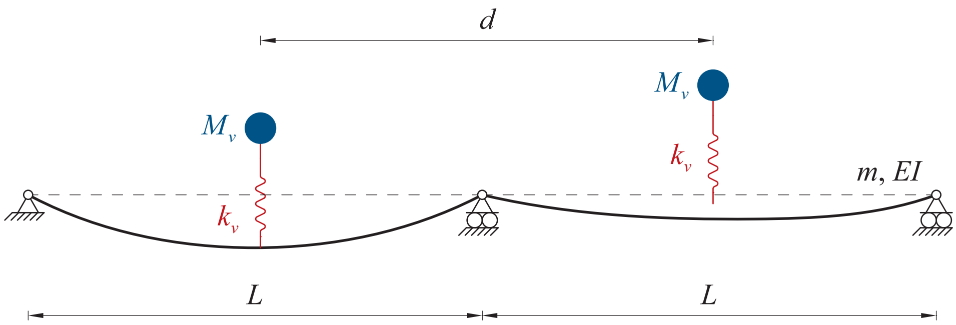

Figure 5.2. Two simply supported spans subjected to a set of moving sprung masses.

The sprung masses move at a constant speed $v = 115$ m/s. The time step is $\Delta t = 0.001$ s and the total number of time steps is 900. The dynamic analyses are first performed using a node-to-segment contact element that does not include an Hertzian spring. The vertical accelerations at the midpoint of the first span, calculated using the direct method, are plotted in Fig. 5.3a for $\alpha = 0$, $\beta = 0.25$ and $\gamma = 0.5$, and in Fig. 5.3b for $\alpha = -0.1$, $\beta = 0.3025$ and $\gamma = 0.6$.

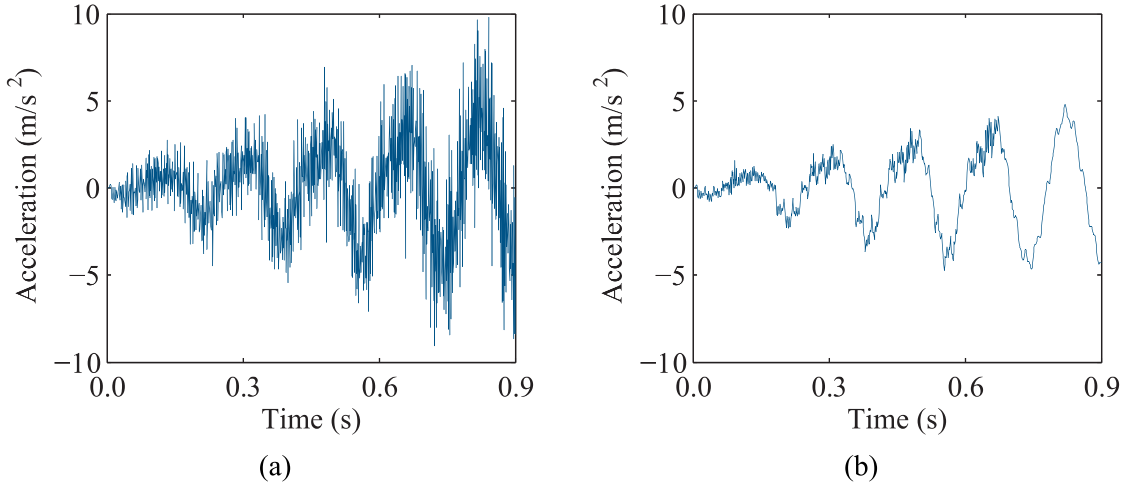

Figure 5.3. Vertical acceleration at the midpoint of the first span considering (a) $\alpha = 0$ and (b) $\alpha = -0.1$.

A nonzero value of the α parameter is useful for controlling the spurious high-frequency content shown in Fig. 5.3a. Hence, the analyses presented in the remainder of this section are performed using $\alpha = -0.1$. The vertical displacements and accelerations at the midpoint of the first span, obtained with both the direct method and ANSYS, are plotted in Figs. 5.4 and 5.5. The vertical displacements of the first and fourth sprung masses are compared in Fig. 5.6. The results obtained with the direct method and ANSYS show an excellent agreement. The slight differences observed in Fig. 5.5 may be due to the fact that the contact elements available in ANSYS use linear interpolation for the displacements and the contact elements presented in this work use cubic functions.

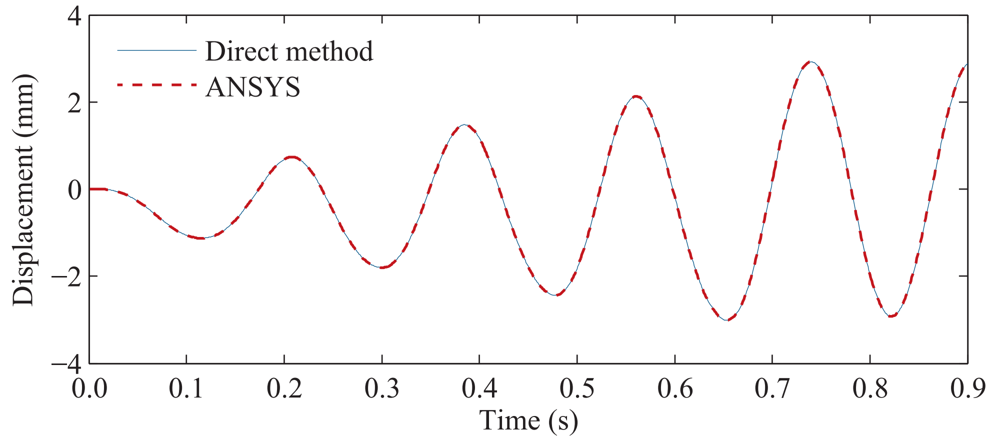

Figure 5.4. Vertical displacement at the midpoint of the first span.

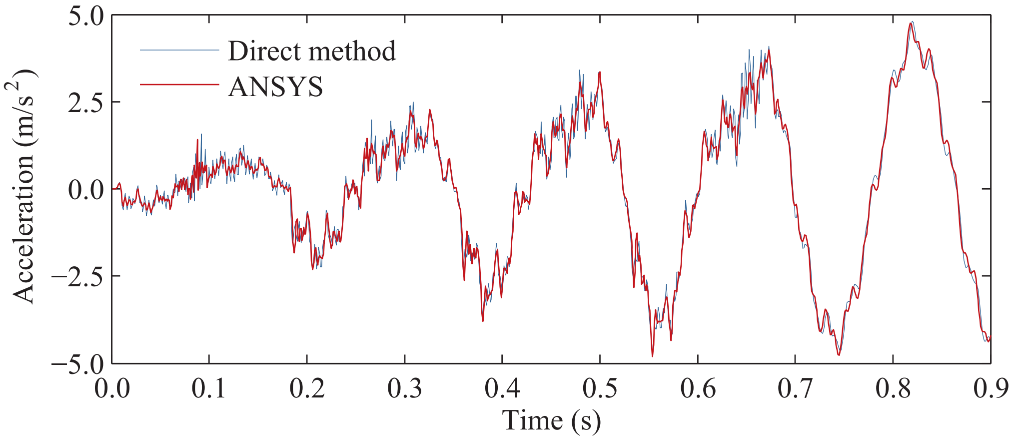

Figure 5.5. Vertical acceleration at the midpoint of the first span.

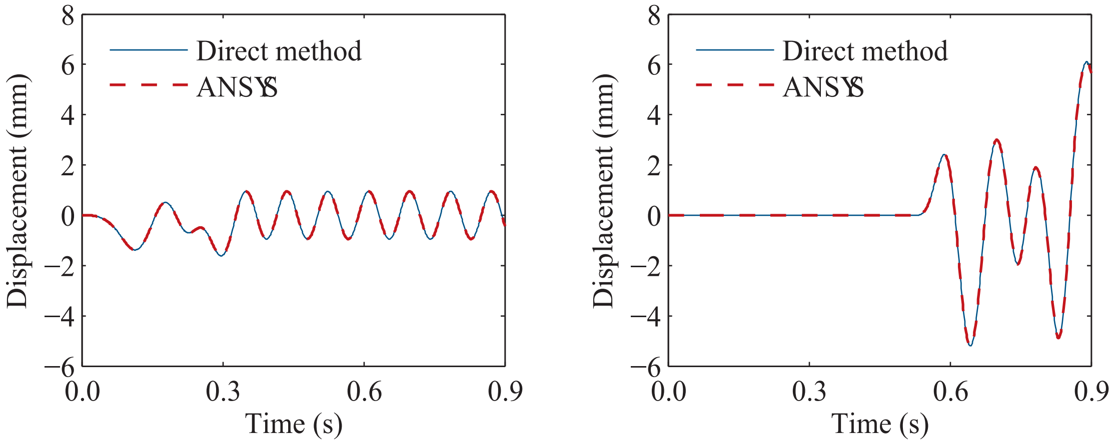

(a) (b)

Figure 5.6. Vertical displacement of the (a) first and (b) fourth sprung masses.

Finally, the contact forces of the first and fourth sprung masses are plotted in Fig. 5.7. The results obtained with the direct method perfectly match the corresponding ANSYS solutions obtained using the classical Lagrange multiplier method. The first sprung mass is in contact with the beam during the analysis period, since the motion of the beam is not large enough to cause a separation. However, as can be observed in Fig. 5.7b, a null contact force in the fourth sprung mass indicates the occurrence of a separation. Therefore, it can be concluded that the proposed methodology is capable of accurately modelling the contact and separation between two bodies.

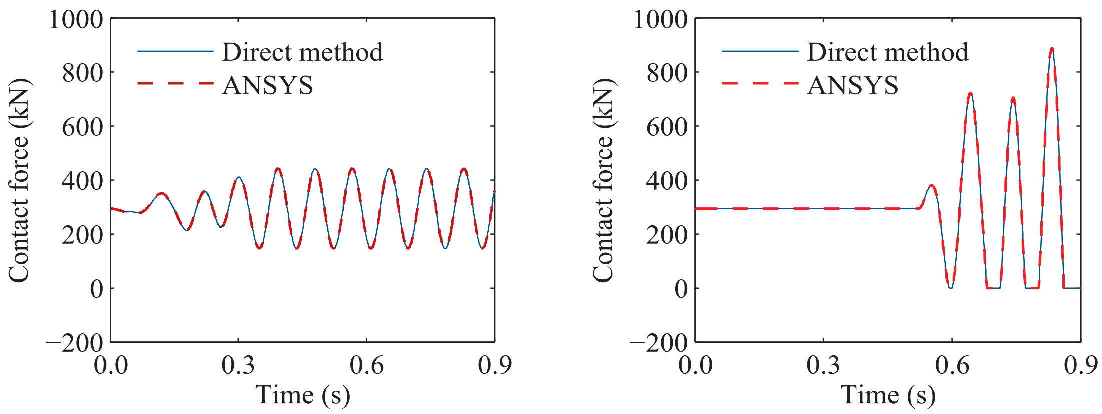

(a) (b)

Figure 5.7. Normal contact force of the (a) first and (b) fourth sprung masses.

The dynamic interaction between the sprung masses and the simply supported spans is now analysed considering the Hertzian contact spring. The Hertz constant K_h is calculated assuming the wheelset centred on the track and is equal to $7.958\times10^{7}\ \mathrm{kN/m}^{3/2}$ (see

Section 3.4). The linearized value of the contact stiffness around a static wheel load of 294300 N (30 t) is equal to 1.846×10^6 kN/m. The analyses are performed using the direct method. The vertical displacements of the first and fourth contact points, calculated without a contact spring and with a linear spring, are plotted in Fig. 5.8. The black vertical dashed lines mark the instants when the first and fourth sprung masses reach the end of the second span and the beginning of the rigid beam. As expected, the displacements of the contact points obtained using the linear spring are higher than those calculated without a spring. The corresponding contact forces are shown in Fig. 5.9. A significant difference between the forces calculated using the two different node-to-segment contact elements can be observed.

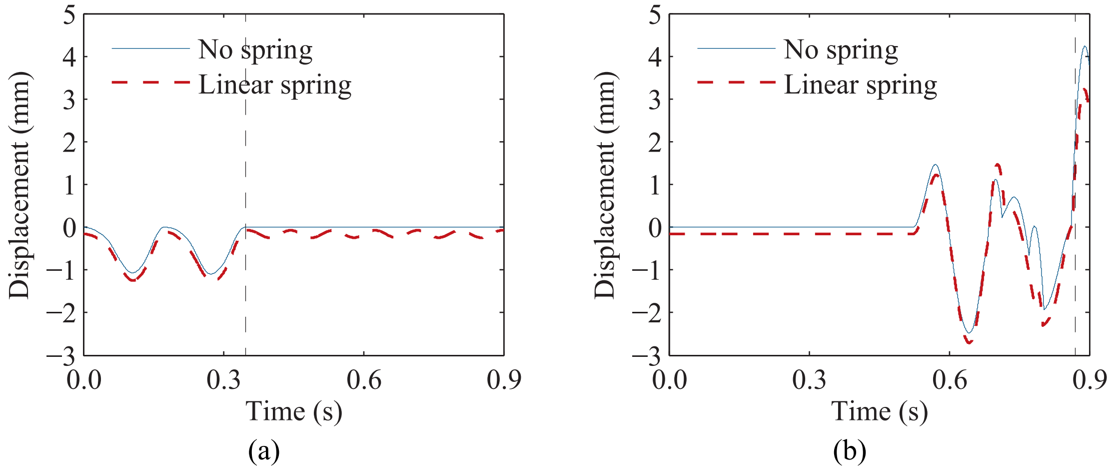

Figure 5.8. Vertical displacements of the (a) first and (b) fourth contact points.

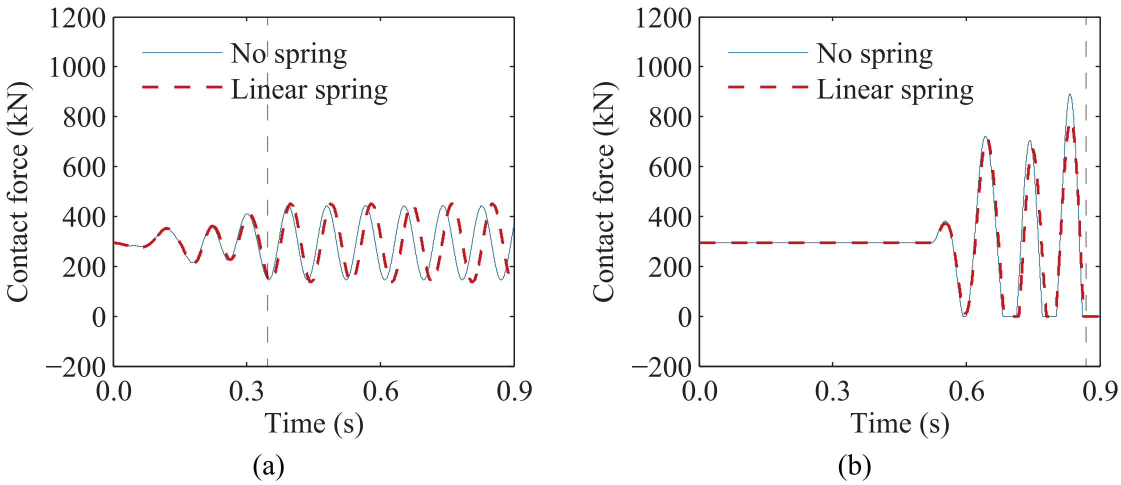

Figure 5.9. Normal contact forces of the (a) first and (b) fourth sprung masses.

The vertical displacements and contact forces of the first and fourth contact points, calculated assuming a linear and nonlinear force-deflection relationships, are plotted in

Figs. 5.10 and 5.11, respectively. There is also a slight difference between the displacements calculated using the two force-deflection relationships, but the contact forces show a very good agreement. It can be concluded that using the enhanced node-to-segment contact element proposed here leads to more accurate results. The influence of assuming a linear or nonlinear relationship is further analysed in Chapters 6 and 7 using a railway track and viaduct.

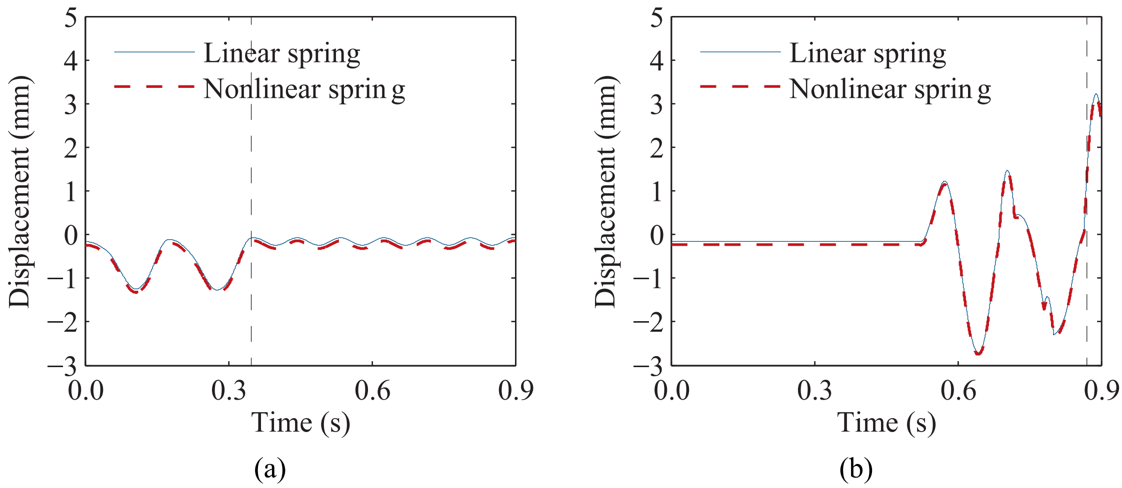

Figure 5.10. Vertical displacements of the (a) first and (b) fourth contact points.

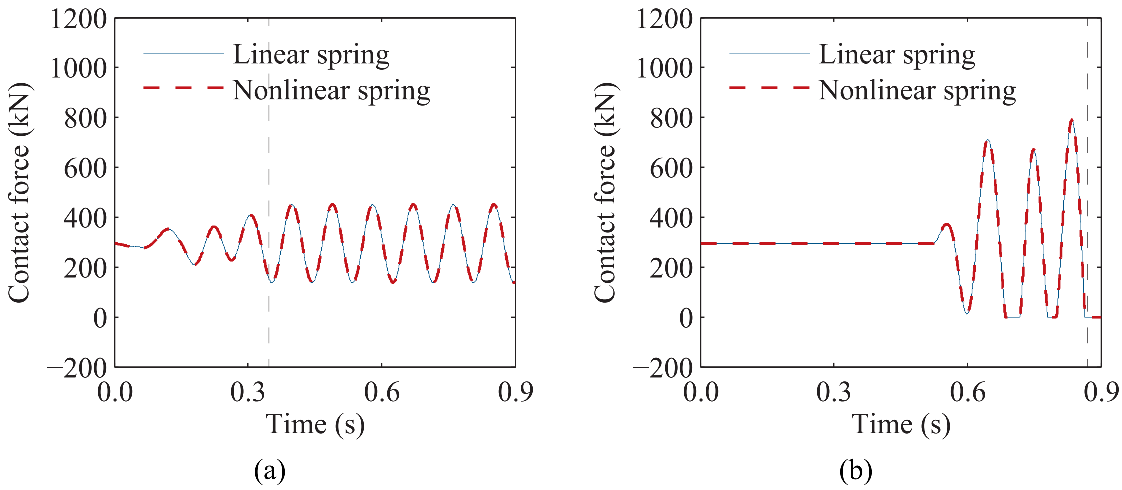

Figure 5.11. Normal contact forces of the (a) first and (b) fourth sprung masses.

5.3.2 Two simply supported spans modelled with 3D solid elements

The previous example demonstrates the excellent accuracy of the proposed algorithm. In order to assess the computational efficiency of the algorithm the two simply supported spans are now modelled with 16,000 eight-node solid elements (2×80×10×10), as shown in Fig. 5.12. This model has 58,696 unconstrained d.o.f. and a square cross-section of width $b = 2.45$ m, in correspondence with the geometrical properties of the previous beams. Since the sprung masses move along a path that is coincident with the edges of the solid elements, node-to-segment contact elements are used.

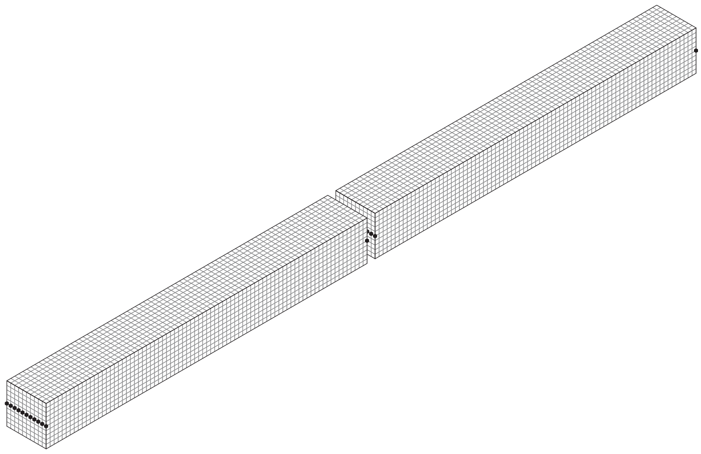

Figure 5.12. Two simply supported spans modelled with 3D solid elements.

The vertical displacement at the midpoint of the first span is plotted in Fig. 5.13, while the vertical displacement of the fourth sprung mass is shown in Fig. 5.14. The contact force of the fourth sprung mass is depicted in Fig. 5.15. Once more the results obtained with the proposed methodology show an excellent agreement with the corresponding ANSYS solutions.

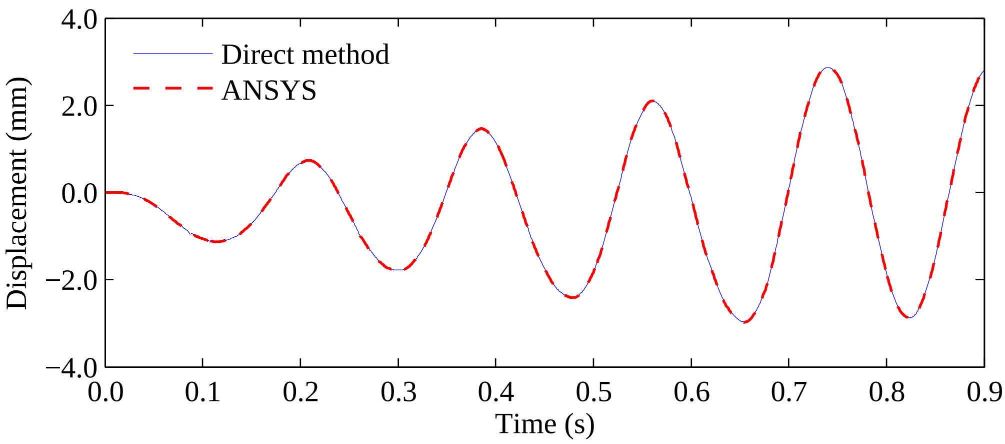

Figure 5.13. Vertical displacement at the midpoint of the first span.

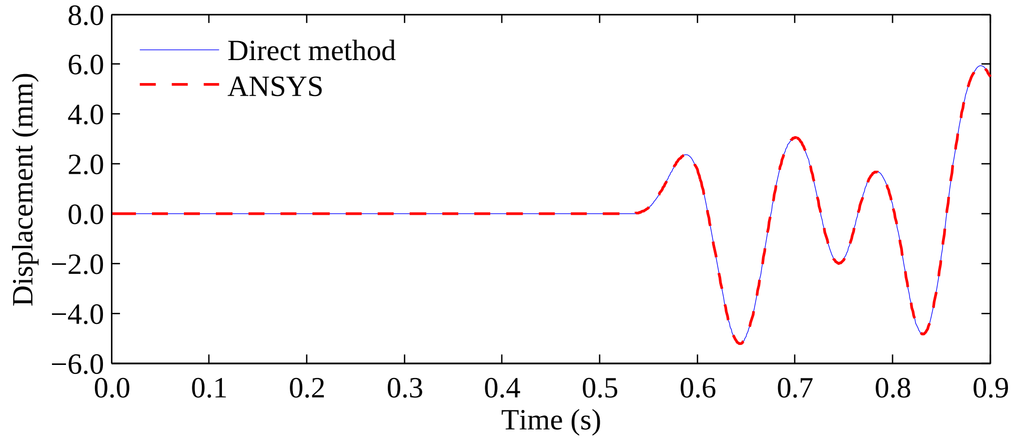

Figure 5.14. Vertical displacement of the fourth sprung mass.

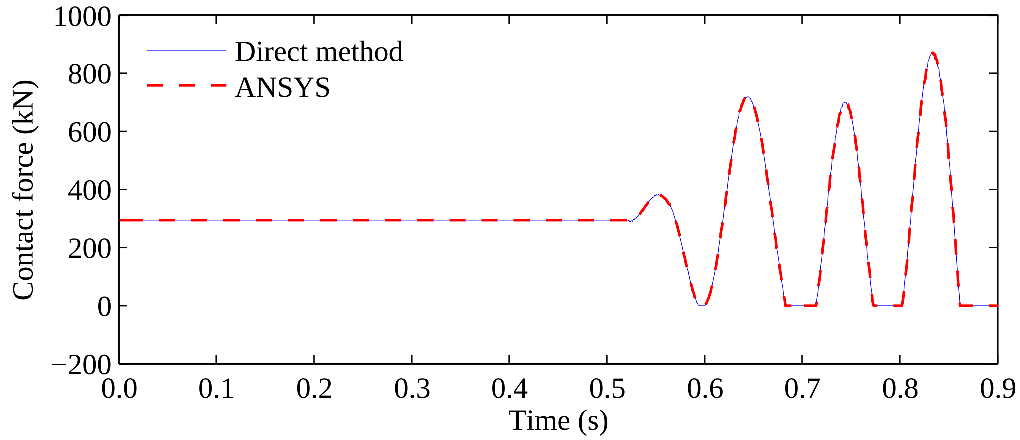

Figure 5.15. Normal contact force of the fourth sprung mass.

In the analysis executed with MATLAB, a total of 1026 iterations have been performed with a maximum of 2 iterations in the time steps that require a change in the contact status. A convergence tolerance of $\varepsilon = 10^{-6}$ is used (see Section 5.2.3). All the calculations have been performed using a workstation with an Intel Xeon E5620 dual core processor running at 2.40 GHz. For a more accurate comparison, the calculations in ANSYS and MATLAB have been performed using a single execution thread. The elapsed time is 16,623 s using ANSYS and 261 s using the direct method with the optimised block factorisation algorithm, which is about 64 times faster.

5.3.3 Inclined rigid beam

The inclined rigid beam shown in Fig. 5.16 is subjected to a moving two-axle vehicle. The frame of the vehicle is also rigid. A horizontal load of 20 N is applied to each axle of the vehicle. This example is only used to test that the MATLAB code works with inclined beams; the geometrical properties and applied loads are not typical of railway applications. The Hertzian contact spring with nonlinear force-deflection relationship is used (see Section 5.3.1). In this example, using this spring or a rigid contact leads to the same results; the contact spring is only used to test the MATLAB code associated with this type of element.

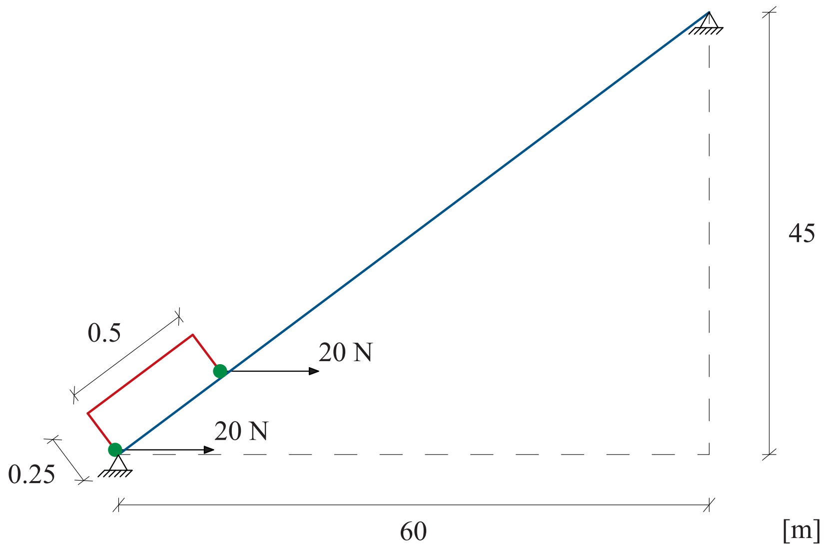

Figure 5.16 – Test example consisting of a rigid beam subjected to a two-axle vehicle.

The time step is $\Delta t = 0.01$ s and the total number of time steps is 500. The following parameters for the HHT-α method are considered: $\beta = 0.25$, $\gamma = 0.5$ and $\alpha = 0$. The analytical solutions for the displacements and contact forces of the two contact points and the corresponding finite element approximations based on the direct method are plotted in Figs. 5.17 to 5.19.

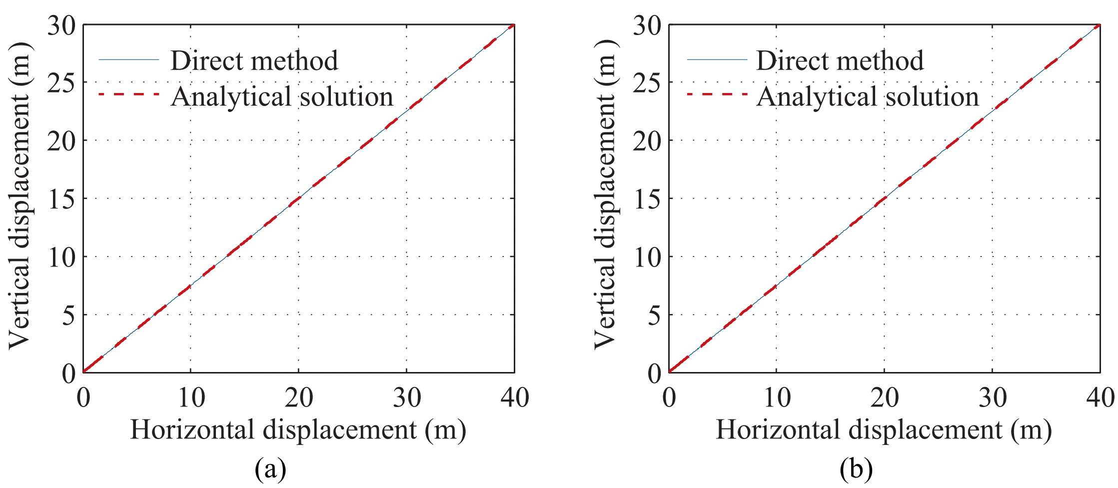

Figure 5.17. Displacements of the (a) front and (b) rear contact points.

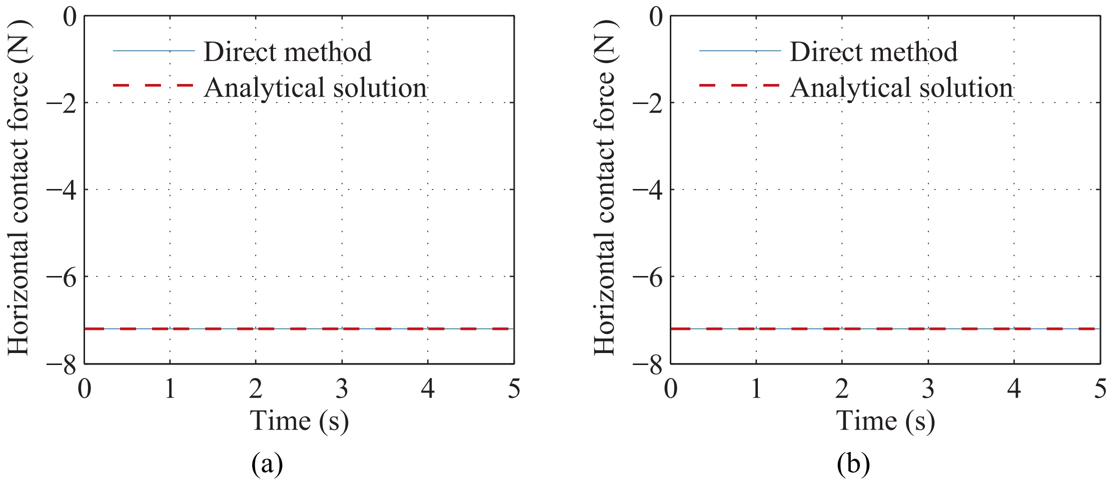

Figure 5.18. Horizontal contact forces of the (a) front and (b) rear contact points.

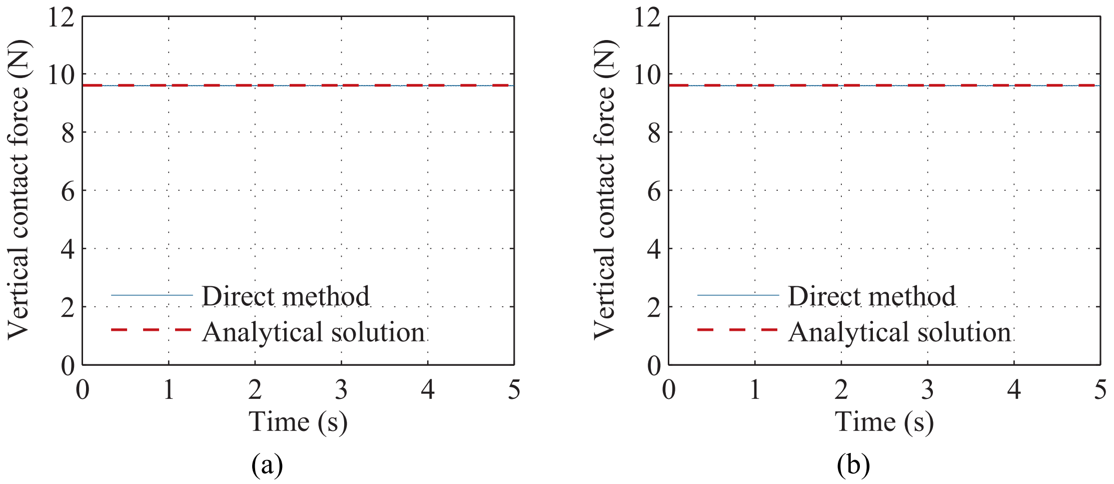

Figure 5.19. Vertical contact forces of the (a) front and (b) rear contact points.

An excellent agreement can be observed between all the numerical and analytical results.

5.4 CONCLUDING REMARKS

An accurate, efficient and robust method for analysing the nonlinear vehicle-structure interaction is presented. The direct method is used to formulate the governing equations of motion and to impose the constraint equations that relate the displacements of the contact node to the displacements of the corresponding target element. The accuracy of the method has been confirmed using three numerical examples; all the results calculated with the direct method have been validated against those obtained with ANSYS and a good agreement has been found. The proposed method uses an optimised block factorisation algorithm to solve the system of linear equations. The numerical examples used here demonstrate the efficiency of the developed algorithm. The calculations performed using the direct method have been 64 times faster than those performed with ANSYS.

Since in the present method the tangential creep forces acting at the interface are not considered, the lateral vehicle-structure interaction cannot be taken into account. To determine these forces, the material and geometric properties of the wheel and rail, and also the relative velocity between the two bodies at the contact point have to be considered. The extension of the present method to three-dimensional contact problems is presented in Montenegro (2015) and Montenegro *et al.* (2015).

6 MODELLING AND DYNAMIC ANALYSIS OF THE TRAIN-TRACK SYSTEM

6.1 INTRODUCTION

The numerical modelling of the train-track system is addressed here. Special focus is given to the development and validation of the numerical models to guarantee that the discussion and interpretation of the results are not affected by inaccuracies of the modelling process. The train and track models are developed using the ANSYS finite element software (2014a).

The numerical model of the Korean high-speed train (KHST) is described in Section 6.2. It consists of an articulated train with a power car at each end connected to 16 passenger cars by means of two motorised trailers. Since the analysis of the train-track interaction can be very complex, a simple vehicle model based on the KHST is also developed to facilitate the interpretation of the results and the detection of errors and inaccuracies.

The numerical modelling of the ballasted track is explained in Section 6.3. The geometrical and mechanical properties of the ballasted track of the Alverca viaduct are adopted here. This viaduct is located on the Northern Line of the Portuguese railway network and is used in Chapter 7. The response of the track in the frequency domain is also analysed in Section 6.3. The ballast and sleepers are modelled with 3D solid elements and a very refined mesh is initially used. The number of finite elements is optimised by comparing the track receptance of the initial model with those of the models with fewer elements.

In order to analyse the passage of the KHST over a bridge or viaduct, a significant length of track must be modelled before and after the structure to support the vehicle. The total length between the first and last axles of the KHST is 380.15 m (see Section 6.2.1). A 2D track model is used before and after the 3D track in order to avoid a prohibitive computational cost of the dynamic analyses. The influence of using a 2D rigid or flexible track model, the force-deflection relationship considered for the Hertzian contact spring and the numerical dissipation provided by the time integration scheme are studied in Section 6.4. The results calculated using the direct method and the ANSYS software are also compared in this section, as well as the efficiency of both approaches.

6.2 NUMERICAL MODELLING OF THE KHST

6.2.1 General description

The Korean high-speed train is used in this chapter for analysing the dynamic train-track interaction. A high-speed train is chosen to analyse scenarios characterised by large dynamic amplifications. In railway structures, this kind of effects generally occurs at high speeds, where the risk of resonance is higher. This phenomenon can be a major factor in the design and maintenance of high-speed railway lines (Goicolea *et al.*, 2006). The KHST is designed for a maximum speed of 350 km/h (Kwark *et al.*, 2004). There are few published articles with all the geometrical and mechanical properties necessary to build a 3D model of a high-speed train. This train has been chosen because it is similar to the French TGV.

The KHST has been introduced in South Korea under a technology transfer agreement between Alstom and the South Korean companies and therefore has several similarities with the French TGV. Most vehicle designs are based on a pair of two-axle bogies on each carbody. However, the KHST is an articulated train that has two-axle bogies positioned between the car bodies. The model adopted in this study is composed of a power car at each end connected to 16 passenger cars by means of two motorised trailers (see Fig. 6.1). The train has a total of 23 bogies and 46 axles; the axle load at each wheelset is about 17 t. The total length between first and last axles is 380.15 m. Lee and Kim (2010) developed 3D vehicle models composed of 7, 10, 16 and 20 cars for analysing the dynamic interaction between high-speed trains and bridges and concluded that the smaller models composed of 7 and 10 cars may lead to less accurate results, especially at resonance speeds.

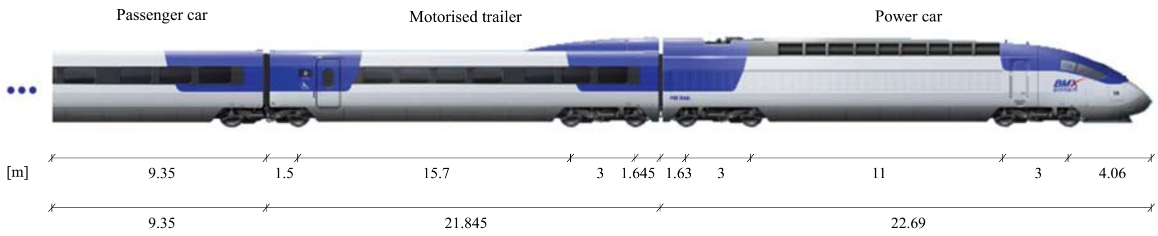

Figure 6.1 – Main dimensions of the KHST.

6.2.2 Finite element model

The finite element model of the KHST is developed in ANSYS. The vehicle body, wheelsets and bogie frames schematically illustrated in Fig. 6.2 are represented by rigid bodies connected with spring-dampers in the three coordinate directions. The meaning of the symbols is explained in Tables 6.1 to 6.3. The rigid bodies are modelled in ANSYS using beam elements with a large value of the axial and flexural stiffness. The axes x, y and z of the global coordinate system correspond to the longitudinal, lateral and vertical directions, respectively.

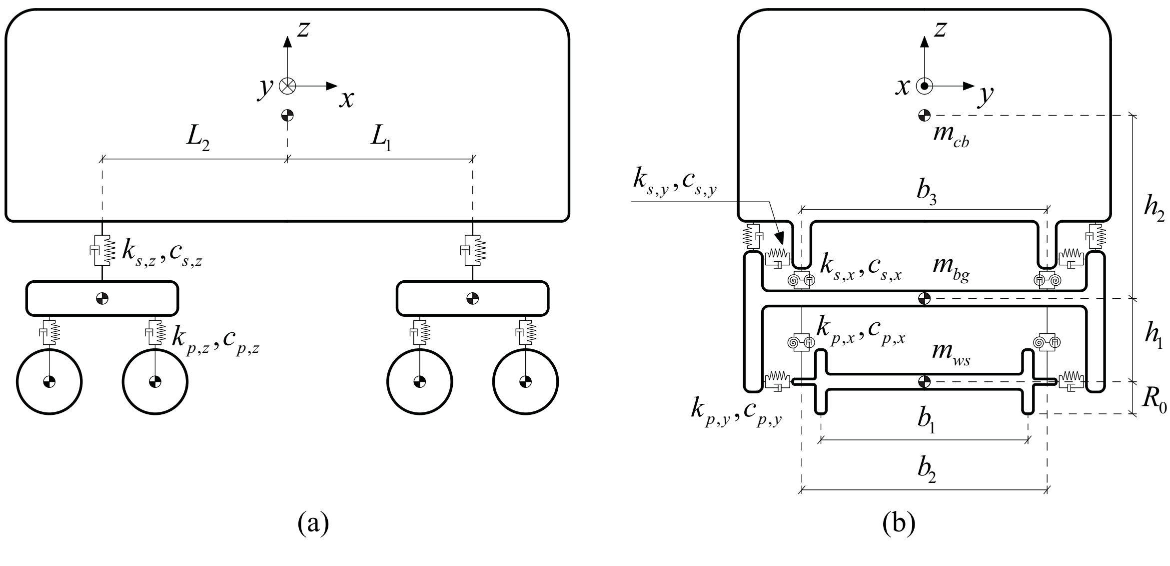

Figure 6.2 – Finite element model of the KHST: (a) lateral view and (b) front view.

The mechanical and geometrical properties are based on Kwark *et al.* (2004) and Lee and Kim (2010) and are listed in Tables 6.1 to 6.3. The values adopted for the masses of the carbody of the motorised trailer and passenger car have been modified to obtain an axle load of 17 t, as given in Shin *et al.* (2010). The longitudinal and lateral damping of the primary suspensions provided by Kwark *et al.* (2004), as well as the longitudinal damping of the secondary suspensions, are equal to zero. Since only the vertical vehicle–structure interaction is considered in the present work, these null values are acceptable. The nominal rolling radius of the wheel r_0 is equal to 0.46 m.

Table 6.1 –Mechanical and geometrical properties of the power car.

Parameter	Value	Unit
Mass of the carbody (m_{cb})	54960	kg
Moment of inertia of the carbody ($I_{cb,x}$, $I_{cb,y}$, $I_{cb,z}$)	59.4×10^3, 1132.8×10^3, 1112.9×10^3	kg m^2
Mass of the bogie (m_{bg})	2420	kg
Moment of inertia of the bogie ($I_{bg,x}$, $I_{bg,y}$, $I_{bg,z}$)	1645, 2593, 3068	kg m^2
Mass of the wheelset (m_{ws})	2050	kg
Moment of inertia of the wheelset ($I_{ws,x}$, $I_{ws,y}$, $I_{ws,z}$)	1030, 0.8, 1030	kg m^2
Stiffness of the primary suspension ($k_{p,x}$, $k_{p,y}$, $k_{p,z}$)	40000, 9000, 1250	kN/m
Damping of the primary suspension ($c_{p,x}$, $c_{p,y}$, $c_{p,z}$)	0, 0, 10	kN s/m
Stiffness of the secondary suspension ($k_{s,x}$, $k_{s,y}$, $k_{s,z}$)	303, 303, 1270	kN/m
Damping of the secondary suspension ($c_{s,x}$, $c_{s,y}$, $c_{s,z}$)	0, 100, 20	kN s/m
Dimensions L_1, L_2, b_1, b_2, b_3, h_1, h_2	7, 7, 1.435, 2, 2.46, 0.1, 1.16	m

Table 6.2 –Mechanical and geometrical properties of the motorised trailer.

Parameter	Value	Unit
Mass of the carbody (m_{cb})	39770	kg
Moment of inertia of the carbody ($I_{cb,x}$, $I_{cb,y}$, $I_{cb,z}$)	55.5×10^3, 1641.51×10^3, 1694.89×10^3	kg m^2
Mass of the bogie (m_{bg})	2514	kg
Moment of inertia of the bogie ($I_{bg,x}$, $I_{bg,y}$, $I_{bg,z}$)	2070, 3260, 3860	kg m^2
Mass of the wheelset (m_{ws})	2050	kg
Moment of inertia of the wheelset ($I_{ws,x}$, $I_{ws,y}$, $I_{ws,z}$)	1030, 0.8, 1030	kg m^2
Stiffness of the primary suspension ($k_{p,x}$, $k_{p,y}$, $k_{p,z}$)	40000, 9000, 1250	kN/m
Damping of the primary suspension ($c_{p,x}$, $c_{p,y}$, $c_{p,z}$)	0, 0, 10	kN s/m
Stiffness of the secondary suspension ($k_{s,x}$, $k_{s,y}$, $k_{s,z}$)	100, 150, 370	kN/m
Damping of the secondary suspension ($c_{s,x}$, $c_{s,y}$, $c_{s,z}$)	0, 30, 20	kN s/m
Dimensions L_1, L_2, b_1, b_2, b_3, h_1, h_2	5.977, 12.723, 1.435, 2, 2.46, 0.1, 0.975	m

Table 6.3 –Mechanical and geometrical properties of the passenger car.

Parameter	Value	Unit
Mass of the carbody (m_{cb})	26950	kg
Moment of inertia of the carbody ($I_{cb,x}$, $I_{cb,y}$, $I_{cb,z}$)	33.94×10^3, 971.81×10^3, 971.81×10^3	kg m^2
Mass of the bogie (m_{bg})	3050	kg
Moment of inertia of the bogie ($I_{bg,x}$, $I_{bg,y}$, $I_{bg,z}$)	2030, 3200, 3790	kg m^2
Mass of the wheelset (m_{ws})	2000	kg
Moment of inertia of the wheelset ($I_{ws,x}$, $I_{ws,y}$, $I_{ws,z}$)	1030, 0.8, 1030	kg m^2
Stiffness of the primary suspension ($k_{p,x}$, $k_{p,y}$, $k_{p,z}$)	55000, 11000, 800	kN/m
Damping of the primary suspension ($c_{p,x}$, $c_{p,y}$, $c_{p,z}$)	0, 0, 6	kN s/m
Stiffness of the secondary suspension ($k_{s,x}$, $k_{s,y}$, $k_{s,z}$)	100, 170, 303	kN/m
Damping of the secondary suspension ($c_{s,x}$, $c_{s,y}$, $c_{s,z}$)	0, 0, 0	kN s/m
Dimensions L_1, L_2, b_1, b_2, b_3, h_1, h_2	8.926, 9.774, 1.435, 2, 2.46, 0.1, 1.063	m

Two different approaches can be used to generate the numerical model in ANSYS: solid modelling or direct generation. With solid modelling, the geometry is first defined in terms of keypoints, lines, areas and volumes, and then the nodes and elements are generated automatically using meshing algorithms. The program has several mesh commands that can be used to control the size and shape of the elements. In the direct generation approach, the location of every node and the connectivity of every element have to be defined manually by the user. Therefore the vehicle model has been developed using the solid modelling approach, which is the most powerful and versatile one.

Since the solid modelling features of ANSYS are known to have robustness issues (ANSYS®, 2014b), the solid model of the vehicle has been created using AutoCAD® (2012), which is a better CAD platform. The geometry of the rigid bodies and the spring-dampers are represented using lines, whereas the centre of mass of each body is defined using keypoints. Entities with similar attributes are grouped into the same layer and saved as a separate IGES file. These files are then imported by ANSYS and assigned the appropriate element attributes: element type and real constant set (spring constant, damping coefficient, concentrated mass or rotary inertia). This approach proved to be very efficient and versatile for creating, validating and updating the model of the vehicle.

The carbody, bogie frame and wheelset are composed of a structural mass, modelled using the ANSYS element type MASS21, and rigid beam elements, modelled using the element type BEAM188. The suspensions are modelled using the spring-damper element type COMBIN14. Since only the vertical vehicle–structure interaction is considered in the present thesis and the main objective is not to thoroughly analyse the vehicle behaviour, a linear elastic model is assumed for the suspensions. Two parallel longitudinal dampers between the car bodies are used to avoid low damped vibration modes. These dampers are particularly important in high-speed trains where, for example, significant carbody oscillations might occur due to the aerodynamic phenomenon in tunnels (Iwnicki, 2006).

The numerical models of the power cars, motorised trailers and passenger cars are represented in Figs. 6.3 to 6.5, respectively, and the model of the bogie of the power car is depicted in more detail in Fig. 6.6. The complete model of the KHST has 1507 nodes, 2093 elements and 8374 unconstrained degrees of freedom (d.o.f).

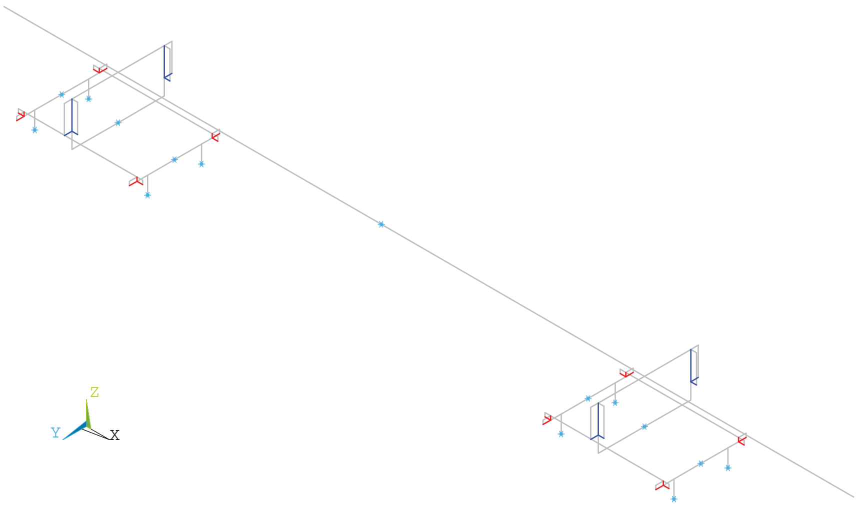

(a)

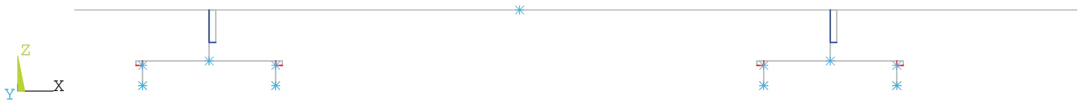

(b)

Figure 6.3 – Numerical model of the power car: (a) isometric view and (b) lateral view.

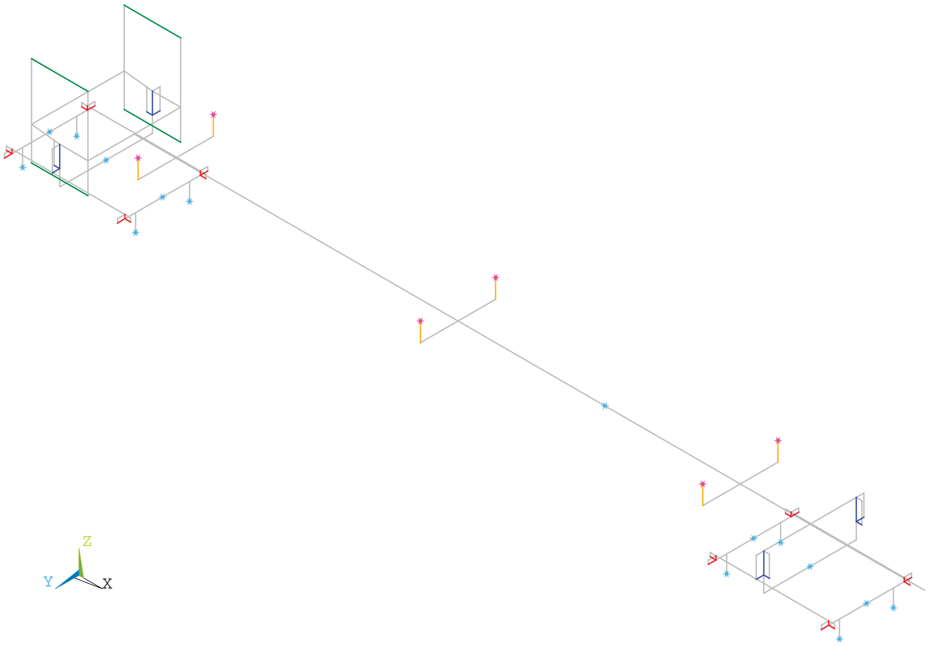

Figure 6.4 – Numerical model of the motorised trailer.

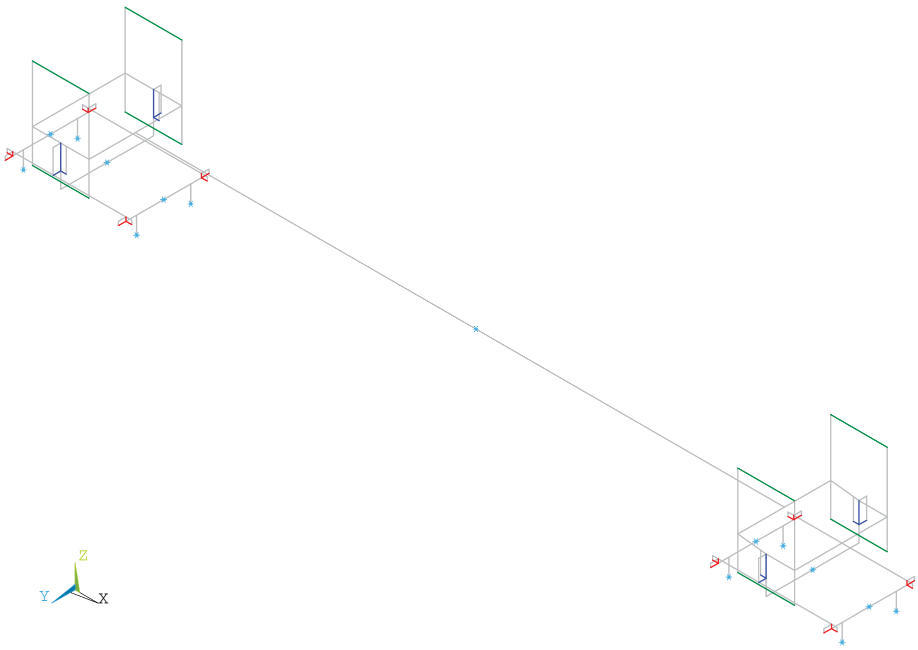

Figure 6.5 – Numerical model of the passenger car.

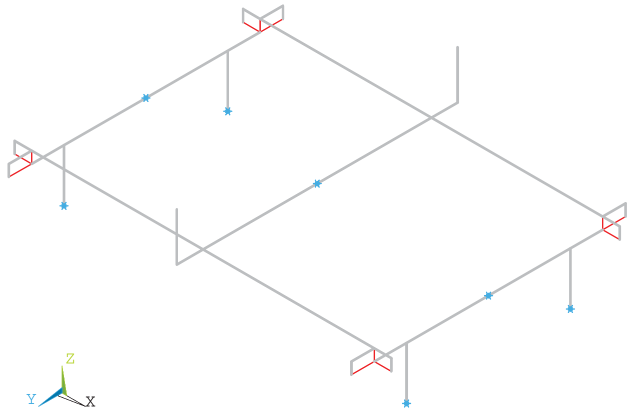

Figure 6.6 – Detailed view of the numerical model of the bogie of the power car.

The upper and lower part of the longitudinal dampers connecting the car bodies (see Fig. 6.5) have damping coefficients of 49.5 and 66 kN s/m, respectively. Since only the vertical vehicle–structure interaction is considered in the present work, the Hertz constant K_h is calculated assuming the wheelset centred on the track and is equal to 7.958×10^7 kN/m$^{3/2}$ (see Section 3.4). The linearized value of the contact stiffness around a static wheel load of 83385 N (8.5 t) is equal to 1.212×10^6 kN/m.

6.2.3 Static and modal analyses

The static wheel loads of the KHST have been calculated to validate the correctness of the structural masses and constraints. A linear static analysis has been performed with ANSYS to obtain the corresponding numerical values. The theoretical values have been calculated by considering the static equilibrium equations of the rigid bodies of the train. An excellent agreement between the theoretical and numerical values has been obtained.

A modal analysis is performed using ANSYS to understand the dynamic behaviour of the KHST. The first vibration modes and natural frequencies of the train and power car are represented in Figs. 6.7 and 6.8, respectively.

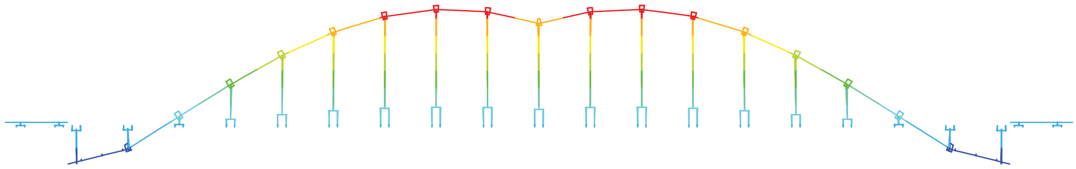

$f = 0.69$ Hz

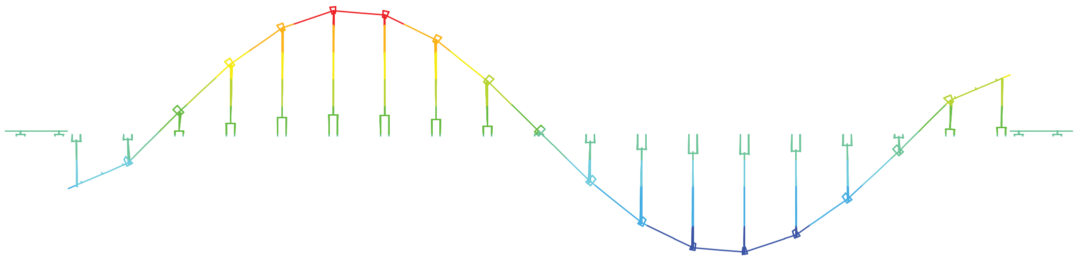

$f = 0.70$ Hz

Figure 6.7 – Vibration modes and natural frequencies of the train.

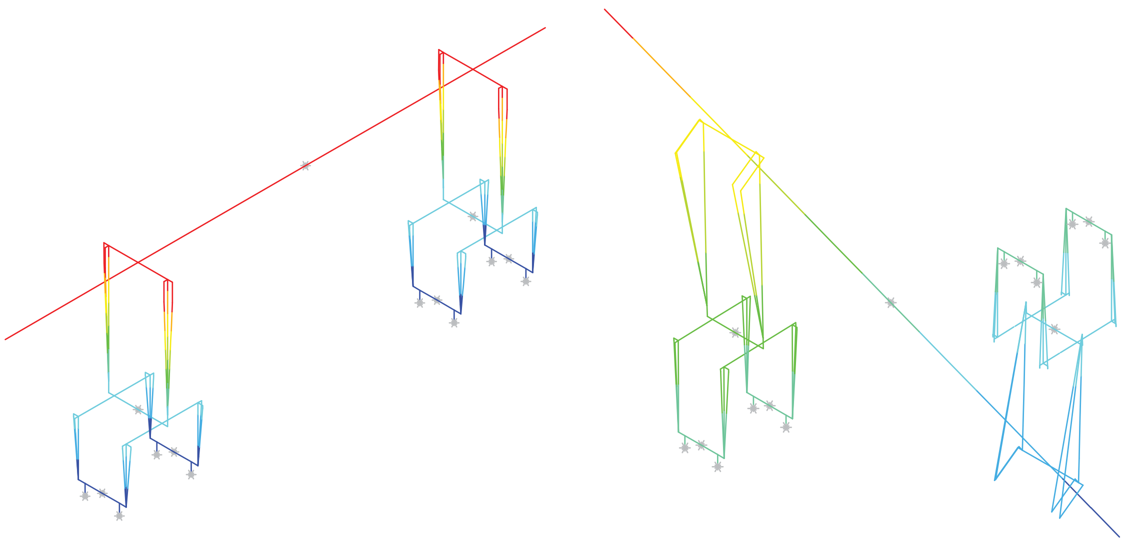

(a) $f = 1.24$ Hz (b) $f = 1.90$ Hz

Figure 6.8 – Vibration modes and natural frequencies of the power car: (a) bouncing and (b) pitching.

The vibration modes and natural frequencies associated with the bouncing, pitching and rolling movements of the bogies of the power car are represented in Fig. 6.9.

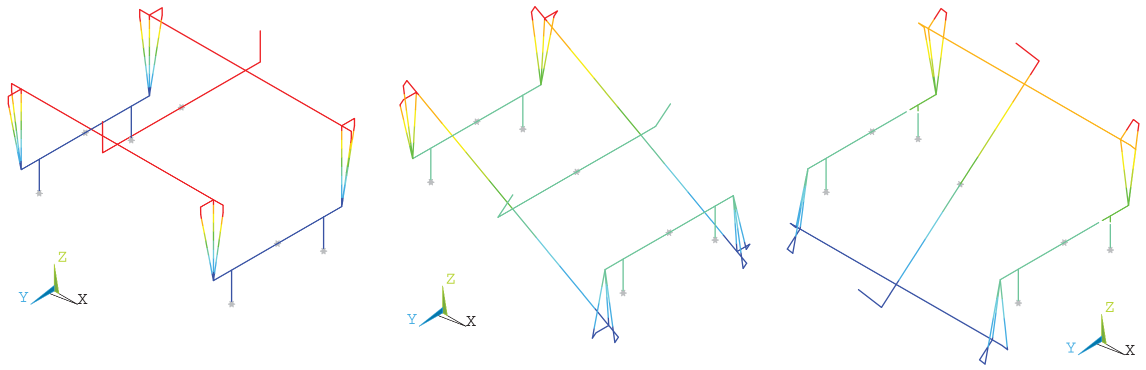

(a) f = 8.99 Hz (b) f = 10.50 Hz (c) f = 11.71 Hz

Figure 6.9 – Vibration modes and natural frequencies of the bogie of the power car: (a) bouncing, (b) pitching and (c) rolling.

The unsprung masses of the vehicle greatly influence the forces and noise generated at the contact interface. Reducing the unsprung masses generally leads to lower wheel-rail interaction forces. These forces also depend on the contact stiffness, rail mass and track stiffness. Figure 6.10 shows the mode shape and frequency corresponding to the vibration of the unsprung masses of the power car. This vibration mode depends only on the unsprung masses and contact stiffness and not on the track properties. Nevertheless, it is an important indicator of the dynamic behaviour of the wheel-rail contact interface.

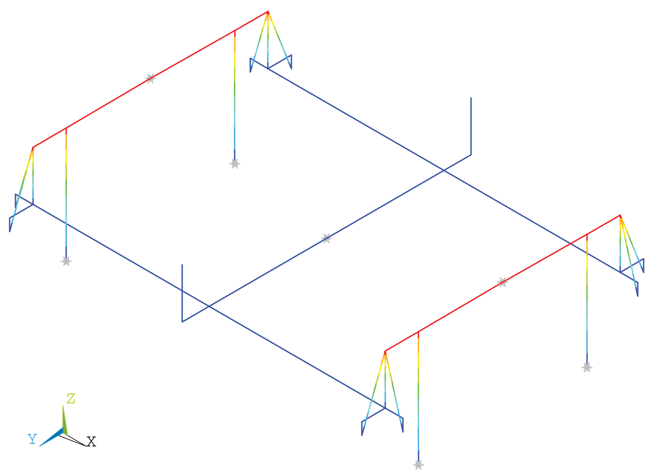

f = 172.2 Hz

Figure 6.10 – Vibration mode of the unsprung masses of the power car.

6.2.4 Simplified model of the KHST

Since the train-track interaction can be very complex, a validation of the numerical models used is very important. Thus, a simple one-eighth model based on the KHST (see

Fig. 6.11) has been developed to facilitate the detection of errors and inaccuracies. The carbody, bogie frame and wheelset are modelled as structural masses using the ANSYS element type MASS21, and the suspensions are modelled using the spring-damper element type COMBIN14. The mechanical properties listed in Table 6.4 are based on those of the power car.

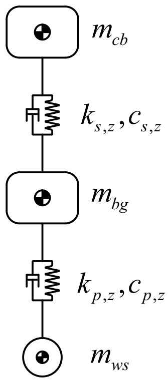

Figure 6.11 – Simplified model of the KHST.

Table 6.4 –Mechanical properties of the simplified model of the KHST.

Parameter	Value	Unit
Mass of 1/8 carbody (m_{cb})	6870	kg
Mass of 1/4 bogie (m_{bg})	605	kg
Mass of 1/2 wheelset (m_{ws})	1025	kg
Stiffness of the primary suspension ($k_{p,z}$)	1250	kN/m
Damping of the primary suspension ($c_{p,z}$)	10	kN s/m
Stiffness of the secondary suspension ($k_{s,z}$)	635	kN/m
Damping of the secondary suspension ($c_{s,z}$)	10	kN s/m
Hertzian contact stiffness	1.212×10^6	kN/m

The vibration modes associated with the bouncing of the carbody, bogie and wheelset are shown in Fig. 6.12.

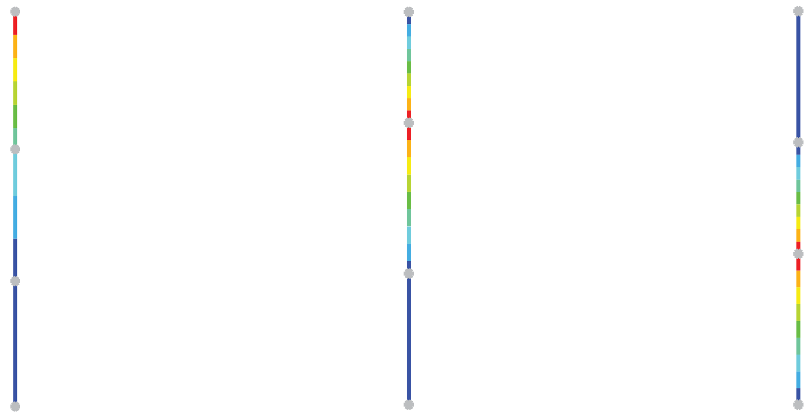

Carbody: f = 1.24 Hz   Bogie: f = 8.93 Hz   Wheelset: f = 173.2 Hz

Figure 6.12 – Vibration modes and natural frequencies of the simplified model of the KHST.

6.3 NUMERICAL MODELLING OF THE TRACK

6.3.1 General description

The ballasted track consists of rails and sleepers connected by the fastening system, which are supported by a ballast layer that guarantees the distribution of the loads to the subsoil or bridge deck. This concept has not changed significantly since the early developments of railways. Developments such as the use of concrete sleepers, continuously welded rails and heavier rail-profiles were introduced after the Second World War and are still used in highly demanding applications such as high-speed railway lines (Esveld, 2001).

The main functions of the rail are to distribute the wheel loads over the sleepers, provide guidance to the vehicle and act as an electrical conductor (Esveld, 2001). There are several types of rail profiles such as flat-bottom rail, nonstandard profile and grooved rail. The flat-bottom rail profile is based on an I-profile with a modified upper flange to provide a better support and guidance for the wheel. The track gauge is the distance between the inside of the rail heads usually measured 14 mm below the top of the rail.

The main functions of the fastening system are to transfer the wheel loads to the sleeper and filter their high frequency components, guarantee the required track gauge and rail inclination and provide electrical insulation between the rail and sleeper.

The sleeper should uniformly distribute the rail loads to the ballast bed, preserve the track gauge and rail inclination and provide electrical insulation between both rails. The sleepers can be made of concrete, timber or steel. The concrete sleepers are the most commonly used because they usually have a long service life and are less vulnerable to climate change (Esveld, 2001).

The ballast layer is composed of crushed granite that is capable of resisting significant compressive stresses, but not tensile stresses. Usually, the thickness of the ballast is between 25 and 30 cm, measured from the lower side of the sleeper, in order to guarantee that the subgrade is uniformly loaded (Esveld, 2001).

6.3.2 Geometrical and mechanical properties

The flat-bottom rail profile 60E1 (see Table 6.5) and the standard track gauge of 1.435 m are used in the Alverca viaduct (BS EN 1993-1-1, 2005; BS EN 13674-1, 2011). The number used in the rail profile name refers to the rounded weight in kilograms per meter.

Table 6.5 – Mechanical and geometrical properties of the rail profile 60E1.

Property	Value
Young’s modulus	210 GPa
Poisson’s ratio	0.3
Density	7850 kg/m^3
Cross-sectional area	76.70 cm^2
Moment of inertia about the horizontal axis	3038.3 cm^4
Moment of inertia about the vertical axis	512.3 cm^4
Torsional moment of inertia	220.9 cm^4
Centre of gravity (measured from the bottom)	80.92 mm

In order to simplify the numerical model, the rail pads are modelled with spring-dampers connected to the rail and sleeper. A stiffness of 500 MN/m and a damping of 200 kN s/m are assumed (ERRI D 214/RP 5, 1999).

The sleeper is modelled using the simplified geometry illustrated in Fig. 6.13 and its mechanical properties are presented in Table 6.6. Each sleeper has a mass of 300 kg and the adopted sleeper spacing is equal to 0.6 m.

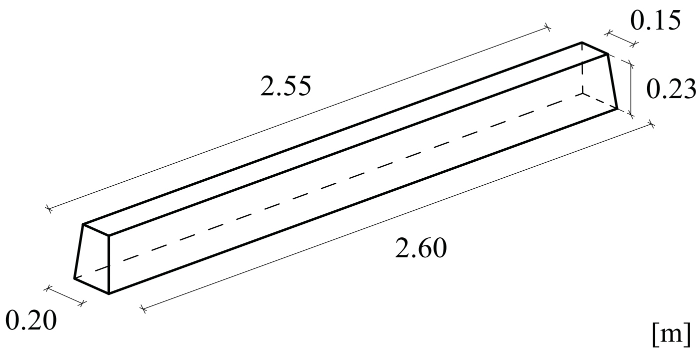

Figure 6.13 – Simplified geometry of the sleeper.

Table 6.6 – Mechanical properties of the sleeper.

Property	Value
Young's modulus	36 GPa
Poisson's ratio	0.2
Density	2890 kg/m^3

The geometry of the ballast used in the Alverca viaduct is represented in Fig. 6.14. It is assumed that the minor approximations made in the geometry of the ballast do not significantly influence the overall dynamic behaviour of the track.

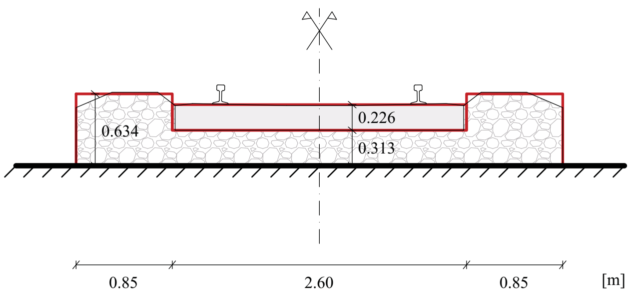

Figure 6.14 – Shape and dimensions of the ballast layer.

The mechanical properties of the ballast are defined in Malveiro *et al.* (2013) and are presented in Table 6.7.

Table 6.7 – Mechanical properties of the ballast.

Property	Value
Young's modulus	145 MPa
Poisson's ratio	0.15
Density	2039 kg/m^3

6.3.3 Finite element model

The 3D numerical model of the ballasted track is developed in ANSYS using the APDL scripting language (ANSYS®, 2014d) in order to automate all the steps involved in the model generation, such as creating the basic geometric entities, defining the attributes of the elements and meshing the solid model. The macro file containing all the commands is based on previous studies (Fernandes, 2010; Horas, 2011; Meixedo, 2012; Jorge, 2013) but has been completely rewritten using an identifier naming convention based on the Hungarian notation (McConnell, 2004) in order to improve its readability. The rail is modelled with the beam element type BEAM4 using a discretisation of 0.075 m. The rail pads are modelled using the spring-damper element type COMBIN14 and the ballast and sleepers are modelled using the solid element SOLID186. The size of the finite elements of the ballast must be selected based on the wavelength of the maximum frequency of interest in order to adequately model the wave propagation. The shortest wavelength (λ) of interest is given by

$$\lambda = \frac{C_S}{f_{\max}} \tag{6.41}$$

where C_S is the velocity of the S-waves and f_{max} is the maximum frequency of interest. The wavelength of the P-waves is longer than that of the S-waves and therefore the former are not considered in the criteria. The S-waves velocity is defined by

$$C_S = \sqrt{\frac{G}{\rho}} \tag{6.42}$$

in which ρ is the density of the ballast and G is the shear modulus of the ballast given by

$$G = \frac{E}{2(1+\nu)} \tag{6.43}$$

The maximum frequency of interest considered in the present study is associated with the bouncing of the wheelset of the KHST and is around 170 Hz (see Fig. 6.10). Therefore, for the mechanical properties of the ballast described in Table 6.7, the shortest wavelength is approximately 1 m. Kausel (2008) suggests that the size of the finite elements should be one-sixth of the shortest wavelength considered, and thus a discretisation of 0.1 m is used in the longitudinal direction of the ballast.

The numerical model of the track is shown in Fig. 6.15. Initially, a refined mesh is considered so that the results are not affected by the size of the elements. This model is optimised in Section 6.3.6 in order to reduce the number of finite elements.

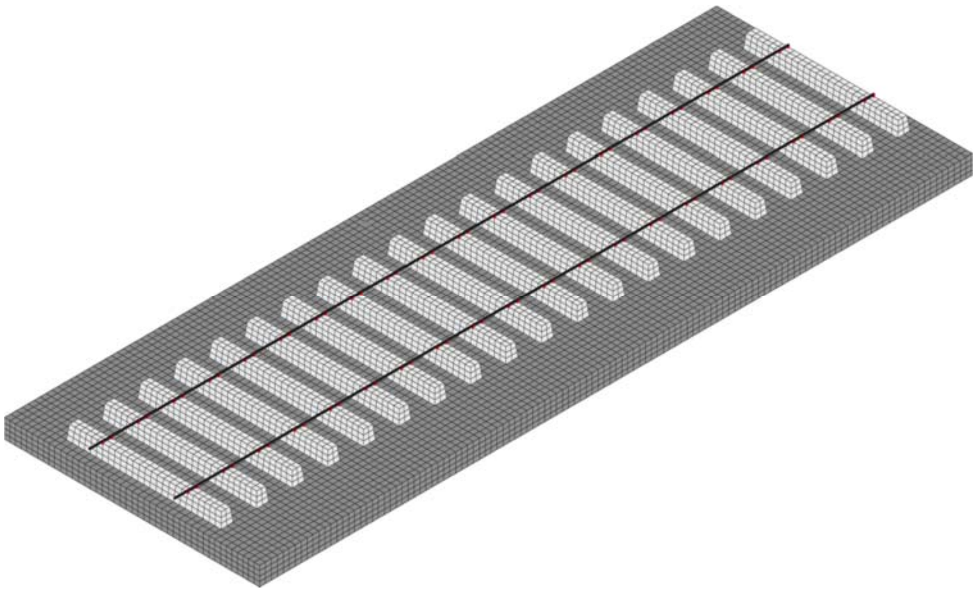

Figure 6.15 – Initial numerical model of the ballasted track.

6.3.4 Response in the frequency domain

The choice of the finite element model that is used to analyse the behaviour of the track depends on the frequency range of interest. For frequencies below 20 Hz the track can be modelled in a simplified way using spring-dampers (Popp *et al.*, 1999). For frequencies up to 250 Hz, the properties of the ballast and subsoil have a significant influence on the behaviour of the track and must be taken into account, and for frequencies up to 700 Hz the properties of the pads become important. For higher frequencies, the geometry of the rail has to be considered. In the present work, only the behaviour of the track in the low- and mid-frequency range up to 200 Hz is taken into account.

The track receptance is a good indicator of the dynamic behaviour of the track (Popp *et al.*, 1999). This function is the quotient of the displacement amplitude by the load amplitude for a standing harmonic time-variant excitation. The excitation used for calculating the track receptance is a Ricker pulse applied between sleepers and defined at time t by

$$F(t)=\left[2\left[\frac{\pi(t-t_s)}{T_R}\right]^2-1\right]\exp\left(-\left[\frac{\pi(t-t_s)}{T_R}\right]^2\right) \tag{6.44}$$

where the characteristic period T_R is 0.005 s and the time shift t_s is 0.05 s. The time history and Fourier transform of this wavelet are represented in Fig. 6.16. The time step is $\Delta t = 5\times10^{-4}$ s and the total number of time steps is 2048.

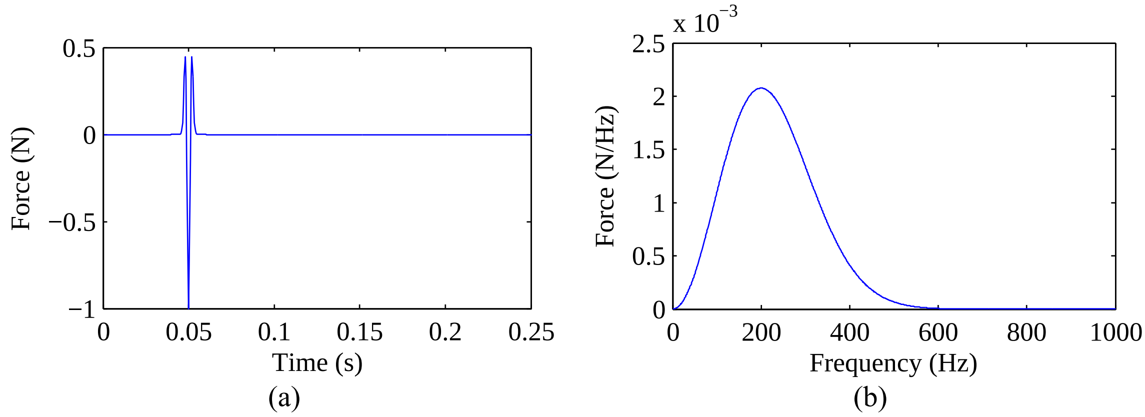

Figure 6.16 – Ricker pulse: (a) time history and (b) frequency content.

The track receptance of the initial numerical model of the track (see Fig. 6.15) is shown in Fig. 6.17. The shape of the function is similar to that found in Popp *et al.* (1999).

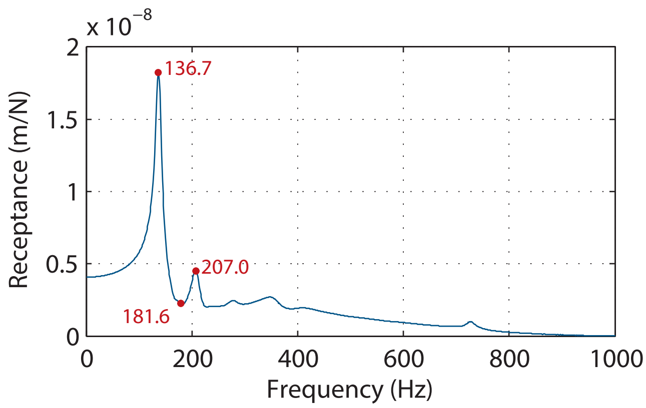

Figure 6.17 – Track receptance of the initial numerical model of the track.

The vibration modes of the track associated with the first resonant frequencies are represented in Fig. 6.18. The undeformed shape is represented in grey. The resonant frequency of 136.7 Hz is associated with the first vertical vibration mode of the track, which is characterised by the vibration of the rail and all the sleepers (see Fig. 6.18a) and is mainly influenced by the geometrical and mechanical properties of the ballast and subsoil. The second resonant frequency of 207 Hz is associated with the vibration of the rail and pads (see Fig. 6.18b). For the anti-resonant frequency of 181.6 Hz, the sleepers vibrate almost independently from the rail.

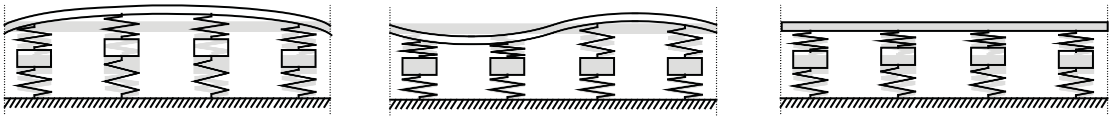

Figure 6.18 – Vibration modes of the track associated with the first resonant frequencies (De Man, 2002).

6.3.5 Damping of the track

The damping of the rail is provided by the pads (see Section 6.3.2). The energy dissipation mechanism of the sleepers and ballast is accounted for using the Rayleigh damping, which is a combination of the mass and stiffness matrices (Clough & Penzien, 1993). A viscous damping ratio of 3% is considered for the frequencies 90 Hz and 160 Hz (Alves Ribeiro, 2012), which leads to the damping factors $a_0 = 21.7\ s^{-1}$ (mass proportional) and $a_1 = 3.82\times10^{-5}$ s (stiffness proportional). These values are chosen to obtain a damping ratio close to 3% in the frequency interval 90 to 200 Hz; the highest track receptance occurs in this interval (see Fig. 6.17). The relationship between the frequency and Rayleigh damping is shown in Fig. 6.19.

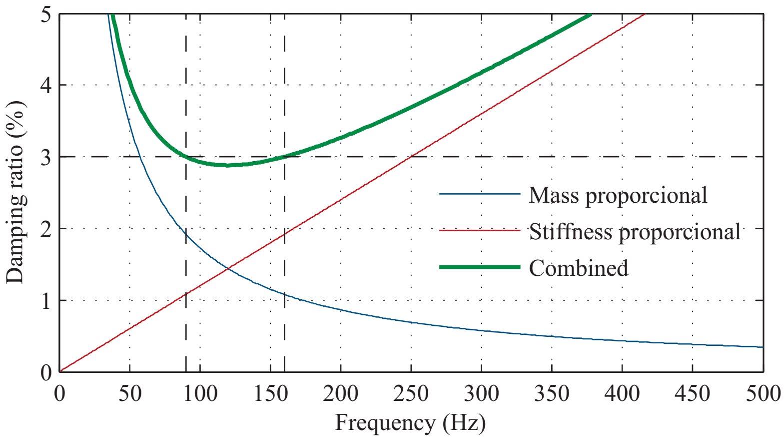

Figure 6.19 – Relationship between frequency and Rayleigh damping ratio.

6.3.6 Optimisation of the mesh

The numerical model illustrated in Fig. 6.15 is optimised in this section in order to reduce the size of the mesh and therefore decrease the computational cost. The different models considered in the optimisation process are listed in Table 6.8, with the main differences illustrated in Fig. 6.20. Only one-half of the track is modelled due to the geometric and loading symmetry.

Table 6.8 – Numerical models of the ballasted track.

Model	Description
Model A	Half model with 20 sleepers and the most refined mesh (see Fig. 6.15)
Model B	Based on model A; decreased the number of sleepers to 10
Model C	Based on model B; decreased the number of elements along the ballast height
Model D	Based on model C; decreased the number of elements along the sleeper height
Model E	Based on model D; decreased the number of elements along the transverse direction
Model F	Based on model E; further decreased the number of elements along the transverse direction
Model G	Based on model F; decreased the number of elements along the longitudinal direction
Model H	Based on model G; decreased the number of elements along the transverse direction
Model I	Based on model H; decreased the number of elements along all the directions
Model J	Based on model H; decreased the number of elements along the transverse direction and sleeper height

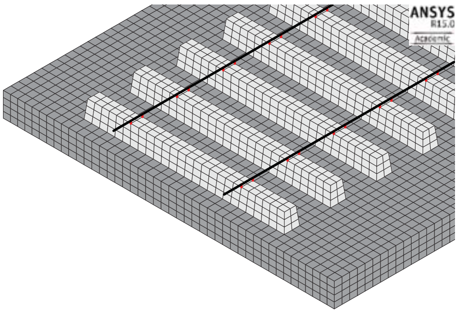

(a) Model B

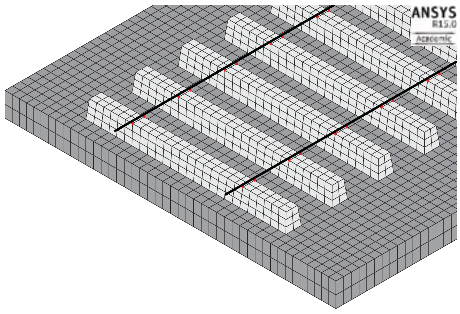

(b) Model C

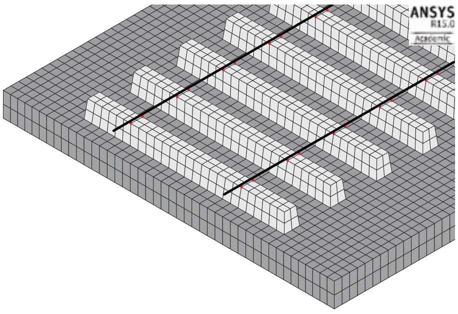

(c) Model D

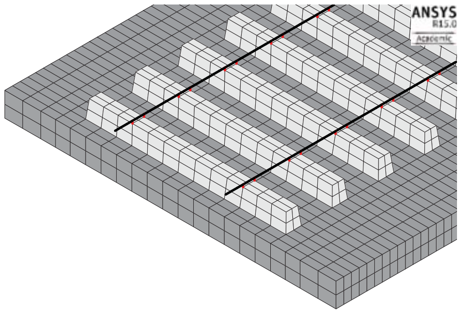

(d) Model E

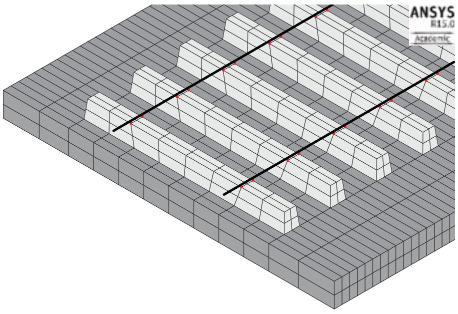

(e) Model F

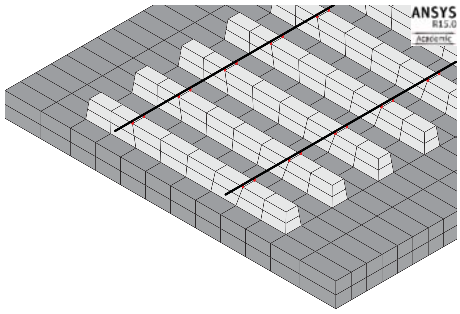

(f) Model G

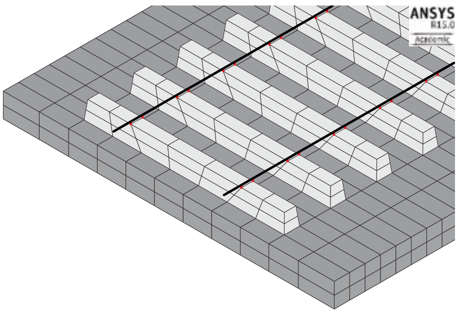

(g) Model H

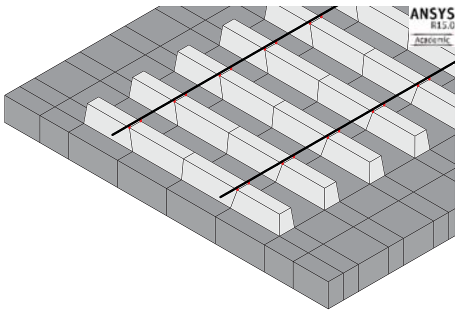

(h) Model I

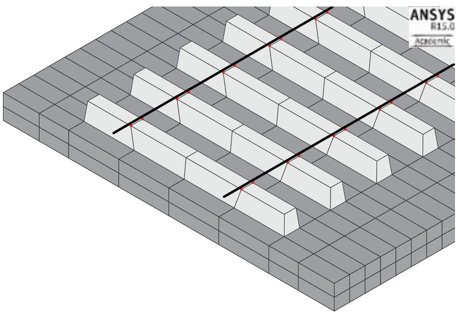

(i) Model J

Figure 6.20 – Numerical models of the ballasted track.

The track receptance is used to compare the dynamic behaviour of the different numerical models, as illustrated in Fig. 6.21.

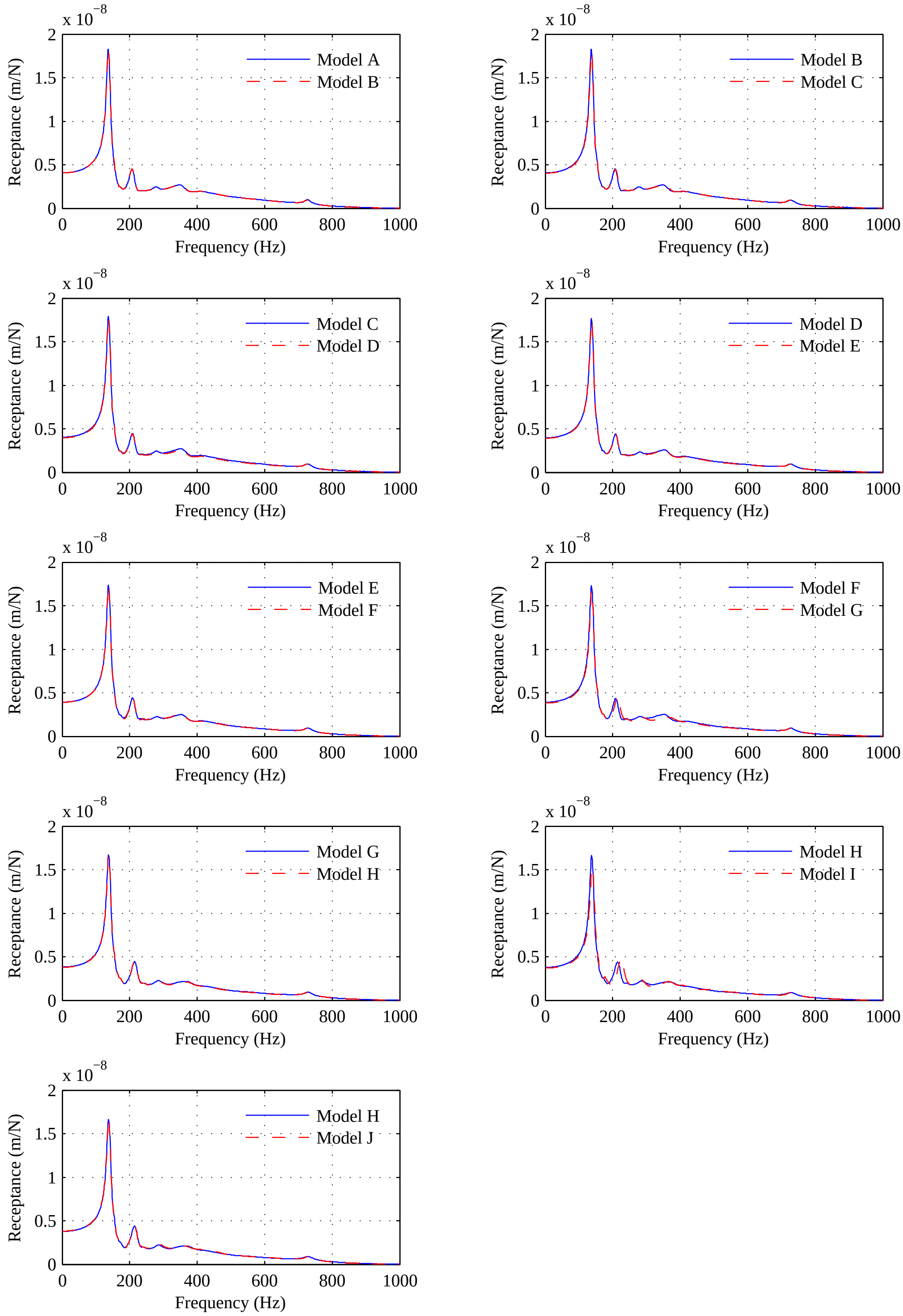

Figure 6.21 – Comparison of the track receptances of the numerical models of the track.

An excellent agreement can be observed between almost all the models. Since there is only a slight difference between the track receptances of models F and G for frequencies higher than 180 Hz, the modifications introduced in Model G are considered to be acceptable. The differences between the track receptances of models H and I are already significant and therefore the modifications introduced in Model G have been disregarded. Thus, model J is adopted from this point forward.

The number of degrees of freedom (d.o.f.) of all the models and the elapsed times for running the dynamic analyses of the track subjected to a Ricker pulse are given in Table 6.9. All the calculations have been performed with ANSYS program using a desktop computer with an Intel i7-4790 quad core processor running at 3.6 GHz.

Table 6.9 – Number of d.o.f. of the models and elapsed times of the dynamic analyses.

Model	Number of d.o.f.	Elapsed time (s)
Model A	313168	48446
Model B	157108	23232
Model C	92132	14560
Model D	83312	14097
Model E	41336	6776
Model F	24968	3942
Model G	13688	2106
Model H	12536	1920
Model I	3943	937
Model J	8090	1464

The optimisation of the finite element model of the track allowed the reduction of the number of d.o.f. from 313168 to 8090 (97% reduction) and the elapsed time of the dynamic analysis from 48446 s to 1464 s (97% reduction).

6.4 DYNAMIC RESPONSE OF THE TRAIN-TRACK SYSTEM

The passage of the simplified model of the KHST (see Section 6.2.4) over the railway track is analysed in Sections 6.4.1 and 6.4.2. This simplified model is used to evaluate the influence of the type of 2D track used and the force-deflection relationship considered for the Hertzian contact spring. In order to focus on the vertical behaviour of the track, the vehicle is applied to the left and right rails. The passage of the full KHST model (see Section 6.2) over the railway track is analysed in Sections 6.4.3 and 6.4.4. The influence of the numerical dissipation provided by the time integration scheme is studied in Section 6.4.3 and a comparison of the results calculated using the direct method and the ANSYS commercial software is presented in Section 6.4.4.

A constant speed of the vehicle is chosen so that the frequency of the harmonic excitation (f) caused by the discrete support of the sleepers is similar to the frequency of vibration of the unsprung mass of the vehicle. For the linearized value of the contact stiffness around the static wheel load, the frequency of vibration of the unsprung mass of the simplified model of the KHST is 173.2 Hz. Since this frequency can be higher when considering a nonlinear contact stiffness, a rounded value of 200 Hz is adopted. The speeds that lead to resonance phenomena are given by

$$v = \frac{d\,f}{i},\; i = 1,2,3,4,\ldots,\frac{1}{2},\frac{1}{3},\frac{1}{4},\ldots \tag{6.45}$$

where d is the sleeper spacing. A sleeper spacing equal to 0.6 m and $i = 1$ lead to a constant speed of 120 m/s. Special care has been taken to select the time step used in each analysis to ensure that the modes of vibration that contribute most to the response of the system and the dynamic excitation are accurately taken into account (Ribeiro, 2004).

6.4.1 Influence of the 2D track model

The total length between the first and last axles of the KHST is 380.15 m (see Section 6.2.1). In order to analyse the passage of this train over a bridge or viaduct, a significant length of track before and after the structure has to be considered to support the vehicle. If the entire track is modelled using 3D solid elements, the computational cost of the dynamic analyses becomes prohibitive. Since in the present thesis the dynamic behaviour of the vehicle before and after the structure is not analysed in detail, the 2D rigid track model represented in Fig. 6.22 is used (only part of the rigid track is shown in the figure). This part of the track is modelled with the ANSYS truss element type LINK180, considering a cross-sectional area of 1 m^2. As there are no horizontal forces acting on the vehicle, this element type behaves as a rigid beam. Each side of the track has a length of

400 m and is modelled with only one finite element with the d.o.f. constrained at both ends.

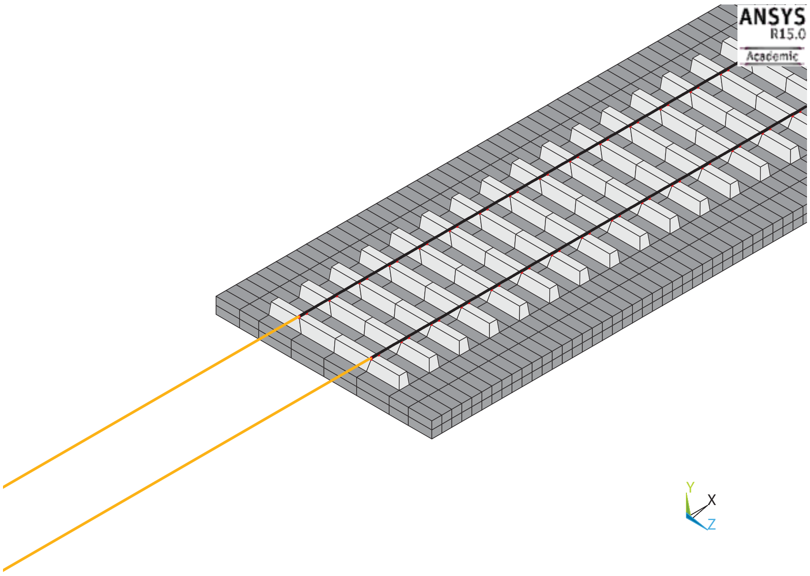

Figure 6.22 – Numerical model of the track with 220 sleepers and rigid track.

The section of the track modelled with solid elements has 220 sleepers. A time step equal to 2.5×10^{-4} s and a total of 5000 time steps are used to analyse the passage of the simplified model of the KHST over the railway track. The following parameters of the HHT-α method are considered: $\alpha = 0$, $\beta = 0.25$ and $\gamma = 0.5$ (see Chapter 4). The time history and frequency content of the vertical displacement of the contact point are plotted in Fig. 6.23. The black vertical dashed lines mark the beginning and end of the 3D track modelled with solid elements. Since the rigid beam is constrained at both ends, the 3D track is completely unloaded until the vehicle leaves the rigid beam. As can be observed in Fig. 6.23, when the vehicle moves from the rigid to the flexible track and vice-versa, the latter is suddenly loaded and unloaded, and the system vibrates with a frequency of 67.9 Hz. This frequency of vibration is associated with the first vertical vibration mode of the coupled vehicle-track model, as illustrated in Fig. 6.24.

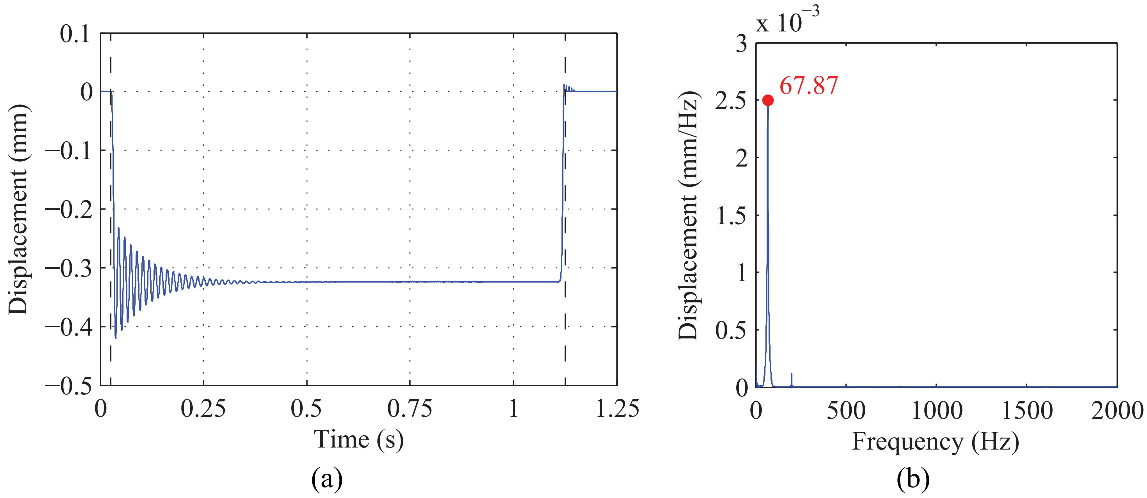

Figure 6.23 – Vertical displacement of the contact point: (a) time history and (b) frequency content.

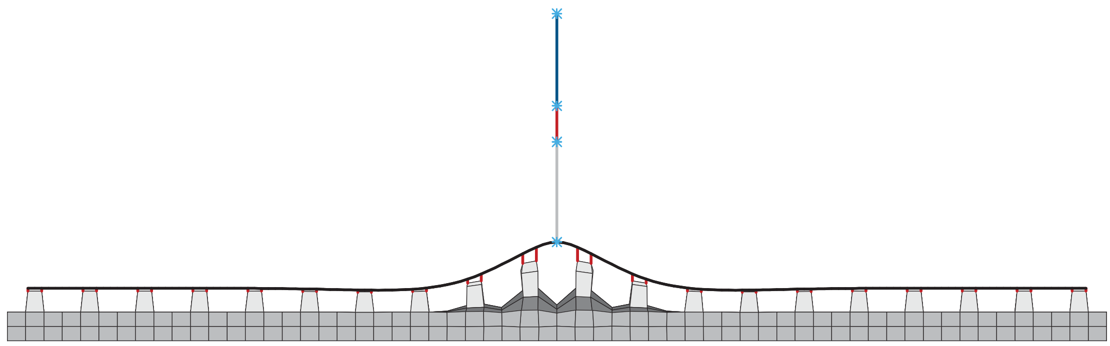

Figure 6.24 – First vertical vibration mode of the coupled vehicle-track model (f = 68.9 Hz).

The time history and frequency content of the contact force are plotted in Fig. 6.25. The impulsive loading observed in Fig. 6.23 is also present. The additional frequency of vibration of 200.2 Hz is related to the harmonic excitation caused by the discrete support of the sleepers.

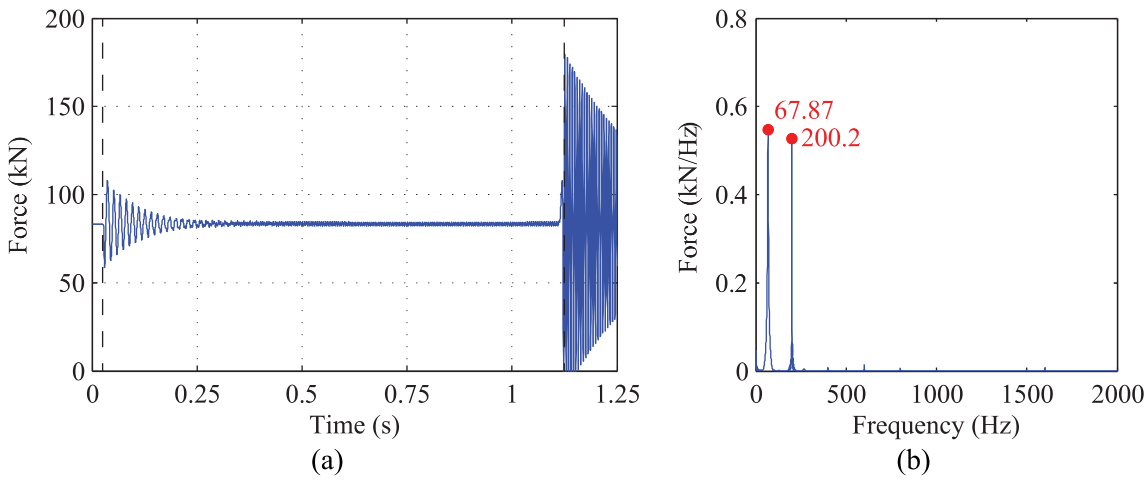

Figure 6.25 – Contact force: (a) time history and (b) frequency content.

The vertical acceleration of the wheelset, bogie and carbody are plotted in Figs. 6.26 to 6.28, respectively.

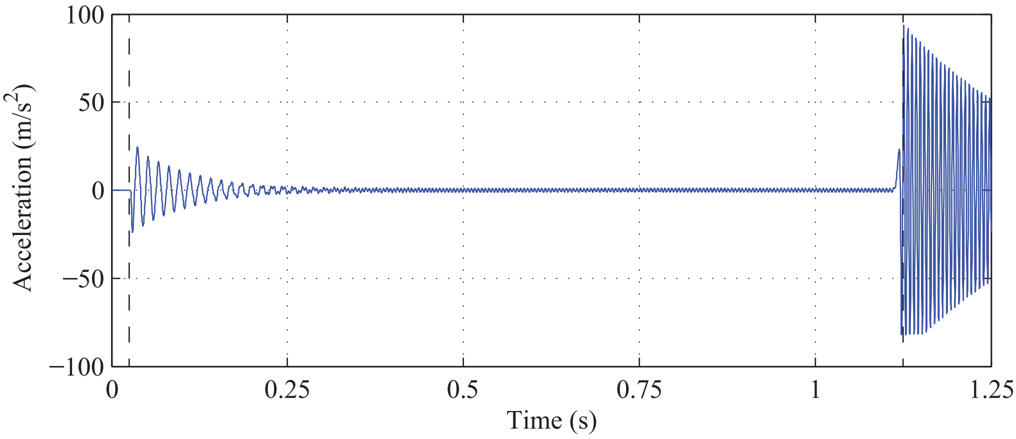

Figure 6.26 – Vertical acceleration of the wheelset.

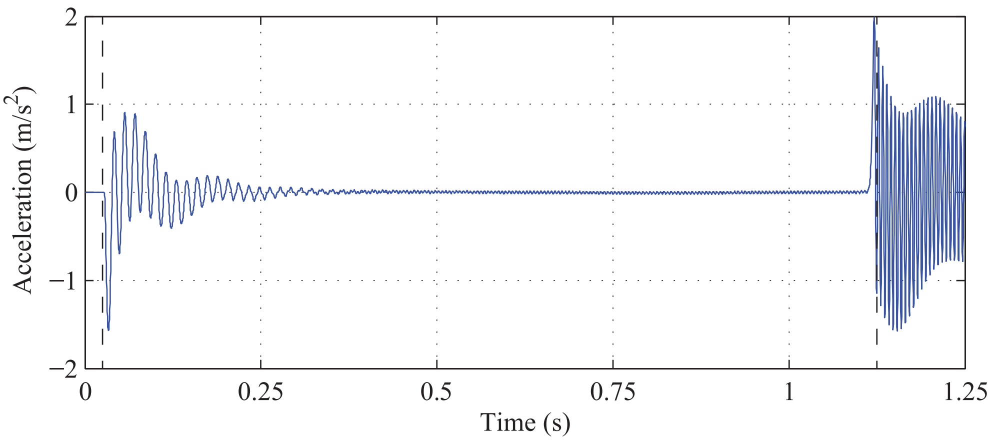

Figure 6.27 – Vertical acceleration of the bogie.

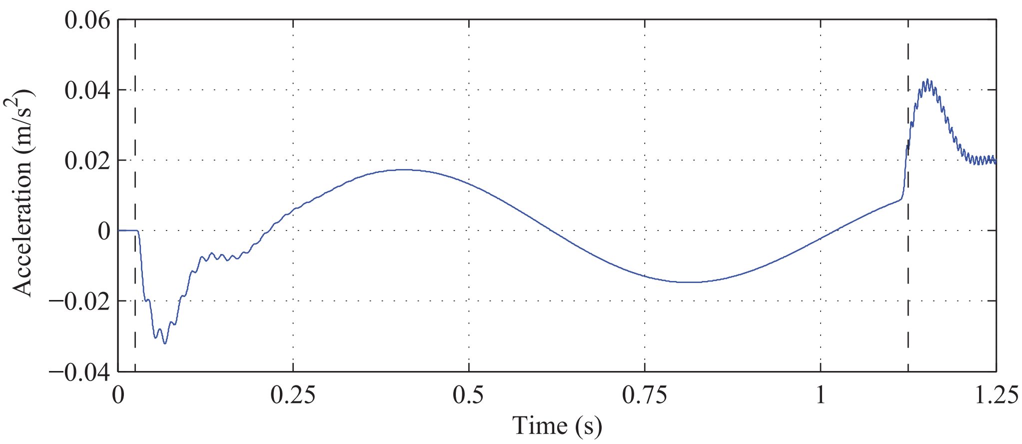

Figure 6.28 – Vertical acceleration of the carbody.

The execution time of the dynamic analysis is 1993 s. Modelling the track before and after the structure with rigid beams is very efficient from the computational point of view, but can lead to inaccurate results, especially when the behaviour of the vehicle is of interest. The high frequency vibrations might be quickly damped but the low frequency vibrations such as the bouncing of the carbody can take several seconds to damp out. In order to avoid the sudden transition between the rigid and flexible track, a 2D flexible track model has been developed (see Fig. 6.29). The rail and pads are modelled with the same finite elements described in Section 6.3.3. The ballast is modelled using the spring-damper element type COMBIN14 and the structural mass element MASS21. This structural mass also accounts for the mass of the sleeper.

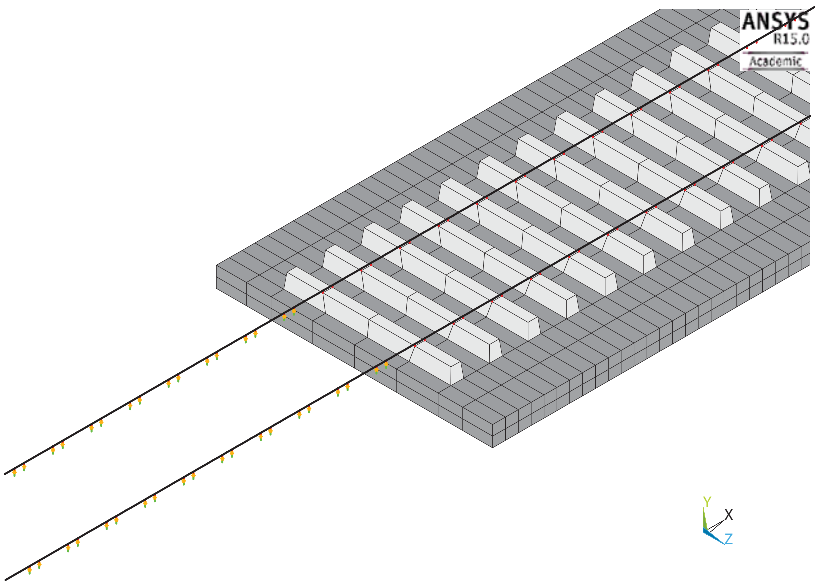

Figure 6.29 – 3D track modelled with solid elements and 2D flexible track.

The values of the stiffness and damping coefficients of the spring-damper and the value of the structural mass are calibrated separately by comparing the structural responses of the 2D and 3D track models. The optimised values are calculated using the MATLAB optimisation function *fmincon* (MATLAB®, 2013). First, the stiffness is optimised by applying a unit load between sleepers and by comparing the vertical displacement at the same point. The objective function used to optimise the mass compares the natural frequencies associated with the first vertical vibration mode of the track (see Section 6.3.4). Finally, the receptance value at this natural frequency is used to calibrate the damping. The bound constraints of the track parameters used in the optimisation process are shown in Table 6.10 and have been obtained based on the values indicated in

ERRI D 214/RP 5 (1999) and by trial and error. The optimised track parameters are: $k = 0.935\times10^8$ N/m, $m = 103.8$ kg and $c = 11930$ N s/m.

Table 6.10 – Bound constraints of the track parameters.

Parameter	Bound constraints	Unit
k	$[0.5, 1.5] \times 10^8$	N/m
m	[50, 150]	kg
c	[10000, 13000]	N s/m

The track receptances of the 2D and 3D track models are compared in Fig. 6.30 and a good agreement can be observed for frequencies up to 170 Hz. Since the main objective of using the 2D track model is to avoid the sudden transition between the 2D and 3D track models, the agreement observed in Fig. 6.30 is considered acceptable.

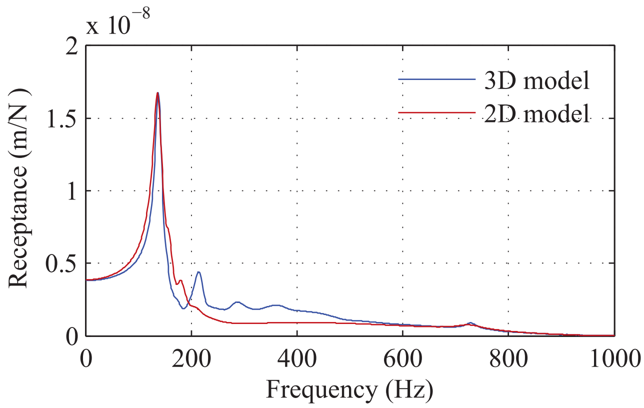

Figure 6.30 – Track receptances of the 2D and 3D track models.

The passage of the simplified model of the KHST over the railway track is now analysed using the 2D flexible track. The time histories and frequency content of the vertical displacement of the contact point and the contact forces are plotted in Figs. 6.31 and 6.32, respectively. As can be observed, the sudden loading and unloading of the 3D track is still present but has an almost negligible magnitude (see Figs. 6.23 and 6.25).

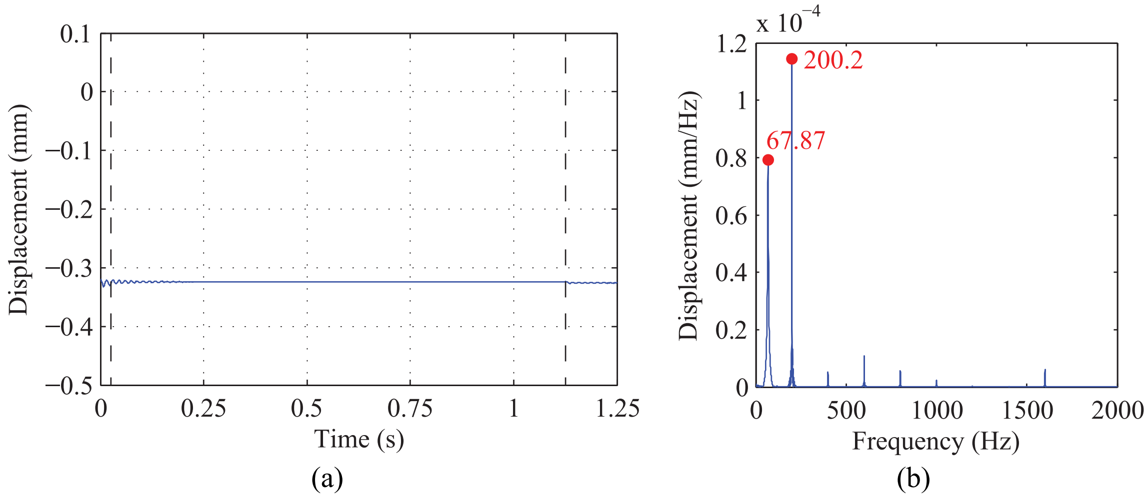

Figure 6.31 – Vertical displacement of the contact point: (a) time history and (b) frequency content.

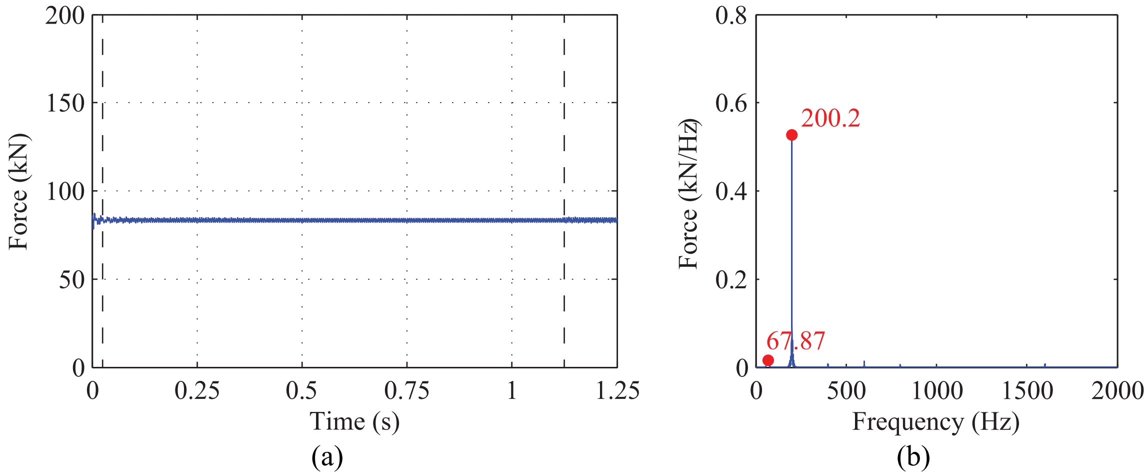

Figure 6.32 – Contact force: (a) time history and (b) frequency content.

The vertical acceleration of the wheelset, bogie and carbody are plotted in Figs. 6.33 to 6.35, respectively. Again, the sudden loading and unloading of the 3D track has an almost negligible magnitude.

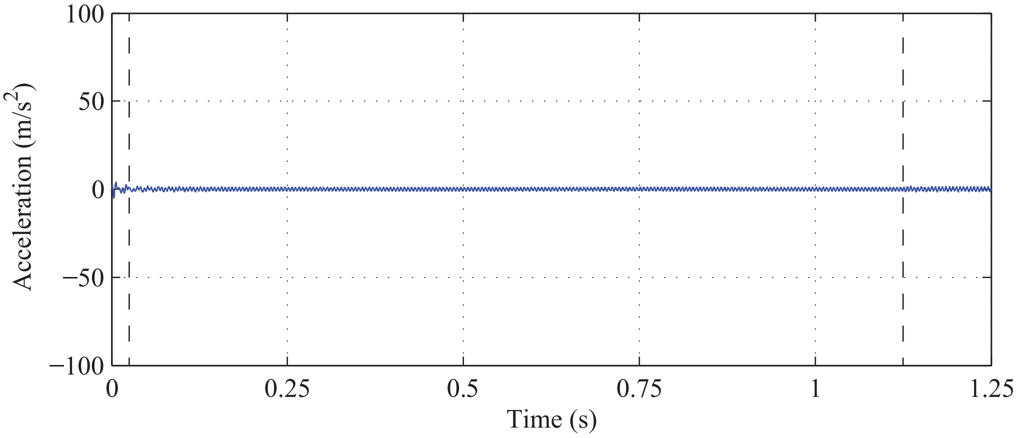

Figure 6.33 – Vertical acceleration of the wheelset.

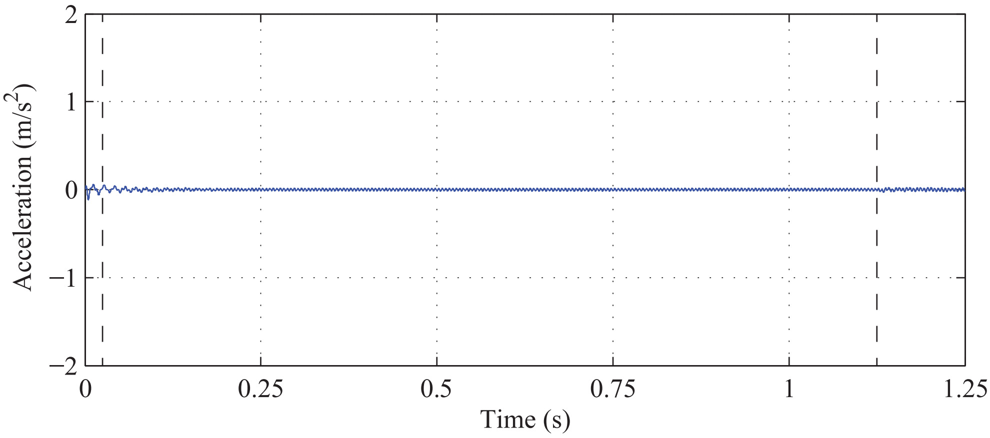

Figure 6.34 – Vertical acceleration of the bogie.

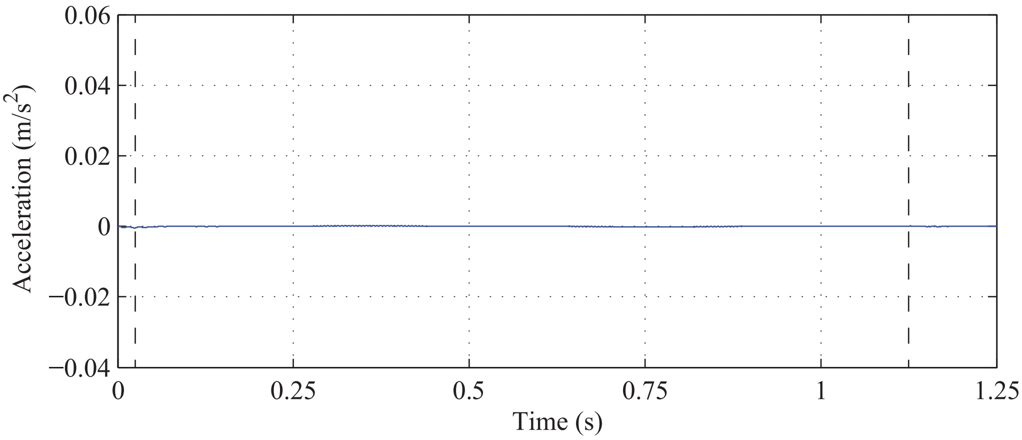

Figure 6.35 – Vertical acceleration of the carbody.

The execution time of the dynamic analysis using the 2D flexible track model is 2312 *s*, which is only 16% higher than that obtained when using the rigid track model. Since this difference is not very significant, the 2D flexible track model is adopted from this point forward.

6.4.2 Influence of the Hertzian contact spring

The influence of the force-deflection relationship considered for the Hertzian contact spring is analysed in this section. The linear and nonlinear relationships described in Section 3.3 are used. The linearized value of the contact stiffness is calculated for a static wheel load of 83385 N. The section of the track modelled with solid elements has 100 sleepers. A time step equal to 2.5×10^{-4} s and a total of 2200 time steps are used to analyse the passage of the simplified model of the KHST over the railway track.

The vertical displacement of the contact point and the contact force are plotted in Figs. 6.36 and 6.37, respectively. A detailed view of the contact force for the time interval [0, 0.1](s) is shown in Fig. 6.38. As expected, since the value of the contact force is close to the static wheel load, the displacement of the contact point obtained using the linear model is lower than that of the nonlinear model (see Fig. 3.23). This difference does not influence the wheel-rail interaction and is, therefore, acceptable. For the case of plane track without irregularities, there is no difference between the contact forces obtained using the two models, as can be observed in Fig. 6.37.

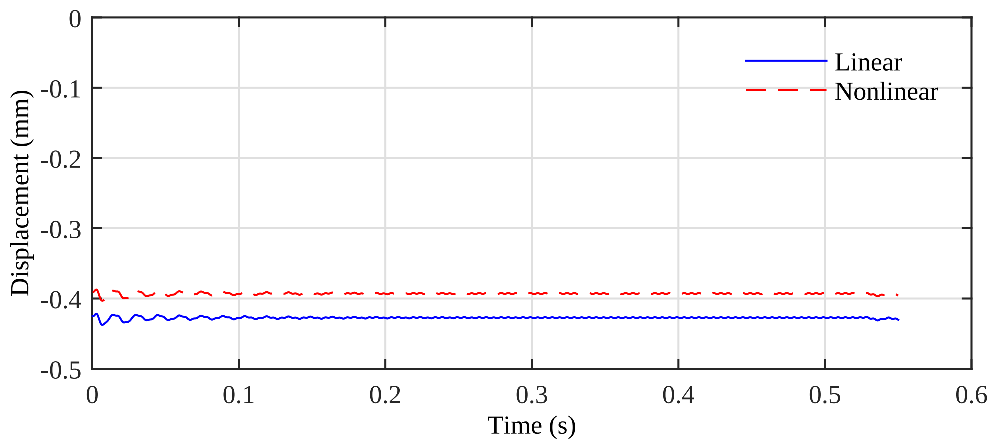

Figure 6.36 – Vertical displacement of the contact point.

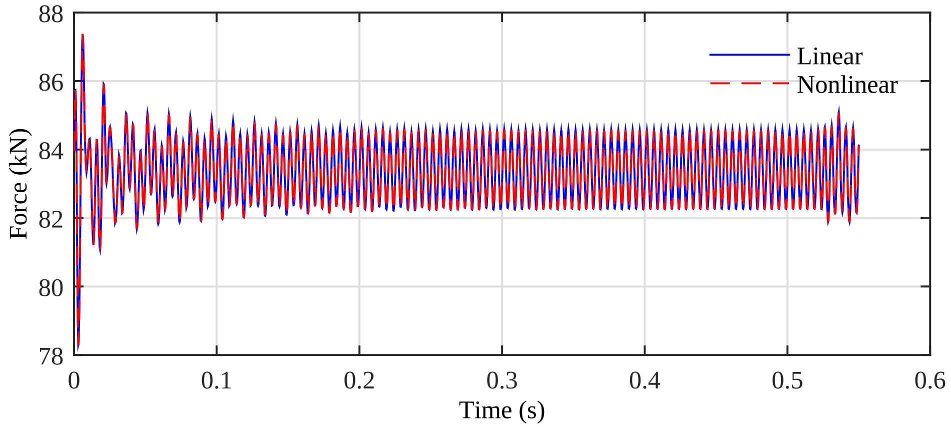

Figure 6.37 – Wheel-rail contact force.

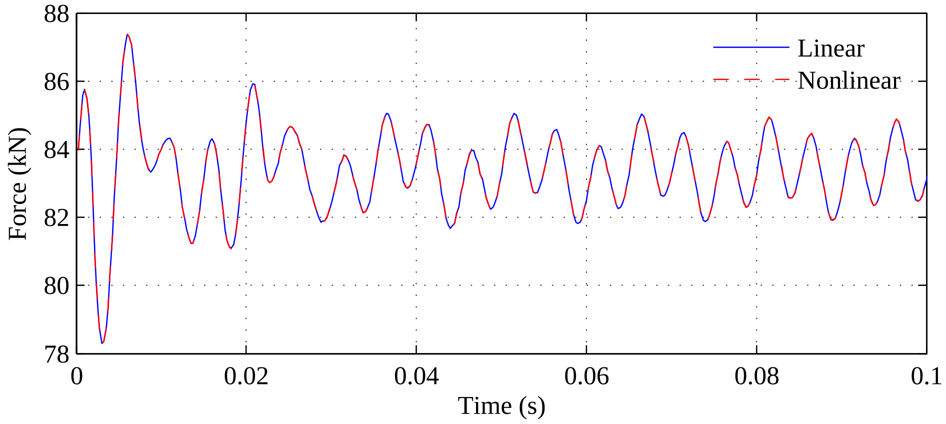

Figure 6.38 – Detailed view of the wheel-rail contact force.

The vertical acceleration of the wheelset is shown in Fig. 6.39 and a detailed view for the time interval [0, 0.1](s) is shown in Fig. 6.40. As expected, since the wheel-rail interaction strongly depends on the unsprung mass, the time histories of the contact force and the vertical acceleration are very similar.

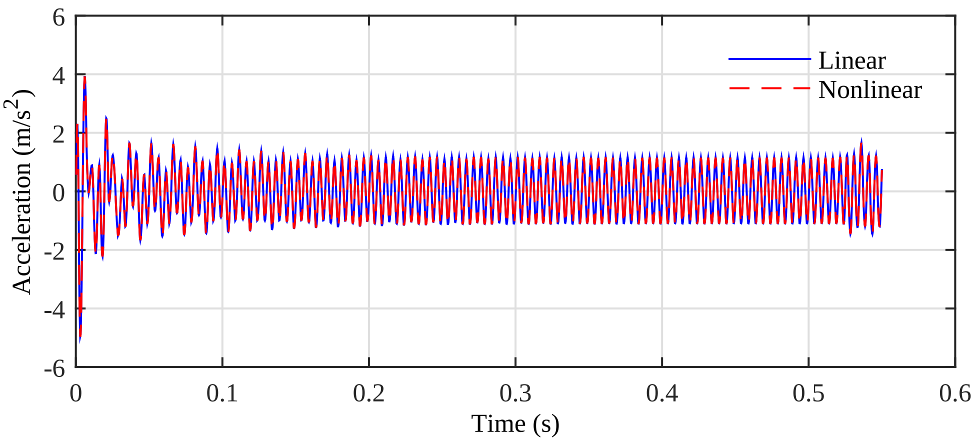

Figure 6.39 – Vertical acceleration of the wheelset.

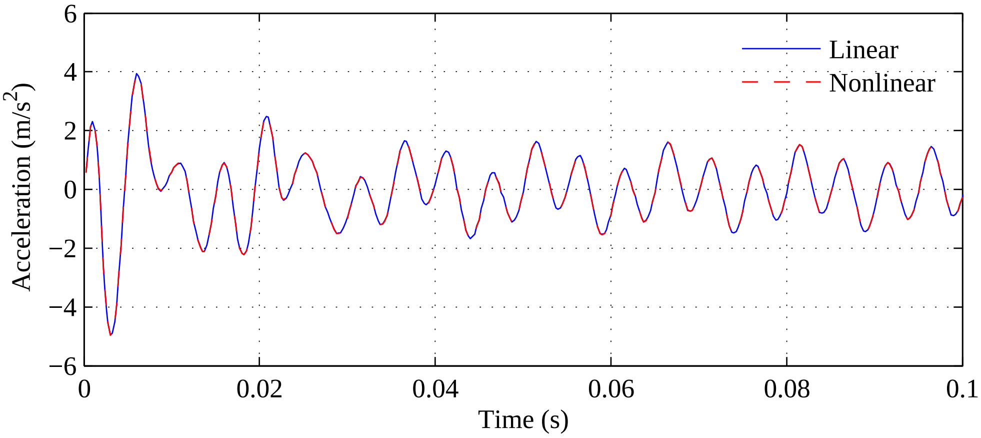

Figure 6.40 – Detailed view of the vertical acceleration of the wheelset.

All the calculations have been performed using a desktop computer with an Intel i7-4790 quad core processor running at 3.6 GHz. For a more accurate comparison, a single execution thread is used. The elapsed time of the dynamic analysis using the linear spring is 682 *s*. When using a nonlinear spring, the elapsed time is 1648 *s*, which is about 2.4 times slower. Since for certain analyses, the use of a linear or nonlinear spring leads to similar results, this additional computational cost might not be justifiable. Therefore, the type of spring to use should be evaluated for each type of analysis and should take into account the loading conditions and which results are of interest. The dynamic analysis using the linear spring has been also performed using the ANSYS software. The elapsed time is 21969 *s,* which is about 33 times slower when compared with the MATLAB program.

6.4.3 Influence of the numerical dissipation of the time integration scheme

The passage of the full KHST model over the railway track is analysed using a time step equal to 2.5×10^{-4} s and a total of 2200 time steps The dynamic analysis without numerical dissipation has been performed using the parameters $\alpha = 0$, $\beta = 0.25$ and $\gamma = 0.5$ and the parameters $\alpha = -0.05$, $\beta = 9/20$ and $\gamma = 9025/40000$ (Hughes, 2000) are used in the analysis with numerical dissipation. The value of $\alpha = -0.05$ is recommended for controlling the spurious high-frequency content without affecting the participation of the lower modes (ANSYS®, 2014c). In the case of plane track without irregularities, there are no significant differences between using the linear and nonlinear force-deflection relationships, and therefore only the former is considered in this section.

The vertical displacement and contact force of the first right wheel are plotted in Figs. 6.41 and 6.42, respectively. A detailed view of the contact force for the time interval [0, 0.2](s) is shown in Fig. 6.43. As can be observed, the numerical dissipation provided by the time integration scheme does not affect the participation of the most important vibration modes, and therefore the parameters used in this analysis are adopted from this point forward.

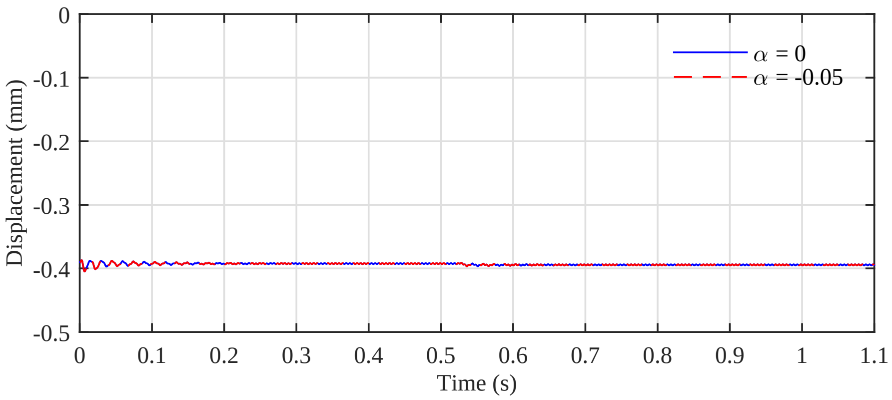

Figure 6.41 – Vertical displacement of the first right wheel.

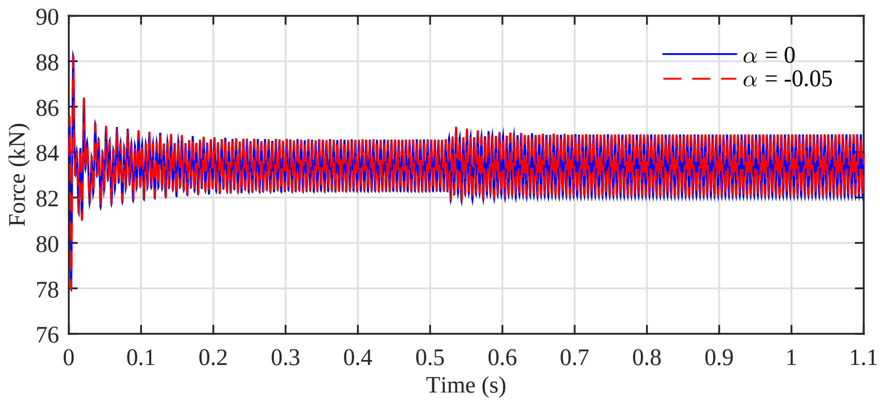

Figure 6.42 – Contact force of the first right wheel.

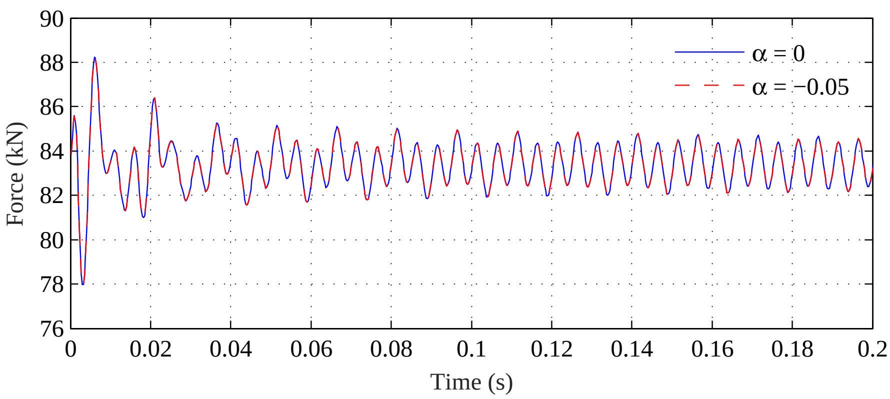

Figure 6.43 – Detailed view of the contact force of the first right wheel.

6.4.4 Comparison between the MATLAB and ANSYS programs

In order to validate the accuracy and efficiency of the method proposed in this thesis for the analysis of the vehicle-structure interaction, the passage of the full KHST model over the railway track is also analysed using the ANSYS commercial software. In the analyses performed with this software, the Lagrange multiplier method is used. The system of linear equations used in this method is the same as that used in the direct method, as explained in Section 2.3.2.The section of the track modelled with solid elements has 100 sleepers. A time step equal to 2.5×10^{-4} s and a total of 2200 time steps are used. The vertical displacement and contact force of the first right wheel obtained using both programs are plotted in Figs. 6.44 and 6.45, respectively.

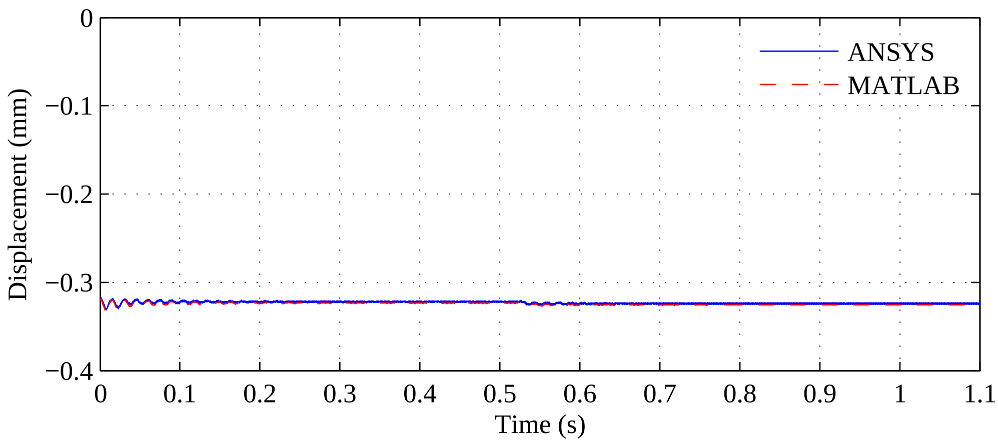

Figure 6.44 – Vertical displacements of the first right wheel.

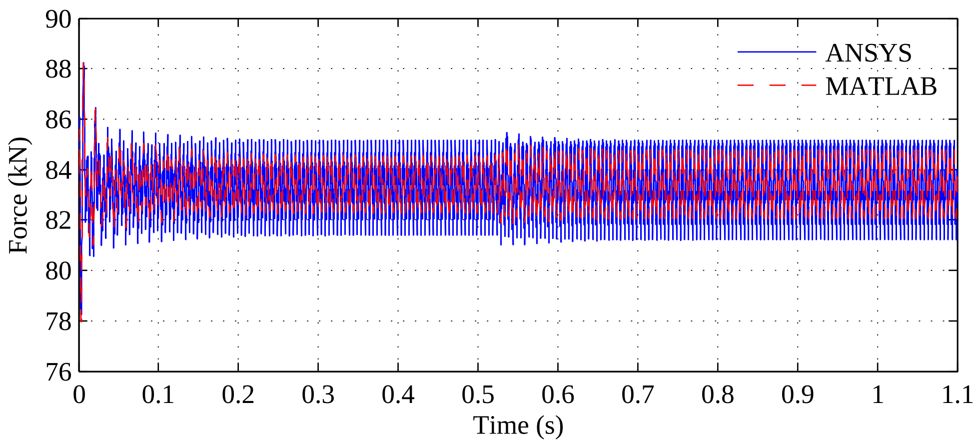

Figure 6.45 – Contact forces of the first right wheel.

The amplitudes of the contact force obtained using ANSYS are slightly higher than those obtained using MATLAB. A detailed view of these results for the time interval [0.3, 0.315](s) and the corresponding Fourier transforms are shown in Figs. 6.46 and 6.47, respectively. The high frequency oscillations observed in the response obtained with ANSYS are a spurious excitation caused by the spatial discretisation of the target elements used in this software (Alves Ribeiro, 2012). This is due to the fact that these elements use linear displacement interpolation functions, whereas the target elements implemented in MATLAB use cubic functions. The frequencies of these harmonic excitations are given by

$$f = \frac{vi}{d},\, i = 1,2,3,4,\ldots,\frac{1}{2},\frac{1}{3},\frac{1}{4},\ldots \tag{6.46}$$

where v is the vehicle speed and d is the length of the target elements. A length of 0.075 m and $i = 1$ and 1/2 lead to 1600 and 800 Hz, respectively, which correspond to the frequencies observed in Fig. 6.47a.

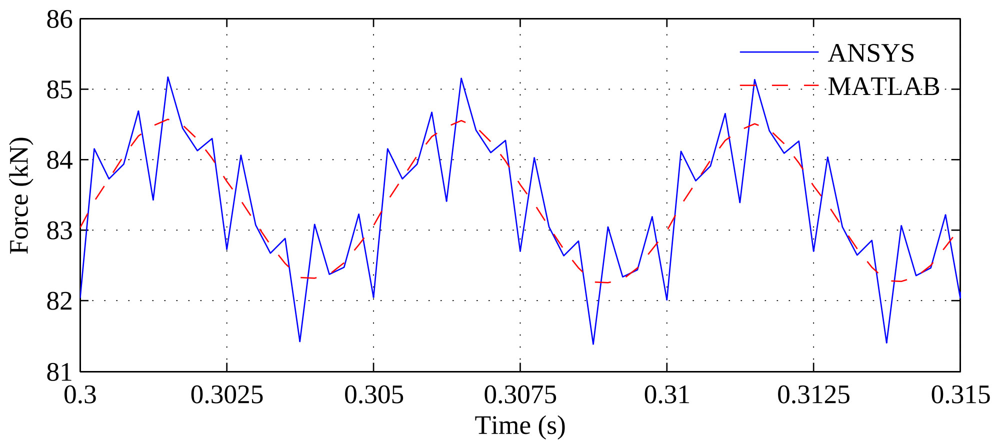

Figure 6.46 – Detailed view of the contact forces of the first right wheel.

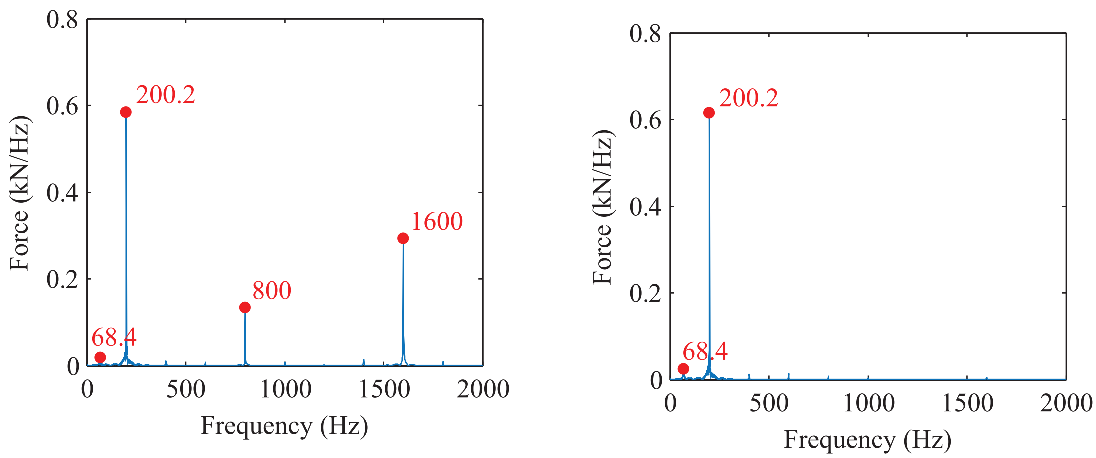

(a) (b)

Figure 6.47 – Frequency content of the contact forces obtained using: (a) ANSYS (b) MATLAB.

Figure 6.48 compares the contact force obtained with ANSYS, filtered by means of a low-pass Chebyshev (type II) filter with a cut-off frequency of 700 Hz, with the contact force obtained using MATLAB. The response obtained with ANSYS is slightly more damped than that obtained with MATLAB.

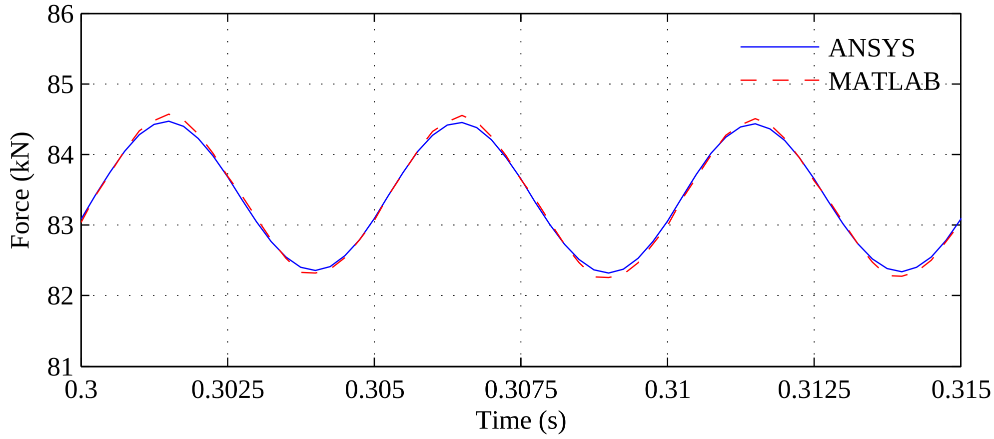

Figure 6.48 – Detailed view of the contact forces of the first right wheel.

The vertical acceleration of the wheelset and bogie are plotted in Figs. 6.49 and 6.50, respectively. As can be observed, there is a good agreement between the results obtained with both programs.

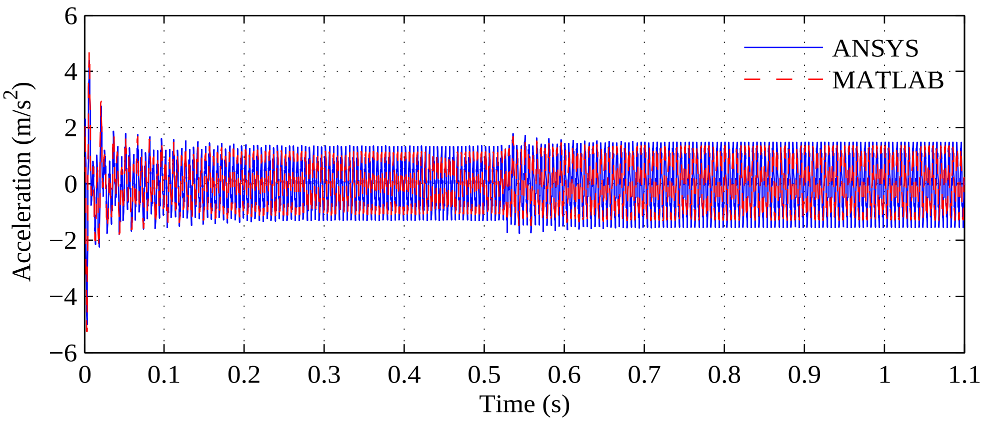

Figure 6.49 – Vertical accelerations of the first wheelset.

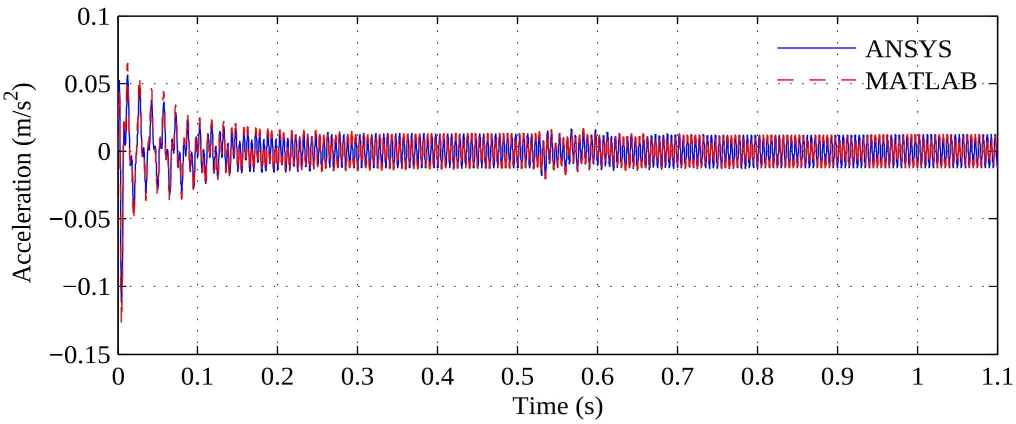

Figure 6.50 – Vertical accelerations of the first bogie.

All the calculations have been performed using a desktop computer with an Intel i7-4790 quad core processor running at 3.6 GHz. For a more accurate comparison, all the calculations have been performed using a single execution thread. The elapsed time is 47891 s using ANSYS and 3368 s using MATLAB, which is about 14 times faster. In Section 6.4.2, the execution time of MATLAB is 33 times faster than ANSYS. This loss of computational efficiency may be related to the fact that the MATLAB functions used to solve the system of linear equations might be less optimised than those implemented in ANSYS when a large number of contact points is considered

6.5 CONCLUDING REMARKS

The numerical models of the train and track have been developed and validated in this chapter. The ballasted track is first modelled using a large number of finite elements to adequately simulate the wave propagation. This number is then reduced using an iterative process that compares the responses of the different models. A 97% reduction of the number of d.o.f. of the track has been obtained without loss of accuracy.

The vehicle is initially supported before and after the track modelled with 3D solid elements using rigid beams. This is computationally efficient, but leads to sudden transitions between the rigid and flexible tracks and consequently to inaccurate results, especially when the behaviour of the vehicle is of interest. A 2D flexible track model has been developed to eliminate these sudden transitions. The stiffness, damping and structural mass of the track are calibrated by comparing the structural responses of the 2D and 3D track models and a good agreement has been obtained. The execution time of the dynamic analysis performed using the 2D flexible track model is only 16% higher than that obtained when using the rigid track model, and thus the flexible track model has been adopted.

The passage of the simplified model of the KHST over the ballasted track has been analysed using the Hertzian spring with a linear and nonlinear force-deflection relationships. Since the results obtained using both relationships are very similar, the significantly higher computational cost associated with the nonlinear spring might not be justifiable. The use of numerical dissipation is important for controlling the spurious high-frequency content. The parameters β and γ of the time integration scheme define the variation of the displacements, velocities and accelerations during a time step, and the parameter α controls the numerical dissipation. It has been concluded that using the parameters $\alpha = -0.05$, $\beta = 9/20$ and $\gamma = 9025/40000$ does not affect the participation of the most important vibration modes.

The dynamic response of the train-track system has been calculated using the direct method and the ANSYS program, and a good agreement between the results has been obtained. The contact forces calculated using ANSYS have a spurious excitation that depends on the spatial discretisation of the target elements and is likely caused by the linear interpolation of displacements used by these elements. The target elements implemented in MATLAB use cubic functions and do not lead to spurious excitations. When using the simplified model of the KHST, the dynamic analysis performed using ANSYS is about 33 times slower when compared with the MATLAB program, and only 14 times slower when using the complete model of the train. This might be due to the fact that the MATLAB functions used to solve the system of linear equations might be less optimised than those implemented in ANSYS when a large number of contact points is considered.

7 CASE STUDY OF THE ALVERCA RAILWAY VIADUCT

7.1 INTRODUCTION

The dynamic interaction that occurs during the passage of the Korean high-speed train (KHST) over the Alverca railway viaduct is analysed and discussed in this chapter using the direct method developed in Chapters 4 and 5. The numerical modelling of the KHST and of the ballasted track are described in Chapter 6. The Alverca viaduct is a flyover type structure located on the Northern Line of the Portuguese railway network. It has 47 spans and a total length of 1091 m. Each span is composed of a prefabricated U-shaped prestressed beam and an upper slab cast in situ, which form a single-cell box-girder deck.

The geometrical and mechanical properties and the numerical modelling of the viaduct are described in Section 7.2. A 3D model composed of shell elements is used. The viaduct is first modelled using a large number of finite elements (FE), in a similar way to that employed for the ballasted track (see Section 6.3.6). This number is then reduced by comparing the natural frequencies and mode shapes of the different models. The natural frequencies, mode shapes and modal damping ratios of the vibration modes of the viaduct were obtained during an ambient vibration test performed by Malveiro *et al.* (2013). An FE model updating is then performed, using different optimisation algorithms, in order to calibrate the values adopted for the geometrical and mechanical properties of the viaduct.

The passage of the KHST over the Alverca viaduct is analysed in Section 7.3. The dynamic analyses are performed using a 3D model with a large mesh size to accurately model the complex mechanical behaviour of the structure and to verify the computational efficiency of the direct method. Particular emphasis is placed on high speeds, where resonance effects and large dynamic amplifications are more likely to occur. Special attention is given to the transition between plane track and viaduct to guarantee a smooth behaviour. The influence of isolated defects and periodic irregularities of the longitudinal level of the track on the dynamic behaviour of the train-structure system is analysed based on the standards EN 13848-1 (2003) and EN 13848-5 (2008). The instability of the ballast is also assessed in terms of the vertical accelerations of the deck. Particular attention is given to local deformations of the slab, which can be adequately taken into account with the 3D FE model used. The influence of using a linear or nonlinear force-deflection relationships of the Hertzian contact spring is also analysed in Section 7.3. Finally, the results calculated using MATLAB® (2013) and ANSYS® (2014a) programs are compared, as well as the relative computational efficiency.

7.2 NUMERICAL MODELLING OF THE ALVERCA VIADUCT

7.2.1 General description

The Alverca flyover viaduct is located on the Northern Line of the Portuguese railway network, between the cities of Lisbon and Porto, in the vicinity of Vila Franca de Xira (km +18.676), as shown in Fig. 7.1. Figure 7.2 shows the intersection of the railway lines.

(a)

(b)

Figure 7.1 – Alverca railway viaduct: (a) geographical location and (b) aerial view.

Figure 7.2 – Intersection of the railway lines.

The single track viaduct has a total length of 1091 m and is divided into three parts: the north ramp (see Fig. 7.3a) has a length of 527 m and is composed of 27 spans (5×16.5 m + 5×17.5 m + 17×21 m), the pergola has a length of 176 m and the south ramp (see Fig. 7.3b) has a length of 388 m and is composed of 20 spans (4×16.5 m + 4×17.5 m + 12×21 m). The 47 spans are simply supported on the piers and abutments.

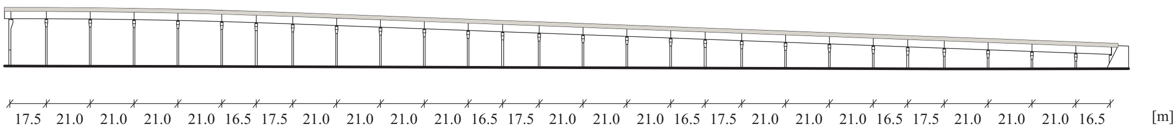

(a)

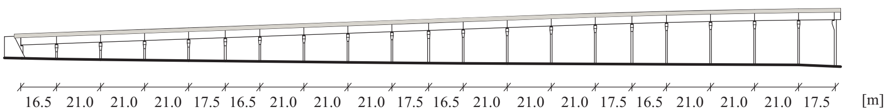

(b)

Figure 7.3 – Elevation view of the (a) north ramp and (b) south ramp.

The modelling and analyses presented in this chapter are focused on the first three spans of the north ramp, adjacent to the abutment, as shown in Fig. 7.4.

Figure 7.4 – First three spans of the north ramp.

7.2.2 Geometrical and mechanical properties

The cross-section of the spans of the viaduct supporting the single track is illustrated in Fig. 7.5. Each span is composed of a prefabricated U-shaped prestressed beam and an upper slab cast in situ, which form a single-cell box-girder deck. The ballast retaining walls are monolithically connected to the upper slab of the deck. The non-structural elements such as the safeguards and edge beams are also represented in Fig. 7.5.

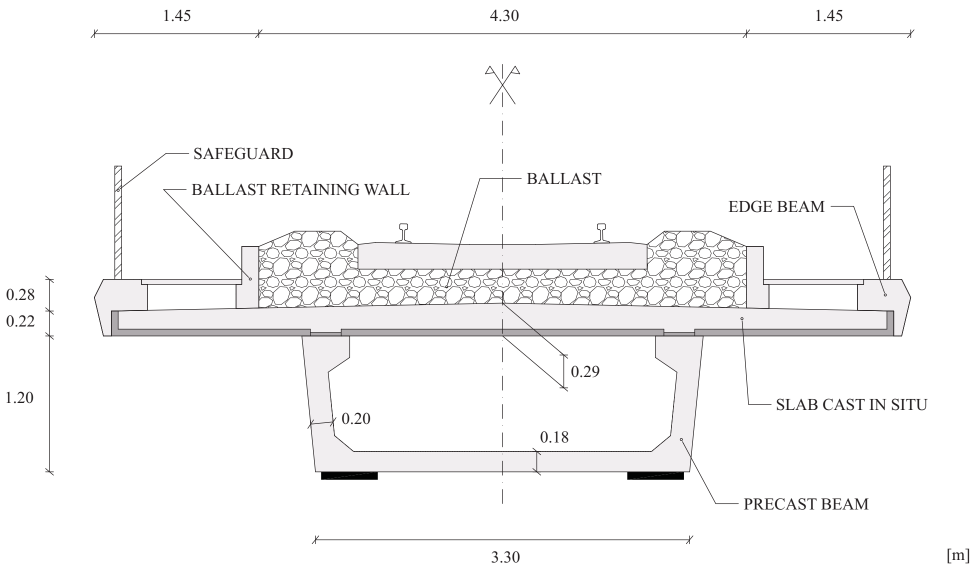

Figure 7.5 – Cross-section of the viaduct.

The geometrical and mechanical properties of the deck have been previously defined in Malveiro *et al.* (2013) and are summarised in Table 7.1.

Table 7.1 – Geometrical and mechanical properties of the deck.

Parameter	Property	Value
e_c	Thickness of the upper slab	0.27 m
ρ_c	Density of the concrete	2469.8 kg/m^3
E_{c1}	Modulus of elasticity of concrete of the upper slab (span 1)	35.4 GPa
E_{c2}	Modulus of elasticity of concrete of the upper slab (span 2)	35.4 GPa
E_{c3}	Modulus of elasticity of concrete of the upper slab (span 3)	35.4 GPa
E_c	Modulus of elasticity of concrete of the prefabricated beam	40.9 GPa
ν_c	Poisson's ratio of the concrete	0.2
k_v	Vertical stiffness of the supports	5200 MN/m
k_{h1}	Longitudinal stiffness of the supports (span 1)	3.6 MN/m
k_{h2}	Longitudinal stiffness of the supports (span 2)	3.6 MN/m
k_{h3}	Longitudinal stiffness of the supports (span 3)	3.6 MN/m

Each span has two fixed supports at one extremity and two longitudinally guided supports at the other extremity. The supports consist of elastomeric reinforced bearings composed of four layers of neoprene interleaved with steel plates with dimensions of 500 × 300 mm^2 and a thickness of 8 mm (see Fig. 7.6).

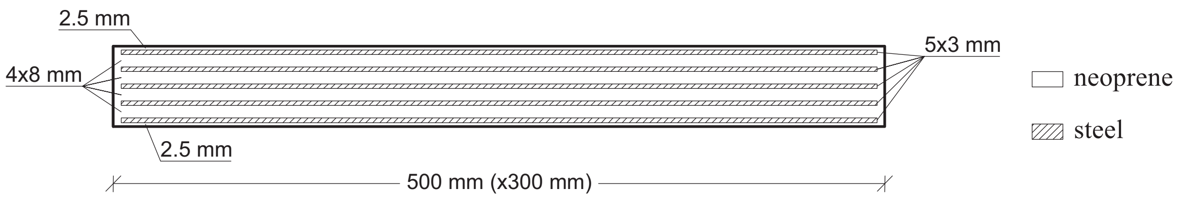

Figure 7.6 – Elastomeric reinforced bearings (Meixedo, 2012).

7.2.3 Finite element model

The numerical model of the Alverca viaduct is developed in ANSYS using the APDL scripting language (ANSYS®, 2014d) in order to automate all the steps involved in the model generation. The macro file containing all the commands is based on previous studies (Fernandes, 2010; Horas, 2011; Meixedo, 2012; Jorge, 2013) but has been completely rewritten using an identifier naming convention based on the Hungarian notation (McConnell, 2004) in order to improve the readability of the code. A three-dimensional model has been adopted due to the complex geometry and mechanical behaviour of the structure. Although the spans of the viaduct are simply supported on the piers and abutments, there is a longitudinal continuity due to the continuously welded rails and ballast that is not accurately modelled with more simplified models. The ballasted track must be taken into account to accurately calculate the vertical accelerations of the deck of the viaduct (Rigueiro *et al.*, 2010).

Analysing the nonlinear vehicle-structure interaction of the complete 3D model of the viaduct using a personal computer would be impracticable due to the high computational cost. Since the spans are simply supported on the piers and abutments, only the three spans adjacent to the north abutment are modelled in the present work (see Fig. 7.7). An extension of the track with a length of 18 m is considered before the first span to simulate the continuity of the track over the adjacent embankment. The origin of the global coordinate system is located at the beginning of the first span, at the bottom centre of the U-shaped beam, as shown in Fig. 7.8. The *x*, *y* and *z* axes correspond to the longitudinal, lateral and vertical directions, respectively.

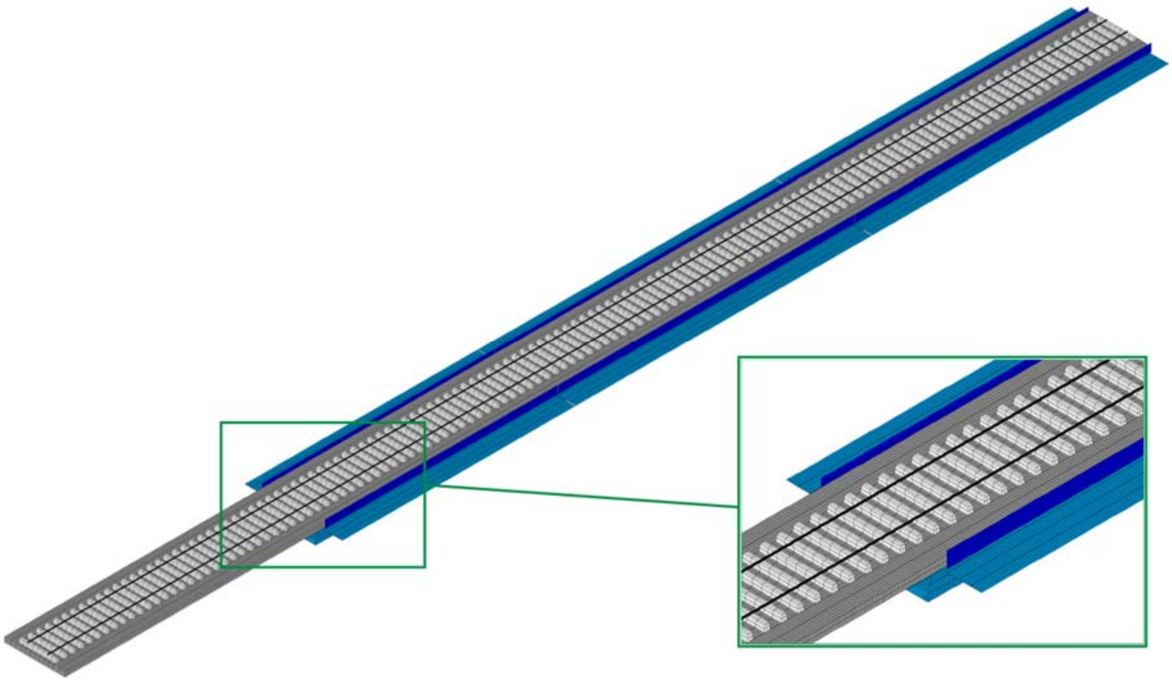

Figure 7.7 – Numerical model of the first three spans of the viaduct.

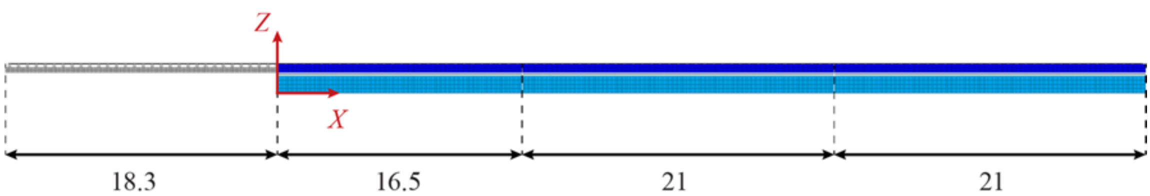

Figure 7.8 – Origin of the global coordinate system.

The U-shaped beams, the upper slabs and the ballast retaining walls are modelled with the shell element type SHELL281 (see Fig. 7.9). The mass of non-structural elements such as safeguards and edge beams is taken into account using the truss element type LINK180.

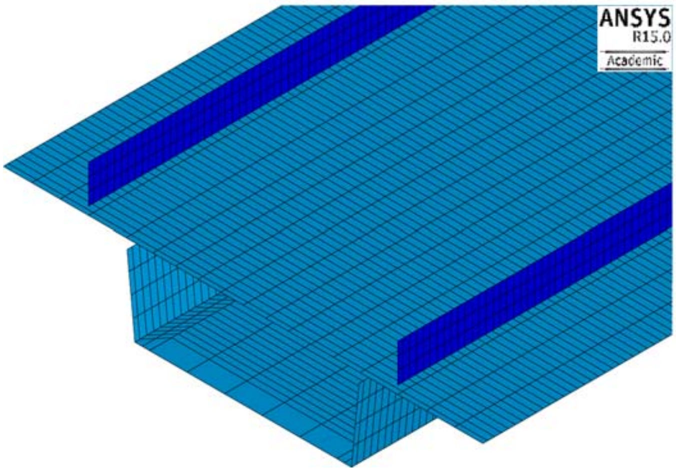

Figure 7.9 – U-shaped beams, upper slabs and ballast retaining walls.

The numerical model of the three spans adjacent to the north abutment has 755131 unconstrained degrees of freedom (d.o.f.) The modelling of the track is explained in Section 6.3.3 and the numerical model with the optimised mesh is defined in Section 6.3.6. The mesh discretisation of the viaduct along the longitudinal and lateral directions depends on the mesh of the track. For the remaining elements, a refined mesh is considered initially so that the results are not affected by the size of the elements. This model is optimised in Section 7.2.6.4 in order to reduce the number of finite elements.

7.2.4 Modal parameters

A modal analysis has been performed using ANSYS in order to understand the dynamic behaviour of the viaduct. The first four vertical vibration modes of the viaduct associated with the bending of the spans and the first torsional vibration mode are represented in Fig. 7.10. The natural frequencies of the first two vibration modes are not sorted in ascending order to preserve that used in Malveiro *et al.* (2013).

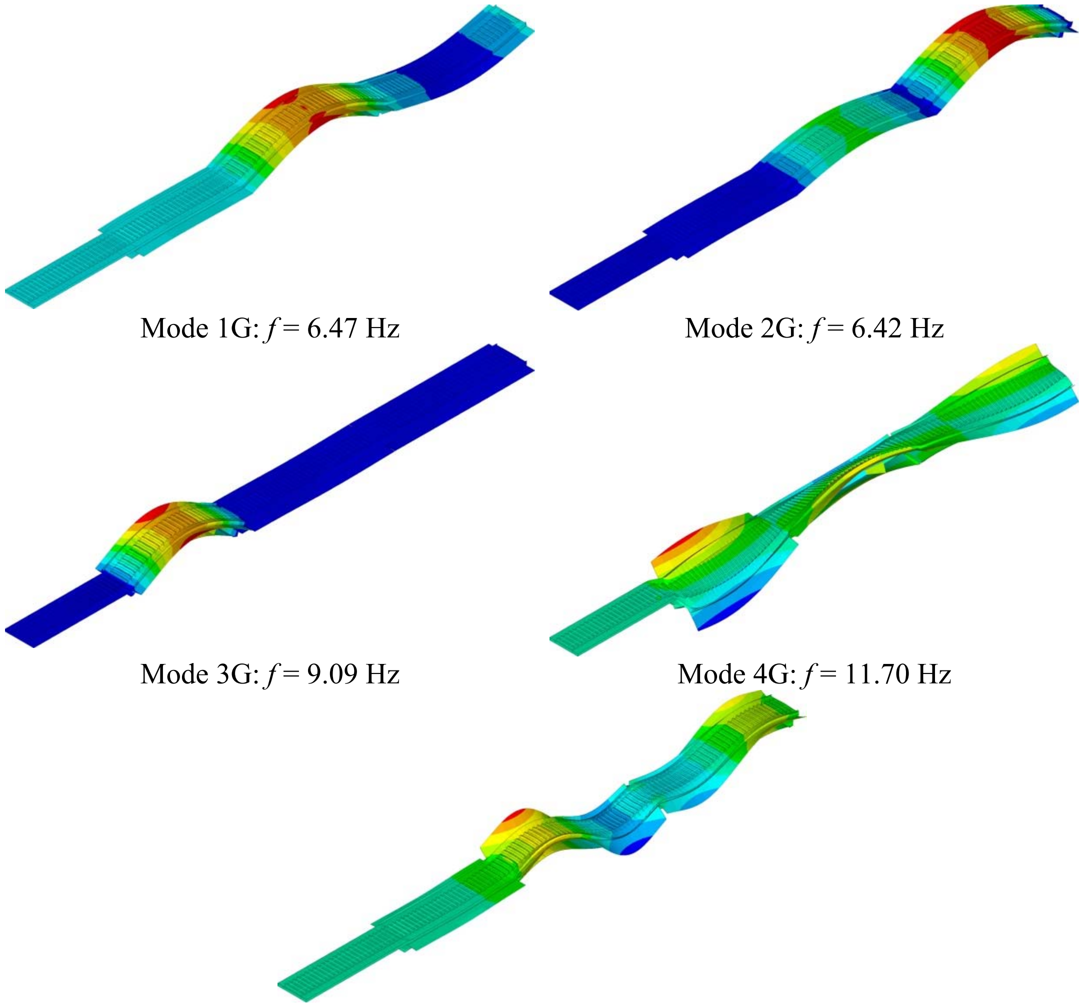

Mode 1G: f = 6.47 Hz Mode 2G: f = 6.42 Hz

Mode 3G: f = 9.09 Hz Mode 4G: f = 11.70 Hz

Mode 5G: f = 17.25 Hz

Figure 7.10 – Global vibration modes and natural frequencies of the viaduct.

7.2.5 Ambient vibration test

The level of uncertainty associated with the development of numerical models can be reduced by using model updating techniques that compare the response of the numerical model with measured data, as described in Section 0. The ambient vibration test performed by Malveiro *et al.* (2013) allowed the identification of the modal parameters of the viaduct, namely the natural frequencies, mode shapes and modal damping ratios of the vibration modes. These modal parameters were calculated based on the accelerations measured in the longitudinal, transverse and vertical directions. The calculations have been performed with the ARTeMIS software (2009) using the stochastic subspace identification method.

The experimental campaign has been divided into two phases: the accelerations used to calculate the global modal parameters of the viaduct were measured during the first phase and those used to identify the local modal parameters of the upper slab of the deck were measured during the second phase. The accelerations have been measured at 60 points distributed along the three spans considered in this study: 50 points are located in the ballast retaining wall, 6 points at the extremity of the cantilever and 4 in the webs of the prefabricated beam (see Fig. 7.11). The accelerations have been measured along the longitudinal, transverse and vertical directions using a technique based on fixed reference points and mobile measuring points (Malveiro *et al.*, 2013).

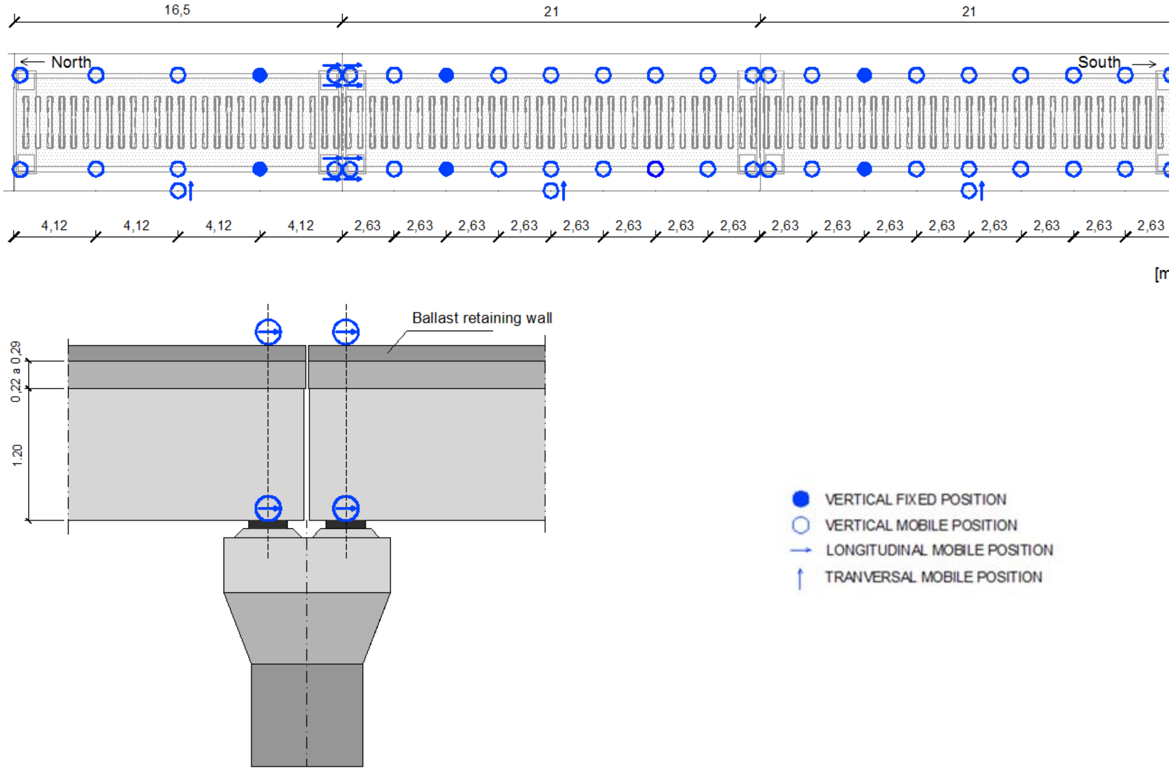

Figure 7.11 – Measuring points used in the ambient vibration test (Malveiro *et al.*, 2013).

The first five experimental vibration modes of the viaduct and the associated natural frequencies calculated using the ARTeMIS software are presented in Fig. 7.12.

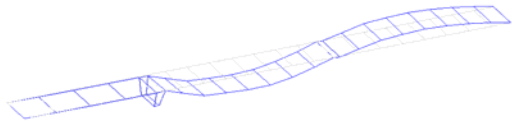

Mode 1G: f = 6.76 Hz

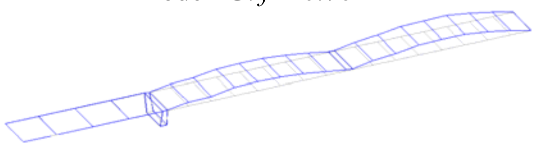

Mode 2G: f = 6.95 Hz

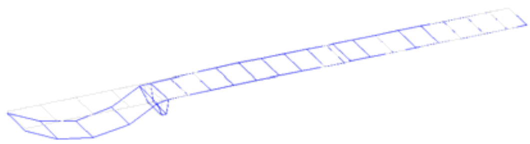

Mode 3G: f = 9.65 Hz

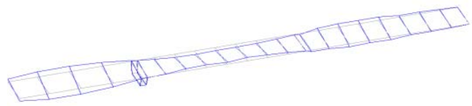

Mode 4G: f = 13.04 Hz

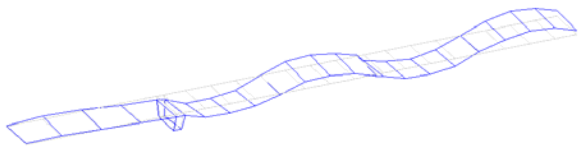

Mode 5G: f = 20.94 Hz

Figure 7.12 – Identified vibration modes and natural frequencies of the viaduct (Malveiro *et al.*, 2013).

The natural frequencies of the vibration modes represented in Fig. 7.12 and the associated modal damping ratios are listed in Table 7.2.

Table 7.2 – Modal damping ratios of the global vibration modes.

Mode	f (Hz)	Damping ratio (%)
1G	6.76	1.63
2G	6.95	3.56
3G	9.65	2.39
4G	13.04	4.99
5G	20.94	3.46

7.2.6 Model updating techniques

The development of finite element models has a considerable number of uncertainties associated, for example, with the geometrical and mechanical properties, joints and support conditions, or inadequate modelling. This level of uncertainty can be reduced by using model updating techniques that compare the response of the numerical model with measured data. The experimental data can be obtained using static or quasi-static load tests, dynamic tests, such as ambient or forced vibration, or a combination of these (Ribeiro, 2012). The model updating techniques are based on the minimisation of an objective function that can be, for example, a weighted sum of the differences between the numerical and experimental natural frequencies and mode shapes.

The finite element model updating can be performed using direct or indirect methods (Brehm, 2011). In the former, which emerged first, the elements of the mass, damping and stiffness matrices are updated directly to minimise the objective function, and therefore, understanding the physical meaning of the changes made can be very difficult. This approach can also lead to sparse or ill-conditioned matrices which may cause numerical problems (Ribeiro, 2012). In the indirect methods, since the objective function is minimised by modifying the parameters that define the numerical model, such as the geometrical and mechanical properties or the support conditions, the physical meaning of the updated values can be easily interpreted and validated.

The finite element model updating is used in this chapter to calibrate and validate the model of the Alverca railway viaduct. Updating a numerical model is not straightforward and should be used carefully since minimising the objective function does not always guarantee that the model is closer to reality. In order to validate the procedures used in model updating, a simple railway bridge is considered in Appendix C.

7.2.6.1 Sensitivity analysis

Before performing an optimisation process, a sensitivity analysis should be carried out in order to identify and select the variables that most influence the terms considered in the objective function. In finite element model updating, the input variables are the parameters of the numerical model and the output variables are the terms of the objective function.

Sensitivity analyses can be classified as either local or global. In a local sensitivity analysis, the sensitivity of an input variable can be assessed by changing its value and evaluating the influence on the output variables while keeping the values of the remaining input variables constant. However, if a strong correlation exists between the uncertainties in an input distribution and output distribution then it is preferable to use a global sensitivity analysis in which all variables are varied simultaneously (Iman & Hora, 1990). The techniques for generating random observations from probability distributions and for determining the correlation between variables form the building blocks of global sensitivity analyses.

The Monte Carlo simulation is widely used for generating random sampling and the only requirement is that the input variables of the model can be described by probability density functions (McKenzie *et al.*, 2008). This method is based on repeated random sampling from the assumed input probability distributions and subsequent calculation of a set of sample values for the output distribution. The Monte Carlo simulation is a full distribution technique, i.e., at each iteration the entire statistical range of each input variable is available for sampling. If the size of the sample is large, the Monte Carlo method often leads to good results; otherwise, it may lead to clustering of sampling in some parts of the distribution while other parts are not sampled at all. The Latin hypercube sampling and sectioning methods can be used to reduce the sample size drawn from the distribution while preserving the statistics. The Latin hypercube sampling, adopted in the present thesis, is a stratified-random procedure in which the cumulative distribution function is first partitioned into nonoverlapping intervals of equal probability, in line with the number of required iterations. This represents a significant improvement over the conventional full distribution techniques and may reduce significantly the computational cost.

The probabilistic dependence between the input and output variables can be calculated using parametric correlation coefficients, such as the Pearson product-moment correlation coefficient, or nonparametric, such as the Spearman or Kendall rank correlation coefficients (Garthwaite *et al.*, 2002). Parametric methods make several assumptions such as that the input variables consist of values on an interval or ratio measurement scale and follow a normal distribution (Corder & Foreman, 2014). Nonparametric methods do not depend on distributional assumptions and can also be used with numbers that are classified in the nominal or ordinal scale. Also, for input values with different magnitudes, the Spearman coefficient is less sensitive than the Pearson coefficient (Ribeiro, 2012). Therefore, the Spearman coefficient is used for calculating the probabilistic dependence between the input and output variables.

7.2.6.2 Optimisation algorithms

Optimisation algorithms are applied in almost every branch of science and technology. In this work, these techniques are used to update the parameters of the numerical model in order to get a better agreement between the numerical response and the measured data. The measure of goodness of fit is the objective function, which might be, for example, a weighted sum of the differences between the numerical and experimental modal parameters, and the constraints of the problem are the ranges of valid values for the parameters.

There are several optimisation techniques to find the minimum of a function such as direct search methods, gradient-based methods and evolutionary algorithms (Everitt, 1987; Bäck, 1996; Ribeiro, 2012). The choice of the method depends on the characteristics of the objective function (e.g., continuity and differentiability) and the type of constraints considered (unconstrained, linearly constrained or nonlinearly constrained).

The direct search algorithms do not require the explicit evaluation of any partial derivatives of the objective function and are generally used when the objective function or its partial derivatives are discontinuous. Generally, these methods are not very robust and efficient and should only be used when there is no alternative method available (Everitt, 1987). The gradient methods require the evaluation of the objective function and its partial derivatives. Most of them are based on quadratic functions but can be applied iteratively to minimise general functions (Gill *et al.*, 1981; Everitt, 1987).The evolutionary algorithms are based on the model of organic evolution which was formulated for the first time by Charles Darwin (Bäck, 1996; Ribeiro *et al.*, 2012). The parameters of the numerical model are referred as the population. An important principle is that the changes in population follow the principle of natural selection, which favours the individuals that are fitter for survival and further evolution. Another important factor is the existence of small variations between the parents and their offspring, which are called mutations. These mutations only prevail through selection if they prove their worth in light of the current environment;

otherwise, they perish. The natural evolution towards populations with individuals of higher quality will lead to the minimisation of the objective function.

7.2.6.3 Automatic mode pairing

The objective function used to perform the model updating of the Alverca viaduct is a weighted sum of the differences between the numerical and experimental natural frequencies and mode shapes. The experimental and numerical natural frequencies are easy to compare, whereas evaluating the correlation between the experimental and numerical mode shapes is not a straightforward task. There are several criteria that can be used to evaluate the correlation between the two mode shapes (Brehm, 2011). One of the criteria is the modal scale factor which is a nonnormalised indicator that significantly depends on the scaling of the two vectors. The most widely used indicator is the Modal Assurance Criterion (MAC), which does not depend on the scaling of the two mode shapes and it is straightforward to implement. Several other criteria have been developed based on the MAC, such as the linear MAC, coordinate MAC, enhanced coordinate MAC and weighted MAC (Brehm, 2011). However, these criteria might fail for certain conditions, especially when trying to identify local modes of vibration (Brehm, 2011). Brehm (2011) developed the energy-based MAC that takes into account the stiffness distributions of the model and can be applied to systems with several weakly coupled substructures.

In the optimisation process, the natural frequencies and mode shapes have to be calculated for each combination of values of the parameters of the numerical model. Since the natural frequencies are sorted in ascending order, the ordering of the mode shapes might change. Therefore, an automatic mode pairing technique is an essential requisite for performing the optimisation process. Since in the present thesis only the first numerical and experimental global modes of the Alverca viaduct are correlated, the MAC defined by Eq. (7.1) is used.

$$MAC_{ij} = \frac{\left(\hat{\Phi}_i^T \hat{\Phi}_j\right)^2}{\left(\hat{\Phi}_i^T \hat{\Phi}_i\right)\left(\hat{\Phi}_j^T \hat{\Phi}_j\right)} \tag{7.1}$$

The variables $\widehat{\Phi}_i$ and $\widehat{\Phi}_j$ are the reduced eigenvectors of modes i and j containing only the selected degrees of freedom. The MAC value ranges from zero to one, with one indicating a perfect correlation between the two vectors and zero indicating that there is no correlation. The automatic mode pairing is performed by selecting the pairs of mode shapes with the highest values of MAC.

7.2.6.4 Optimisation of the mesh

The numerical model illustrated in Fig. 7.7 is optimised in this section in order to reduce the size of the finite element mesh and decrease the computational cost. The several models considered in the optimisation process are listed in Table 7.3, with the main differences illustrated in Fig. 7.13.

Table 7.3 – Numerical models of the Alverca viaduct.

Model	Modifications
Model A	Model with the most refined mesh
Model B	Based on model A; decreased the number of elements along the U beam transverse and vertical directions
Model C	Based on model B; decreased the number of elements along the slab transverse direction
Model D	Based on model C; decreased the number of elements along the cantilever transverse direction
Model E	Based on model D; decreased the number of elements along the ballast wall vertical direction
Model F	Based on model E; decreased the number of elements along the longitudinal direction

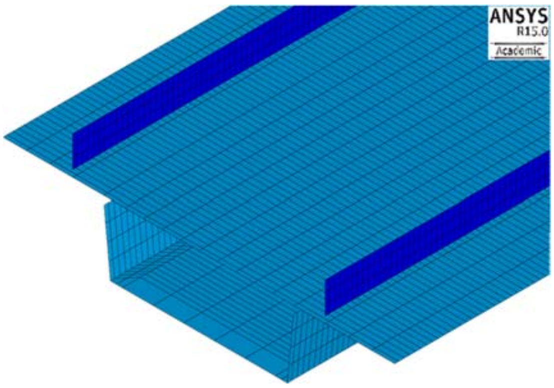

(a) Model A

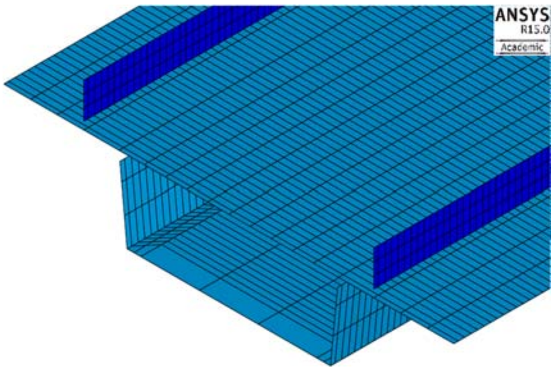

(b) Model B

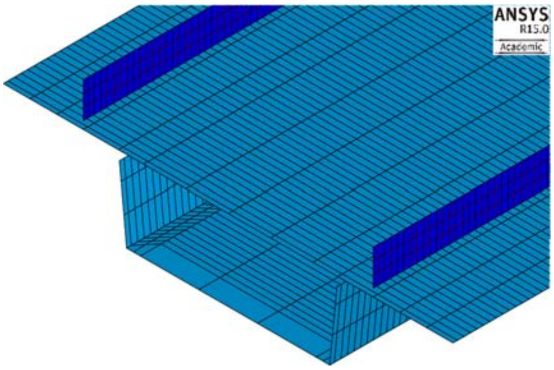

(c) Model C

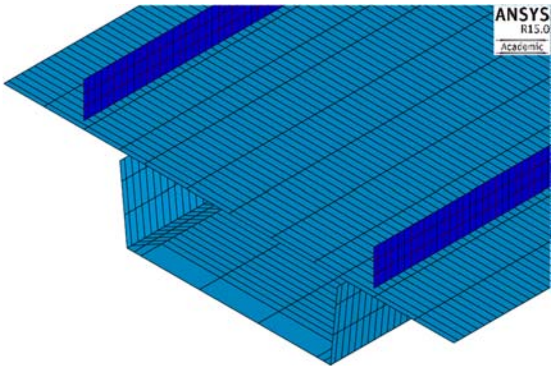

(d) Model D

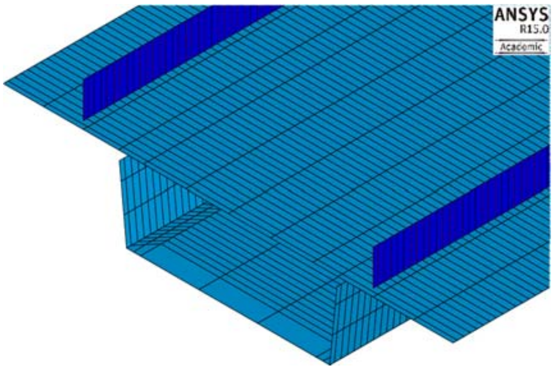

(e) Model E

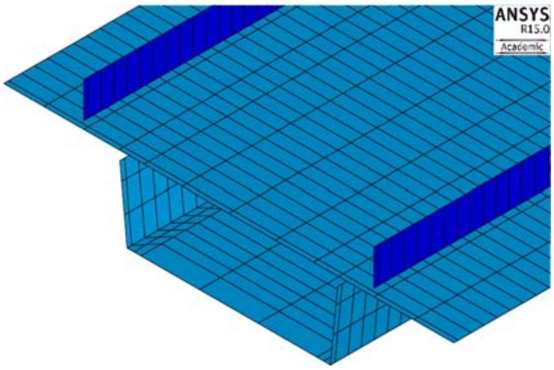

(f) Model F

Figure 7.13 – Numerical models of the Alverca viaduct.

The relative differences between the natural frequencies of the different numerical models and the MAC values between the mode shapes are listed in Tables 7.4 and 7.5, respectively, and are used to compare the modal behaviour of the different models.

Table 7.4 – Differences between the natural frequencies of the numerical models.

Models	Mode				
	1G	2G	3G	4G	5G
Model B / Model A	-0.1%	0.0%	0.0%	0.1%	0.0%
Model C / Model B	-0.2%	-0.2%	-0.4%	-0.5%	-0.1%
Model D / Model C	0.0%	0.0%	0.0%	0.0%	0.0%
Model E / Model D	0.0%	0.0%	0.0%	0.0%	0.0%
Model F / Model E	-0.9%	-0.9%	0.1%	1.7%	-0.7%

Table 7.5 – MAC values between the mode shapes of the different numerical models.

Models	Mode				
	1G	2G	3G	4G	5G
Model B / Model A	1.0	1.0	1.0	1.0	1.0
Model C / Model B	1.0	1.0	1.0	1.0	1.0
Model D / Model C	1.0	1.0	1.0	1.0	1.0
Model E / Model D	1.0	1.0	1.0	1.0	1.0
Model E / Model F	0.99	0.99	1.0	0.99	1.0

A good agreement can be observed between almost all the models. Therefore, model F is adopted from this point forward. The mesh spacing of the slab located underneath the ballast and that of the ballasted track model described in Section 6.3.6 are the same. The natural frequencies of the first five global vibration modes of model F are listed in Table 7.6.

Table 7.6 – Natural frequencies of the first five global vibration modes of model F.

Mode	Natural frequency (Hz)
1G	6.39
2G	6.34
3G	9.07
4G	11.85
5G	17.10

The number of d.o.f. of all the models and the elapsed times for calculating the first 20 vibration modes are given in Table 7.7. All the calculations have been performed using a desktop computer with an Intel i7-4790 quad core processor running at 3.6 GHz.

Table 7.7 – Number of d.o.f. of the models and elapsed times of the modal analyses.

Model	Number of d.o.f.	Elapsed time (s)
Model A	755131	828
Model B	712867	84
Model C	562927	53
Model D	541795	55
Model E	499531	51
Model F	242530	21

The optimisation of the finite element model of the viaduct lead to a reduction of the number of d.o.f. from 755131 to 242530 (68% reduction) and of the elapsed time of the modal analysis from 828 to 21 s (98% reduction).

7.2.6.5 Model updating of the Alverca viaduct

The numerical and experimental responses are compared in this section is order to validate and calibrate the numerical model of the Alverca viaduct. The experimental and numerical natural frequencies of the first five global vibration modes, their relative differences and the MAC values between the corresponding mode shapes are listed in Table 7.8. All the numerical natural frequencies are lower than the experimental frequencies. There is a good agreement between the shapes of the first three experimental and numerical vertical bending vibration modes. Mode 5G, which is also associated with the bending of the spans, shows a reasonably high MAC value but a significant difference between the natural frequencies. The poor agreement observed for the torsional vibration mode might mean that the values adopted for the geometrical and mechanical properties or some modelling aspects, such as the joints and support conditions, could be defined more accurately.

Table 7.8 – Experimental and numerical natural frequencies and MAC values.

Mode	Natural frequency			MAC
	Experimental (Hz)	Numerical (Hz)	δ (%)	
1G	6.76	6.39	-5.5%	0.98
2G	6.95	6.34	-8.8%	0.95
3G	9.65	9.07	-6.0%	0.98
4G	13.04	11.85	-9.1%	0.77
5G	20.94	17.10	-18.3%	0.90

A finite element model updating is performed in order to improve the values adopted for the geometrical and mechanical properties. The parameters considered in the optimisation process as well as their statistical properties and initially adopted values have been defined by Malveiro *et al.* (2013) and are listed in Table 7.9. The finite element model updating performed by Malveiro *et al.* (2013) used a model with a coarse mesh. The modal parameters of this model and those of the model developed in this thesis are significantly different, and therefore it has been necessary to improve the model updating.

Table 7.9 – Statistical properties of the optimisation parameters.

Parameter	Distribution type	Mean value / Standard deviation	Bound constraints	Adopted value	Unit
e_c	Normal	0.27 / 0.0056	[0.26, 0.28]	0.27	m
ρ_c	Normal	2446.5 / 122.3	[2245.9, 2647.1]	2469.8	kg/m^3
E_{c1}, E_{c2}, E_{c3}	Normal	35.4 / 4.3	[28.4, 42.4]	35.4	GPa
E_c	Normal	40.9 / 4.9	[32.9, 49.0]	40.9	GPa
e_{bal}	Normal	0.25 / 0.013	[0.23, 0.27]	0.25	m
ρ_{bal}	Uniform	1875 / 129.9	[1650, 2100]	2039	kg/m^3
E_{bal}	Uniform	140 / 34.6	[80, 200]	145	MPa
K_v	Uniform	5400 / 2020.7	[1900, 8900]	5200	MN/m
k_{h1}, k_{h2}, k_{h3}	Uniform	3.35 / 0.89	[1.8, 4.9]	3.6	MN/m

The objective function used in the sensitivity analyses and by the optimisation algorithm is defined by

$$f = a\sum_{i=1}^{n}\frac{\left|f_i^{num} - f_i^{\exp}\right|}{f_i^{\exp}} + b\sum_{i=1}^{n}\left(1 - MAC\left(\phi_i^{num}, \phi_i^{\exp}\right)\right) \tag{7.2}$$

where the superscripts *exp* and *num* denote experimental and numerical values, respectively. The variables f_i and ϕ_i are the natural frequencies and mode shapes and n is the number of vibration modes. Since all the terms of the objective function range from zero to one, the weighting factors a and b are assumed to be equal to one.

The sensitivity analysis was performed by Malveiro *et al.* (2013) in order to identify the variables that most influence the terms considered in the objective function. The Spearman correlation matrix plotted in Fig. 7.14 was obtained using 800 samples generated by the Latin Hypercube method (see Section 7.2.6.1). This sensitivity analysis takes into account the first three global vibration modes (see Fig. 7.10) and the first three local vibration modes (Malveiro *et al.*, 2013). The values in the interval [-0.25, 0.25] were filtered to highlight the parameters that most influence the objective function. As can be observed, the value of the objective function is significantly influenced by the modulus of elasticity and density of the concrete and by the longitudinal stiffness of the supports. Conversely, the thicknesses of the upper slab and of the ballast, the modulus of elasticity and density of the ballast and the vertical stiffness of the supports have lower correlation coefficients and are not considered in the model updating performed in this section. Also, only the terms of the objective function associated with the first three global vibration modes are considered in this study.

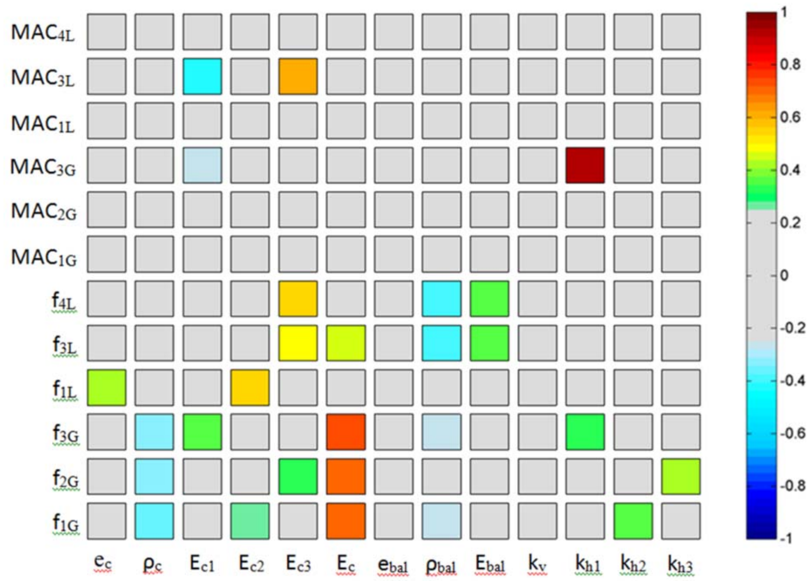

Figure 7.14 – Spearman correlation matrix.

The model updating of the railway viaduct is performed using the MATLAB function *fmincon* with the options *interior-point*, *sqp* or *active-set* (see Appendix C). A tolerance of 0.1 is used in all algorithms for the value of the objective function. Figure 7.15 shows the relation between the value of the objective function and the iteration number obtained using the active set algorithm. The sum of the absolute relative differences between the initial and optimised parameters is also represented in the figure. An important limitation of the objective function considered in this study is that the statistical properties of the parameters such as the distribution type and standard deviation are not taken into account. That is, if the mean value and the lower or upper bounds of an optimisation parameter lead to the same value of the objective function, they are equally valid. However, for example, in a normal distribution, the probability density is zero at the lower and upper bounds and maximum at the mean value. The adopted objective function does not take into account these statistical properties. Thus, some measure of engineering common sense is also required when choosing the optimised values of the numerical parameters. If two different sets of parameters have similar values of the objective function, the set that leads to the lowest absolute relative differences between the adopted and optimised values should be chosen.

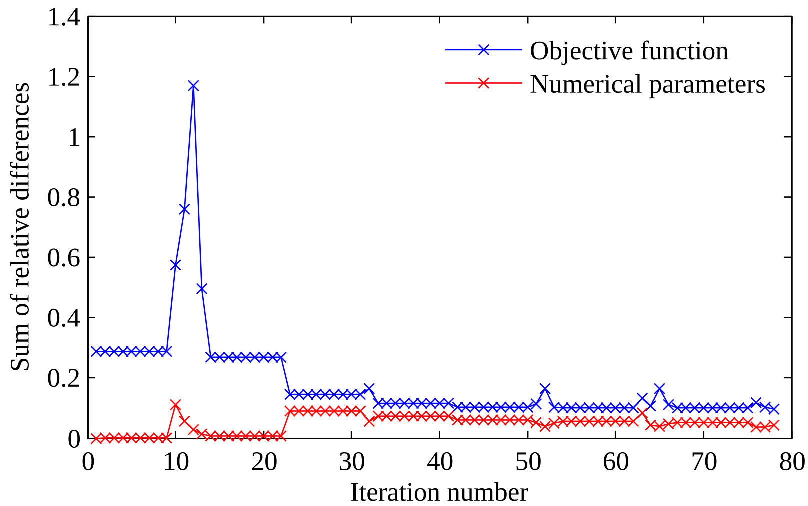

Figure 7.15 – Value of the objective function and sum of the absolute relative differences between the initial and optimised parameters.

The evolution of the numerical parameters and their respective lower and upper bounds is shown in Fig. 7.16. The optimum solution of the modulus of elasticity of the concrete of the prefabricated beam converges quickly to the upper limit which is in line with the fact that the natural frequencies of the initial numerical model are lower than the experimental frequencies (see Table 7.8). The longitudinal stiffness of the supports remains constant throughout the iterations and therefore does not significantly influence the value of the objective function.

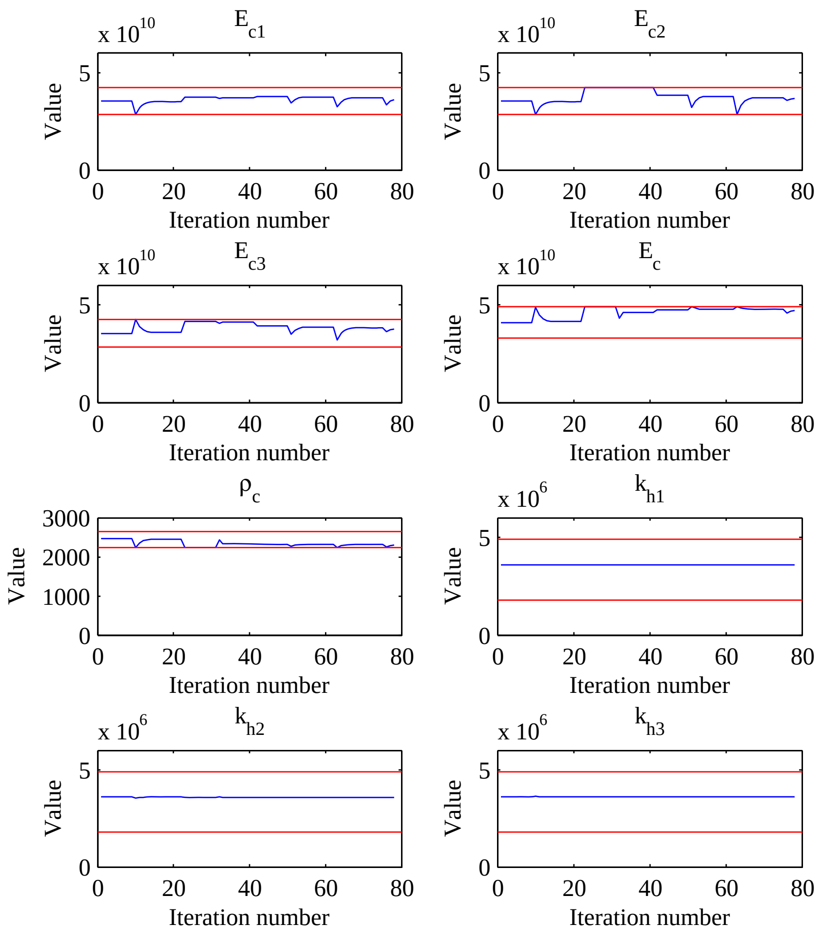

Figure 7.16 – Values and bounds of the numerical parameters.

The values of each term of the objective function defined by Eq. (7.2) as a function of the iteration number are plotted in Fig. 7.17. As can be observed, all terms converge to small values.

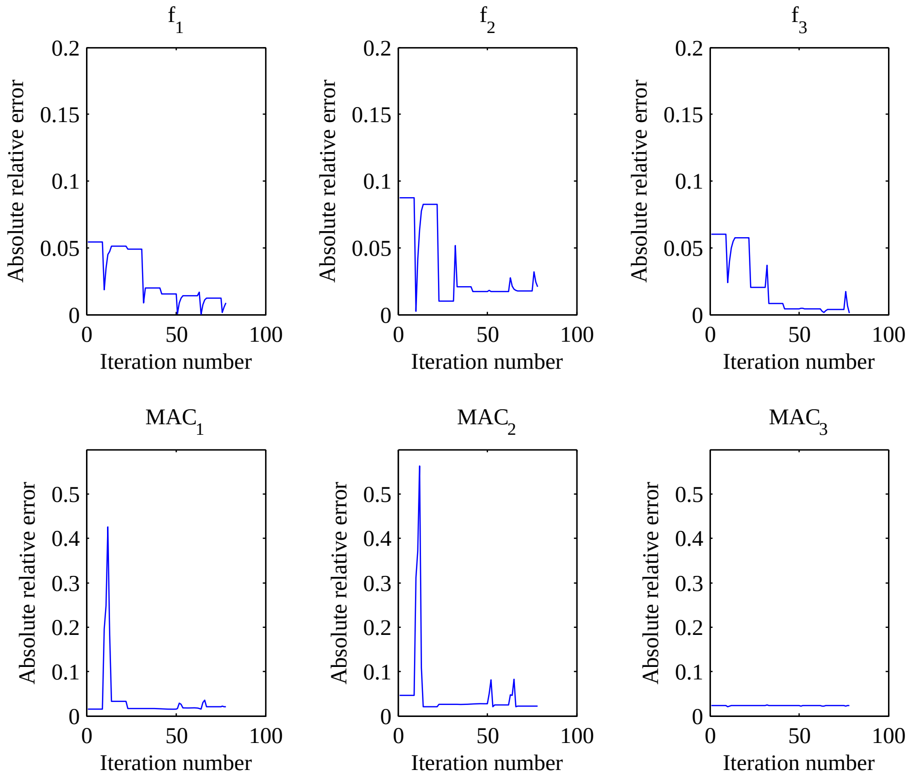

Figure 7.17 – Absolute relative error of each term of the objective function.

The optimised values of the parameters of the numerical model obtained using the MATLAB function *fmincon* with the options *interior-point*, *sqp* or *active-set* (see Appendix C), and the relative differences between these and the initially adopted values are shown in Table 7.10. Aside from the modulus of elasticity of the concrete of the prefabricated beam, all other parameters do not show a very significant variation.

Table 7.10 – Optimised values of the parameters and relative difference between these and the initially adopted values.

Parameter	*interior-point*		*active-set*		*sqp*	
	Optimised	δ (%)	Optimised	δ (%)	Optimised	δ (%)
E_{c1}	36.9	4.3	36.2	2.3	37.5	6.0
E_{c2}	36.6	3.5	36.8	3.9	38.0	7.3
E_{c3}	37.6	6.3	37.6	6.3	38.7	9.3
E_c	47.1	15.0	47.2	15.3	47.5	16.0
ρ_c	2346.2	-5.0	2299.3	-6.9	2363.3	-4.3
k_{h1}	3.4	-6.7	3.6	0.1	3.6	0.1
k_{h2}	3.4	-6.8	3.6	-0.3	3.6	-0.3
k_{h3}	3.4	-6.6	3.6	0.3	3.6	0.2

The natural frequencies obtained using the model with the optimised values of the numerical parameters, the MAC values between the numerical and experimental mode shapes and the corresponding terms of the objective function are shown in Table 7.11. The total number of iterations, the average absolute relative difference between the optimised and initial values of the numerical parameters ($\bar{\delta}$) and the value of the objective function are listed in Table 7.12. All the three options converge to the same value of the objective function, but the option *active-set* leads to the lowest values of the average relative difference between the initial and optimised values. Thus, the corresponding parameters are used in the optimised numerical model of the Alverca viaduct. The *sqp* option required a significantly lower number of iterations to converge to the optimised solution and might be the best approach when the computational efficiency is an issue.

Table 7.11 – Natural frequencies, MAC values and values of the objective function.

Mode	*interior-point*			*active-set*			*sqp*		
	f (Hz)	MAC	Obj. func.	f (Hz)	MAC	Obj. func.	f (Hz)	MAC	Obj. func.
1G	6.78	0.98	0.02	6.82	0.98	0.03	6.82	0.98	0.03
2G	6.76	0.98	0.05	6.79	0.98	0.04	6.80	0.98	0.04
3G	9.61	0.98	0.03	9.64	0.98	0.03	9.64	0.98	0.02

Table 7.12 – Summary of the optimisations performed with the three *fmincon* options.

Algorithm	Iterations	$\bar{\delta}(\%)$	Objective function value
interior-point	82	6.8	0.10
active-set	78	4.4	0.10
sqp	54	5.4	0.10

7.2.7 Damping of the viaduct

The damping of the railway track is defined in Section 6.3.5. The damping of the viaduct is described in Jorge (2013) and is summarised in this section. The modal damping ratios listed in Table 7.2 are plotted in Fig. 7.18.

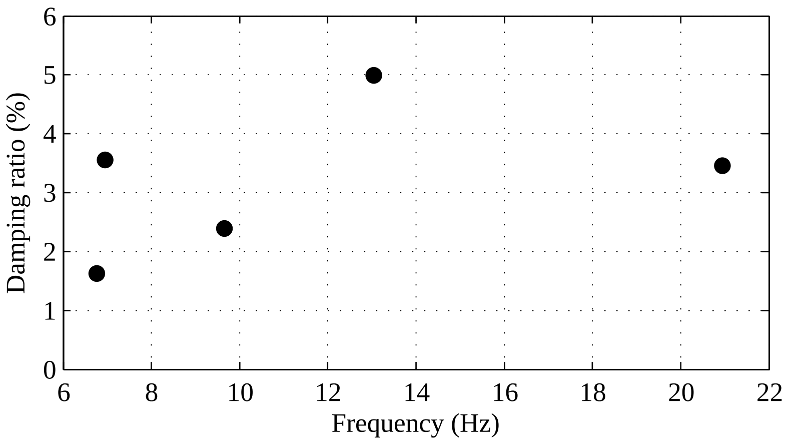

Figure 7.18 – Modal damping ratios of the global vibration modes.

When the dynamic response of a system is calculated using the mode-superposition method, the total response is given by the sum of the uncoupled modal responses of each mode of vibration and the damping of the system can be defined in terms of the different modal damping ratios of each mode. When step-by-step numerical integration techniques are used for directly solving the equations of motion in their original coupled form, the damping of the system cannot be defined in terms of the modal damping ratios and an explicit damping matrix has to be used. The damping matrix of the viaduct is formulated assuming Rayleigh damping, which only ensures the damping ratios of two vibration modes. In order to derive a damping matrix that best fits the damping ratios shown in Fig. 7.18, it is necessary to identify which vibration modes contribute most to the dynamic response of the system. Therefore, the dynamic response of the viaduct when subjected to the passage of the KHST has been evaluated in Jorge (2013) using the MATLAB code developed by Ribeiro (2012), which uses the mode-superposition method to solve the equations of motion of the viaduct. This study concludes that the global vibration modes 2G and 3G are those that contribute most to the dynamic response of the system. The viscous damping ratios of 3.4% and 3.35% are considered for the frequencies 6.4 and 61 Hz, respectively, in order to obtain the best fit of the modal damping ratios of the global vibration modes. This leads to the damping factors $a_0 = 2.48\ s^{-1}$ (mass proportional) and $a_1 = 1.58 \times 10^{-4}$ s (stiffness proportional). The relationship between frequency and Rayleigh damping and the modal damping ratios of the global vibration modes are plotted in Fig. 7.19.

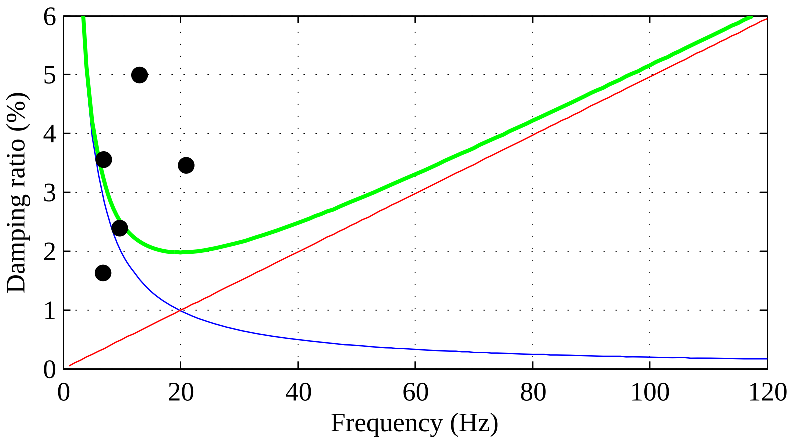

Figure 7.19 – Relationship between frequency and damping ratio (using Rayleigh damping).

7.3 DYNAMIC RESPONSE OF THE TRAIN-VIADUCT SYSTEM

The passage of the KHST over the Alverca viaduct is analysed in this section. The simplified model is used in Section 7.3.1 and the full model is used in Sections 7.3.2 to 7.3.4. The influence of the transition between plane track and viaduct, the track irregularities and the force-deflection relationship of the Hertzian contact spring are analysed in Sections 7.3.1 to 7.3.3, respectively. A comparison between the results calculated using the direct method implemented in MATLAB and the ANSYS software is presented in Section 7.3.4. Since the transitions between the plane track and viaduct are modelled in a simplified way, the boundary conditions of the first and third spans are not accurately taken into account. Therefore, only the results of the second span and vehicle are analysed in this section.

A 2D flexible track model is used to support the vehicle before and after the structure (see Section 6.4.1). Each side of the track has a length of 510 m. The following parameters of the HHT-α method are considered in all the dynamic analyses presented in this section: α = -0.05, β = 9/20 and γ = 9025/40000 (Hughes, 2000).

7.3.1 Influence of the transition between plane track and viaduct

The passage of the simplified model of the KHST over the railway viaduct is analysed in this section in order to study the influence of the transition between plane track and viaduct. A constant speed of the vehicle of 120 m/s is chosen so that the frequency of the harmonic excitation caused by the discrete support of the sleepers is similar to the frequency of vibration of the unsprung mass of the vehicle (see Section 6.4). A linear force-deflection relationship is considered for the Hertzian contact spring (see Section 3.4). The dynamic analyses are performed using a time step equal to 2.5×10^{-4} s.

The vertical displacement of the contact point and the contact force are plotted in Figs. 7.20 and 7.21, respectively. As can be observed in both figures, when the vehicle moves from the plane track to the viaduct and vice-versa, there is a significant variation of the vertical displacement and contact force. This abrupt transition is mainly caused by the deformation of the cross-section of the viaduct (see Fig. 7.22).

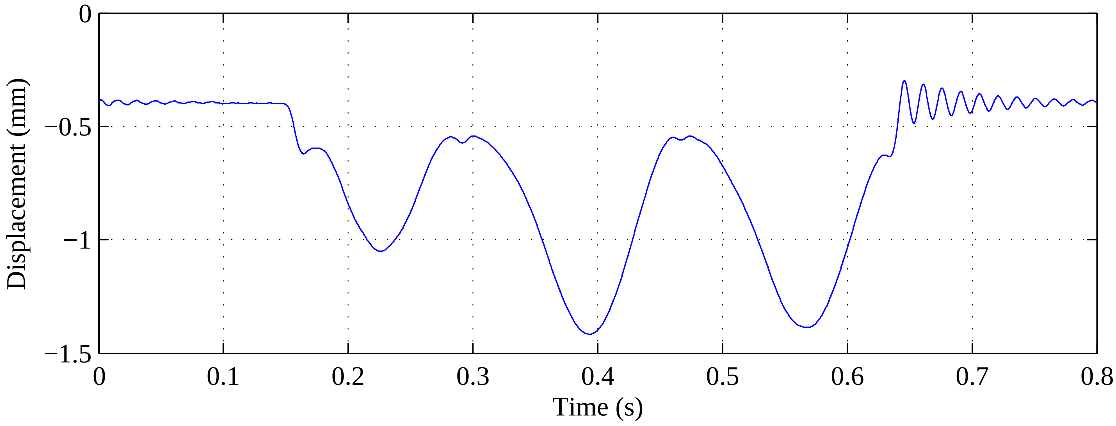

Figure 7.20 – Vertical displacement of the contact point obtained using the track without transitions.

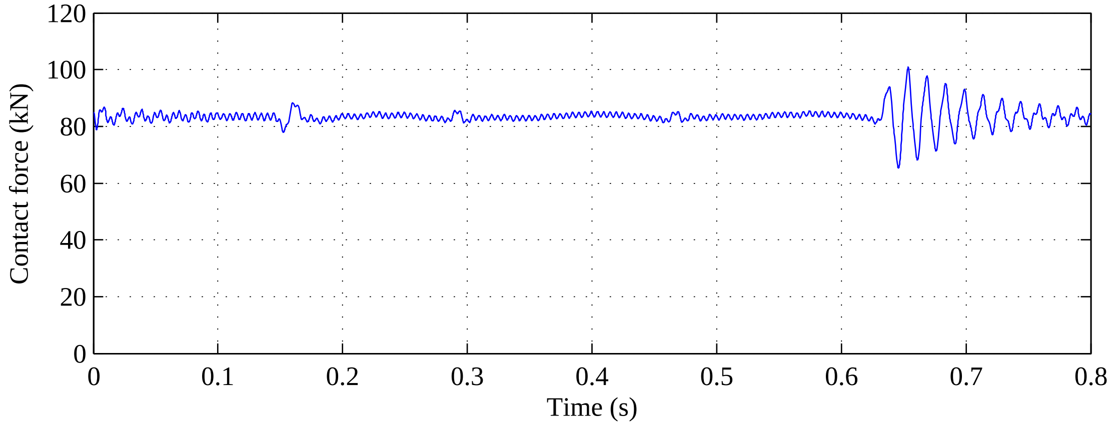

Figure 7.21 – Contact force obtained using the track without transitions.

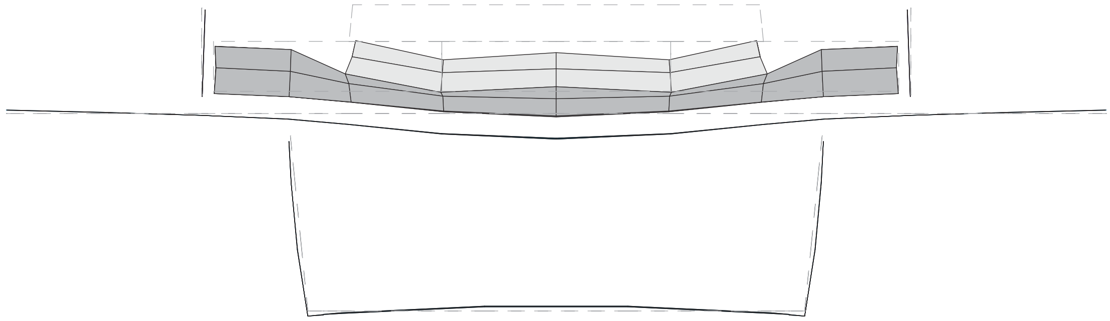

Figure 7.22 – Deformed shape of the cross-section of the viaduct.

Since studying this type of phenomenon is not the objective of this work, two transition zones with varying pad stiffness are considered before and after the viaduct. Each zone has a length of 6 m and the pad stiffness varies linearly from 500 MN/m to 125 MN/m. The vertical displacement of the contact point and the contact force obtained using the new model are plotted in Figs. 7.23 and 7.24, respectively. As can be observed, the sudden transition is still present but has a much lower magnitude.

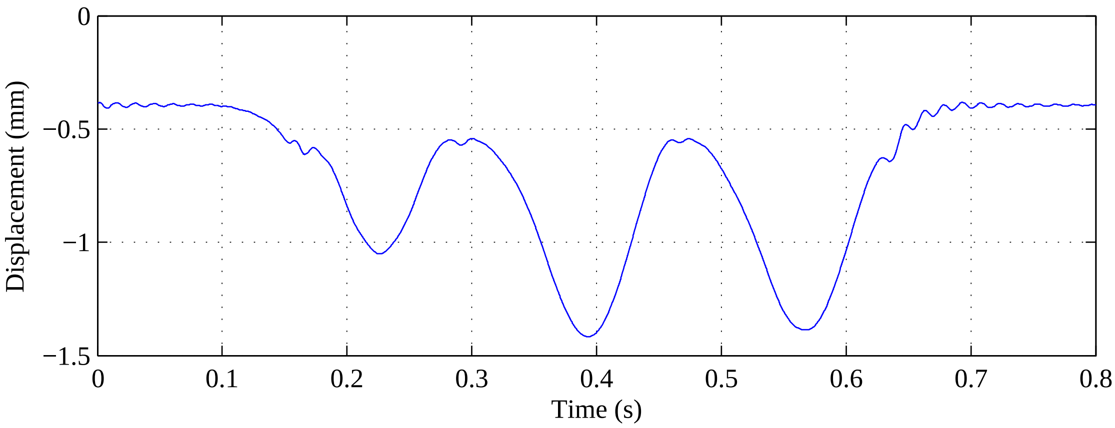

Figure 7.23 – Vertical displacement of the contact point obtained using the track with transitions.

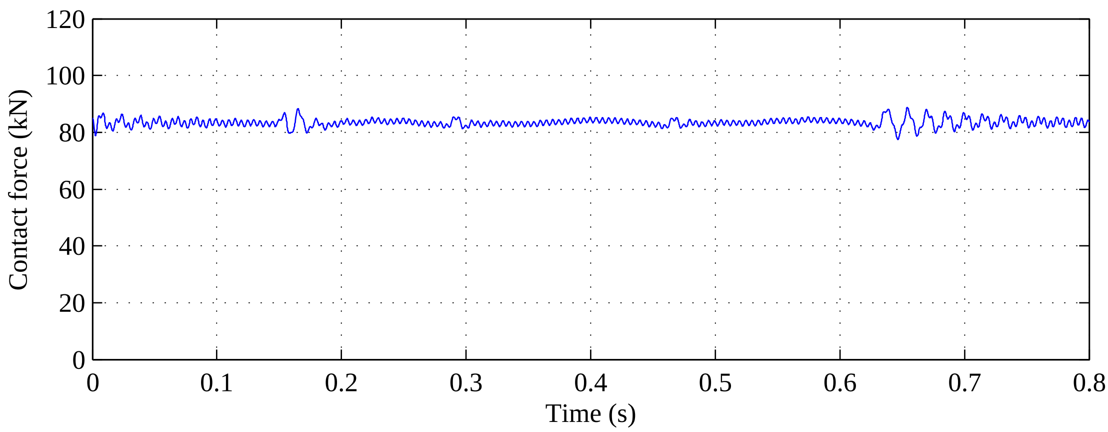

Figure 7.24 – Contact force obtained using the track with transitions.

7.3.2 Influence of the track irregularities

Track irregularities are one of the most important sources of dynamic excitation generated by the passage of a train (Esveld, 2001). If the rail is not correctly levelled and aligned, the irregularities may cause vibrations of the train and track, which in turn may cause track settlement or passenger discomfort.

The track irregularities can be classified as isolated defects (caused by weld imperfections, rail joints, etc.) or periodic irregularities (caused by track settlement, railhead corrugation due to the train traffic, etc.). The isolated defects are defined by the mean to peak value or the zero to peak value (EN 13848-1, 2003). The periodic irregularities are normally divided into short and long wavelength irregularities and are defined by the standard deviation over a defined length. The track irregularities can also be divided into four categories: alignment, longitudinal level, gauge and cross level (Iwnicki, 2006). The influence of the isolated defects and periodic irregularities of the longitudinal level of the track on the dynamic behaviour of the train-structure system is analysed in this section based on the standards EN 13848-1 (2003) and EN 13848-5 (2008).

7.3.2.1 Isolated defects

The shape and sequence of the isolated defects strongly influence the dynamic behaviour of the train-structure system. However, these characteristics are not addressed in the standard EN 13848-5 (2008). In order to generate a shape of the defect that corresponds to realistic values of the rail stresses and track forces, the following smooth function with a continuous second derivative is adopted (Vale, 2010).

$$r(x) = Ae^{-1/2\left(\bar{k}x\right)^2} \tag{7.3}$$

The parameter A is the zero to peak value and $\bar{k}$ is used to control the wavelength of the defect. The maximum mean to peak values of the isolated defects are specified in EN 13848-5 (2008) for the wavelength ranges $D1$ ($3 < \lambda \leq 25\,\text{m}$) and $D2$ ($25 < \lambda \leq 70\,\text{m}$). Since the mean to peak value is calculated over a length of at least twice the higher wavelength of each range, in practice it is reasonable to consider that the mean to peak value is equal to the zero to peak value.

A sensitivity analysis is performed to evaluate how the parameters A and $\bar{k}$ influence the dynamic response of the system. The values 0.5, 0.7 and 0.9 are considered for the parameter $\bar{k}$ and correspond to wavelengths belonging to the range $D1$. The values 10, 12 and 16 mm are adopted for the parameter A and correspond to the alert, intervention and immediate action limits defined in EN 13848-5 (2008) for the wavelength range $D1$ and the speed range $230 < V \leq 300\,\text{km/h}$. The different irregularities considered in the sensitivity analysis are plotted in Figs. 7.25 and 7.26.

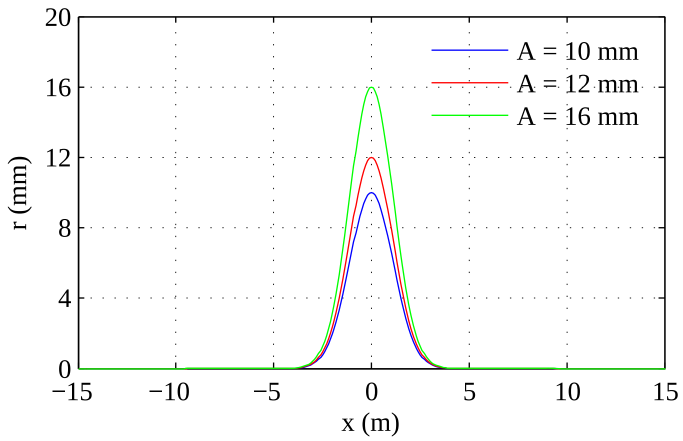

Figure 7.25 – Shape of the track isolated defects for a value of $\bar{k} = 0.9$.

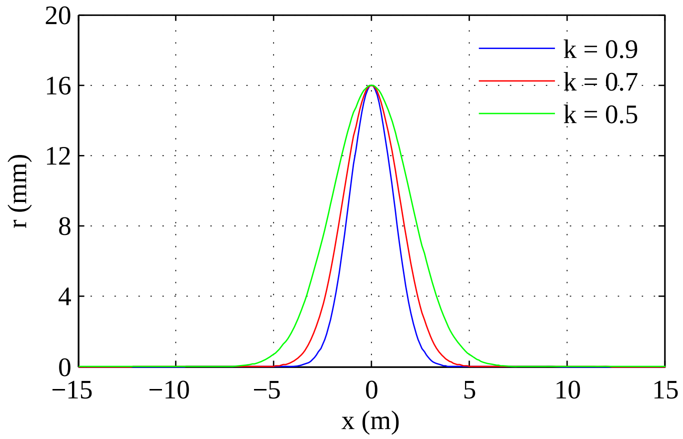

Figure 7.26 – Shape of the track isolated defects for a constant value of A = 16 mm.

The passage of the KHST over the railway viaduct is analysed for the speeds $v = 300$ and 350 km/h. The standard EN 13848-5 (2008) only defines the mean to peak value of the isolated defects for speeds up to 300 km/h. The speed of 350 km/h is also considered because current high-speed lines are designed for speeds equal to or higher than this value. The maximum design speed of the KHST is also 350 km/h. The isolated defect is considered only in the right rail in the middle of the second span, i.e., $x = 27$ m (see Fig. 7.8). The dynamic analyses are performed using a time step equal to 1×10^{-4} s in order to accurately simulate the response of the system due to the impulsive loading caused by the isolated defects.

The contact forces of the first right wheel when using a constant value of $\bar{k} = 0.9$, A = 10, 12 and 16 mm and v = 300 km/h are plotted in Fig. 7.27. As expected, an increase of the zero to peak value leads to a larger amplitude of the contact forces. In the case of A = 16 mm, there is a loss of contact between the wheel and the rail.

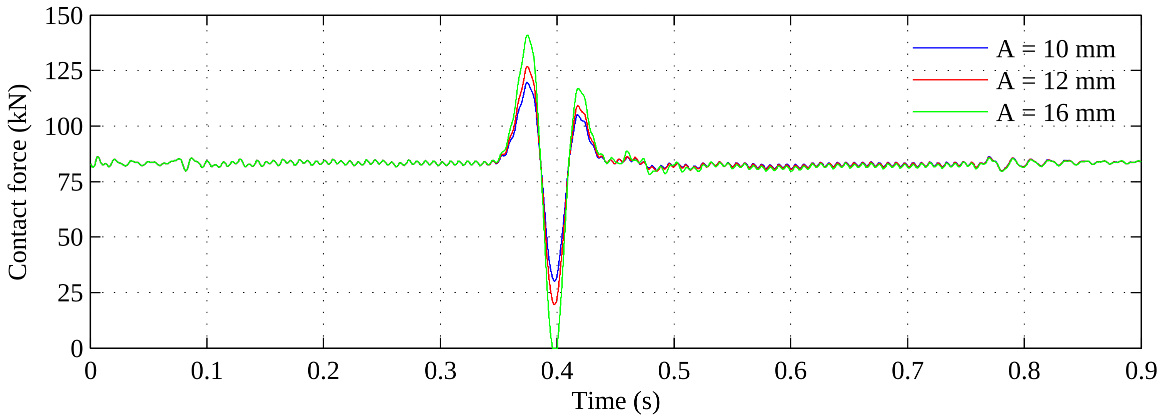

Figure 7.27 – Contact forces of the first right wheel for $\bar{k} = 0.9$.

The contact forces of the first and last right wheels for A = 16 mm are plotted in Fig. 7.28. Since the results for both wheels are similar, only the first wheel is analysed in this section.

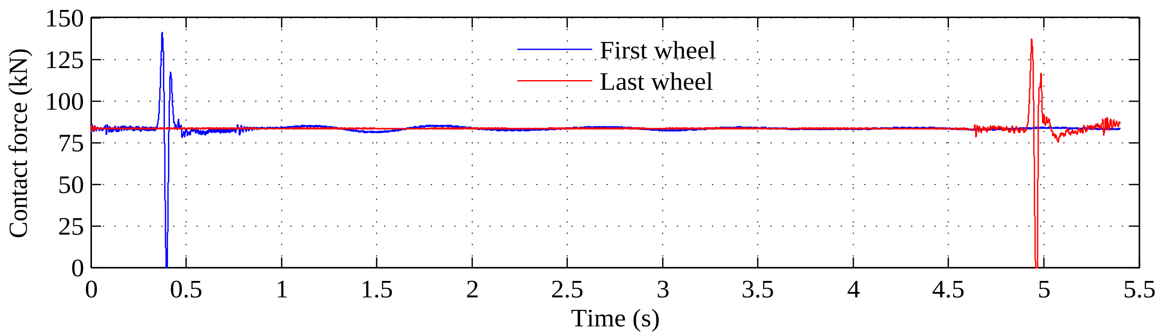

Figure 7.28 – Contact forces of the first and last right wheels for A = 16 mm.

The maximum vertical accelerations of the upper slab of the deck that occur when the first wheelset passes the isolated defect for A = 10, 12 and 16 mm are plotted in Figs. 7.29 to 7.31, respectively. Since the isolated defect is considered only in the right rail, the distribution of accelerations is not symmetrical about the centre line of the slab.

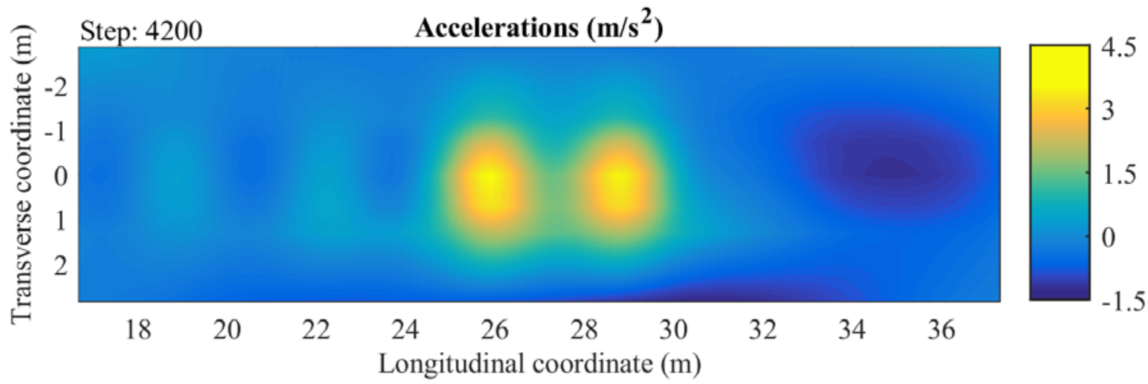

Figure 7.29 – Vertical accelerations of the upper slab of the deck for A = 10 mm and v = 300 km/h.

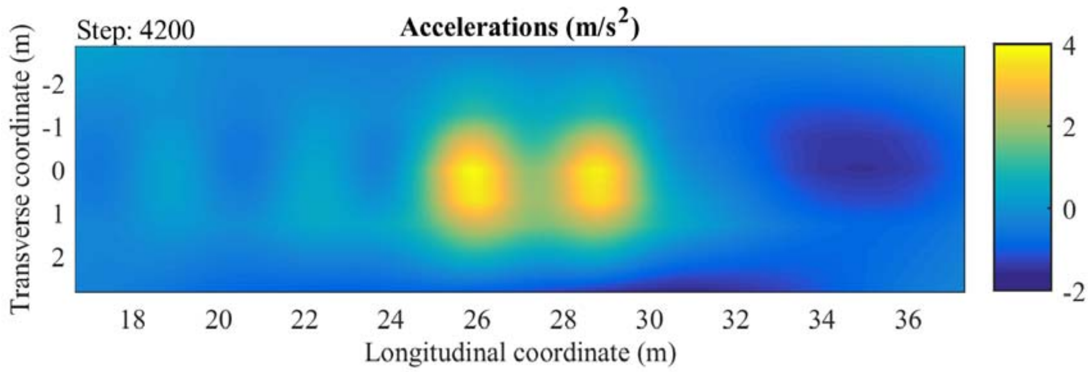

Figure 7.30 – Vertical accelerations of the upper slab of the deck for A = 12 mm and v = 300 km/h.

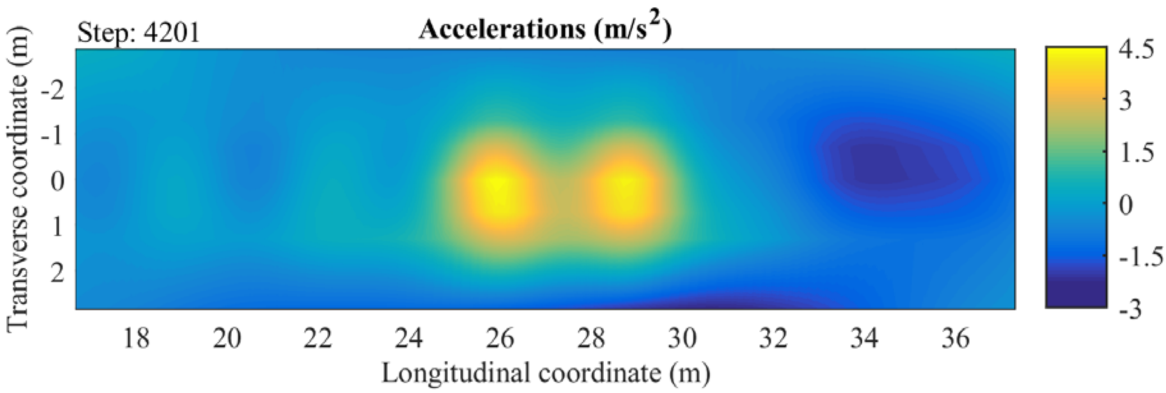

Figure 7.31 – Vertical accelerations of the upper slab of the deck for A = 16 mm and v = 300 km/h.

The high accelerations of the upper slab that occur near the contact regions are a localised phenomenon. The standard EN 1990-A2 (2005) specifies the deflection and vibration limits that must be taken into account in the design of railway bridges. These limits guarantee traffic safety in terms of, for example, vertical acceleration and torsion of the deck, and vertical and horizontal deformation of the deck. For the case of ballasted deck bridges, in order to prevent instability of the ballast, the standard specifies that the vertical acceleration of the deck should not exceed 3.5 m/s^2 (≈ 0.35g). However, this does not take into account the local deformation of the slab. The localised regions of ballast subjected to high accelerations might be confined by the surrounding ballast which has much lower accelerations. Thus it is possible that the vertical acceleration might exceed the limit without causing instability. Further studies taking into account the wheel-rail interaction and the local deformations of the slab are necessary to validate this assumption. The higher contact forces observed for the higher zero to peak values (see Fig. 7.27) do not necessarily lead to a similar increase of the upper slab accelerations.

The contact forces of the first right and left wheels when using a constant value of $\bar{k} = 0.9$, A = 10, 12 and 16 mm and v = 350 km/h are plotted in Figs. 7.32 and 7.33, respectively. There is a loss of contact between the right wheel and the rail for A = 12 and 16 mm. In the latter, this loss of contact occurs during a longer period of time, which might explain the much higher peak observed at t = 0.36 s. The isolated defect is considered only in the right rail and therefore the level of forces of the left wheel is much lower.

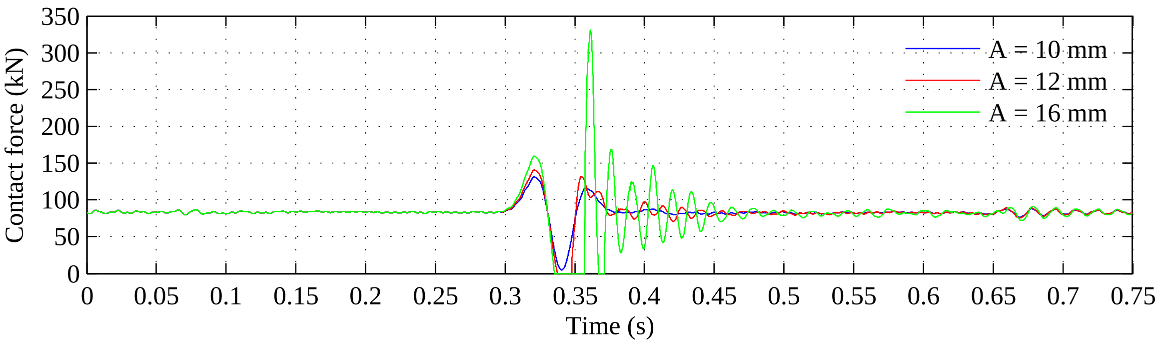

Figure 7.32 – Contact forces of the first right wheel for $\bar{k} = 0.9$ and v = 350 km/h.

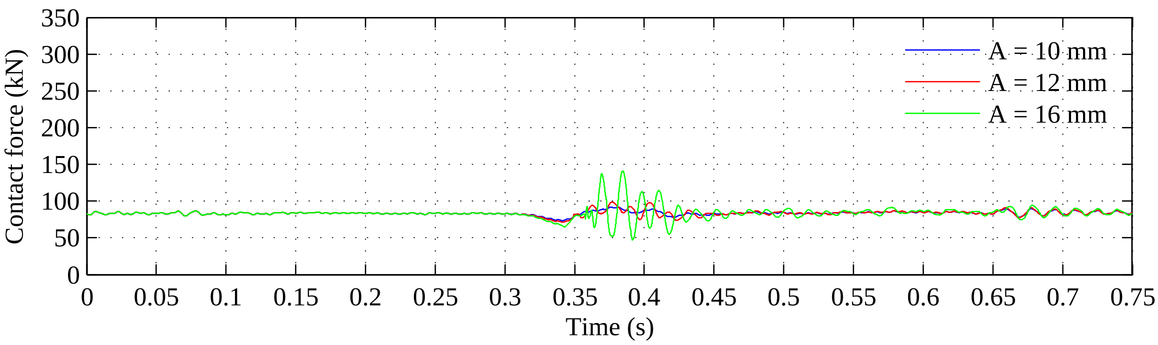

Figure 7.33 – Contact forces of the first left wheel for $\bar{k} = 0.9$ and v = 350 km/h.

The maximum values of the dynamic component of the contact forces that occur at $t = 0.37$ s for $v = 300$ km/h (X_1) and at $t = 0.32$ s for $v = 350$ km/h (X_2) are plotted in Fig. 7.34. The ratio X_2/X_1 is also shown in the figure. As can be observed, the maximum value of the contact force varies linearly with the zero to peak value for both speeds. The ratio X_2/X_1 is constant and equal to 132%. Since the speed only increases 17%, this suggests that the maximum contact forces do not vary linearly with the speed of the vehicle.

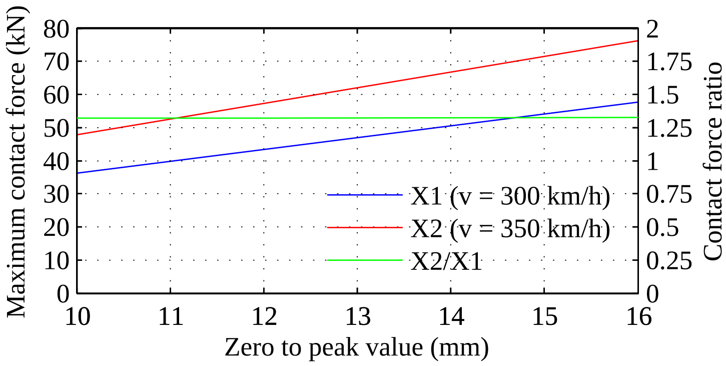

Figure 7.34 – Maximum dynamic contact forces of the first right wheel for $\bar{k} = 0.9$.

The maximum vertical accelerations of the upper slab of the deck that occur when the first wheel set passes the isolated defect when considering A = 10, 12 and 16 mm and $v = 350$ km/h are plotted in Figs. 7.35 to 7.37, respectively. As previously observed, the high accelerations of the upper slab that occur near the contact regions are a localised phenomenon. The high accelerations that occur for A = 16 mm might be associated with the fact that the loss of contact between the wheel and the rail occurs during a long period of time, which leads to a high impact force.

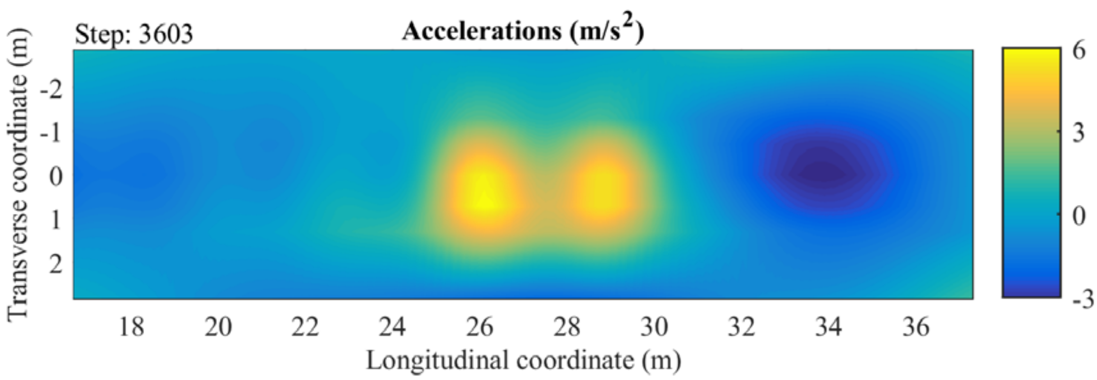

Figure 7.35 – Vertical accelerations of the upper slab of the deck for $A = 10$ mm and $v = 350$ km/h.

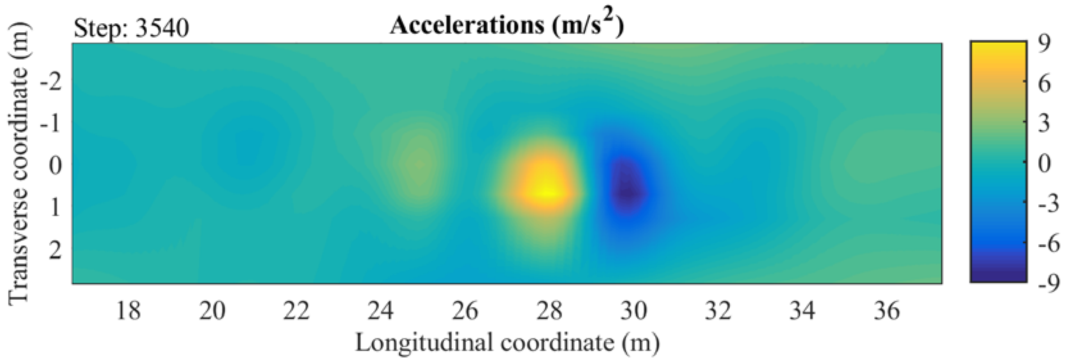

Figure 7.36 – Vertical accelerations of the upper slab of the deck for A = 12 mm and v = 350 km/h.

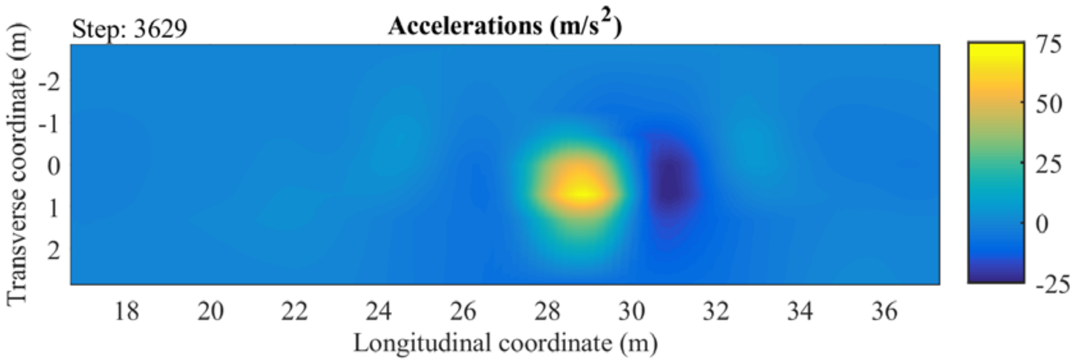

Figure 7.37 – Vertical accelerations of the upper slab of the deck for A = 16 mm and v = 350 km/h.

The contact forces of the first right wheel using a constant value of A = 16 mm, $\bar{k}$ = 0.9, 0.7 and 0.5 and v = 350 km/h are plotted in Fig. 7.38. As expected, the isolated defects with a smoother variation (see Fig. 7.26) lead to a lower variation of the contact forces. The maximum values of the dynamic component of the contact forces that occur before any loss of contact between the wheel and the rail are plotted in Fig. 7.39. As can be observed, the maximum value of the contact force does not vary linearly with the value of the parameter $\bar{k}$.

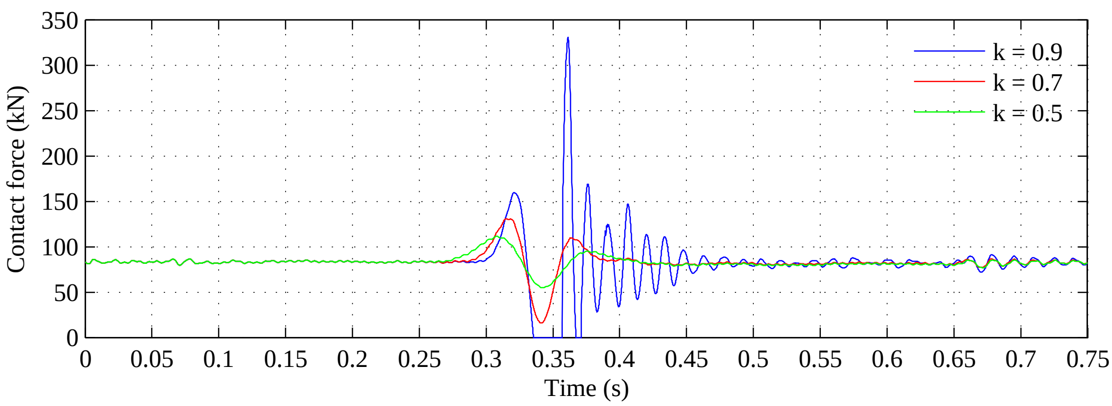

Figure 7.38 – Contact forces of the first right wheel for A = 16 mm and v = 350 km/h.

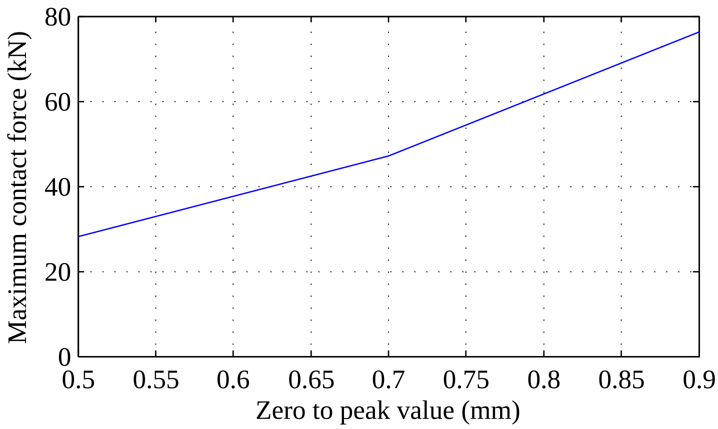

Figure 7.39 – Maximum dynamic contact forces of the first right wheel for A = 16 mm.

7.3.2.2 Periodic irregularities

The periodic irregularities considered in this study have been calculated using a MATLAB function developed by Montenegro (2015). The irregularities are defined as a stochastic Gaussian ergodic process and are generated using the modified spectral representation method described in Hu and Schiehlen (1997). The algorithm uses power spectral density functions and cosine waves with different amplitudes, frequencies and random phase angles to generate the irregularities. Since the function developed by Montenegro (2015) uses as input parameters the desired scale factors instead of the standard deviation, an iterative procedure, which generates several irregularities until the desired standard deviation is achieved, has been implemented in MATLAB.

The irregularity plotted in Fig. 7.40 is generated considering a standard deviation of 1.5 mm, which corresponds to the alert limit defined in the standard EN 13848-5 (2008). The irregularity has a total length of 70 m and starts at the beginning of the first span, i.e., $x = 0$ m (see Fig. 7.8). In order to focus on the vertical behaviour of the track, the same irregularity is applied on the left and right sides.

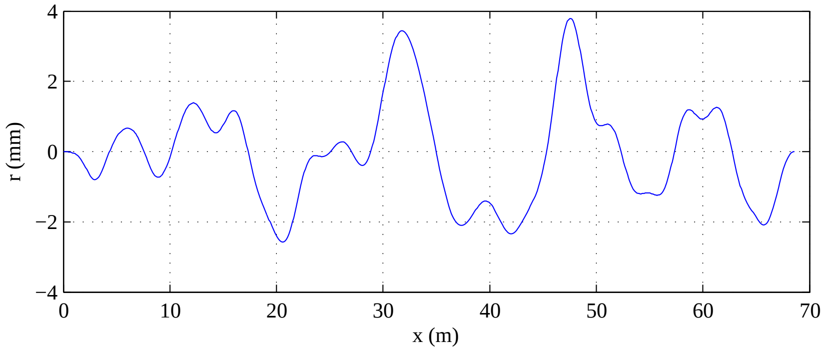

Figure 7.40 – Periodic irregularity corresponding to the alert limit.

The passage of the KHST over the railway viaduct is analysed for a speed of 120 m/s and for the cases with and without irregularities. The dynamic analyses are performed using a time step equal to 2.5×10^{-4} s. The time histories of the vertical accelerations of the upper slab in the middle of the second span are shown in Fig. 7.41. In both cases, there is a significant increase of the accelerations due to the resonant response of the structure. The maximum resonance of the first vertical vibration mode of the second span occurs for a speed of 122 m/s (Jorge, 2013). The accelerations for the case with irregularities are slightly higher than those observed for the case without irregularities, but the resonance of the structure clearly governs the dynamic response.

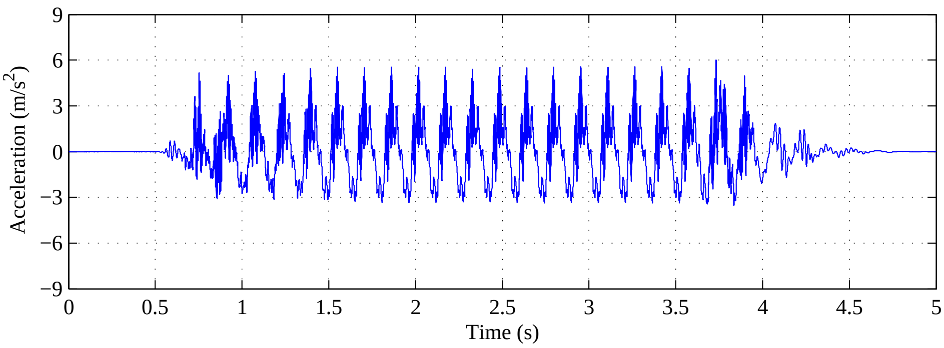

(a)

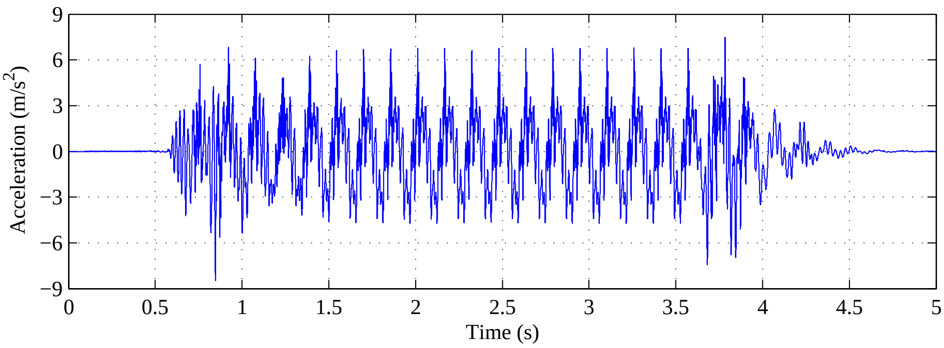

(b)

Figure 7.41 – Vertical accelerations at the midspan of the upper slab of the deck: a) without and b) with irregularities.

The contact forces of the first and last right wheels are plotted in Fig. 7.42. When the irregularities are not considered the dynamic component of the contact force is very small. For the case with irregularities, a significant variation of the contact force can be observed for both wheels. The behaviour of the contact forces is governed more by the presence of irregularities rather than the resonance of the structure.

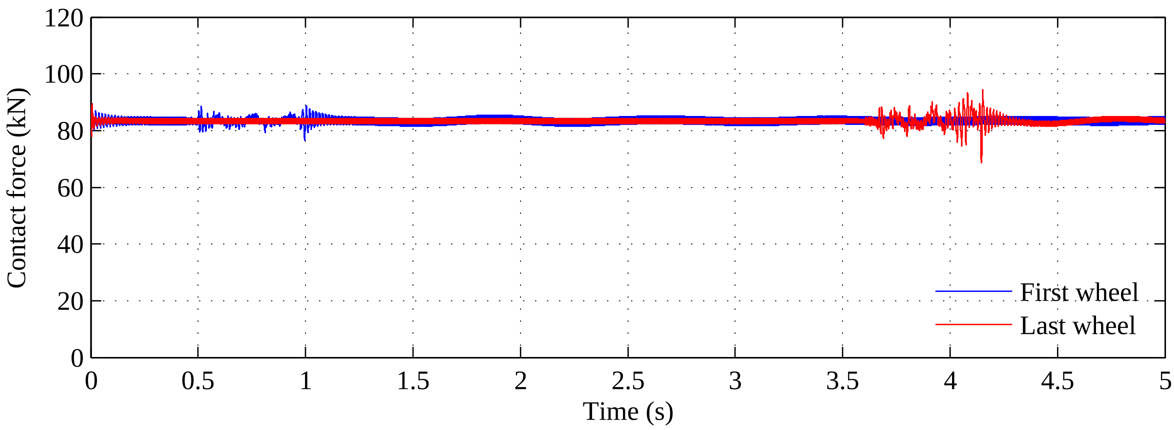

(a)

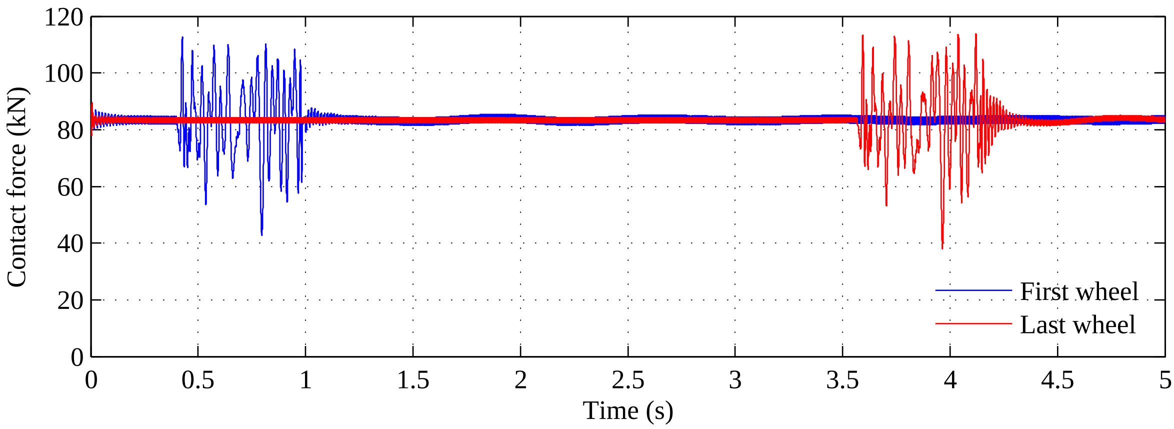

(b)

Figure 7.42 – Contact forces of the first and last right wheels: a) without and b) with irregularities.

The maximum vertical accelerations of the upper slab of the deck are plotted in Fig. 7.43. As previously observed for the isolated defects, the high accelerations of the upper slab that occur near the contact regions are a localised phenomenon.

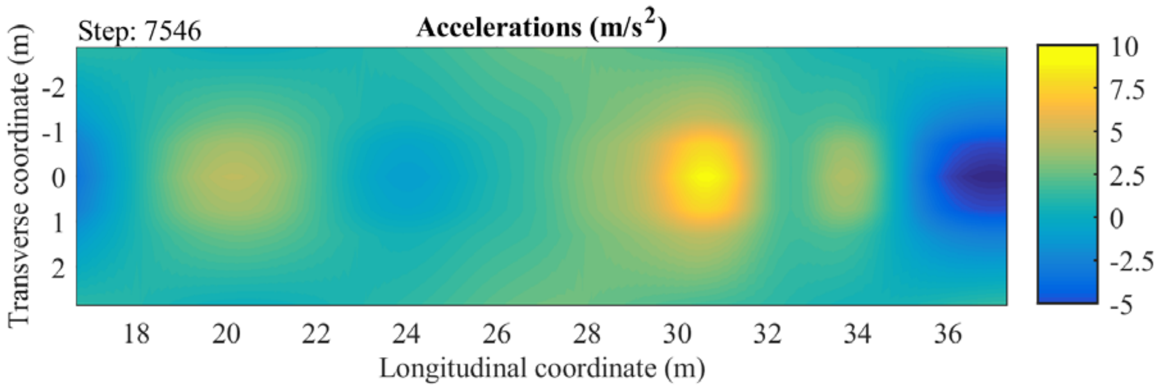

Figure 7.43 – Vertical accelerations of the upper slab of the deck.

7.3.3 Influence of the Hertzian contact spring

In this section, the influence of the force-deflection relationship of the Hertzian contact spring on the dynamic behaviour of the system when the train is subjected to a dynamic excitation caused by isolated defects and periodic irregularities is analysed. The linear and nonlinear relationships described Section 3.3 are used.

The passage of the KHST over an isolated defect using $\bar{k} = 0.9$ and $v = 350$ km/h is analysed in Section 7.3.2.1. The contact forces generated by the passage of the first right wheel of the KHST over the isolated defects with zero to peak values of 10 and 16 mm are plotted in Figs. 7.44 and 7.45, respectively. As can be observed, the results obtained using the different force-deflection relationships are very similar.

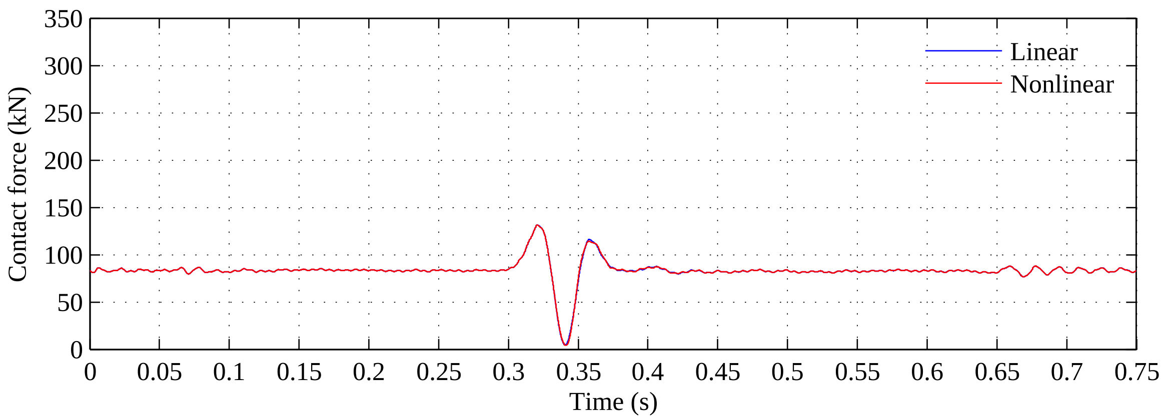

Figure 7.44 – Contact forces of the first right wheel for A = 10 mm.

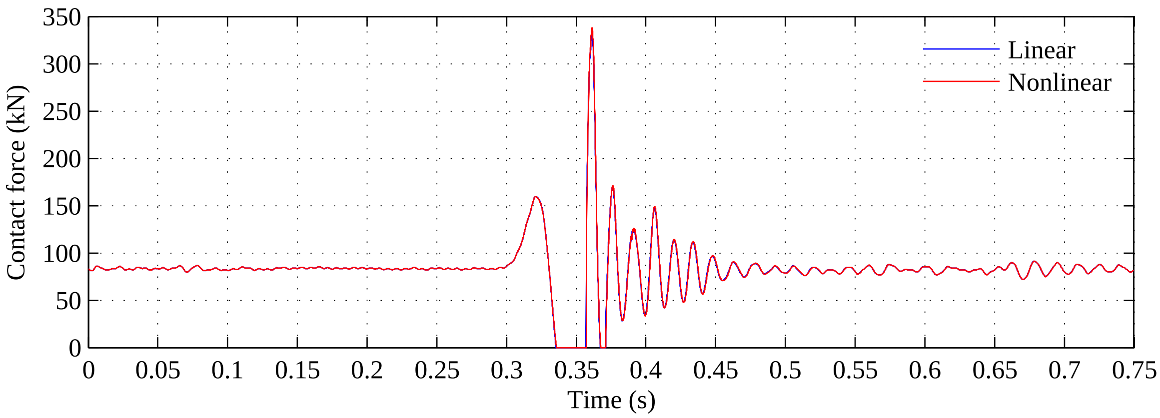

Figure 7.45 – Contact forces of the first right wheel for A = 16 mm.

The passage of the KHST over a periodic irregularity is analysed in Section 7.3.2.2. The vertical accelerations of the upper slab in the middle of the second span, the vertical displacements of the contact point and the wheel-rail contact forces are plotted in Figs. 7.46 to 7.48, respectively. Again, there is no significant difference between the two contact spring models. The differences observed in the displacements of the contact point do not influence the wheel-rail interaction.

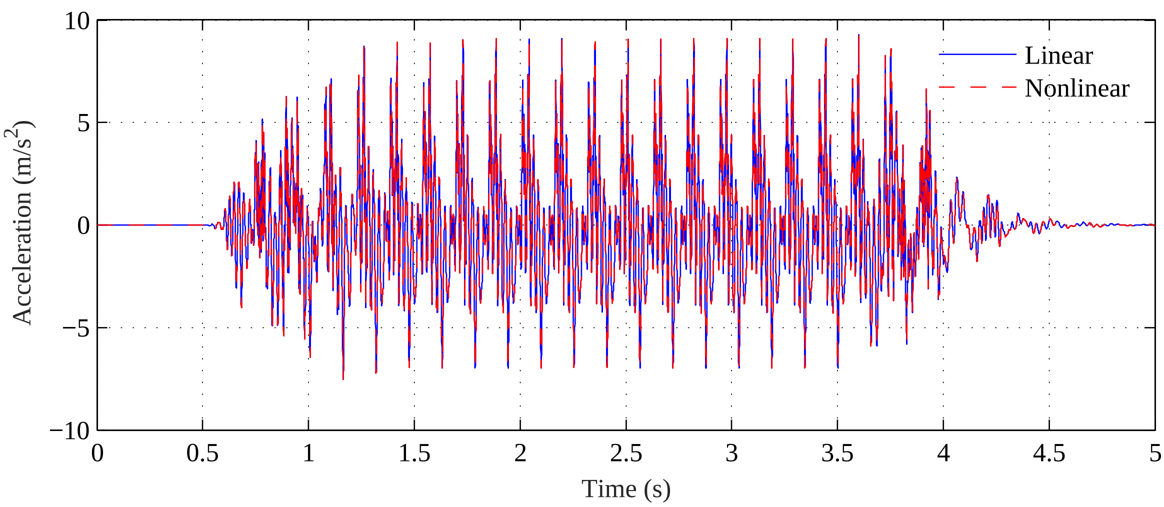

Figure 7.46 – Vertical acceleration at the midspan of the upper slab of the deck.

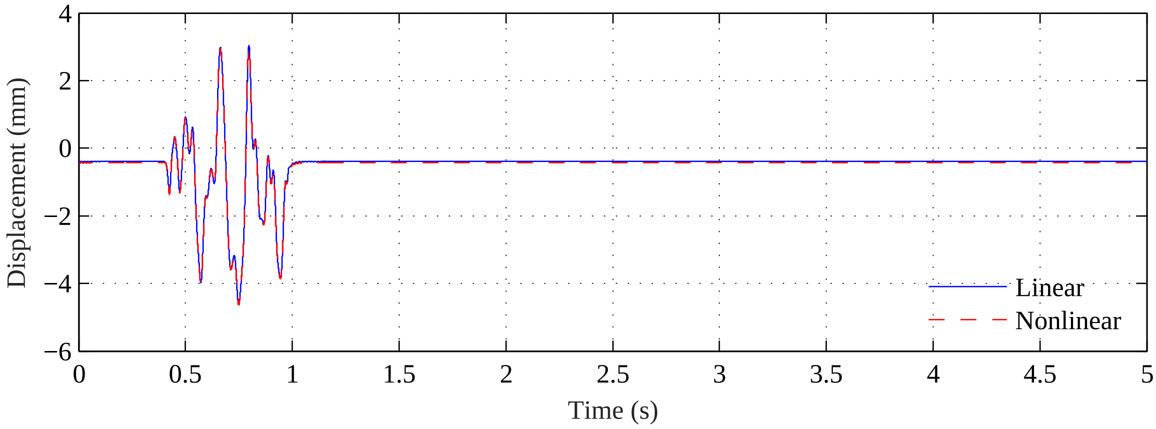

Figure 7.47 – Vertical displacements of the first right wheel.

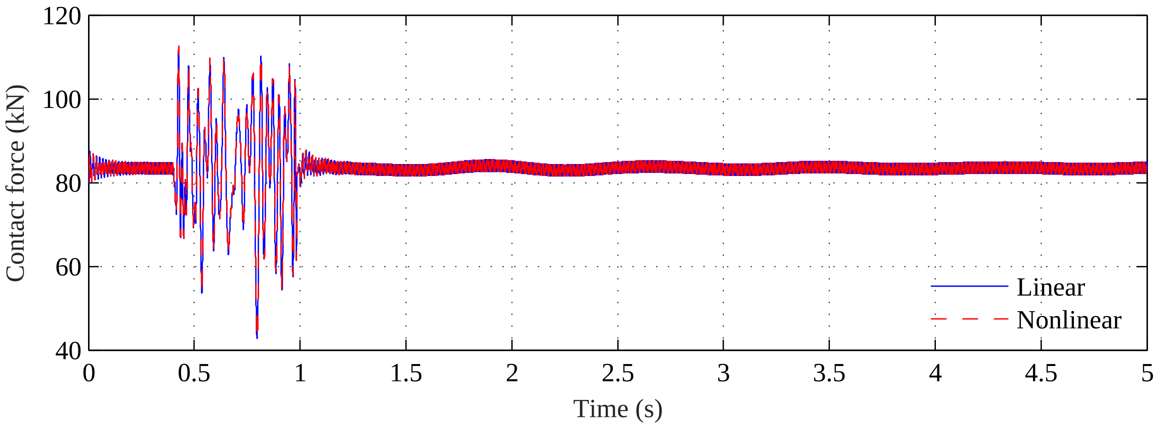

Figure 7.48 – Contact forces of the first right wheel.

7.3.4 Comparison between the MATLAB and ANSYS programs

In order to validate the accuracy and efficiency of the method proposed in this thesis for analysing the vehicle-structure interaction, the passage of the KHST over the railway viaduct is analysed using the ANSYS commercial software. In the analyses performed with this software, the Lagrange multiplier method is used. The system of linear equations used in this method is the same as that used in the direct method, as explained in Section 2.3.2. The train travels at a constant speed of 120 m/s. A time step of 2.5×10^{-4} s is used and the total number of time steps is 6500. The vertical accelerations at the midpoint of the second span are plotted in Fig. 7.49.

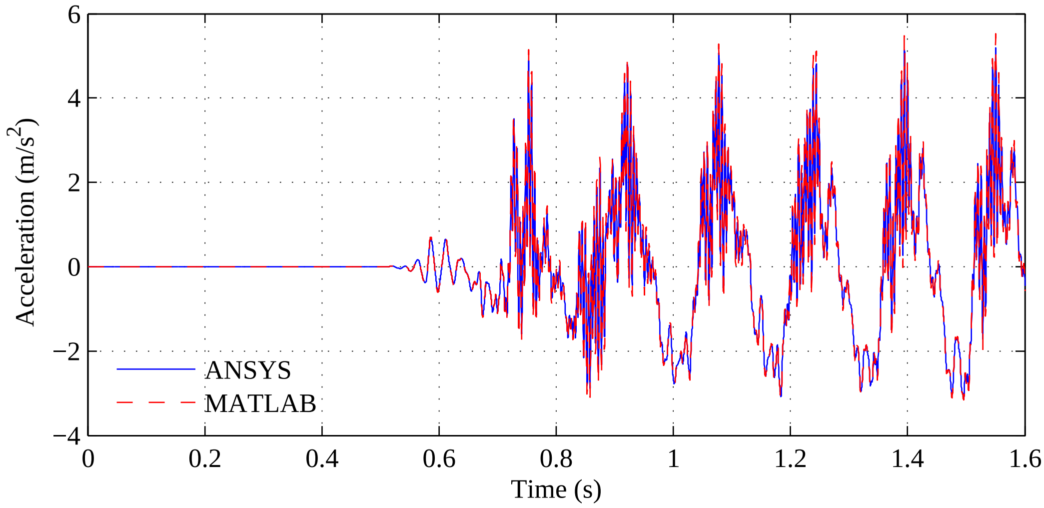

Figure 7.49 – Vertical accelerations at the midspan of the upper slab of the deck.

The vertical displacements of the first and tenth right wheels are plotted in Figs. 7.50 and 7.51, respectively. The corresponding contact forces are shown in Figs. 7.52 and 7.53, respectively.

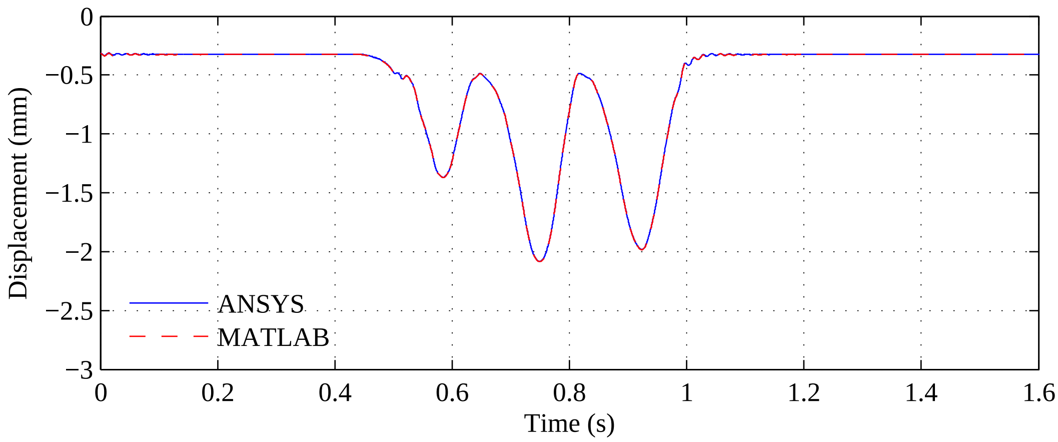

Figure 7.50 – Vertical displacements of the first right wheel.

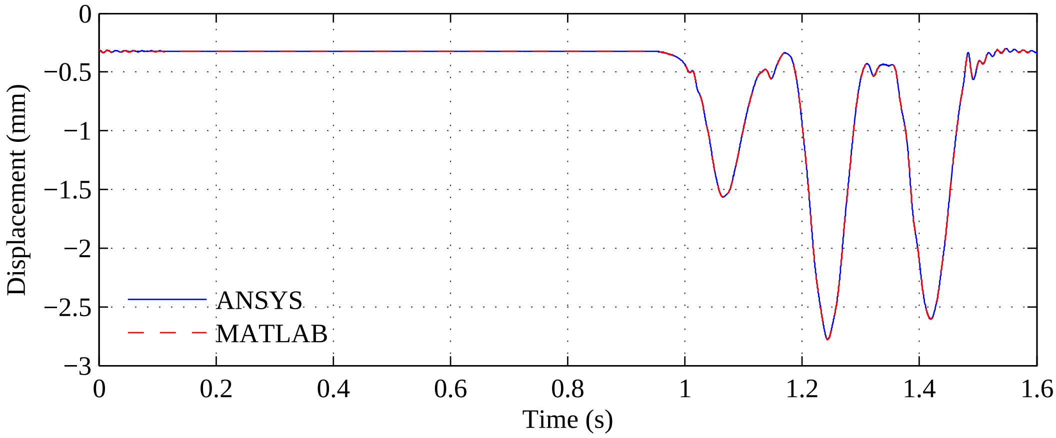

Figure 7.51 – Vertical displacements of the tenth right wheel.

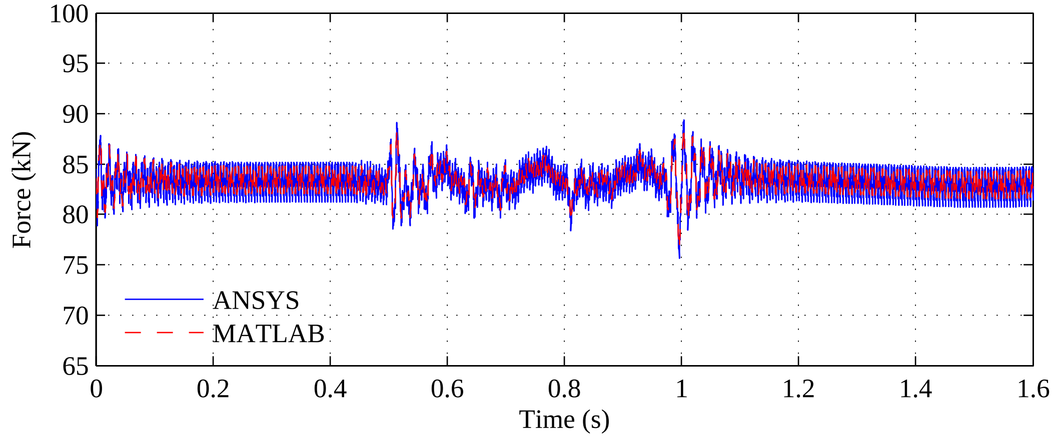

Figure 7.52 – Contact forces of the first right wheel.

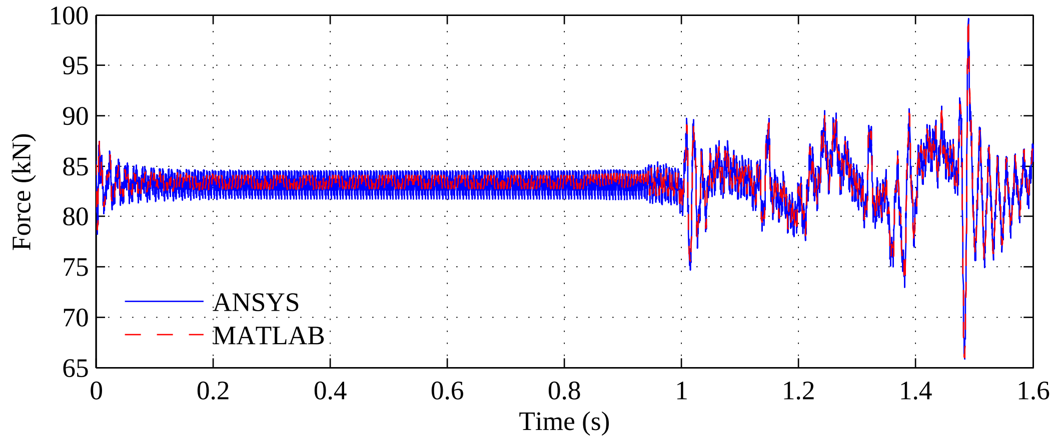

Figure 7.53 – Contact forces of the tenth right wheel.

The contact forces of the tenth wheel are higher than those of the first wheel due to the higher accelerations of the slab of the deck that occur during the passage of the tenth wheel. The frequency content of the contact forces of the first right wheel is plotted in Fig. 7.54. The spurious high frequency oscillations observed in the response obtained using ANSYS are due to the spatial discretisation of the target elements, as explained in Section 6.4.4.

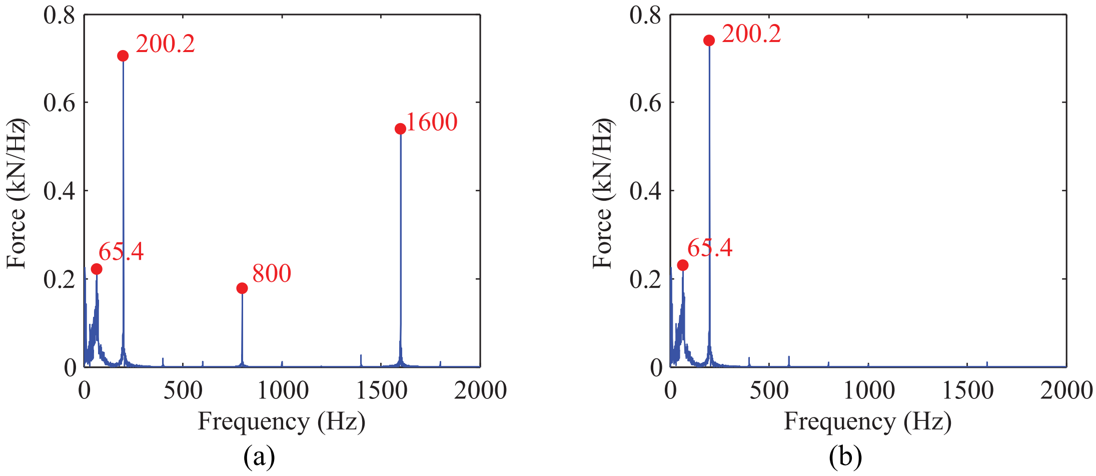

Figure 7.54 – Frequency content of the contact forces obtained using: (a) ANSYS (b) MATLAB.

The vertical accelerations of the first and fifth bogies are plotted in Figs. 7.55 and 7.56, respectively. The vertical accelerations of the first and fourth carbodies are plotted in Figs. 7.57 and 7.58, respectively. The results obtained using both programs show an excellent agreement.

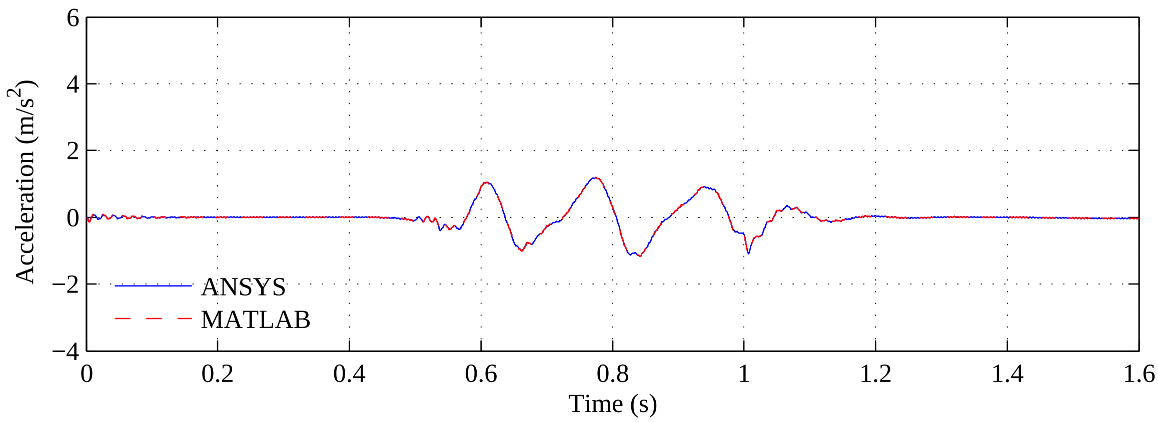

Figure 7.55 – Vertical accelerations of the first bogie.

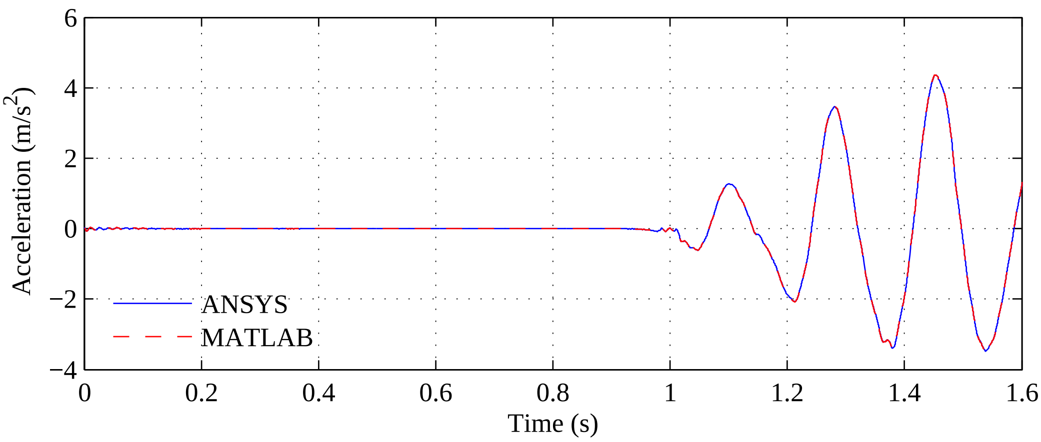

Figure 7.56 – Vertical accelerations of the fifth bogie.

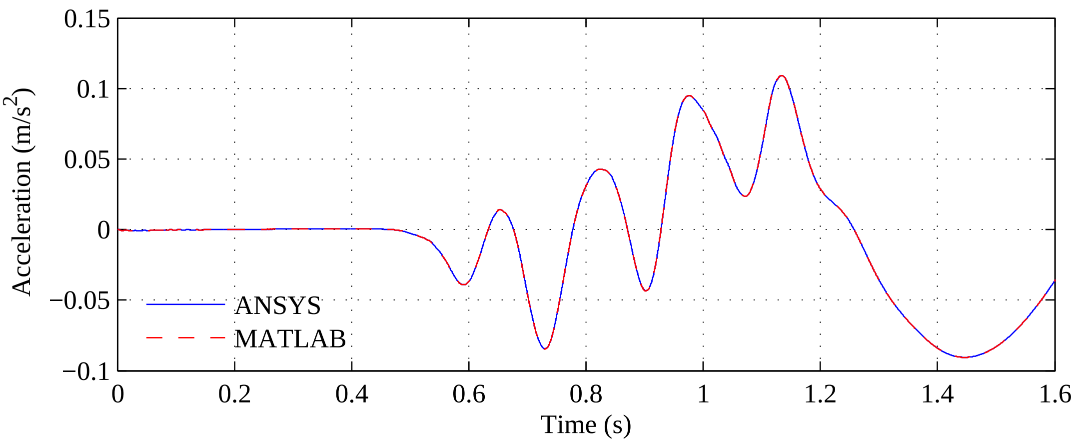

Figure 7.57 – Vertical accelerations of the first carbody.

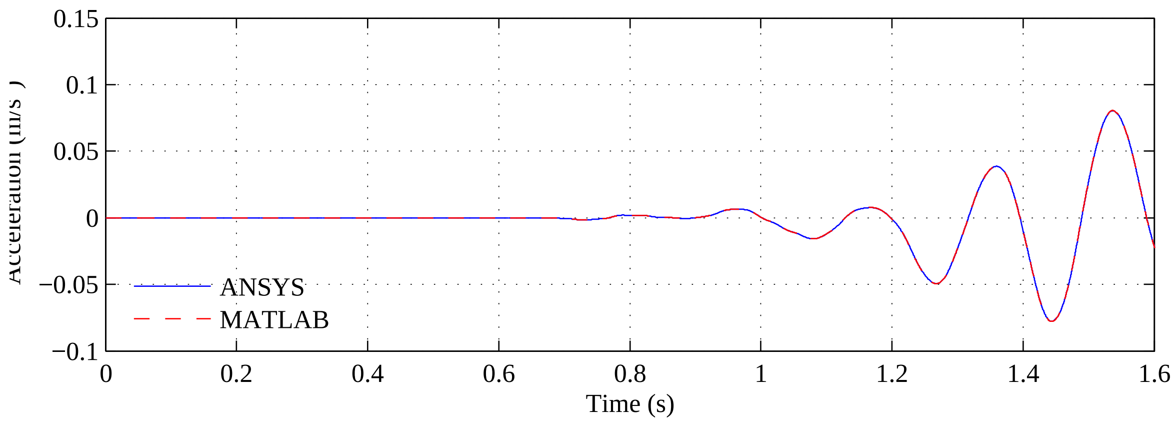

Figure 7.58 – Vertical accelerations of the fourth carbody.

All the calculations have been performed using a desktop computer with an Intel i7-4790 quad core processor running at 3.6 GHz. For a more accurate comparison, the calculations in ANSYS and MATLAB have been performed using a single execution thread. The elapsed time is 204975 *s* using ANSYS and 18257 *s* using MATLAB, which is about 11 times faster. This ratio is similar to that obtained in Section 6.4.4, where the execution time of MATLAB is 14 times faster than ANSYS. The sizes of the ANSYS and MATLAB working directories are 470 GB and 45.4 GB, respectively. This difference may be important since for example, during the design of bridges or viaducts, several trains running at tens of different speeds may have to be considered, resulting in hundreds of dynamic analyses.

7.4 CONCLUDING REMARKS

The numerical modelling of the Alverca viaduct and the analysis of the dynamic interaction that occurs during the passage of a high-speed train are presented in this chapter. The viaduct is first modelled using a refined mesh that is then reduced using an iterative process. The natural frequencies and the modal assurance criterion between mode shapes are used to compare the different numerical models. This optimisation allowed a 68% reduction of the number of d.o.f. of the FE model. The natural frequencies, mode shapes and modal damping ratios of the vibration modes of the viaduct were obtained by Malveiro *et al.* (2013) based on an ambient vibration test. The values adopted for the geometrical and mechanical properties have been calibrated using an FE model updating technique. A good agreement between the first three experimental and numerical global vibration modes has been obtained. The maximum difference between the experimental and numerical natural frequencies is 2.2%, and the lowest value of the modal assurance criterion is 0.98.

The influence of the isolated defects and periodic irregularities of the longitudinal level of the track on the dynamic behaviour of the train-structure system has been analysed based on the standards EN 13848-1 (2003) and EN 13848-5 (2008). The results obtained show that the shape of the isolated defects strongly influences the dynamic behaviour of the train-structure system. However, in the standards mentioned before, the isolated defects are only evaluated in terms of the mean to peak value. The high accelerations of the upper slab that occur due to the isolated defects during the passage of the KHST are a localised phenomenon that strongly depends on the deformation of the slab. The standard EN 1990-A2 (2005), which defines the deflection and vibration limits for the design of railway bridges, does not take into account the local deformations of the slab. The high accelerations of the slab occur only in the vicinity of the wheel-rail contact points, and thus it is possible that the vertical accelerations exceed the limit without causing instability of the ballast. Further studies taking into account the wheel-rail interaction and the local deformations of the slab are necessary to validate this assumption. When the periodic irregularities are taken into account and the train travels at a speed that leads to resonance effects, the behaviour of the contact forces is governed more by the presence of irregularities rather than by the resonance of the structure. The accelerations of the upper slab for the case with periodic irregularities are slightly higher than those observed for the case without irregularities, but clearly, the resonance of the structure governs the dynamic response of the viaduct.

The passage of the KHST over the Alverca viaduct has been analysed using the Hertzian contact spring with linear and nonlinear force-deflection relationships. Since the results obtained in all the analysis are very similar, the higher computational cost associated with the nonlinear spring might not be justifiable.

The dynamic response of the train-viaduct system has been calculated with the direct method and the ANSYS program, and a good agreement has been obtained. The calculations performed with the direct method have been at least 11 times faster.

8 CONCLUSIONS AND FUTURE DEVELOPMENTS

8.1 CONCLUSIONS

In this work, an accurate, robust and efficient algorithm to analyse the nonlinear vehicle-structure interaction has been developed, implemented and validated. The first task of this work has been to carry out a comprehensive literature review and comparison of the vehicle-structure interaction methods in order to choose the most suitable one (see Chapter 2). The methods addressed have one of the following disadvantages: requiring an iterative procedure, introducing additional variables into the system of equations or leading to time-dependent structural matrices. Estimating the loss of computational efficiency associated with each disadvantage is not a straightforward task. A rigorous comparison of these different methods can only be performed by using the same numerical example. As far as the author is aware, this type of comparison has not yet been published. Therefore, the selection of the most suitable method cannot be made based on the computational efficiency.

There is little information in the literature regarding the convergence properties of the iterative methods used for solving vehicle-structure interaction problems. This work has demonstrated that even for a simple example, the iterative techniques can diverge. An analytical expression to verify the convergence characteristics of the iterative methods has been provided. The direct method is a more robust and accurate algorithm because it does not require an iterative procedure to couple the structure and vehicles. This becomes even more relevant for the case of nonlinear analyses, in which the convergence characteristics are very important. The Lagrange multiplier method leads to the same system of equations as the direct method. The penalty method does not satisfy exactly the constraint equations and leads to an increased complexity related to the selection of the values of the penalty parameters that ensure an accurate coupling between the vehicles and structures. In the condensation methods, the equations of motion of the coupled vehicle-structure system might be difficult to determine when nonlinearities are considered in the vehicle models. The only disadvantage of the direct and Lagrange multiplier methods is the loss of computational efficiency due to the introduction of additional variables. Unlike the

Lagrange multiplier method, the direct method is based on simple concepts that are easily understood, such as force equilibrium and constraint equations, and is, therefore, the method adopted in this work. The simplicity of the method contributed to an efficient optimisation of the algorithm used to solve the system of linear equations.

An enhanced node-to-segment contact element that includes an Hertzian spring, which relates the forces acting at the interface to the local deformations in the vicinity of the contact region, has been developed. The Hertz theory is explained in Chapter 3. Hertz provided a few tabulated values to calculate the force-deflection relationship of the contact spring as a function of a parameter that depends only on the geometrical properties of the two contacting bodies. Other values must be interpolated. Additional tabulated values are provided in this work, thus reducing the errors associated with the interpolation.

The direct method proposed in Chapters 4 and 5 uses a search algorithm to detect which elements are in contact and only imposes the constraint equations when contact occurs. Due to the nonlinear nature of the constraint equations and of the enhanced node-to-segment contact element, an incremental formulation based on the Newton-Raphson method is adopted. The constraint equations take into account the irregularities present at the contact interface. In the ANSYS software (2014a), the finite element mesh of the structure must take into account the irregularities, and so the structural matrices have to be calculated and assembled for each set of irregularities. Also, the target elements implemented in ANSYS use linear displacement interpolation functions, which results in a spurious excitation caused by the spatial discretisation of these elements (see Chapters 6). The enhanced node-to-segment contact element developed in this work uses cubic interpolation functions and does not lead to these spurious excitations.

The proposed vehicle-structure interaction methodology has been implemented in MATLAB® (2013), which has a vast library of optimised and tested prebuilt toolboxes. The structures and vehicles are modelled using ANSYS commercial software, which has a large library of finite elements. This program is able to model structures and vehicles with a high degree of complexity and with several types of finite elements. The accuracy, robustness and efficiency of the proposed method have been validated with several numerical examples. The results obtained with the direct method have been validated against semi-analytical solutions and those calculated with the ANSYS program, and an excellent agreement has been obtained. The calculations performed with the direct method have been at least 11 times faster when compared with the ANSYS software. The integration of these two commercial programs widely used in engineering simulation and a state-of-the-art vehicle-structure interaction method allowed the development of an innovative solution that can be used to analyse very complex and challenging problems. This is a very important step towards closing the gap between finite element and multibody simulation programs. This work focuses on railways, but the developed algorithm is generic and can be used to model other types of vehicles such as trucks or cars.

The numerical modelling of a train-track system and the analysis of the dynamic interaction due to the passage of the Korean high-speed train (KHST) are presented in Chapter 6. The ballast and sleepers are modelled with 3D solid elements. A simplified 2D track model is also developed to support the vehicle before and after the 3D track and is first modelled with rigid beams. This leads to sudden transitions between the rigid and flexible track models and consequently to inaccurate results, especially when the behaviour of the vehicle is of interest. A 2D flexible track model has been developed to overcome these problems. The execution time of the dynamic analysis performed using the flexible track model is only 16% higher than that obtained when using the rigid track model and, for that reason, the flexible track model has been adopted for all the analyses. When using the simplified model of the KHST, the dynamic analysis performed using ANSYS is about 33 times slower when compared with the proposed MATLAB algorithm, and only 14 times slower when using the complete model of the train. This might be due to the fact that the MATLAB functions used to solve the system of linear equations might be less optimised than those implemented in ANSYS when a large number of contact points is considered.

The passage of the KHST over the Alverca viaduct is analysed in Chapter 7. The values adopted for the geometrical and mechanical properties are calibrated using a finite element model updating technique. An excellent agreement is obtained between the first three experimental and numerical global vibration modes. The maximum difference between the experimental and numerical natural frequencies is 2.2% and the lowest value of the modal assurance criterion is 0.98. The influence of the track isolated defects and periodic irregularities of the longitudinal level of the track on the dynamic behaviour of the train-structure system is also analysed. It has been concluded that the shape of the isolated defects strongly influences the dynamic behaviour of the train-track system. However, this is not taken into account in most of the existing standards, such as the EN 13848-1 (2003) and EN 13848-5 (2008). When the periodic irregularities are considered and the train travels at a speed that leads to resonance effects, the behaviour of the contact forces is governed more by the presence of irregularities rather than by the resonance of the structure. The accelerations of the upper slab are more influenced by the resonance of the structure rather than by the presence of the irregularities. The track irregularities lead to localised high accelerations of the upper slab that strongly depend on its deformation. The standard EN 1990-A2 (2005) specifies that the vertical acceleration of the deck should not exceed 3.5 m/s^2 ($\approx$ 0.35g). However, this does not take into account the local deformation of the slab. The localised regions of ballast subjected to high accelerations might be confined by the surrounding ballast which has much lower accelerations. Thus it is possible that the vertical acceleration might exceed the limit without causing instability. Further studies taking into account the wheel-rail interaction and the local deformations of the slab are necessary to validate this assumption. The influence of the force-deflection relationship of the Hertzian contact spring is also analysed. In all the analyses performed, the use of a linear or nonlinear relationship leads to similar results.

Finally, the vehicle-structure interaction algorithm proposed in this work has been used and further developed in several doctoral dissertations and articles published in international journals. Santos (2013) developed a numerical tool for the simulation of the track-ground vibrations induced by railway traffic and used the direct method to couple the train and track. Montenegro *et al*. (Montenegro, 2015; Montenegro *et al.*, 2016) extended the vehicle-structure interaction algorithm to account for the lateral interaction and developed a methodology to assess the running safety of trains moving over bridges subjected to seismic excitations. Rocha *et al*. (Rocha *et al.*, 2012; Rocha, 2016) proposed an efficient probabilistic methodology to assess the running safety of high-speed trains passing over short-span bridges and used the direct method to analyse the train-bridge interaction.

8.2 FUTURE DEVELOPMENTS

Several research questions that arose during the course of this work were not addressed. The following paragraphs provide some suggestions for future research.

- The work developed by Montenegro (2015) extends the formulation developed in this thesis to take into account the lateral vehicle-structure interaction and is an important contribution to the field. However, no information is given about the computational efficiency. The program developed here will be extended to also deal with three-dimensional contact problems and the corresponding computational efficiency will be assessed. The time taken to solve the system of linear equations represents a significant part of the total elapsed time. Implementing the mode-superposition method could also lead to a significant reduction of the computational cost.

- The vehicles and structures have been modelled with ANSYS. All the data regarding these models, such as the structural matrices, the contact nodes and the target elements, is exported by ANSYS in batch mode and subsequently imported by MATLAB. Implementing a similar procedure to extract all the vehicle data from commercial multibody simulation software, which generally has comprehensive libraries of detailed vehicle models, would also be an important contribution.

- The formulation presented in Chapter 5 is capable of dealing with the nonlinear material behaviour. However, since the global structural matrices are exported by ANSYS and subsequently imported by MATLAB at the beginning of the analysis, some of the finite element matrices cannot be updated at each time step, and therefore the developed program cannot take into account the nonlinear material behaviour. This is not a significant limitation because there are several vehicle-structure interaction problems that do not require this type of nonlinearity to be taken into account. Nevertheless, implementing the finite element procedures necessary to update the materially nonlinear element matrices in MATLAB would be an important improvement.

- The enhanced node-to-segment contact element developed in this work does not take into account the inertial and damping forces present at the contact interface, which might lead to some numerical problems. There are several studies describing the advantage of accounting for the energy dissipation occurring during contact. The influence of these forces should be further investigated.

- The Hertz theory provides a good compromise between accuracy and computational efficiency. However, it is based on assumptions that are not always satisfied in railway applications, such as parabolic profiles with constant curvature along the contact area. Also, this theory only uses the curvatures at the contact point as the input data, which significantly depend on the smoothing and interpolation performed during the geometrical processing of the profiles. These limitations can lead to inaccuracies when calculating stresses, which are particularly important to assess fatigue and wear. Multi-Hertzian or semi-Hertzian methods can be used to overcome these limitations (Ayasse & Chollet, 2005; Iwnicki, 2006). Multi-Hertzian methods split the contact patch into strips and apply the Hertz theory to each strip. The semi-Hertzian methods assume non-Hertzian conditions to account for the non-constant curvatures in the lateral direction and consider constant longitudinal curvatures like in the Hertzian hypothesis.

- As far as the author is aware, there are no published studies with a rigorous comparison of the computational efficiency of the existing vehicle-structure interaction methods. The only objective way to perform this comparison is to solve the same numerical example using the different methods. This would allow a more informed choice of the most suitable method.
- The influence of the isolated defects of the longitudinal level of the track on the dynamic behaviour of the train-viaduct system is analysed in Chapter 7. The results obtained demonstrate that the contact forces are strongly influenced by the shape of the isolated defects and the train speed. However, the shape of the isolated defects is not taken into account in the standards EN 13848-1 (2003) and EN 13848-5 (2008). For example, Steenbergen and Esveld (2006) demonstrated that there is a good correlation between the gradient of the rail weld geometry and the maximum contact forces. Further research that takes into account a broader range of shapes and train speeds is needed to better understand the relation between the shape of different types of isolated defects and the dynamic response of the train-structure system.

APPENDIX A – A 2-BY-2 BLOCK FACTORISATION SOLVER

The block factorisation of the system of linear equations (4.30) is presented below using the following notation

$$\begin{bmatrix} \mathbf{A}_{11} & \mathbf{A}_{21}^T \\ \mathbf{A}_{21} & \mathbf{0} \end{bmatrix} \begin{bmatrix} \mathbf{x}_1 \\ \mathbf{x}_2 \end{bmatrix} = \begin{bmatrix} \mathbf{b}_1 \\ \mathbf{b}_2 \end{bmatrix} \tag{A.1}$$

and

$$\mathbf{A} = \begin{bmatrix} \mathbf{A}_{11} & \mathbf{A}_{21}^T \\ \mathbf{A}_{21} & \mathbf{0} \end{bmatrix} \tag{A.2}$$

It is assumed that $\mathbf{A}_{11}$ is a symmetric and positive definite matrix and $\mathbf{A}_{21}^T$ has full rank. With these assumptions, matrix $\mathbf{A}$ admits the following $\mathbf{L}\mathbf{D}\mathbf{L}^T$ factorisation without pivoting (Benzi *et al.*, 2005)

$$\begin{bmatrix} \mathbf{A}_{11} & \mathbf{A}_{21}^T \\ \mathbf{A}_{21} & \mathbf{0} \end{bmatrix} = \begin{bmatrix} \mathbf{L}_{11} & \mathbf{0} \\ \mathbf{L}_{21} & \mathbf{L}_{22} \end{bmatrix} \begin{bmatrix} \mathbf{D}_{11} & \mathbf{0} \\ \mathbf{0} & \mathbf{D}_{22} \end{bmatrix} \begin{bmatrix} \mathbf{L}_{11}^T & \mathbf{L}_{21}^T \\ \mathbf{0} & \mathbf{L}_{22}^T \end{bmatrix} \tag{A.3}$$

where $\mathbf{L}_{11}$ and $\mathbf{L}_{22}$ are unit lower triangular matrices, $\mathbf{D}_{11}$ is a positive definite diagonal matrix, and $\mathbf{D}_{22}$ is a negative definite diagonal matrix. By equating the corresponding blocks in Eq. (A.3), the following relations are obtained

$$\mathbf{A}_{11} = \mathbf{L}_{11}\,\mathbf{D}_{11}\,\mathbf{L}_{11}^T \tag{A.4}$$

$$\mathbf{A}_{21} = \mathbf{L}_{21}\,\mathbf{D}_{11}\,\mathbf{L}_{11}^T \tag{A.5}$$

$$\overline{\mathbf{A}}_{22} = \mathbf{L}_{22}\,\mathbf{D}_{22}\,\mathbf{L}_{22}^T \tag{A.6}$$

where

$$\overline{\mathbf{A}}_{22} = -\mathbf{L}_{21}\,\mathbf{D}_{11}\,\mathbf{L}_{21}^T \tag{A.7}$$

Therefore, the components of the right-hand side of Eq. (A.3) can be obtained by factorisation of $\mathbf{A}_{11}$, calculation of $\mathbf{L}_{21}$ by forward substitution and factorisation of $\overline{\mathbf{A}}_{22}$. The solution of the system of linear equations can be obtained with the following two steps

$$\begin{bmatrix} \mathbf{L}_{11} & \mathbf{0} \\ \mathbf{L}_{21} & \mathbf{L}_{22} \end{bmatrix} \begin{bmatrix} \mathbf{y}_1 \\ \mathbf{y}_2 \end{bmatrix} = \begin{bmatrix} \mathbf{b}_1 \\ \mathbf{b}_2 \end{bmatrix} \tag{A.8}$$

$$\begin{bmatrix} \mathbf{L}_{11}^T & \mathbf{L}_{21}^T \\ \mathbf{0} & \mathbf{L}_{22}^T \end{bmatrix} \begin{bmatrix} \mathbf{x}_1 \\ \mathbf{x}_2 \end{bmatrix} = \begin{bmatrix} \mathbf{D}_{11}^{-1} & \mathbf{0} \\ \mathbf{0} & \mathbf{D}_{22}^{-1} \end{bmatrix} \begin{bmatrix} \mathbf{y}_1 \\ \mathbf{y}_2 \end{bmatrix} \tag{A.9}$$

The vectors $\mathbf{y}_1$ and $\mathbf{y}_2$ are obtained by forward substitution

$$\mathbf{L}_{11}\,\mathbf{y}_1 = \mathbf{b}_1 \tag{A.10}$$

$$\mathbf{L}_{22}\,\mathbf{y}_2 = \mathbf{b}_2 - \mathbf{L}_{21}\,\mathbf{y}_1 \tag{A.11}$$

and the solution of the system ($\mathbf{x}_1$ and $\mathbf{x}_2$) is obtained by back substitution

$$\mathbf{L}_{22}^T\,\mathbf{x}_2 = \mathbf{D}_{22}^{-1}\,\mathbf{y}_2 \tag{A.12}$$

$$\mathbf{L}_{11}^T\,\mathbf{x}_1 = \mathbf{D}_{11}^{-1}\,\mathbf{y}_1 - \mathbf{L}_{21}^T\mathbf{x}_2 \tag{A.13}$$

APPENDIX B – A 3-BY-3 BLOCK FACTORISATION SOLVER

Since the matrix $\overline{\mathbf{K}}_{YY}$ presented in Eq. (5.40) may be indefinite and therefore may not have a stable factorisation without pivoting, the lines and columns of the system matrix corresponding to the incremental displacements $\Delta\mathbf{a}_Y$ and contact forces $\Delta\mathbf{X}$ have to be grouped together. Hence the block factorisation of the system of equations (5.40) is presented below using the following notation.

$$\begin{bmatrix} \mathbf{A}_{11} & \mathbf{A}_{21}^T & \mathbf{A}_{31}^T \\ \mathbf{A}_{21} & \mathbf{A}_{22} & \mathbf{A}_{32}^T \\ \mathbf{A}_{31} & \mathbf{A}_{32} & \mathbf{A}_{33} \end{bmatrix} \begin{bmatrix} \mathbf{x}_1 \\ \mathbf{x}_2 \\ \mathbf{x}_3 \end{bmatrix} = \begin{bmatrix} \mathbf{b}_1 \\ \mathbf{b}_2 \\ \mathbf{b}_3 \end{bmatrix} \tag{B.1}$$

where $\mathbf{x}_1$ and $\mathbf{x}_2$ correspond to $\Delta\mathbf{a}_I$ and $\Delta\mathbf{a}_R$, respectively, and $\mathbf{x}_3$ corresponds to the group formed by $\Delta\mathbf{a}_Y$ and $\Delta\mathbf{X}$. The coefficient matrix presented in Eq. (B.1) admits the following factorisation

$$\begin{bmatrix} \mathbf{A}_{11} & \mathbf{A}_{21}^T & \mathbf{A}_{31}^T \\ \mathbf{A}_{21} & \mathbf{A}_{22} & \mathbf{A}_{32}^T \\ \mathbf{A}_{31} & \mathbf{A}_{32} & \mathbf{A}_{33} \end{bmatrix} = \begin{bmatrix} \mathbf{L}_{11} & \mathbf{0} & \mathbf{0} \\ \mathbf{L}_{21} & \mathbf{L}_{22} & \mathbf{0} \\ \mathbf{L}_{31} & \mathbf{L}_{32} & \mathbf{L}_{33} \end{bmatrix} \times \begin{bmatrix} \mathbf{L}_{11}^T & \mathbf{L}_{21}^T & \mathbf{L}_{31}^T \\ \mathbf{0} & \mathbf{L}_{22}^T & \mathbf{L}_{32}^T \\ \mathbf{0} & \mathbf{0} & \mathbf{U}_{33} \end{bmatrix} \tag{B.2}$$

where $\mathbf{L}$ and $\mathbf{U}$ are lower and upper triangular matrices, respectively. For simplicity, the permutation matrices associated with the factorisation of $\mathbf{A}_{33}$ are not represented. The block factorisation solver is divided into three stages, which are described below.

By equating part of the corresponding blocks in Eq. (B.2) the following relations are obtained

$$\mathbf{A}_{11} = \mathbf{L}_{11}\mathbf{L}_{11}^T \tag{B.3}$$

$$\mathbf{A}_{21}^T = \mathbf{L}_{11}\mathbf{L}_{21}^T \tag{B.4}$$

The first stage consists of factorising $\mathbf{A}_{11}$, which is assumed to be symmetric positive definite and therefore admits a Cholesky factorisation (Burden & Faires, 1997), and calculating $\mathbf{L}_{21}$ by forward substitution. Since $\mathbf{A}_{11}$ and $\mathbf{A}_{21}^T$ are time-independent, the operations associated with Eqs. (B.3) and (B.4) have to be performed only once at the beginning of the analysis.

By equating the remaining blocks in Eq. (B.2) the following relations are obtained

$$\mathbf{A}_{31}^{T} = \mathbf{L}_{11}\,\mathbf{L}_{31}^{T} \tag{B.5}$$

$$\overline{\mathbf{A}}_{22} = \mathbf{L}_{22}\,\mathbf{L}_{22}^{T} \tag{B.6}$$

$$\mathbf{A}_{32}^{T} = \mathbf{L}_{21}\,\mathbf{L}_{31}^{T} + \mathbf{L}_{22}\,\mathbf{L}_{32}^{T} \tag{B.7}$$

$$\overline{\mathbf{A}}_{33} = \mathbf{L}_{33}\,\mathbf{U}_{33} \tag{B.8}$$

where

$$\overline{\mathbf{A}}_{22} = \mathbf{A}_{22} - \mathbf{L}_{21}\,\mathbf{L}_{21}^{T} \tag{B.9}$$

$$\overline{\mathbf{A}}_{33} = \mathbf{A}_{33} - \mathbf{L}_{31}\,\mathbf{L}_{31}^{T} - \mathbf{L}_{32}\,\mathbf{L}_{32}^{T} \tag{B.10}$$

The second stage consists of obtaining the remaining matrices of the right-hand side of Eq. (B.2) in an analogous way. It is assumed that the matrix $\overline{\mathbf{A}}_{22}$ admits a Cholesky factorisation, whereas the matrices $\mathbf{L}_{33}$ and $\mathbf{U}_{33}$ are obtained using an *LU* factorisation with pivoting. Since the matrices involved in Eqs. (B.5) to (B.8) depend on time and contact conditions, the operations belonging to the second stage have to be performed in each Newton-Raphson iteration.

Finally, the third stage of the block factorisation algorithm consists of the calculation of the solution of the system of equations through the following two steps.

$$\begin{bmatrix} \mathbf{L}_{11} & \mathbf{0} & \mathbf{0} \\ \mathbf{L}_{21} & \mathbf{L}_{22} & \mathbf{0} \\ \mathbf{L}_{31} & \mathbf{L}_{32} & \mathbf{L}_{33} \end{bmatrix} \begin{bmatrix} \mathbf{y}_1 \\ \mathbf{y}_2 \\ \mathbf{y}_3 \end{bmatrix} = \begin{bmatrix} \mathbf{b}_1 \\ \mathbf{b}_2 \\ \mathbf{b}_3 \end{bmatrix} \tag{B.11}$$

$$\begin{bmatrix} \mathbf{L}_{11}^{T} & \mathbf{L}_{21}^{T} & \mathbf{L}_{31}^{T} \\ \mathbf{0} & \mathbf{L}_{22}^{T} & \mathbf{L}_{32}^{T} \\ \mathbf{0} & \mathbf{0} & \mathbf{U}_{33} \end{bmatrix} \begin{bmatrix} \mathbf{x}_1 \\ \mathbf{x}_2 \\ \mathbf{x}_3 \end{bmatrix} = \begin{bmatrix} \mathbf{y}_1 \\ \mathbf{y}_2 \\ \mathbf{y}_3 \end{bmatrix} \tag{B.12}$$

The vectors $\mathbf{y}_1$ to $\mathbf{y}_3$ are obtained by forward substitution as follows

$$\mathbf{L}_{11}\,\mathbf{y}_1 = \mathbf{b}_1 \tag{B.13}$$

$$\mathbf{L}_{22}\,\mathbf{y}_2 = \mathbf{b}_2 - \mathbf{L}_{21}\,\mathbf{y}_1 \tag{B.14}$$

$$\mathbf{L}_{33}\,\mathbf{y}_3 = \mathbf{b}_3 - \mathbf{L}_{31}\,\mathbf{y}_1 - \mathbf{L}_{32}\,\mathbf{y}_2 \tag{B.15}$$

being the solution of the system of equations (B.1) obtained by back substitution

$$\mathbf{U}_{33}\,\mathbf{x}_3 = \mathbf{y}_3 \tag{B.16}$$

$$\mathbf{L}_{22}^T\,\mathbf{x}_2 = \mathbf{y}_2 - \mathbf{L}_{32}^T\,\mathbf{x}_3 \tag{B.17}$$

$$\mathbf{L}_{11}^T\,\mathbf{x}_1 = \mathbf{y}_1 - \mathbf{L}_{21}^T\,\mathbf{x}_2 - \mathbf{L}_{31}^T\,\mathbf{x}_3 \tag{B.18}$$

APPENDIX C – VALIDATION OF THE MODEL UPDATING TECHNIQUES

In order to validate the procedures used to update the finite element models of the Alverca viaduct, a simple example consisting of a railway bridge is studied in this appendix. The numerical model has been developed in ANSYS® (2014a) by Ribeiro (2012) using the APDL scripting language (ANSYS®, 2014d) in order to automate all the steps involved in the model generation and updating. The railway bridge consists of a simply supported concrete slab and a railway track (see Fig. C.1). The concrete slab has a span of 15 m and a constant rectangular cross-section. Both the slab and the track are modelled with the beam element type BEAM3 using a discretisation of 0.5 m. The vertical stiffness of the slab supports and the track-slab horizontal interaction are modelled using the spring element type COMBIN14.

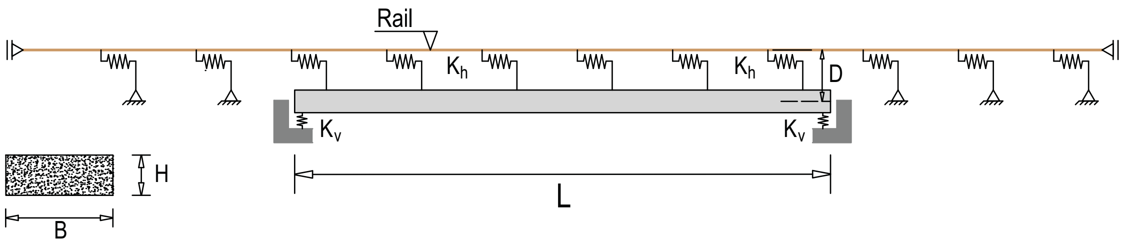

Figure C.1 – Numerical model of the railway bridge (adapted from Ribeiro (2012)).

The mechanical and geometrical properties of the numerical model are listed in Table C.1. The values adopted for the parameters L, B, H and E are based on the final report of the specialists committee D 214 of the European Rail Research Institute (ERRI D 214/RP 9, 2001).

Table C.1 –Mechanical and geometrical properties of the railway bridge.

Parameter	Value
Span length (L)	15 m
Width of the cross-section (B)	5 m
Height of the cross-section (H)	0.85 m
Young's modulus of the concrete (E)	30 GPa
Mass per unit length of the slab (m)	18.7 kg/m
Vertical stiffness of the supports (k_v)	4 GN/m
Horizontal stiffness of the track-slab connection (k_h)	30 MN/m
Distance between the gravity centres of the rail and slab	1.075 m

The parameters considered in the optimisation process, as well as their mean values, standard deviations and lower and upper bounds, are listed in Table C.2.

Table C.2 – Statistical properties of the optimisation parameters.

Parameter	Distribution type	Mean value / standard deviation	Bound constraints	Unit
H	Uniform	0.75 / 0.14	[0.7, 1.2]	m
m	Uniform	17500 / 4330	[10000, 25000]	kg/m
k_v	Uniform	8 / 4.04	[1, 15]	GN/m

The objective function used in the model updating of the railway bridge is defined by

$$f = a\sum_{i=1}^{3}\frac{\left|f_i^{updt} - f_i^{theo}\right|}{f_i^{theo}} + b\sum_{i=1}^{3}\left(1 - MAC\left(\phi_i^{updt}, \phi_i^{theo}\right)\right) + c\left|\frac{\delta_{LM71}^{updt} - \delta_{LM71}^{theo}}{\delta_{LM71}^{theo}}\right| \tag{C.1}$$

where the superscripts *theo* and *updt* denote variables associated with the theoretical model, defined using the correct values of the parameters, and with the model updated during the optimisation, respectively. The variables f_i and ϕ_i are the natural frequencies and mode shapes, and δ_{LM71} is the vertical displacement of the bridge at midspan when subject to the load model LM71 defined in EN 1991-2 (2003). Since all the terms of the objective function range from zero to one, the weighting factors *a, b* and *c* are assumed to be equal to one. It is considered that the global response of the structure calculated using the first three vertical vibration modes has a reasonable degree of accuracy.

The first three vertical vibration mode shapes and corresponding frequencies of the railway bridge are represented in Fig. C.2.

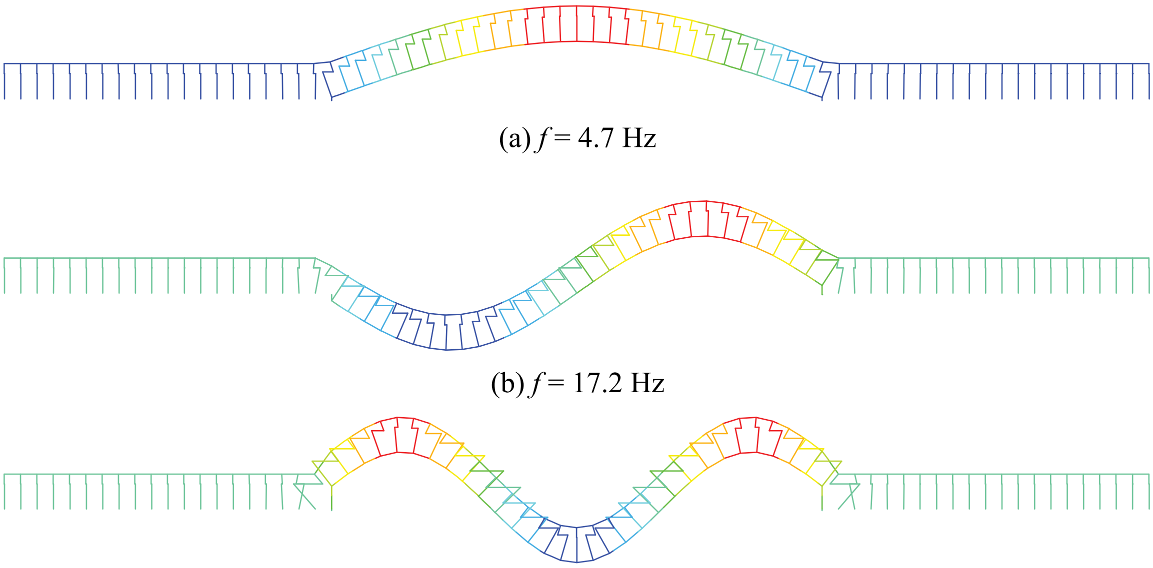

(a) $f = 4.7$ Hz

(b) $f = 17.2$ Hz

(c) $f = 36.3$ Hz

Figure C.2 – First three vibration modes and natural frequencies of the railway bridge.

A sensitivity analysis is performed in order to identify the variables that most influence the terms considered in the objective function. The Spearman correlation matrix plotted in Fig. C.3 is obtained using 1000 samples generated by the Latin Hypercube method (see Section 7.2.6.1). The values in the interval [-0.2, 0.2] have been filtered to highlight the parameters that significantly influence the objective function. As can be observed, the height of the cross-section is the parameter that has the highest correlation coefficients. The vertical support stiffness presents the lowest values and is only included in the optimisation process to provide a further understanding of this aspect. As expected, the terms of the objective function associated with the mode shapes have the smallest variations.

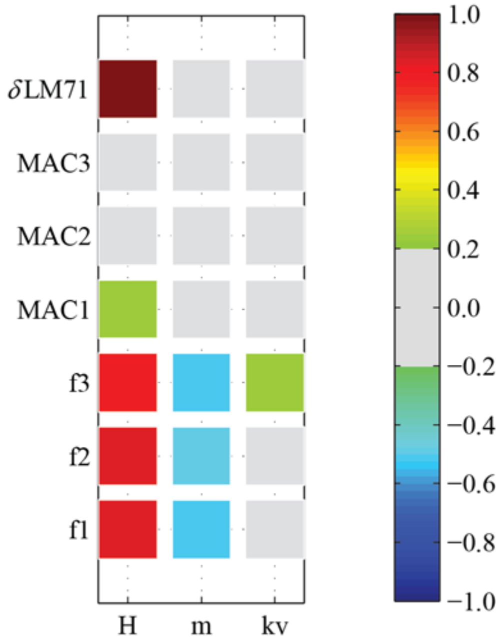

Figure C.3 – Spearman correlation matrix of the optimisation parameters.

The model updating of the railway bridge is performed using the MATLAB functions *fmincon* and *ga* (MATLAB®, 2013). The function *ga* finds the minimum of a function using a genetic algorithm (Goldberg, 1989). The function *fmincon* is used to find the minimum of constrained nonlinear multivariable functions and has different optimisation algorithms implemented, such as sequential quadratic programming methods or the preconditioned conjugate gradient method. Some algorithms are based on interior point techniques that generate only feasible iterates, and some methods use active set techniques that select a working set of constraints that generally includes only constraints that are exactly satisfied at the current point. The optimisation algorithm and technique used depend on the following four options of the function *fmincon*: *interior-point* (Byrd *et al.*, 2000), *sqp* (Tone, 1983; Spellucci, 1998), *active-set* (Gill *et al.*, 1984; Gill *et al.*, 1991) and *trust-region-reflective*. In order to evaluate the influence of the number of parameters considered, the optimisation scenarios listed in Table C.3 are considered.

Table C.3 –Optimisation scenarios with a different number of parameters.

Scenario	Optimised parameters
O1	H
O2	H, m
O3	H, m, k_v

The function *fmincon* requires an initial estimation of the parameters, whereas the function *ga* uses MATLAB internal functions to randomly generate the initial population of parameters. To allow a better comparison of the different approaches, three different initial estimations of the parameters used by the function *fmincon* are generated using the Latin hypercube sampling. The optimisations performed with the genetic algorithm use an initial population consisting of 30 individuals and the default values specified in MATLAB for all the remaining options (number of elites and substitute individuals, crossing and mutation rates, etc.). A tolerance of 0.02 is used for the value of the objective function in all the optimisations. The functions *PropertiesOptimization.m*, *OptimizeFunction.m* and *ObjectiveFunction.m* have been implemented in MATLAB in order to update the model of the railway bridge. The function *PropertiesOptimization.m* defines the initial data of the case study, such as the initial estimate of the parameters, the variables used to calculate the value of the objective function and the name of the APDL macro used to create the numerical model. This function calls the function *OptimizeFunction.m*, which defines the input arguments of the MATLAB functions *fmincon* or *ga*. One of these input arguments is the function *ObjectiveFunction.m*, which contains all the code necessary to calculate the value of the objective function. The initial APDL macro contains the keywords *OPTI_PARAM_1* to *OPTI_PARAM_n*, where n is the number of optimised parameters. At each iteration, these keywords are replaced with the optimised values and the APDL macro is executed. The optimised values of the parameters, the relative differences between the optimised and theoretical values and the total number of iterations obtained for the optimisation scenarios described in Table C.3 are presented in Tables C.4 to C.6.

Table C.4 – Results obtained for optimisation scenario O1.

Algorithm	Simulation	*H* (m)	Error	Iterations
fmincon - interior-point	1	0.849	-8.5E-04	16
	2	0.853	3.1E-03	20
	3	0.849	-7.0E-04	20
fmincon - sqp	1	0.848	-2.7E-03	18
	2	0.853	3.1E-03	17
	3	0.852	2.5E-03	22
fmincon - active-set	1	0.849	-8.5E-04	16
	2	0.852	2.8E-03	12
	3	0.849	-8.1E-04	15
ga	1	0.849	-1.0E-03	120
	2	0.852	2.0E-03	300
	3	0.851	9.4E-04	330

Table C.5 – Results obtained for optimisation scenario O2.

Algorithm	Simulation	*H* (m)	Error	*m* (kg/m)	Error	Iterations
fmincon - interior-point	1	0.850	0.0E+00	18783	4.4E-03	24
	2	0.849	-1.2E-03	18742	2.2E-03	38
	3	0.850	0.0E+00	18646	-2.9E-03	15
fmincon - sqp	1	0.852	1.9E-03	18769	3.7E-03	43
	2	0.851	1.0E-03	18773	3.9E-03	39
	3	0.854	5.0E-03	18991	1.6E-02	35
fmincon - active-set	1	0.847	-4.1E-03	18577	-6.6E-03	27
	2	0.849	-8.3E-04	18745	2.4E-03	30
	3	0.850	2.0E-04	18606	-5.0E-03	23
ga	1	0.851	9.4E-04	18548	-8.1E-03	480
	2	0.854	4.1E-03	18828	6.9E-03	420
	3	0.855	6.4E-03	18988	1.5E-02	660

Table C.6 – Results obtained for optimisation scenario O3.

Algorithm	Simulation	*H* (m)	Error	*m* (kg/m)	Error	k_V (GN/m)	Error	Iterations
fmincon - interior-point	1	0.847	-3.5E-03	18636	-3.4E-03	4.7	1.8E-01	20
	2	0.846	-4.3E-03	18928	1.2E-02	5.4	3.5E-01	183
	3	0.846	-4.3E-03	18925	1.2E-02	5.4	3.5E-01	76
fmincon - sqp	1	0.853	3.8E-03	18614	-4.6E-03	3.7	-7.6E-02	49
	2	0.848	-2.3E-03	18566	-7.1E-03	4.4	9.0E-02	59
	3	0.854	4.6E-03	18916	1.2E-02	4.1	3.6E-02	63
fmincon - active-set	1	0.851	1.5E-03	18657	-2.3E-03	3.5	-1.3E-01	28
	2	0.845	-6.4E-03	18442	-1.4E-02	4.0	3.2E-03	146
	3	0.848	-2.6E-03	18546	-8.2E-03	3.7	-7.1E-02	41
ga	1	0.849	-1.4E-03	18993	1.6E-02	5.0	2.6E-01	1110
	2	0.850	-3.4E-05	18441	-1.4E-02	3.5	-1.1E-01	930
	3	0.854	4.5E-03	18608	-4.9E-03	3.2	-1.9E-01	840

As expected, since the parameters *H* and *m* have higher correlation coefficients (see Fig. C.3), the errors obtained between the theoretical and updated values are very low for all the optimisation scenarios. On the other hand, the parameter k_V presents significant errors due to the low correlation coefficients. Therefore, optimisation parameters with low correlation coefficients should be avoided when performing model updating. The average number of evaluations of the objective function required by the optimisation algorithms for each optimisation scenario are plotted in Fig. C.4. The algorithm *fmincon-sqp* shows an almost linear relation between the number of functions evaluations and the number of parameters optimised. All the optimisations performed using the function *fmincon* need a much lower number of functions evaluations to satisfy the required tolerance than those using the function *ga*. The performance of the genetic algorithm might be improved by changing the default options defined by MATLAB but would require the user to spend a much longer initial learning period when compared to the function *fmincon*.

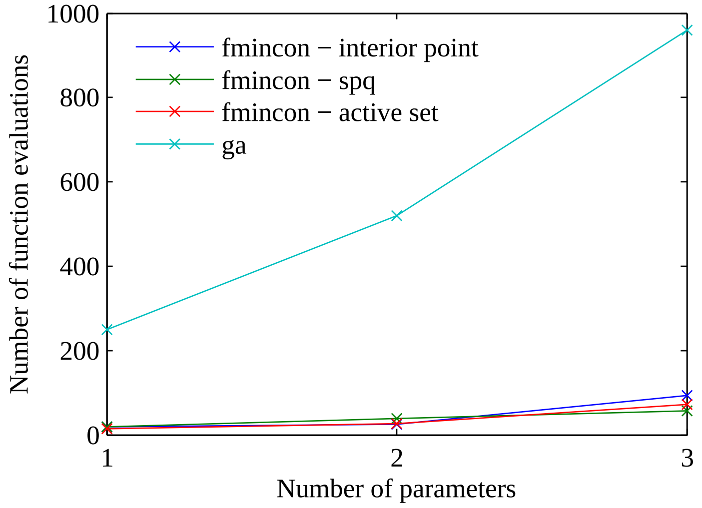

Figure C.4 – Average number of evaluations of the objective function.

The evolution of the parameters optimised in scenario O3 obtained using the MATLAB functions *fmincon* and *ga* and their respective lower and upper bounds are plotted in Figs. C.5 to C.8. For each algorithm, only the simulation with the lowest number of iterations is shown (see Table C.6). The values of each term of the objective function defined by Eq. (C.1) as a function of the iteration number are plotted in Figs. C.9 to C.12.

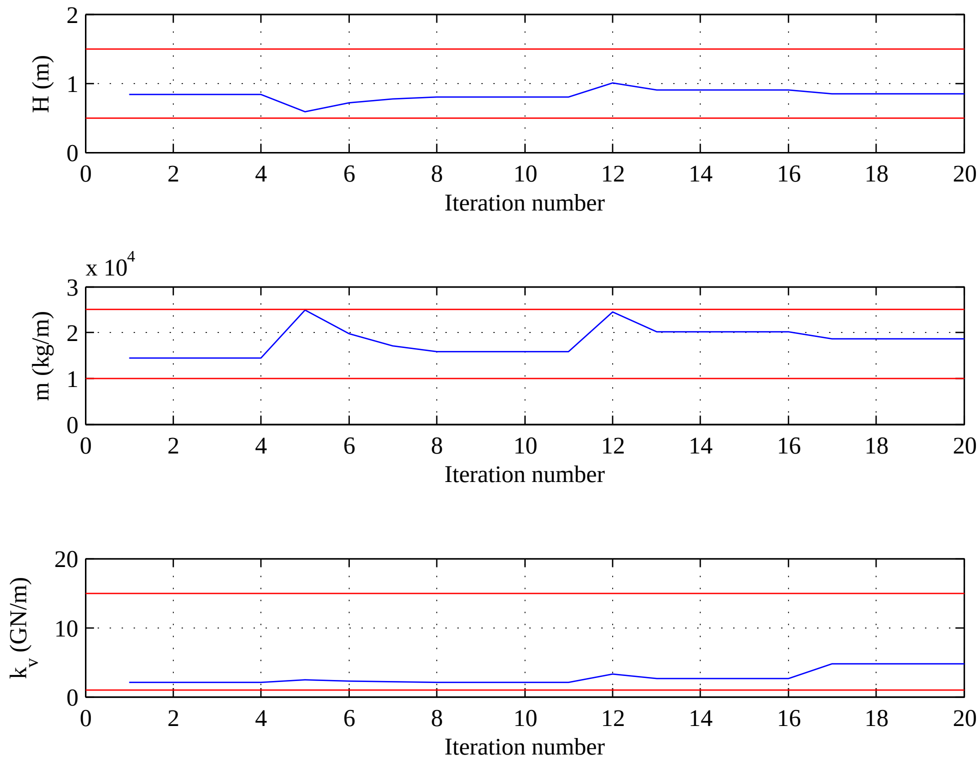

Figure C.5 – Values of the parameters optimised using the function *fmincon* with the option *interior-point*.

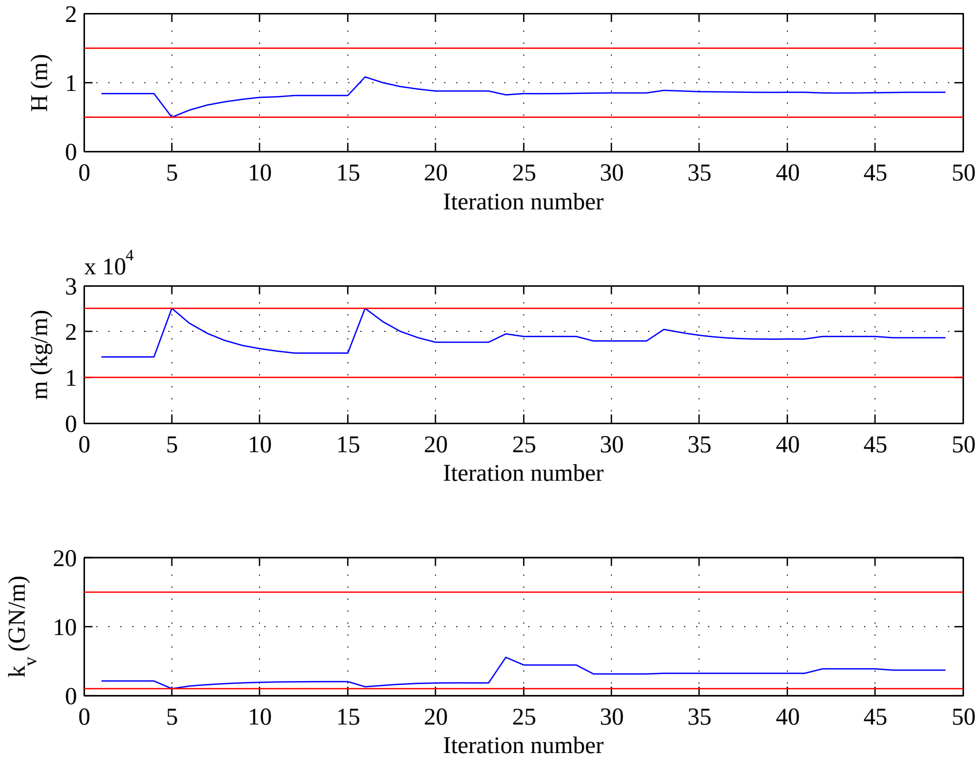

Figure C.6 – Values of the parameters optimised using the function *fmincon* with the option *sqp*.

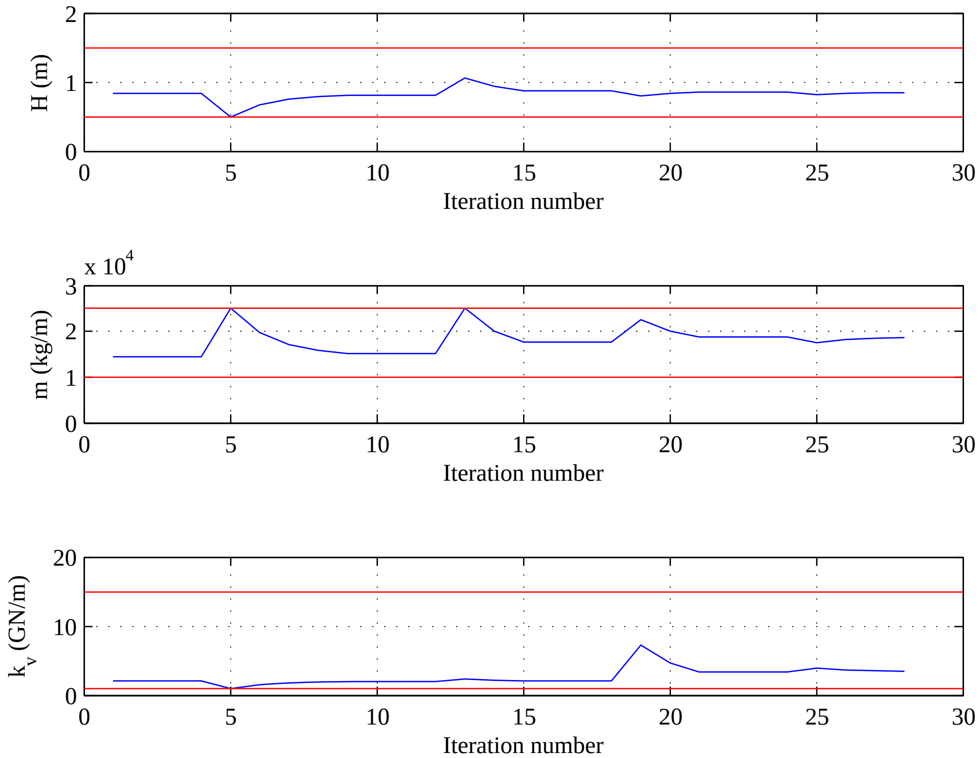

Figure C.7 – Values of the parameters optimised using the function *fmincon* with the option *active-set*.

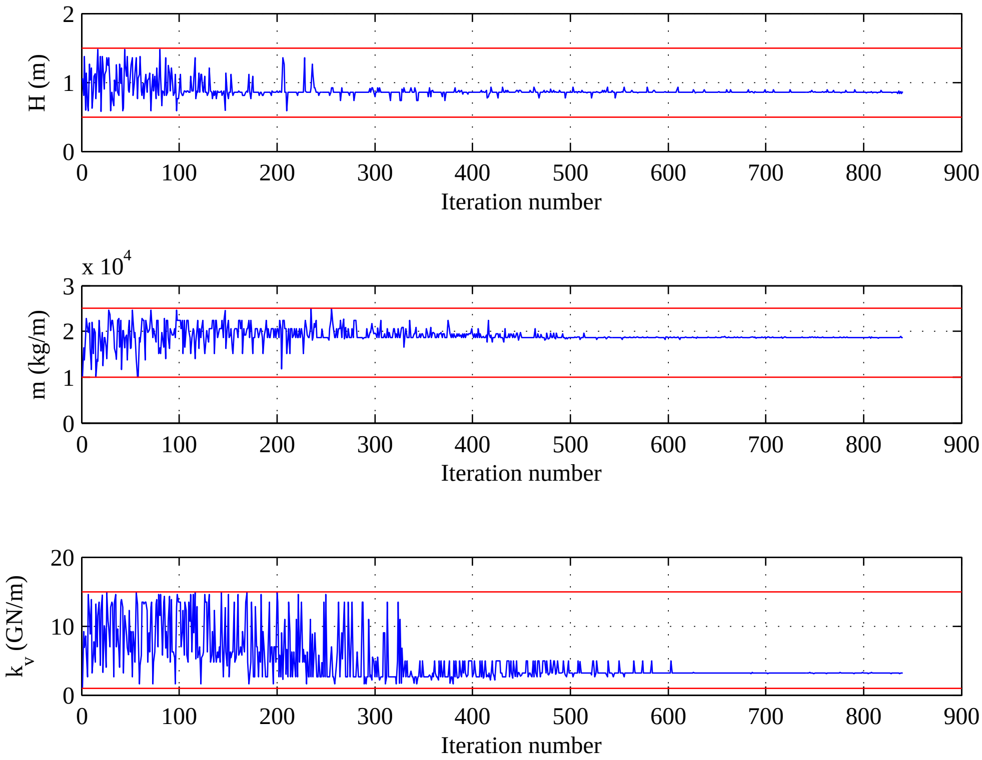

Figure C.8 – Values of the parameters optimised using the function *ga*.

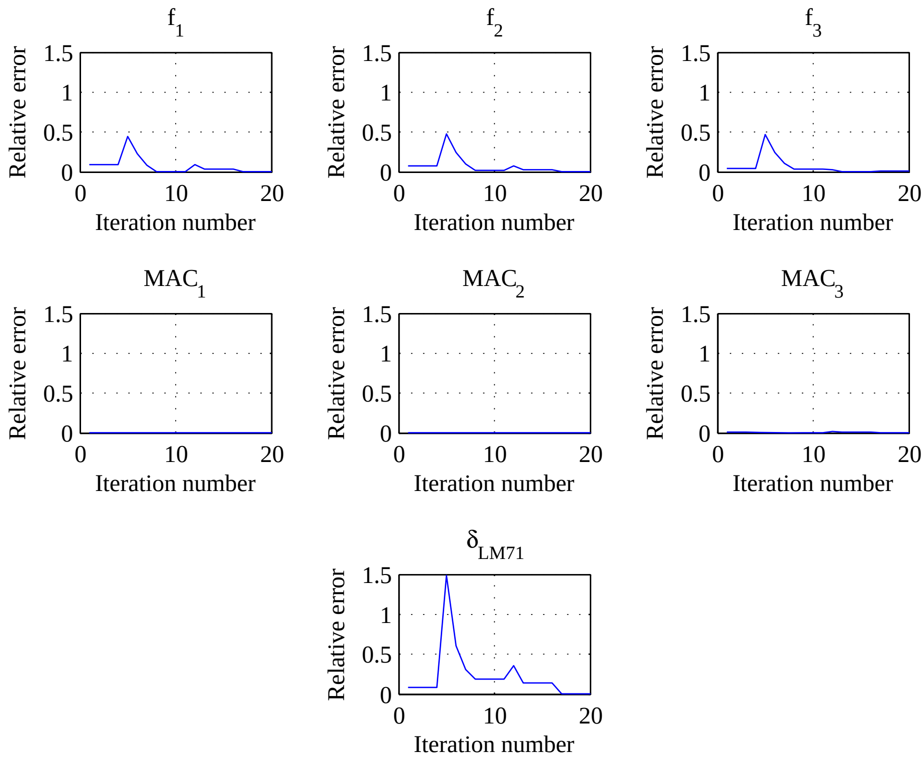

Figure C.9 – Value of each term of the objective function obtained using the function *fmincon* with the option *interior-point*.

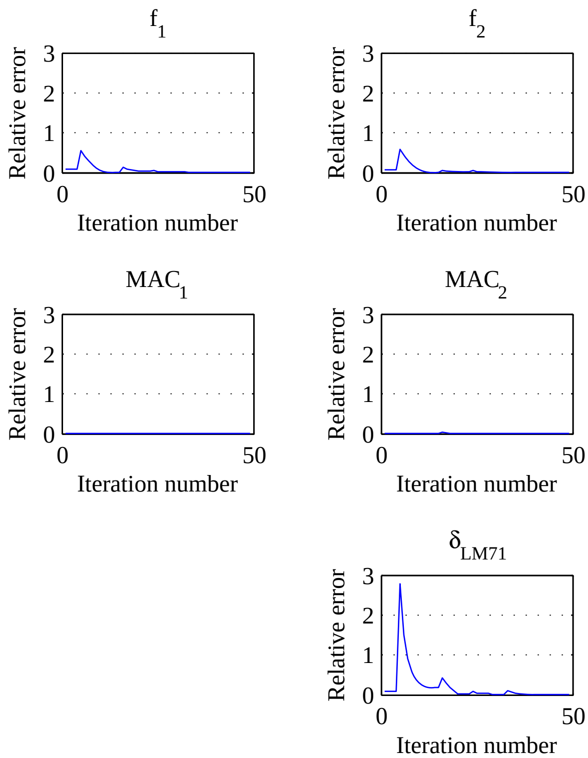

Figure C.10 – Value of each term of the objective function obtained using the function *fmincon* with the option *sqp*.

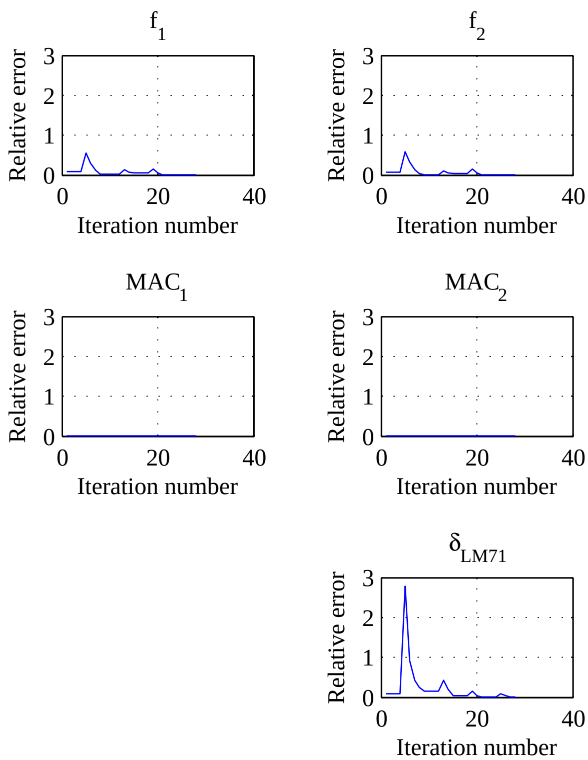

Figure C.11 – Value of each term of the objective function obtained using the function *fmincon* with the option *active-set*.

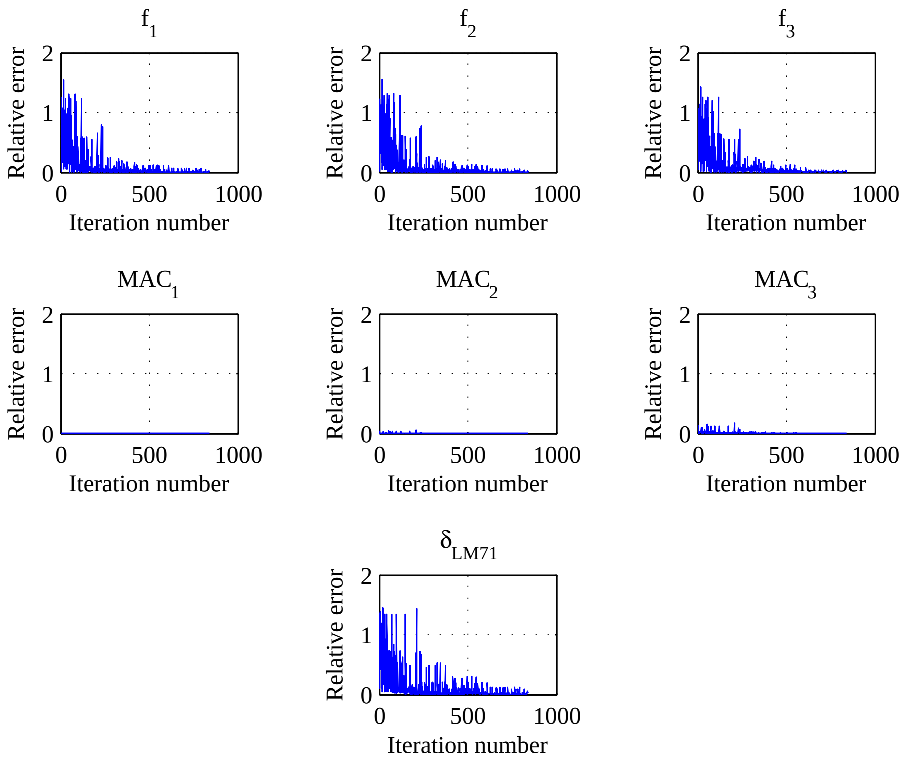

Figure C.12 – Value of each term of the objective function obtained using the function *ga*.

The evolution of the parameters optimised using the function *fmincon* is very similar for the three options considered. The height of the cross-section and the mass per unit length of the slab, which have high correlation coefficients (see Fig. C.3), show a significant variation until reaching the optimised value. On the other hand, the variation of the vertical support stiffness is low. The optimisation performed using the function *ga* leads to a significant variation of all the parameters and requires a much higher number of iterations to satisfy the required tolerance. In all optimisations, the terms of the objective function associated with the natural frequencies and vertical displacement of the bridge at midspan have a much higher variation than that of the mode shapes, which is in line with the Spearman correlation matrix illustrated in Fig. C.3.

REFERENCES

A

Abaqus® (2005). Abaqus Unified FEA (release 6.5). Paris: Dassault Systèmes.

Akin, J. E., & Mofid, M. (1989). Numerical solution for response of beams with moving mass. *Journal of Structural Engineering, 115*, 120-131. DOI:10.1061/(ASCE)0733-9445(1989)115:1(120).

Alves Ribeiro, C. (2012). *Transições aterro–estrutura em linhas ferroviárias de alta velocidade: Análise experimental e numérica* [*Embankment-structure transitions in high-speed railway lines: Experimental and numerical analysis*]. Doctoral dissertation, Faculdade de Engenharia da Universidade do Porto, Porto, Portugal.

ANSYS® (2010). Mechanical APDL. Release 13.0. Canonsburg, PA: ANSYS Inc.

ANSYS® (2014a). Mechanical APDL. Release 15.0. Canonsburg, PA: ANSYS Inc.

ANSYS® (2014b). Mechanical APDL. Release 15.0. Help system, ANSYS Mechanical APDL modelling and meshing guide. Canonsburg, PA: ANSYS Inc.

ANSYS® (2014c). Mechanical APDL. Release 15.0. Help system, ANSYS Mechanical APDL theory reference. Canonsburg, PA: ANSYS Inc.

ANSYS® (2014d). Mechanical APDL. Release 15.0. Help system, ANSYS parametric design language guide. Canonsburg, PA: ANSYS Inc.

Antolín, P., Goicolea, J. M., Oliva, J., & Astiz, M. A. (2012). Nonlinear train-bridge lateral interaction using a simplified wheel-rail contact method within a finite element framework. *Journal of Computational and Nonlinear Dynamics, 7*(4), 041014-041014. DOI:10.1115/1.4006736.

ARTeMIS® (2009). Structural Vibration Solutions.

Au, F. T. K., Wang, J. J., & Cheung, Y. K. (2001). Impact study of cable-stayed bridge under railway traffic using various models. *Journal of Sound and Vibration, 240*(3), 447-465. DOI:10.1006/jsvi.2000.3236.

AutoCAD® (2012). San Rafael, CA: Autodesk Inc.

Ayasse, J. B., & Chollet, H. (2005). Determination of the wheel rail contact patch in semi-Hertzian conditions. *Vehicle System Dynamics, 43*(3), 161-172. DOI:10.1080/00423110412331327193.

Azevedo, A., Barros, J. A. O., Sena-Cruz, J. M., & Ventura-Gouveia, A. (2003). Software no ensino e no projecto de estruturas [*Educational software for the design of structures*]. *3rd Engineering Luso-Mozambican Congress.* Maputo, Moçambique.

Azevedo, A., Neves, S., & Calçada, R. (2008). Dynamic analysis of the train-bridge interaction: an accurate and efficient numerical method. *EURODYN 2008 - 7th European Conference on Structural Dynamics*. Southampton, United Kingdom.

Azevedo, A., Neves, S. G., & Calçada, R. (2007). Dynamic analysis of the vehicle-structure interaction: a direct and efficient computer implementation. In J. C. d. Sá et al. (Eds.), *CMNE 2007 – Congress on Numerical Methods in Engineering / XXVIII CILAMCE - Iberian Latin American Congress on Computational Methods in Engineering.* Porto, Portugal.

B

Bäck, T. (1996). *Evolutionary algorithms in theory and practice: Evolution strategies, evolutionary programming, genetic algorithms*. New York: Oxford University Press.

Bathe, K. J. (1996). *Finite element procedures*. Upper Saddle River, NJ: Prentice-Hall.

Benzi, M., Golub, G. H., & Liesen, J. (2005). Numerical solution of saddle point problems. *Acta Numerica, 14*, 1-137. DOI:10.1017/S0962492904000212.

Biggs, J. M. (1964). *Introduction to structural dynamics*. New York: McGraw-Hill.

Brehm, M. (2011). *Vibration-based model updating: Reduction and quantification of uncertainties*. Doctoral dissertation, Bauhaus-Universitat Weimar, Weimar, Germany.

BS EN 1993-1-1 (2005). Eurocode 3: Design of steel structures. Part 1-1: General rules and rules for buildings. London: British Standards Institution.

BS EN 13674-1 (2011). Railway applications: Track - Rail. Part 1: Vignole railway rails 46 kg/m and above. London: British Standards Institution.

BS EN 13674-1:2011 (2011). Railway applications - Track - Rail - Part 1: Vignole railway rails 46 kg/m and above. London: British Standards Institution.

BS EN 13715:2006+A1:2010 (2006). Railway applications — Wheelsets and bogies — Wheels — Tread profile. London: British Standards Institution.

Burden, R. L., & Faires, J. D. (1997). *Numerical analysis* (6th ed.). Pacific Grove, CA: ITP.

Byrd, H. R., Gilbert, C. J., & Nocedal, J. (2000). A trust region method based on interior point techniques for nonlinear programming. *Mathematical Programming, 89*(1), 149-185. DOI:10.1007/pl00011391.

C

Chopra, A. K. (2007). *Dynamics of structures: Theory and applications to earthquake engineering* (3rd ed.). Upper Saddle River, NJ: Prentice-Hall.

Civity (2013). Further development of the European high-speed rail network.

Clough, R. W., & Penzien, J. (1993). *Dynamics of structures* (2nd ed.). New York: McGraw Hill.

Corder, G. W., & Foreman, D. I. (2014). *Nonparametric statistics : A step-by-step approach* (2nd ed.). Somerset, NJ: Wiley.

D

De Man, A. P. (2002). *A survey of dynamic railway track properties and their quality*. Doctoral dissertation, Delft University of Technology, Delft, The Netherlands.

Delgado, R., & Santos, S. M. (1997). Modelling of railway bridge-vehicle interaction on high speed tracks. *Computers & Structures, 63*, 511-523. DOI:10.1016/S0045-7949(96)00360-4.

Diana, G., Cheli, F., Collina, A., Corradi, R., & Melzi, S. (2002). The development of a numerical model for railway vehicles comfort assessment through comparison with experimental measurements. *Vehicle System Dynamics, 38*, 165-183. DOI:10.1076/vesd.38.3.165.8287.

E

EC communication (2011). A roadmap for moving to a competitive low carbon economy in 2050. Brussels: European Commission.

EEA Report n. 7 (2014). Focusing on environmental pressures from long-distance transport. TERM 2014: transport indicators tracking progress towards environmental targets in Europe. Copenhagen: European Environment Agency.

EN 1990-A2 (2005). Eurocode: basis of structural design. Annex A2: application for bridges. Brussels, Belgium: European Committee for Standardization (CEN).

EN 1991-2 (2003). Eurocode 1: actions on structures. Part 2: traffic loads on bridges. Brussels, Belgium: European Committee for Standardization (CEN).

EN 13848-1 (2003). Railway applications - Track - Track geometry quality. Part 1: Characterisation of track geometry. Brussels, Belgium: European Committee for Standardization (CEN).

EN 13848-5 (2008). Railway applications - Track - Track geometry quality. Part 5: Geometric quality levels - Plain line. Brussels, Belgium: European Committee for Standardization (CEN).

ERRI D 214/RP 5 (1999). Numerical investigation of the effect of track irregularities at bridge resonance. Utrecht, Netherlands: European Rail Research Institute.

ERRI D 214/RP 9 (2001). Railway bridges for speeds >200 km/h: Final Report. Utrecht, Netherlands: European Rail Research Institute.

Esveld, C. (2001). *Modern railway track* (2nd ed.). Zaltbommel: MRT Productions.

Everitt, B. (1987). *Introduction to optimization methods and their application in statistics*. London: Chapman and Hall.

F

Faria, R. (1994). *Avaliação do comportamento sísmico de barragens de betão através de um modelo de dano contínuo* [*Assessment of the seismic behavior of concrete dams based on a continuum damage model*]. Doctoral dissertation, Faculdade de Engenharia da Universidade do Porto, Porto, Portugal.

Faria, R., Vila Pouca, N., & Delgado, R. (2002). Seismic behaviour of a R/C wall: Numerical simulation and experimental validation. *Journal of Earthquake Engineering, 6*(4), 473-498. DOI:10.1142/S136324690200084X.

FEMIX. FEMIX (Release 4.0). http://www.alvaroazevedo.com/femix (Accessed July 8, 2011).

Fernandes, M. A. M. (2010). *Comportamento dinâmico de pontes com tabuleiro pré-fabricado em vias de alta velocidade* [*Dynamic behaviour of bridges with precast deck in high-speed lines*]. Master's thesis, Faculdade de Engenharia da Universidade do Porto, Porto, Portugal.

Frýba, L. (1999). *Vibration of solids and structures under moving loads* (3rd ed.). London: Thomas Telford.

G

García Orden, J. C., & Goicolea, J. M. (2000). Conserving properties in constrained dynamics of flexible multibody systems. *Multibody System Dynamics, 4*(2-3), 225-244. DOI: 10.1023/A:1009871728414.

Garg, V. K., & Dukkipati, V. (1984). *Dynamics of railway vehicle systems*. Academic Press.

Garthwaite, P. H., Jolliffe, I. T., & Jones, B. (2002). *Statistical inference* (Vol. 2nd). Oxford: Oxford University Press.

GENSYS® (2004). Release 0403. AB DEsolver.

Gill, P. E., Murray, W., Saunders, M. A., & Wright, M. H. (1984). Procedures for optimization problems with a mixture of bounds and general linear constraints. *ACM Trans. Math. Softw., 10*(3), 282-298. DOI:10.1145/1271.1276.

Gill, P. E., Murray, W., & Wright, M. H. (1981). *Practical optimization*. London: Academic Press.

Gill, P. E., Murray, W., & Wright, M. H. (1991). *Numerical linear algebra and optimization* (Vol. 1). Addison-Wesley.

Goicolea, J. M., & Antolin, P. (2012). The dynamics of high-speed railway bridges: A review of design issues and new research for lateral dynamics. *International Journal of Railway Technology, 1*(1), 27-55. DOI:10.4203/ijrt.1.1.2.

Goicolea, J. M., Gabaldón, F., & Riquelme, F. (2006). Design issues for dynamics of high speed railway bridges. *3rd International Conference on Bridge Maintenance, Safety and Management - Bridge Maintenance, Safety, Management, Life-Cycle Performance and Cost.*

Goldberg, D. E. (1989). *Genetic algorithms in search, optimization and machine learning*. Addison-Wesley.

Goldsmith, W. (1960). *Impact: The theory and physical behaviour of colliding solids*. London: Edward Arnold.

Green, M. F., & Cebon, D. (1994). Dynamic response of highway bridges to heavy vehicle loads - theory and experimental validation. *Journal of Sound and Vibration, 170*(1), 51-78. DOI:10.1006/jsvi.1994.1046.

Greenwood, J. A., Johnson, K. L., & Matsubara, E. (1984). A surface roughness parameter in Hertz contact. *Wear, 100*(1-3), 47-57. DOI:10.1016/0043-1648(84)90005-X.

Guyan, R. J. (1965). Reduction of stiffness and mass matrices. *AIAA Journal, 3*(2), 380-380. DOI:10.2514/3.2874.

H

Hertz, H. (1882). Ueber die Berührung fester elastischer Körper [On the contact of elastic solids]. *Journal für die reine und angewandte Mathematik, 1882*(92), 156–171. DOI:10.1515/crll.1882.92.156.

Hertz, H., Jones, D. E., & Schott, G. A. (1896). *Miscellaneous papers*. London: Macmillan and Co.

Hilber, H. M., Hughes, T. J. R., & Taylor, R. L. (1977). Improved numerical dissipation for time integration algorithms in structural dynamics. *Earthquake Engineering & Structural Dynamics, 5*(3), 283-292. DOI:10.1002/eqe.4290050306.

Horas, C. C. S. (2011). *Comportamento dinâmico de pontes com tabuleiro pré-fabricado em vias de alta velocidade* [*Dynamic behaviour of bridges with precast deck in high-speed lines*]. Master's thesis, Faculdade de Engenharia da Universidade do Porto, Porto, Portugal.

Hu, B., & Schiehlen, W. (1997). On the simulation of stochastic processes by spectral representation. *Probabilistic Engineering Mechanics, 12*(2), 105-113. DOI:10.1016/S0266-8920(96)00039-2.

Hughes, T. J. R. (2000). *The finite element method: Linear static and dynamic finite element analysis*. New York: Dover Publications.

Hwang, E. S., & Nowak, A. S. (1991). Simulation of dynamic load for bridges. *Journal of Structural Engineering, 117*, 1413-1434. DOI:10.1061/(ASCE)0733-9445(1991)117:5(1413).

I

Iman, R. L., & Hora, S. C. (1990). A robust measure of uncertainty importance for use in fault tree system analysis. *Risk Analysis, 10*(3), 401-406. DOI:10.1111/j.1539-6924.1990.tb00523.x.

Inbanathan, M. J., & Wieland, M. (1987). Bridge vibrations due to vehicle moving over rough-surface. *Journal of Structural Engineering, 113*(9), 1994-2008. DOI:10.1061/(ASCE)0733-9445(1987)113:9(1994).

IPCC. Intergovernmental Panel on Climate Change. http://www.ipcc.ch/ (Accessed July 1, 2016).

Iwnicki, S. (2006). *Handbook of railway vehicle dynamics*. Boca Raton: CRC Press.

J

Johnson, K. L. (1999). *Contact mechanics*. Cambridge: Cambridge University Press.

Jones, S., & Hunt, H. (2011). Voids at the tunnel–soil interface for calculation of ground vibration from underground railways. *Journal of Sound and Vibration, 330*(2), 245-270. DOI:10.1016/j.jsv.2010.08.015.

Jorge, P. F. M. (2013). *Efeitos dinâmicos induzidos por tráfego ferroviário de alta velocidade num viaduto com tabuleiro pré-fabricado* [*Dynamic behaviour of a railway viaduct with a precast deck under traffic loads*]. Master's thesis, Faculdade de Engenharia da Universidade do Porto, Porto, Portugal.

K

Kausel, E. (2008). Commentaries on methods to estimate ground vibrations elicited by fast moving loads. In R. Calçada, A. Carvalho, & G. Degrande (Eds.), *Noise and Vibration on High-Speed Railways.* Porto, Portugal.

Kwark, J. W., Choi, E. S., Kim, Y. J., Kim, B. S., & Kim, S. I. (2004). Dynamic behavior of two-span continuous concrete bridges under moving high-speed train. *Computers & Structures, 82*(4-5), 463-474. DOI:10.1016/S0045-7949(03)00054-3.

L

Lee, Y. S., & Kim, S. H. (2010). Structural analysis of 3D high-speed train-bridge interactions for simple train load models. *Vehicle System Dynamics, 48*(2), 263-281. DOI:10.1080/00423110902751912.

Liu, K., Lombaert, G., & Roeck, G. D. (2014). Dynamic analysis of multispan viaducts with weak coupling between adjacent spans. *Journal of Bridge Engineering, 19*(1), 83-90. DOI:doi:10.1061/(ASCE)BE.1943-5592.0000476.

Lombaert, G., & Degrande, G. (2009). Ground-borne vibration due to static and dynamic axle loads of InterCity and high-speed trains. *Journal of Sound and Vibration, 319*(3–5), 1036-1066. DOI:10.1016/j.jsv.2008.07.003.

M

Malveiro, J., Ribeiro, D., Calçada, R., & Delgado, R. (2013). Updating and validation of the dynamic model of a railway viaduct with precast deck. *Structure and Infrastructure Engineering, 10*(11), 1484-1509. DOI:10.1080/15732479.2013.833950.

Maple® (2009). Release 13. Waterloo, Ontario: Maplesoft, Maple Inc.

MATLAB® (2013). Release R2013b. Natick, MA: The MathWorks Inc.

McConnell, S. (2004). *Code complete* (2nd ed.). Redmond, WA: Microsoft.

McKenzie, N. J., Grundy, M. J., Webster, R., & Ringrose-Voase, A. J. (2008). *Guidelines for surveying soil and land resources* (2nd ed.). Melbourne: CSIRO Publishing.

Meixedo, A. G. (2012). *Comportamento dinâmico de pontes com tabuleiro pré-fabricado em vias de alta velocidade* [*Dynamic behaviour of bridges with precast deck in high-speed lines*]. Master's thesis, Faculdade de Engenharia da Universidade do Porto, Porto, Portugal.

Montenegro, P. A. (2015). *A methodology for the assessment of the train running safety on bridges*. Doctoral dissertation, Faculdade de Engenharia da Universidade do Porto, Porto, Portugal.

Montenegro, P. A., Calçada, R., Vila Pouca, N., & Tanabe, M. (2016). Running safety assessment of trains moving over bridges subjected to moderate earthquakes. *Earthquake Engineering and Structural Dynamics, 45*(3), 483-504. DOI:10.1002/eqe.2673.

Montenegro, P. A., Neves, S. G. M., Azevedo, A. F. M., & Calçada, R. (2013). A nonlinear vehicle-structure interaction methodology with wheel-rail detachment and reattachment. In M. Papadrakakis, N.D.Lagaros, & V. Plevris (Eds.), *COMPDYN 2013 – 4th International Conference on Computational Methods in Structural Dynamics and Earthquake Engineering*. Kos Island, Greece.

Montenegro, P. A., Neves, S. G. M., Calçada, R., Tanabe, M., & Sogabe, M. (2014a). A nonlinear vehicle-structure interaction methodology for the assessment of the train running safety. In A. Cunha, E. Caetano, P. Ribeiro, & G. Müller (Eds.), *EURODYN 2014 - 9th International Conference on Structural Dynamics*. Porto, Portugal.

Montenegro, P. A., Neves, S. G. M., Calçada, R., Tanabe, M., & Sogabe, M. (2014b). A three dimensional train-structure interaction methodology: Experimental validation. In J. Pombo (Ed.), *Railways 2014 - 2nd International Conference on Railway Technology: Research, Development and Maintenance*. Ajaccio, Corsica. Stirlingshire, UK: Civil-Comp Press. DOI:10.4203/ccp.104.71.

Montenegro, P. A., Neves, S. G. M., Calçada, R., Tanabe, M., & Sogabe, M. (2015). Wheel-rail contact formulation for analyzing the lateral train-structure dynamic interaction. *Computers & Structures, 152*, 200-214. DOI:10.1016/j.compstruc.2015.01.004.

N

Neves, S., Azevedo, A., & Calçada, R. (2008). Development of an efficient finite element model for the dynamic analysis of the train-bridge interaction. *IABMAS 2008 – 4th International Conference on Bridge Maintenance, Safety and Management*. Seoul, Korea.

Neves, S. G. M. (2008). *Análise dinâmica com interacção veículo-estrutura em vias de alta velocidade* [*Dynamic analysis of the vehicle-structure interaction in high-speed lines*]. Master's thesis, Faculdade de Engenharia da Universidade do Porto, Porto, Portugal. DOI:10.13140/RG.2.1.1510.9524.

Neves, S. G. M., Azevedo, A. F. M., & Calçada, R. (2012). A direct method for analyzing the vertical vehicle-structure interaction. *Engineering Structures, 34*, 414-420. DOI:10.1016/j.engstruct.2011.10.010.

Neves, S. G. M., Montenegro, P. A., Azevedo, A. F. M., & Calçada, R. (2014a). A direct method for analyzing the nonlinear vehicle-structure interaction. *Engineering Structures, 69*, 83-89. DOI:10.1016/j.engstruct.2014.02.027.

Neves, S. G. M., Montenegro, P. A., Azevedo, A. F. M., & Calçada, R. (2014b). A direct method for analyzing the nonlinear vehicle-structure interaction in high-speed railway lines. In J. Pombo (Ed.), *Railways 2014 - 2nd International Conference on Railway Technology: Research, Development and Maintenance*. Ajaccio, Corsica. Stirlingshire, UK: Civil-Comp Press. DOI:10.4203/ccp.104.81.

Newmark, N. M. (1959). A method of computation for structural dynamics. *Journal of the Engineering Mechanics Division, 85*(3), 67-94.

Nielsen, J. C. O., Lundén, R., Johansson, A., & Vernersson, T. (2003). Train-track interaction and mechanisms of irregular wear on wheel and rail surfaces. *Vehicle System Dynamics, 40*, 3-54. DOI:10.1076/vesd.40.1.3.15874.

Nielsen, J. C. O., & Oscarsson, J. (2004). Simulation of dynamic train-track interaction with state-dependent track properties. *Journal of Sound and Vibration, 275*, 515-532. DOI:10.1016/j.jsv.2003.06.033.

O

Owen, D. R. J., & Hinton, E. (1980). *Finite elements in plasticity: Theory and practice*. Swansea, UK: Pineridge Press Limited.

P

Paris Agreement (2015). The Paris Protocol: A blueprint for tackling global climate change beyond 2020. Brussels: European Commission.

Paz, M. (1984). Dynamic condensation. *AIAA Journal, 22*(5), 724-727. DOI:10.2514/3.48498.

Paz, M. (1989). Modified dynamic condensation method. *Journal of Structural Engineering, 115*(1), 234-238. DOI:10.1061/(ASCE)0733-9445(1989)115:1(234).

Paz, M. (1997). *Structural dynamics : Theory and computation* (4th ed.). New York: Chapman & Hall.

Popp, K., Kruse, H., & Kaiser, I. (1999). Vehicle-track dynamics in the mid-frequency range. *Vehicle System Dynamics, 31*, 423-464. DOI:10.1076/vesd.31.5.423.8363.

R

Ribeiro, D., Calçada, R., Delgado, R., Brehm, M., & Zabel, V. (2012). Finite element model updating of a bowstring-arch railway bridge based on experimental modal parameters. *Engineering Structures, 40*, 413-435. DOI:10.1016/j.engstruct.2012.03.013.

Ribeiro, D. R. F. (2004). *Comportamento dinâmico de pontes sob acção de tráfego ferroviário a alta velocidade* [*Dynamic behaviour of bridges under high-speed railway traffic*]. Master's thesis, Faculdade de Engenharia da Universidade do Porto, Porto, Portugal.

Ribeiro, D. R. F. (2012). *Efeitos dinâmicos induzidos por tráfego em pontes ferroviárias: Modelação numérica, calibração e validação experimental* [*Dynamic effects induced by traffic on railway bridges: Numerical modelling, calibration and experimental validation*]. Doctoral dissertation, Faculdade de Engenharia da Universidade do Porto, Porto, Portugal.

Rigueiro, C. (2007). *Avaliação dos efeitos dinâmicos em pontes ferroviárias de alta velocidade de pequeno e médio vão* [*Assessment of the dynamic effects in short and *medium bridges in high-speed railway lines*]. Doctoral dissertation, Faculdade de Ciências e Tecnologia da Universidade de Coimbra, Coimbra, Portugal.

Rigueiro, C., Rebelo, C., & Simões da Silva, L. (2010). Influence of ballast models in the dynamic response of railway viaducts. *Journal of Sound and Vibration, 329*(15), 3030-3040. DOI:10.1016/j.jsv.2010.02.002.

Rocha, J. M. (2016). *Probabilistic methodologies for the safety assessment of short span railway bridges for high-speed traffic*. Doctoral dissertation, Faculdade de Engenharia da Universidade do Porto, Porto, Portugal.

Rocha, J. M., Henriques, A. A., & Calçada, R. (2012). Safety assessment of a short span railway bridge for high-speed traffic using simulation techniques. *Engineering Structures, 40*, 141-154. DOI:10.1016/j.engstruct.2012.02.024.

S

Santos, N. C. (2013). *Vibrações induzidas por tráfego na via e na envolvente de linhas ferroviárias: Modelação numérica 3D e validação experimental* [*Track ground vibrations induced by railway traffic: 3D numerical modelling and experimental validation*]. Doctoral dissertation, Faculdade de Engenharia da Universidade do Porto, Porto, Portugal.

Shabana, A. A., Berzeri, M., & Sany, J. R. (2001). Numerical procedure for the simulation of wheel/rail contact dynamics. *Journal of Dynamic Systems, Measurement and Control, 123*(2), 168-178. DOI:10.1115/1.1369109.

Shabana, A. A., Zaazaa, K. E., & Sugiyama, H. (2007). *Railroad vehicle dynamics: a computational approach*. Boca Raton, FL: CRC Press.

Shift2Rail (2014). Shift2Rail fact sheet: driving innovation on railways. Brussels: European Commission.

Shin, J.-R., An, Y.-K., Sohn, H., & Yun, C.-B. (2010). Vibration reduction of high-speed railway bridges by adding size-adjusted vehicles. *Engineering Structures, 32*(9), 2839-2849. DOI:10.1016/j.engstruct.2010.05.003.

Simpack®. Gilching: Dassault Systemes GmbH.

Song, M.-K., Noh, H.-C., & Choi, C.-K. (2003). A new three-dimensional finite element analysis model of high-speed train-bridge interactions. *Engineering Structures, 25*(13), 1611-1626. DOI:10.1016/S0141-0296(03)00133-0.

Spellucci, P. (1998). A new technique for inconsistent QP problems in the SQP method. *Mathematical Methods of Operations Research, 47*(3), 355-400. DOI:10.1007/bf01198402.

Steenbergen, M. J. M. M., & Esveld, C. (2006). Relation between the geometry of rail welds and the dynamic wheel-rail response: Numerical simulations for measured welds. *Proceedings of the Institution of Mechanical Engineers, Part F: Journal of Rail and Rapid Transit, 220*(4), 409-423. DOI:10.1243/0954409JRRT87.

T

Thompson, D. (2009). *Railway noise and vibration: Mechanisms, modelling and means of control*. Amsterdam: Elsevier.

Ting, E. C., Genin, J., & Ginsberg, J. H. (1974). A general algorithm for moving mass problems. *Journal of Sound and Vibration, 33*(1), 49-58. DOI:10.1016/S0022-460X(74)80072-6.

Tone, K. (1983). Revisions of constraint approximations in the successive QP method for nonlinear programming problems. *Mathematical Programming, 26*(2), 144-152. DOI:10.1007/bf02592051.

V

Vale, C. (2010). *Influência da qualidade dos sistemas ferroviários no comportamento dinâmico e no planeamento da manutenção preventiva de vias de alta velocidade* [*Influence of railway systems quality on dynamic behaviour and on scheduling preventive maintenance for high-speed railway tracks*]. Doctoral dissertation, Faculdade de Engenharia da Universidade do Porto, Porto, Portugal.

VAMPIRE® (2014). Release 6.3. Derby: DeltaRail Group Ltd.

Veletsos, A. S., & Huang, T. (1970). Analysis of dynamic response of highway bridges. *Journal of the Engineering Mechanics Division, 96*(5), 593-620.

VI-Rail®. Marburg: VI-grade GmbH.

Vollebregt, E. (2009). Release 15.1. User guide for contact, rolling and sliding contact with friction. Technical report TR09-03. Delft: VORtech Computing.

W

Wang, T. L., & Huang, D. (1992). Cable-stayed bridge vibration due to road surface roughness. *Journal of Structural Engineering, 118*(5), 1354-1374. DOI:10.1061/(ASCE)0733-9445(1992)118:5(1354).

White paper (2011). Roadmap to a single European transport area: Towards a competitive and resource efficient transport system. Brussels: European Commission.

Wiest, M., Kassa, E., Daves, W., Nielsen, J. C. O., & Ossberger, H. (2008). Assessment of methods for calculating contact pressure in wheel-rail/switch contact. *Wear, 265*(9–10), 1439-1445. DOI:10.1016/j.wear.2008.02.039.

Willis, R. (1849). *Report of the commissioners appointed to inquire into the application of iron to railway structures. Appendix B: Experiments for determining the effects produced by causing weights to travel over bars with different velocities*. London: HM Stationery Office.

Wriggers, P. (2002). *Computational contact mechanics*. Chichester, England: John Wiley & Sons.

X

Xia, H., & Zhang, N. (2005). Dynamic analysis of railway bridge under high-speed trains. *Computers and Structures, 83*(23-24), 1891-1901. DOI:10.1016/j.compstruc.2005.02.014.

Y

Yan, W., & Fischer, F. D. (2000). Applicability of the Hertz contact theory to rail-wheel contact problems. *Archive of Applied Mechanics, 70*(4), 255-268. DOI:10.1007/s004199900035.

Yang, F. H., & Fonder, G. A. (1996). An iterative solution method for dynamic response of bridge-vehicles systems. *Earthquake Engineering & Structural Dynamics, 25*, 195-215. DOI:10.1002/(SICI)1096-9845(199602)25:2<195::AID-EQE547>3.0.CO;2-R.

Yang, Y.-B., Chang, C.-H., & Yau, J.-D. (1999). An element for analysing vehicle-bridge systems considering vehicle's pitching effect. *International Journal for Numerical Methods in Engineering, 46*, 1031-1047. DOI:10.1002/(SICI)1097-0207(19991110)46:7<1031::AID-NME738>3.0.CO;2-V.

Yang, Y.-B., & Lin, B.-H. (1995). Vehicle-bridge interaction analysis by dynamic condensation method. *Journal of Structural Engineering, 121*(11), 1636. DOI:10.1061/(ASCE)0733-9445(1995)121:11(1636).

Yang, Y.-B., & Wu, Y.-S. (2001). A versatile element for analyzing vehicle-bridge interaction response. *Engineering Structures, 23*, 452-469. DOI:10.1016/S0141-0296(00)00065-1.

Yang, Y.-B., & Yau, J.-D. (1997). Vehicle-bridge interaction element for dynamic analysis. *Journal of Structural Engineering, 123*, 1512-1518. DOI:10.1061/(ASCE)0733-9445(1997)123:11(1512).

Yang, Y. B. (2004). *Vehicle-bridge interaction dynamics with application to high-speed railways*. Singapore: World Scientific.

Yau, J.-D., Yang, Y.-B., & Kuo, S.-R. (1999). Impact response of high speed rail bridges and riding comfort of rail cars. *Engineering Structures, 21*, 836-844. DOI:10.1016/S0141-0296(98)00037-6.

Z

Zhai, W., & Cai, Z. (1997). Dynamic interaction between a lumped mass vehicle and a discretely supported continuous rail track. *Computers & Structures, 63*, 987-997. DOI:10.1016/S0045-7949(96)00401-4.

Zhang, N., Xia, H., & Guo, W. (2008). Vehicle-bridge interaction analysis under high-speed trains. *Journal of Sound and Vibration, 309*, 407-425. DOI:10.1016/j.jsv.2007.07.064.